A modelling study of ridge flank hydrothermal circulation globally, constrained by fluid and rock chemistry, and seafloor heat flow

by

Brock Anderson
B.Sc., University of Victoria, 2004

A Dissertation Submitted in Partial Fulfillment
of the Requirements for the Degree of

DOCTOR OF PHILOSOPHY

in the School of Earth and Ocean Sciences

Supervisory Committee

A modelling study of ridge flank hydrothermal circulation globally, constrained by fluid and rock chemistry, and seafloor heat flow

by

Brock Anderson
B.Sc., University of Victoria, 2004

Supervisory Committee

Dr. Laurence Coogan, (School of Earth and Ocean Sciences)
Co-Supervisor

Dr. Kathryn Gillis, (School of Earth and Ocean Sciences)
Co-Supervisor

Dr. Brian Bornhold, (School of Earth and Ocean Sciences)
Departmental Member

Dr. Dan Smith, (Department of Geography)
Outside Member

Abstract

Supervisory Committee
Dr. Laurence Coogan, (School of Earth and Ocean Sciences)
Co-Supervisor
Dr. Kathryn Gillis, (School of Earth and Ocean Sciences)
Co-Supervisor
Dr. Brian Bornhold, (School of Earth and Ocean Sciences)
Departmental Member
Dr. Dan Smith (Department of Geography)
Outside Member

Hydrothermal circulation through the seafloor on the mid-ocean ridge flanks is responsible for globally significant fluid, heat and chemical fluxes between the ocean and the oceanic crust. This dissertation investigates the locations of fluid ingress and egress, fluid flow paths within the crust, and the hydrology of the crust. Based on a global compilation of sediment interstitial water chemistry and models of interstitial water chemical transport and reaction, it is found that <10% of the ridge flank hydrothermal fluid flux passes through marine sediments globally. This requires that the large majority of hydrothermal fluid enters and leaves the crust through exposed basement outcropping through the sediment ("outcrops"). A probabilistic model of basement topography and sedimentation was used to quantify the distribution of seafloor outcrops globally, estimating that outcrops are, on average, a few kilometres apart on young crust, increasing to tens of kilometres apart as the crust ages. A model in which fluid travels laterally within the crustal aquifer for kilometres to tens of kilometres between discrete outcrops ("outcrop-to-outcrop flow") is consistent with the global heat flow data. This finding supports the proposition that outcrop-to-outcrop flow is the dominant mode of ridge flank hydrothermal circulation globally. An alternative model of ridge flank hydrothermal circulation in which fluid circulation occurs by local convection within

isolated outcrops is also possible, and is probably the dominant mode of circulation in crust younger than 3-5 Myrs old, on average, where there is insufficient sediment cover to support the lateral pressure gradients required by outcrop-to-outcrop flow. Estimated crystallization temperatures of carbonate minerals in the crust suggest that, at some locations in the aquifer, local convective mixing may be restricted (i.e., the aquifer is poorly mixed), whereas the carbonate data for other locations cannot distinguish between a well mixed and a poorly mixed aquifer. A poorly mixed aquifer requires that vertical permeability is 1.5 - 2.5 orders of magnitude lower than horizontal permeability. This permeability anisotropy may arise from interlaying of different lithological units within the upper crust.

Table of Contents

List of Tables

List of Figures

Acknowledgments

Many thanks to my supervisors, Laurence Coogan and Kathryn Gillis, for their support through countless useful discussions and much thoughtful advice.

1. Ridge flank hydrothermal systems

The igneous oceanic crust is the world's largest aquifer. The most porous and permeable zone of the oceanic crust, representing the aquifer, is the upper few hundred metres of igneous rocks where highly fractured lithologic units, such as pillow basalt and breccia, are common [*Fisher*, 1998]. Because the oceanic crust is hydraulically connected to the ocean, the void spaces within these rocks are saturated with fluid. Geothermal heat released by the underlying lithosphere provides an energy source that drives convective circulation of fluid within the aquifer [*Parsons and Sclater*, 1977]. The convective circulation draws seawater into the crust, where heat and chemical exchange between the fluid and the crustal rocks occur, before discharging the fluid back into the ocean.

The most conspicuous evidence for seafloor hydrothermal circulation occurs at mid-ocean ridge axes where magma chambers underlie young oceanic crust, and high temperature fluids (in excess of 350°C) discharge from the crust in focused plumes [e.g., *Macdonald et al.*, 1980]. Hydrothermal fluid also circulates through the crustal aquifer away from the mid-ocean ridge axis, on the ridge flanks (Figure 1.1). This circulation occurs on a global scale, and is responsible for pumping the entire volume of the ocean through the oceanic crust every few hundred thousand years [*Johnson and Pruis*, 2003], with the large majority of the fluid passing through ridge flanks [*Mottl and Wheat*, 1994]. Seafloor hydrothermal circulation also removes heat from the lithosphere.

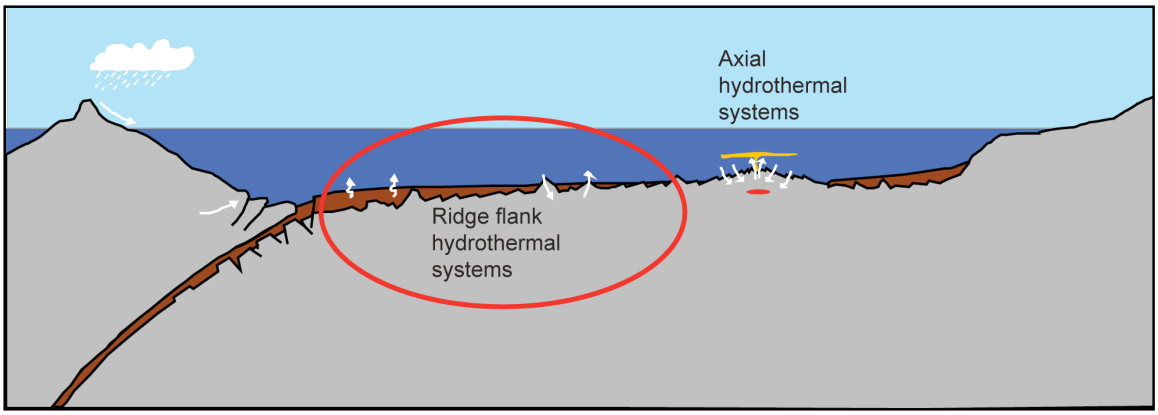

Figure 1.1. A schematic diagram of seafloor hydrothermal systems, modified from Davis and Elderfield [2004]. Ridge flank hydrothermal systems have smaller thermal driving forces than axial systems. Low permeability sediments blanketing the basement impede fluid exchange between the ocean and the crustal aquifer on the ridge flanks.

Hydrothermal circulation is a key process in global geochemical cycling of numerous elements; interaction between hydrothermal fluid and the oceanic crust results in chemical and mineralogical changes to both the igneous crustal rocks [e.g., *Alt*, 2004] and marine sediments [e.g., *Gieskes*, 1976]. The chemistry of fluids circulating within the crust is also altered, and the discharge of these fluids back into the ocean impacts seawater chemistry. Additionally, the seawater pumped into the crust through hydrothermal systems supports a deep biosphere within the crust [*Furnes and Staudigel*, 1999]. Together with the cycle of crustal accretion and subduction, hydrothermal alteration of the oceanic crust provides a means of chemical exchange between the ocean and the mantle.

This chapter begins with a summary of the principal data and models that have been used to quantify the importance seafloor hydrothermal systems globally and in ridge flank environments. Next, an overview of the hydrology of ridge flank hydrothermal systems is given along with supporting evidence, and the important role of marine

sediments on ridge flank hydrothermal circulation is described. The principal unknowns with respect to the hydrology of ridge flank systems are presented, and three studies designed to advance our understanding in these areas are introduced.

1.1. Constraints on global hydrothermal fluid and heat fluxes

Important evidence for ridge flank hydrothermal circulation comes from thousands of measurements of conductive heat flow through seafloor sediments globally, which reveal that much of the seafloor has lower heat flow than is predicted by thermal models of the cooling lithosphere [e.g., *McKenzie*, 1967; *Parsons and Sclater*, 1977; *Stein and Stein*, 1994; *Hasterok et al.*, 2011]. This section reviews the thermal models of the oceanic lithosphere, and describes how and why the global compilation of seafloor heat flow measurements constrain the magnitude of the total advective heat loss from the oceanic crust globally.

1.1.1. Thermal models of the oceanic lithosphere

The oceanic crust forms at mid-ocean ridges from the crystallization of magma expelled out of the mantle. As time elapses, the initially molten oceanic crust cools, and by extension of the cooling into the upper mantle, the lithosphere (i.e., the rigid outer layer of the Earth) is formed. Seafloor spreading carries the oceanic lithosphere away from the mid-ocean ridges towards subduction zones where it eventually descends back into the mantle. Thermal models of the oceanic lithosphere attempt to explain the thermal evolution of the lithosphere between the time of crustal accretion and subduction. The constraints on these models come from observations that the seafloor deepens and conductive heat flow through the seafloor decreases with age over the first 60-80 Myrs

after crustal accretion, then both depth and heat flow approach asymptotic values [*Parsons and Sclater*, 1977; *Stein and Stein*, 1994].

The simplest physical model of lithospheric cooling that attempts to explain temporal changes in seafloor depth and conductive heat flow is represented by a cooling slab that extends infinitely deep. The slab initially has upper mantle temperature throughout, is subject to an upper boundary temperature of seawater, and is cooled by conduction alone [*Davis and Lister*, 1974]. This is known as the "half space" model. Lithospheric cooling predicted by thermal models of the lithosphere, such as this, require temporal density changes to materials within the lithosphere and, thus, isostatic adjustment of the lithosphere within the mantle (i.e. subsidence) that is consistent with observations of seafloor depth for crust younger than about 60 – 80 Myrs. At older ages the half space model predicts seafloor depths larger than the observations suggest and conductive heat flow lower than observations suggest. This result indicates that the natural lithosphere does not cool indefinitely, but may be re-heated at old age as a result of heat transport processes in the mantle [e.g. *Stein and Stein*, 1992]. Alternative thermal models of the lithosphere have been proposed to address this limitation.

One alternative thermal model of the lithosphere that better fits seafloor depth and conductive heat flow data at old ages is the "plate model" [*McKenzie*, 1967]. This model is similar to the half-space model in which an infinite slab is conductively cooled, but the plate model has a finite thickness slab with a constant temperature lower boundary at a finite and constant depth. This means that cool isotherms cannot extend infinitely deep as the lithosphere ages. The plate model is useful because it can explain the approach of seafloor depth and conductive heat flow to asymptotic values at old ages as well as the

more rapid decline of seafloor depth in younger crust. The thickness of the plate, the temperature at the lower plate boundary, and the thermal properties of mantle materials are the unknowns in this model. These parameters have been estimated for the plate model by best fits to seafloor depth and conductive heat flow data [*Sclater and Francbeteau*, 1970; *Parsons and Sclater*, 1977; *Stein and Stein*, 1992; *DeLaughter et al.*, 1999; *Hasterok et al.*, 2011].

Other thermal models of the lithosphere have also been proposed using variations on the basal thermal boundary condition. For example, the base of the slab has been represented by a constant heat flux boundary rather than a constant temperature boundary [e.g., *Sleep*, 1974; *Doin and Fleitout*, 1996]. The plate model and alternative models with constant heat flux lower plate boundaries predict total heat loss of 30-32 TW from the oceanic lithosphere [*Sclater et al.*, 1980; *Stein and Stein*, 1994; *Doin and Fleitout*, 1996].

1.1.2. Models to explain the global oceanic heat flow deficit

A commonality among thermal models of oceanic lithosphere is that they predict higher heat flow than is generally observed in conductive measurements taken on crust younger than about 65 Myrs (Figure 1.2). The discrepancy between modelled and measured oceanic heat flow, integrated globally, is known as the global oceanic heat flow deficit. Based on a parameterization of the plate model, Stein and Stein [1994] estimated the global oceanic deficit to be 11 ± 4 TW. The principal uncertainty in this estimate is scatter in the heat flow data. A secondary uncertainty in the magnitude of the deficit is the choice of lithosphere thermal model, or parameterization of the model, used to determine the deficit. The explanation for the "missing heat" has been the subject of

many studies, and several hypotheses about the cause of the deficit have been explored. This section reviews those hypotheses that have been explored and ruled out, and introduces the prevailing view that the global oceanic heat flow deficit is principally the result of cool seawater-derived fluid circulating through the crust on mid-ocean ridge flanks and removing heat by advection [e.g., *Williams and Von Herzen*, 1974; *Anderson et al.*, 1977; *Davis and Lister*, 1977].

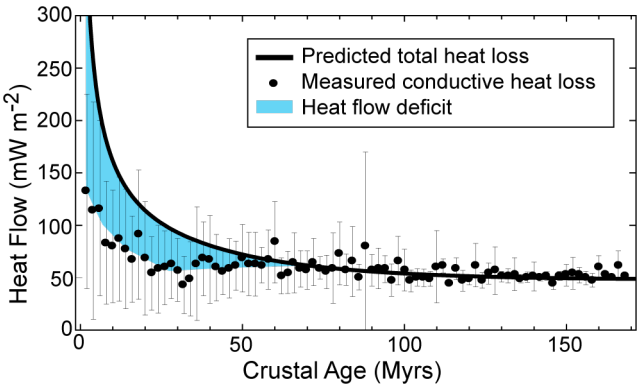

Figure 1.2. The 2 Myr age-binned average and one standard deviation of seafloor conductive heat flow measurements relative to total heat loss predicted by a thermal model of the oceanic lithosphere [*Stein and Stein*, 1994]**. The heat loss predicted by the lithosphere thermal model is constrained by seafloor depth measurements from crust of all ages, and also by measured conductive heat flow on crust older than 55 Myrs (which is assumed to be minimally affected by advective heat loss). See main text for an extended discussion of the lithosphere thermal model. The relative suppression of measured conductive heat flow compared to that predicted by a lithosphere thermal model is called the global oceanic heat flow deficit. The deficit is believed to be caused primarily by hydrothermal circulation within the oceanic crust extracting heat [e.g., *Williams and Von Herzen*, 1974; *Anderson et al.*, 1977; *Davis and Lister*, 1977].**

Lateral changes in the thermal conductivity within the sediment or upper igneous crust are known to cause refraction in conductive heat transfer [*Von Herzen and Uyeda*, 1963]. For example, low conductivity sediment unevenly distributed over higher

conductivity basement rock would result in conductive heat flow channeling more strongly through the thinner sediment. Although models of conductive refraction can explain local variability of heat flow in some settings [e.g., *Von Herzen and Uyeda*, 1963], in other locations the patterns of heat flow are opposite to that predicted by models of conductive refraction [*Lister*, 1972; *Sclater et al.*, 1974; *Davis and Lister*, 1977]. Based on quantitative models of conductive heat loss at the seafloor, conductive refraction is estimated to represent just a few percent of the local variability in heat flow [*Davis and Lister*, 1977], and is unable to explain the extreme high or low heat flow measurements that are commonly reported [e.g., *Hutnak et al.*, 2006].

Newly deposited sediments cool the seafloor until they reach thermal equilibrium with the underlying sediment or crust. Thick beds of sediment deposited rapidly by slumping or turbidity currents have been considered as possible explanations for the low measured heat flow in some settings [*Von Herzen and Uyeda*, 1963; *Davis and Lister*, 1977]. Modelling of this process demonstrates that the sudden deposition of 1 m of sediment will cause a thermal perturbation for about ten years, whereas the sudden deposition of 100 m of sediment will cause a thermal perturbation that lasts thousands of years [*Von Herzen and Uyeda*, 1963]. Von Herzen and Uyeda [1963] estimated that submarine landslides are unlikely to have occurred recently enough and to have affected a sufficiently large proportion of the seafloor to explain the many suppressed heat flow measurements. Additionally, some locations in which low heat flow has been measured have co-located sediment cores that show no recent disturbance to the sediment [e.g., *Sclater et al.*, 1974], so there must be another mechanism of heat flow suppression.

Conductive heat flow through the seafloor is determined by measuring temperatures at multiple depths in the upper few metres of seafloor sediments. The instruments used to measure temperatures commonly also collect sediment core samples on which the thermal conductivity can be measured. Alternatively, thermal conductivity may be determined *in situ* using an approach that involves heating the sediment and monitoring the heat dissipation as a function of time. Using Fourier's law of conduction, the temperature gradient and sediment thermal conductivity are used to calculate the heat flow through the sediment [e.g., *Langseth et al.*, 1966]. In general, these heat flow determinations only represent *conductive* heat loss (although curvature in a measured temperature profile can suggest advection through the sediment [e.g., *Langseth et al.*, 1984]). In locations where measured conductive heat flow is lower than the heat loss predicted by a thermal model of the oceanic lithosphere, the "missing heat" can be interpreted as evidence for advection within the crust. Spatial distributions of conductive heat flow data co-located with bathymetric or seismic surveys have been found to be consistent with models of fluid circulation through the igneous oceanic crust on ridge flanks [*Langseth and Herman*, 1981; *Langseth et al.*, 1992; *Fisher et al.*, 2003; *Hutnak et al.*, 2008]. There is also abundant geochemical evidence in the geologic record (presented later in this chapter) that supports the proposition that a large volume of seawater-derived fluid circulates through the oceanic crust globally.

1.1.3. Implications of the global oceanic heat flow deficit

The prevailing view is that the removal of crustal heat by seafloor hydrothermal circulation on a global scale is the only plausible explanation for the global oceanic heat flow deficit. Integrated globally, the deficit requires that 34 ±12% of the total heat loss

from the oceanic crust globally occurs by advection, and approximately 70% of this advective heat loss occurs off-axis (in crust older than 1 Myrs) through the mid-ocean ridge flanks [*Stein and Stein*, 1994]. Because the hydrothermal fluid passing through the ridge flank aquifer is much cooler than the focused venting at the mid-ocean ridge axis (ridge flank fluid temperatures are a few tens of degrees), orders of magnitude more fluid must pass through the ridge flank aquifer than the axial aquifer globally [*Mottl and Wheat*, 1994]. Although chemical fluxes as a result of hydrothermal circulation are not well constrained, the large estimated flux of fluid through ridge flanks relative to the axial region suggests that even small chemical differences in hydrothermal fluid compared to seawater could result in globally significant chemical fluxes through ridge flank hydrothermal systems [*Mottl and Wheat*, 1994].

1.2. Hydrology of the upper igneous oceanic crust

1.2.1. Lithologies

The majority of the oceanic crust forms at magmatic spreading centers [*Phipps Morgan and Chen*, 1993] which produce extrusive rocks formed from the eruption and subsequent cooling of lava, and intrusive rocks which solidify from magma in the subsurface (Figure 1.3). The thickness of the oceanic crust varies depending on the thermal balance and, thus, the magma supply at mid-ocean ridges [e.g., *Reid and Jackson*, 1981], but the crust is generally 5-7 km thick, except where formed at slow-spreading rates [*Karson*, 2002].

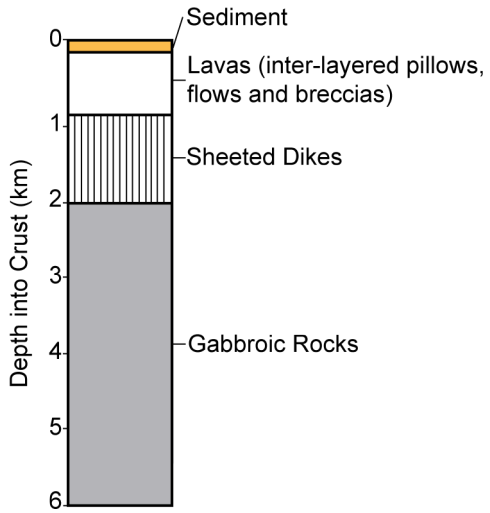

Figure 1.3. A generalized schematic of the lithological structure of oceanic crust formed at a fast or intermediate spreading ridge (i.e., a magmatic spreading ridge), modified from Karson [2002]. See main text for a description of the processes that create these lithological units. Crust formed at slow spreading ridges (which represents about 20% of the seafloor) may be thinner and discontinuous due to reduced magma supply [*Cannat*, 1996; *Ildefonse et al.*, 2007]**.**

The structure and composition of the oceanic crust are known largely from crustal drilling, diving and dredging programs and studies of ophiolites [e.g., *Moores and Vine*, 1971; *Alt et al.*, 1993; *Cannat*, 1996]. In crust formed at magmatic spreading centers, the extrusive rocks representing the uppermost section of the oceanic crust are principally tholeiitic basalts erupted as groups of metre-scale pillows with abundant radial fracture joints, or as laterally contiguous lava flows [*Carbotte and Scheirer*, 2004]. These units are commonly interlayered with one another and with volcanic rubble, forming an extrusive section that is generally hundreds of metres thick. The lower, intrusive crust consists of basaltic sheeted dikes overlying gabbro. The dikes are sub-vertical sheets oriented parallel to mid-ocean ridges and are the solidified remnants of magma conduits between subsurface magma chambers and eruptions at the seafloor. Gabbros form as a

result of the slow cooling of magma chambers as seafloor spreading pulls the oceanic crust away from the mid-ocean ridge heat source [*Henstock et al.*, 1993; *Quick and Denlinger*, 1993]. Hydrologic testing within oceanic drill holes has found that permeability within the extrusive section of the crust is generally higher than that of the sheeted dikes and gabbros [*Fisher*, 2005]. Crust formed at slow spreading rates (about 20% of the seafloor [*Muller et al.*, 2008]) may be discontinuous and thinner than normal oceanic crust, owning to reduced magma supply and tectonism at the ridge axis [*Cannat*, 1996; *Ildefonse et al.*, 2007].

1.2.2. Hydrothermal alteration of the oceanic crust in the off-axis

Crustal rocks are chemically and mineralogically modified by interaction with seawater-derived fluids at low temperatures in off-axis hydrothermal systems [e.g., *Muehlenbachs*, 1980; *Honnorez et al.*, 1983; *Alt and Honnorez*, 1984; *Gillis and Robinson*, 1988]. For example, increases in bulk rock H_2O and $\delta^{18}O$ of upper crustal rocks (relative to fresh rocks) are the result of fluid circulating in the crust [*Muehlenbachs*, 1980; *Alt et al.*, 1992]. Fluid circulation also results in the replacement of primary minerals such as olivine and plagioclase with secondary minerals. Clays, celadonite, iron oxy-hydroxides and carbonates are common secondary minerals that form throughout the lavas in ridge flank settings [e.g., *Alt and Honnorez*, 1984; *Alt et al.*, 1996], typically at temperatures < 100° C [*Muehlenbachs*, 1980; *Alt et al.*, 1986b; *Alt and Teagle*, 2003]. Oxidative alteration (e.g., formation of celadonite and Fe-oxy-hydroxides) tends to be concentrated in the upper few hundred metres of the extrusive igneous crust [e.g., *Gillis and Robinson*, 1990; *Alt et al.*, 2010], suggesting this is where

most of the fluid flux occurs. Within this zone, pillows and breccias are the most intensely altered lithologic units [e.g., *Alt et al.*, 2010].

Petrological studies and radiometric dating of hydrothermal alteration in ridge flank settings suggest that most alteration is complete within about 10-20 Myrs of crustal accretion [*Staudigel et al.*, 1981b; *Staudigel and Hart*, 1985; *Peterson et al.*, 1986]. Seismic P-wave velocities in the upper oceanic crust have been used as proxies for the extent of hydrothermal alteration. Based on a global compilation of seismic survey data, Carlson [1998] found that P-wave velocities in the upper crust decrease rapidly over the first 5-10 Myrs after crustal accretion, but change little thereafter, suggesting a slightly shorter timescale of hydrothermal alteration than that determined by most petrological studies. The global oceanic heat flow deficit, however, suggests that hydrothermal circulation persists for about 65 Myrs on average [*Stein and Stein*, 1994], and even longer in some settings [*Von Herzen*, 2004]. The discrepancy between the timescales of hydrothermal *circulation* and hydrothermal *alteration* has yet to be reconciled.

1.2.3. Drill hole constraints

Hydrologic tests have been conducted in several drill holes within the oceanic crust to elucidate the hydrology of the crustal aquifer [*Fisher*, 2005]. These tests generally pump fluid into a sealed interval within a crustal drill hole, and subsequently monitor pressure within the hole. Pressure changes as a function of time are used to estimate the permeability or hydraulic conductivity of the tens or hundreds of metres of crust surrounding the isolated section [e.g., *Becker et al.*, 1994]. Results from these tests suggest that the bulk permeability of the upper 200-300 m of the igneous oceanic crust is

generally > 10^{-14} m^2, and the deeper crust has orders of magnitude lower permeability (Figure 1.4, Fisher [2005]).

Davis et al. [2000] used long-term pressure records from oceanic drill holes on the Juan de Fuca plate (Holes 1024C and 1025C) and on the flank of the Mid-Atlantic Ridge (Hole 395A), along with known tidal and atmospheric pressure effects, to estimate the bulk permeability of the crustal aquifer on a kilometre scale. It was found that the timescales of pressure dissipation after tidal loading at these locations required upper crustal permeability of about 1.7 x 10^{-10} m^2. Drill hole hydrological testing has also demonstrated that permeability in the oceanic crust must, in some cases, be laterally contiguous for multiple kilometres. For example, Fisher et al. [2008] observed that the crustal pressure sensor in ODP Hole 1027C recorded a pressure perturbation caused by experiments at ODP Site 1301, 2.4 km away. These holes are on the Juan de Fuca plate in 3.5 Ma crust formed at an intermediate spreading rate of about 3 cm yr^{-1} (half rate). Based on a model of fluid mass balance and radial flow within an aquifer, it was found that the pressure perturbation at ODP Hole 1027C is most consistent with an upper crustal aquifer having permeability of about 10^{-12} m^2. Unfortunately, most of the drill hole hydrological testing to date has been conducted in crust younger than 10 Myrs (Figure 1.4), leaving a significant age bias in the permeability estimates.

The limited measurements of pressure within crustal drill holes [*Davis and Becker*, 2002] suggest that pressures in the upper igneous crust are generally within ±20 kPa of hydrostatic pressure. These measurements are roughly in agreement with pressures predicted by numerical modelling of convective fluid circulation within the

igneous crust driven by buoyancy differences due to temperature differences within the aquifer [*Fisher et al.*, 1994; *Hutnak et al.*, 2006].

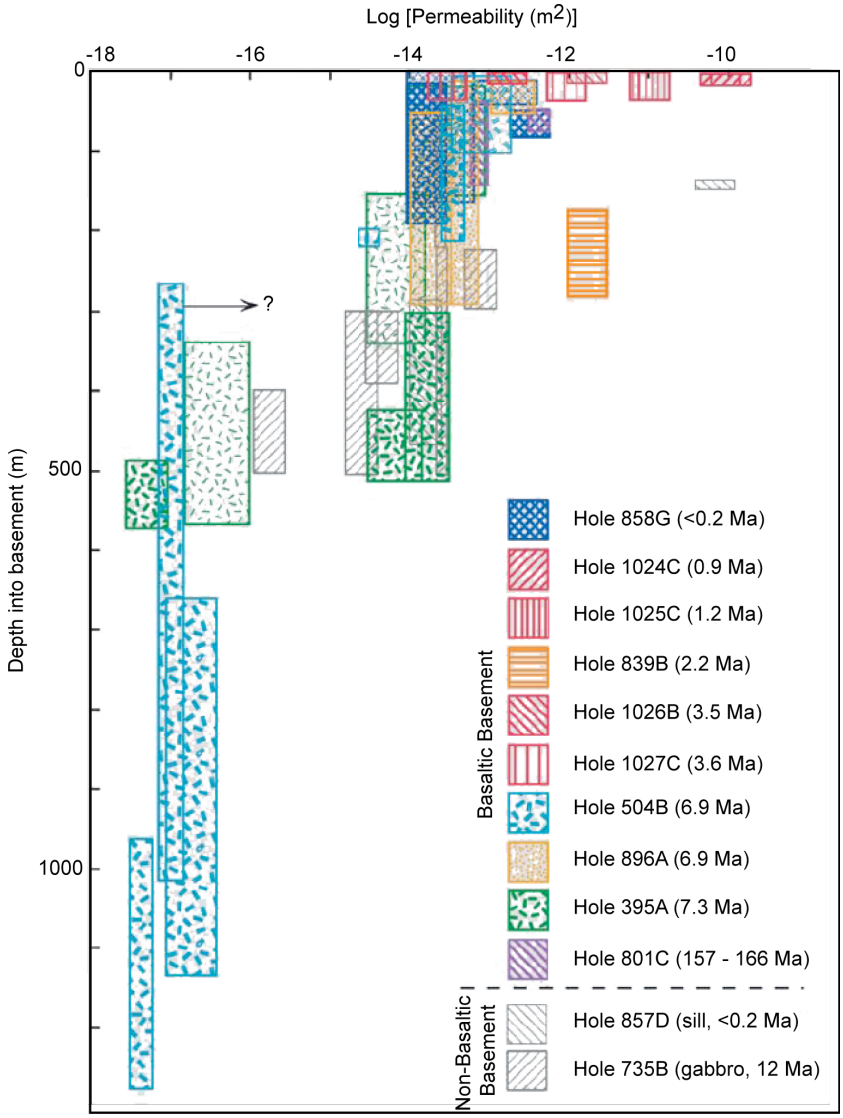

Figure 1.4. A summary of permeability estimates in the igneous oceanic crust determined by pumping tests within drill holes, modified from Fisher [2005]. These tests seal off an interval within the drill hole using inflatable "packers", then pump fluid into that interval and monitor the change in pressure. The permeability is then determined from the temporal changes in pressure using a quantitative model of radial flow within a porous medium surrounding the injection site. Results show the upper few hundred metres of igneous crust are significantly more permeability that the lower units.

1.3. Seafloor sediments

Sediments are important to ridge flank hydrothermal circulation because they are, in general, less permeable than the upper few hundred metres of igneous crust [*Spinelli et al.*, 2004], and therefore impede fluid exchange between the ocean and the aquifer. This section discusses sediment distributions on global and local scales, and gives an overview of the hydrology of marine sediments.

1.3.1. Sediment types and controls on their global distributions

The distribution of marine sediment in the world ocean is determined primarily by the nature and location of sediment sources, sediment transport processes, structural trends in the basement, seafloor age and tectonic history [*Tucholke and Fry*, 1985]. Terrigenous sediment, derived from continental erosion and delivered to the ocean primarily through rivers, represents the largest mass fraction of marine sediments globally, although such sediment is concentrated near continental margins and is the dominant sediment type for only a small proportion of the total seafloor area [*Spinelli et al.*, 2004]. In abyssal settings, away from continental margins, the igneous crust is covered by tens or hundreds of metres [*Divins*, 2011] of pelagic biogenic and lithogenic sediments. Biogenic sediment is derived from the fossil remains of mainly pelagic biota (such as calcium carbonate or amorphous silica shells). The balance between biological productivity in the surface water and dissolution in the water column control the flux of biogenic sediment to the seafloor [*Archer et al.*, 1993]. Lithogenic clay sediment, sourced primarily from windblown dust [*Rea*, 1994], is also an important component of abyssal sediments, especially where the supply or preservation of biogenic material is low.

1.3.2. Impact of bathymetry on local scale (km) sediment distribution

The bathymetry of the oceanic basement affects the distribution of the overlying sediment because gravity tends to draw sediment down slopes. Abyssal hills and seamounts are the principal seafloor structures controlling basement bathymetry on scales of kilometres to tens of kilometres. In abyssal settings, sediment is supplied to the seafloor by a gradual sinking of biogenic and lithogenic particles through the water column. Once the sediment reaches the seafloor, it may be redistributed by processes such as bioturbation [e.g., *Wheatcroft and Jumars*, 1990], bottom currents [e.g., *Dezileau et al.*, 2000] and mass wasting [e.g., *Mitchell*, 1998]. The combined effect of these processes, averaged over geological time, is that sediments are redistributed from topographic highs to topographic lows [*Webb and Jordan*, 1993]. Post-depositional sediment transport can be modelled as a diffusional process, in which down-slope sediment fluxes are proportional to the topographic gradient [*Mitchell*, 1995; *Webb and Jordan*, 2001a].

1.3.3. Sediment hydrology

Knowledge of sediment hydrology comes from laboratory hydrologic testing on sediment samples [e.g., *Bryant et al.*, 1974], down-hole logging of oceanic drill holes [e.g., *Hamilton*, 1976] and quantitative hydrologic modelling of the igneous crust and overlying sediments [e.g., *Snelgrove and Forster*, 1996; *Davis et al.*, 1997]. Using established sediment permeability-depth relationships for different sediment types, Spinelli et al. [2004] estimated the thickness of each sediment type that will support flow at rates detectable by chemical and thermal approaches. It was found that 10-20 m of terrigenous sediment, or 100 m of pelagic clay or calcareous ooze, will restrict any vertical fluid seepage to a rate incapable of distorting the vertical *thermal* gradient in the

sediment, thus making the seepage undetectable from thermal data alone. It was also estimated by Spinelli et al. [2004] that distortions to *chemical* gradients within sediments are more sensitive to slow seepage, and might commonly be detectable from interstitial water chemical advection-diffusion models.

Snelgrove and Forster [1996] used a layered hydrologic model of the igneous crust and the overlying sediments to investigate the ability of silt-rich and clay-rich sediments to restrict convective circulation between the basement and the ocean at their study location on the Juan de Fuca plate. They found that a 200 m thickness of clay-rich sediment would seal the igneous crust from the overlying ocean, whereas the same thickness of silt-rich sediment would support convective circulation across the sediment. Davis et al. [1997a] applied a similar hydrologic model, but allowed non-uniform basement topography and sediment thickness representative of their study area on the Juan de Fuca plate. Their model parameterizations that best fit local heat flow data required super-hydrostatic pressure in the upper igneous crust at basement ridges (driving upward flow across sediment), and sub-hydrostatic pressure at basement troughs (driving downward flow). Although these studies have provided insights into the hydrology of sediment on the Juan de Fuca ridge, the sedimentation rate there is abnormally high due to delivery of Pleistocene glacial sediments from the nearby continental margin, so it is unclear whether these findings are globally applicable.

1.4. Principal unknowns about ridge flank hydrothermal processes

Although fluid fluxes through ridge flank hydrothermal systems are predicted to rival riverine fluid fluxes into the ocean [*Palmer and Edmond*, 1989], the locations of fluid exchange between the ocean and the igneous crust are largely unknown, as are the

fluid flow paths within the crust. These unknowns stand in the way of quantifying chemical fluxes between the ocean and the crust as a result of ridge flank hydrothermal circulation.

On the Juan de Fuca and Cocos plates, heat flow measurements have been used to trace fluid flow in the aquifer [*Elderfield et al.*, 1999; *Fisher et al.*, 2003; *Hutnak et al.*, 2006]. These studies concluded that fluid primarily enters and leaves the igneous crust through discrete basement exposures ("outcrops"), and that fluid travels laterally for tens of kilometres through the aquifer, beneath the sediment, between recharge and discharge outcrops ("outcrop-to-outcrop flow"). Although it is clear that the hundreds of metres of low permeability sediment at these locations hydraulically isolate much of the aquifer from the ocean, thus causing fluid to channel through outcrops, these locations have accumulated sediment substantially more rapidly than is typical of abyssal settings globally. It is, therefore, unclear whether outcrop-to-outcrop flow is a local phenomenon or a globally important process. Fisher and Becker [2000] assumed outcrop-to-outcrop flow is a global scale process, and applied a hydrologic model of outcrop-to-outcrop flow to estimate the average permeability of the crustal aquifer required to explain the global oceanic heat flow deficit. This modelling predicted that global scale outcrop-to-outcrop flow requires the average crustal aquifer permeability (at a scale of multiple kilometres) to be 10^{-8} to 10^{-10} m^2 [*Fisher and Becker*, 2000], which is at the high end of what has been measured in drill holes (Figure 1.4). A plausible alternative model of ridge flank hydrothermal circulation proposes that thermally driven convection cells within an isolated outcrop allows recharge and discharge within the same edifice [*Harris et al.*, 2004; *Kawada et al.*, 2011], without requiring lateral flow between outcrops. Testing the

global applicability of an outcrop-centric model of seafloor hydrothermal circulation requires an understanding of the global distribution of basement outcrops. Although outcrops have been identified in a few local areas from detailed bathymetric and seismic surveys [e.g., *Fisher et al.*, 2003; *Hutnak et al.*, 2008], the distribution of basement outcrops across the seafloor remains poorly known.

If ocean-aquifer fluid exchange primarily occurs through outcrops, the implication is that comparatively little fluid flux occurs across the sediment. The proposition that only minor fluid fluxes occur through sediments is consistent with theoretical predictions based on hydrologic properties of sediments [*Spinelli et al.*, 2004] and limited direct measurements of the driving forces [*Davis and Becker*, 2002], but has not been rigorously tested on a global scale. Rates of vertical seepage through sediment of 10^{-4} – 10^{-2} m yr^{-1} have been previously determined from sediment thermal and interstitial water chemical profiles in a limited number of settings [e.g., *Maris et al.*, 1984; *Langseth et al.*, 1992; *Wheat and McDuff*, 1994]. Given this range of seepage rates, it is unclear whether fluid fluxes through sediments globally are as negligible as outcrop-centric models of ridge flank hydrothermal circulation assume. The research herein includes three studies aimed at understanding how fluid enters and leaves the crust, its flow paths within the crust, and the roles of sediment and outcrops in ridge flank hydrothermal circulation globally.

1.5. Three studies designed to advance our understanding of off-axis hydrothermal circulation

Here, three new studies are introduced which investigate the roles of sediment and basement outcrops in off-axis hydrothermal systems globally. In the first study (Chapter

2; published in the Journal of Geophysical Research as Anderson et al., [2012]), the global distribution of seafloor outcrops is investigated with models of the processes that control sediment distribution. To this end, a numerical model of pelagic sediment supply, post-depositional down-slope sediment redistribution, and crustal hydrogeology is presented. Synthetic seafloor bathymetry, representative of crust formed at different spreading rates is used as the initial basement bathymetry and seamounts are added randomly with a size and frequency distribution representative of the global ocean. Other sedimentation variables are the pelagic sediment supply rate, the diffusivity of sediment transport and the sediment hydrological properties. From this, the model predicts the changing distribution of outcrops (potential sites of hydrothermal fluid exchange between the ocean and the aquifer) in response to sedimentation as a function of time. These results are coupled with a two dimensional model of fluid and heat transport to evaluate the conditions under which lateral fluid flow through the crustal aquifer between discrete outcrops are consistent with the global data set of seafloor heat flow measurements. This extends the work of Fisher and Becker [2000] by: (i) making an improved estimate of the global distribution of basement outcrops based on the processes controlling sediment distribution in abyssal environments, and (ii) extending the model of coupled fluid and heat transport to two horizontal dimensions, which is more representative of natural seafloor. A principal conclusion from this work is that basement outcrops globally may be more abundant, and, therefore, generally closer together than previously estimated. In a model of outcrop-to-outcrop hydrothermal circulation, this finding indicates that larger pressure gradients are available to drive lateral fluid flow in the crustal aquifer than has previously been estimated [*Fisher and Becker*, 2000]. It is also found that the time-

varying average and standard deviation of seafloor heat flow required by a model of outcrop-to-outcrop flow only fit the global heat flow data if the permeability of the crustal aquifer decreases from 10^{-9} to 10^{-11} m^2 over the duration of the heat flow deficit (to approximately 65 Myrs). This range of permeabilities is consistent with previous estimates of upper crustal permeability at similar scales, which supports the proposition that outcrop-to-outcrop fluid flow is the dominant mode of ridge flank hydrothermal circulation globally.

A common assumption of hydrologic models of the oceanic crust is that the uppermost igneous extrusive layer of the aquifer is thermally well mixed. This assumption bears on the lateral pressure differences available to drive outcrop-to-outcrop flow within the aquifer, and therefore also affects estimates of crustal permeability. In the second study (Chapter 3; published in the Journal of Geophysical Research as Anderson et al. [2013]), the assumption of a thermally well mixed aquifer is tested against the geological record using O-isotope-derived crystallization temperatures of carbonates in the lavas as a record of the temperatures experienced by the aquifer. It is found that carbonate formation temperatures are higher than can be explained by a model of outcrop-to-outcrop flow in a thermally well mixed aquifer at four of the seven drilling locations analyzed. A poorly mixed aquifer is developed to further explore the crustal hydrology at these locations. Relative to a well mixed aquifer, a poorly mixed aquifer can achieve higher average temperatures, develops larger lateral pressure gradients driving flow, and requires a lower permeability to achieve a given lateral fluid flux. Oxygen isotope data from most of the carbonate samples analyzed are consistent with temperatures achievable in a poorly mixed aquifer; those samples which are not

consistent can be explained by plausible special circumstances (such as formation at a discharge zone, where ascending fluid may warm the uppermost aquifer). Permeability estimates of the upper crust based on a model of outcrop-to-outcrop flow in a poorly-mixed aquifer are consistent with previous permeability estimates, lending further support to the proposition that outcrop-to-outcrop flow is the dominant mode of ridge flank hydrothermal circulation globally.

The proposition that outcrop-to-outcrop flow is the dominant mode of off-axis hydrothermal circulation globally implies that only a small proportion of hydrothermal fluid flux passes through marine sediments. In the third study (Chapter 4; submitted to the Journal of Geophysical Research), models of interstitial water chemical transport and reaction are fitted to measured profiles of sediment interstitial water SO_4^{2-}, Mg^{2+} and Ca^{2+} from 140 drill holes globally to estimate advection rates through the sediment. It is found that advection through sediments ("seepage") is generally slower than 5×10^{-4} m yr^{-1} (500 m $Myrs^{-1}$). About 52% of the holes analyzed host upward seepage, 20% downward seepage, and 28% have no detectible seepage. Based on previously established relationships between sediment thickness and permeability for particular sediment types, the seepage rates generally require the crustal aquifer to have super- or sub-hydrostatic pressures of a few tens of kPa, consistent with measurements in crustal drill holes [*Davis and Becker*, 2004]. Extrapolating the new compilation of seepage rate estimates to a global scale suggests that seepage through sediments comprises no more than a few percent of the total ridge flank hydrothermal fluid flux. This is consistent with the proposition that outcrops are primary sites of fluid exchange between the ocean and the crustal aquifer. Based on the estimated global flux of fluid through sediments, and the

differences in chemical concentration between hole-top pore fluids and seawater, upward fluxes of SO_4^{2-}, Mg^{2+} and Ca^{2+} through sediments globally are estimated to be only a few percent of riverine fluxes, and thus, are not globally significant.

The final chapter synthesises the findings of chapters 2-4 into a model of the hydrology of off-axis hydrothermal systems. This is followed by suggestions for future studies to test this model and further refine our understanding of the globally important process of off-axis hydrothermal circulation.

2. The role of outcrop-to-outcrop fluid flow in off-axis oceanic hydrothermal systems under abyssal sedimentation conditions

2.1. Introduction

Fluid advection through the oceanic crust as it ages is an important mechanism for redistributing and extracting heat, for driving chemical fluxes between the ocean and the crust, and, potentially, for supporting a deep biosphere. Due to the dramatic decrease of crustal permeability with depth in the upper oceanic crust [e.g., *Fisher et al.*, 2008] , it is generally thought that the upper few hundred metres of oceanic crust acts as the main aquifer through which fluid circulation occurs. Estimated water-to-rock mass ratios also generally decrease with depth in the upper crust and support this interpretation [*Staudigel*, 2003]. Within the lavas, the pillows, breccias and fault zones are typically more altered than sheet flows, suggesting these units host most of the aquifer's permeability [e.g., *Alt*, 2004; *Gillis and Robinson*, 1990]. In the off-axis, sediment overlying the igneous crust has significantly lower permeability than the lavas [*Spinelli et al.*, 2004], restricting fluid exchange between the ocean and the crustal aquifer.

Globally, hydrothermal circulation is responsible for ~30% of all heat extracted from the oceanic crust, with the majority of that heat loss occurring off-axis (crustal age > 1 Myrs) [*Stein and Stein*, 1994]. Additionally, on the order of 10-100 times more fluid is estimated to flow through off-axis systems than through axial systems [*Mottl and Wheat*, 1994; *Mottl*, 2003]. Although fluid temperatures in off-axis hydrothermal systems are relatively low compared to axial hydrothermal systems, the large predicted fluid flux through off-axis systems has the potential to support globally important chemical exchange between the ocean and the crust [*Mottl and Wheat*, 1994].

An important question for quantifying fluid and chemical fluxes is how fluid enters and leaves the crust in off-axis settings, and its flow paths therein. Focused fluid recharge into the crustal aquifer through basement exposures ("outcrops") and lateral fluid advection beneath the sedimentary layer (Figure 2.1) has been proposed to explain local patterns of seafloor heat flow variability in numerous settings via a quantitative model of this process (Figure 2.2) [e.g., *Baker et al.*, 1991; *Fisher et al.*, 2003; *Hutnak et al.*, 2008; *Langseth et al.*, 1992, 1984; *Langseth and Herman*, 1981]. Lateral fluid flow through the aquifer and/or vigorous local convection can homogenize upper basement temperatures by redistributing heat. Homogenous upper basement temperatures have been identified between pairs of nearby crustal drill holes overlain by different thicknesses of sediment (ODP Holes 1026C and 1027B, 2 km apart; ODP Holes 504B and 896A, 1 km apart), consistent with lateral flow redistributing crustal heat [*Davis and Becker*, 2004]. On thickly sedimented regions of the Juan de Fuca and Cocos plates (>400 m average sediment thickness on 3.5 Myr and 20 Myr crust respectively), heat flow measurements have been used to identify specific seamounts, and other types of basement outcrops, as locations of either fluid recharge into or discharge from the crustal aquifer, with outcrop-to-outcrop flow interpreted to occur beneath the sediment between these sites [*Fisher et al.*, 2003; *Hutnak et al.*, 2008]. It has been proposed that this mode of hydrothermal circulation, between distal outcrops separated by expanses of hydraulically resistive sediment, may be characteristic of off-axis, seafloor hydrothermal systems globally [*Fisher and Becker*, 2000]. However, in the two regions where outcrop-to-outcrop circulation has been studied in most detail, the anomalously thick sediment

relative to typical abyssal sediment thickness, calls into question the global applicability of this model.

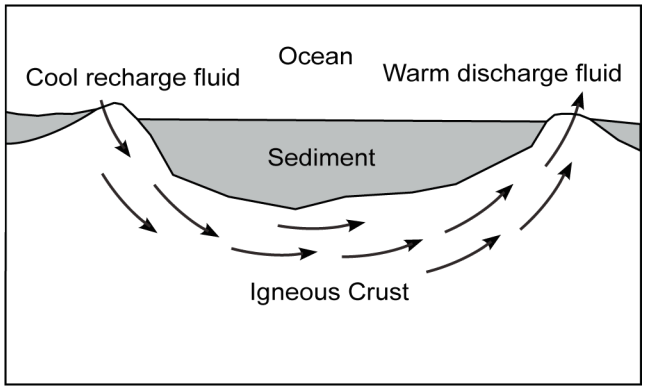

Figure 2.1. A conceptual diagram of the outcrop-to-outcrop flow model of off-axis hydrothermal circulation. In this model ocean-aquifer fluid exchange occurs entirely through basement outcrops, with lateral fluid flow in the upper igneous crust between the outcrops.

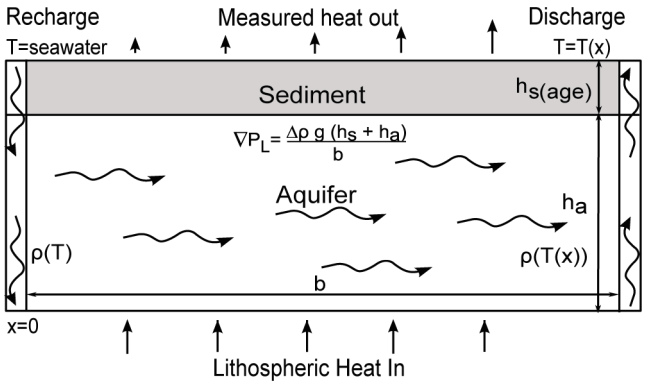

Figure 2.2. Schematic of the 1D idealized model of lateral fluid flow and heat exchange in the crustal aquifer (following *Fisher and Becker* [2000]). Parameters not included in the diagram are: aquifer permeability (*k*), fluid specific heat capacity (*c*), fluid specific discharge (*Q*), and sediment thermal conductivity (λ_s).

In this paper results are presented for a numerical model developed to investigate the conditions under which outcrop-to-outcrop fluid flow within the upper oceanic crust are likely to be thermally important under normal abyssal sedimentation conditions. The

present study builds on the analytical model of this process applied by Fisher and Becker [2000], and determines the conditions in which outcrop-to-outcrop flow globally can explain the global heat flow deficit. As basement outcrops are a critical component of the outcrop-to-outcrop flow model, I begin with a method to quantify the distribution of outcrops globally. The distribution of outcrops is modelled as a function of crustal age by generating synthetic basement bathymetry representing crust formed at different spreading rates, modelling pelagic sediment supply and post-depositional sediment transport on that bathymetry, and identifying outcrops from the time-variable sediment distribution. The outcrops are classified as focused fluid recharge or discharge sites. Using this distribution of recharge and discharge outcrops, heat transport in the aquifer via outcrop-to-outcrop flow is modelled, allowing a determination of aquifer temperatures and seafloor heat flow over the model domain. It is found that the outcrop-to-outcrop flow model simultaneously fits the average and standard deviation of the global heat flow data if the average permeability of the aquifer decreases from $\sim 10^{-9}$ m^2 to $\sim 10^{-11}$ m^2 over 5-65 Myrs of crustal age. This range is consistent with the limited permeability data measured in boreholes and inferred by hydrological models of local settings, lending support to the suggestion that outcrop-to-outcrop flow may be the dominant mode of off-axis hydrothermal circulation globally.

2.2. Model setup

Synthetic bathymetry is generated to represent igneous crust formed at different spreading rates. The supply and post-depositional transport of sediment are then simulated on these initial bathymetries. Simulated distributions of sediment are used to determine the distributions of outcrops as a function of time. Finally, using these outcrop

distributions, a model of lateral fluid transport and heat exchange within the aquifer is developed. A series of models are run with parameters randomly drawn from appropriate global distributions, such that the ensemble results are a probabilistic representation of sediment, outcrops, and outcrop-to-outcrop flow globally.

Table 2.1. Table of symbols used in Chapter 2

Symbol	Meaning (Unit)	Value [Reference]
H	Root-mean-square height of abyssal hills (m)	Slow spreading: 235.8±7.9 m Intermediate spreading: 78.5± 6.0 m Fast spreading: 56.1± 2.3 m [a]
L_n	Characteristic abyssal hill width (km)	Slow spreading: 8.2±0.3 m Intermediate spreading: 4.2± 0.5 m Fast spreading: 2.0± 0.1 m [a]
L_s	Characteristic abyssal hill length along strike (km)	Slow spreading: 24.7±3.5 m Intermediate spreading: 13.6± 2.2 m Fast spreading: 12.3± 1.2 m [a]
D	Abyssal hill fractal dimension.	2.2 [Goff, 1991]
F	Sediment rain rate (m $Myrs^{-1}$)	From distribution in Figure 2.4
κ	Apparent diffusivity of sediment (m^2 yr^{-1})	0.007-0.34 m^2 yr^{-1} (Section 2.2.2)
h_s	Thickness of sediment (m)	Calculated
$k_s(z)$	Permeability of sediment at depth z in the sediment column (m^2)	Calculated (Section 2.3.1)
k_{bulk}	The bulk permeability of a column of sediment (m^2)	Calculated
I	Hydraulic impedance of a column of sediment (m^{-1})	Calculated
h_a	Thickness of the upper crustal aquifer (m)	100-500 m
ρ	Aquifer fluid density (kg m^{-3})	Average of recharge and discharge ρ
c	Specific heat capacity of aquifer fluid (J kg^{-1} K^{-1})	4200 J kg^{-1} K^{-1}
λ_s	Thermal conductivity of the sediment (W m^{-1} K^{-1})	1.2 W m^{-1} K^{-1} [Pribnow et al., 2000]
k	Aquifer permeability (m^2)	Calculated
μ	Dynamic viscosity of aquifer fluid (Pa s)	1.08×10^{-3} Pa s
P	Pressure (Pa)	Calculated
P_0	Pressure at a recharge or discharge site, relative to seafloor pressure (Pa)	Calculated
Q	Specific discharge of aquifer fluid (m s^{-1})	Calculated
T	Temperature of aquifer fluid (°C)	Calculated
q_m	Conductive heat flow out the top of the aquifer (W m^{-2})	Calculated
q_L	Conductive heat flow into aquifer base (W m^{-2})	Lithospheric heat flow, GDH1 [b]
r_0	Radius of an outcrop's ingress or egress zone (m)	75 m
r_e	Radius of influence of a recharge or discharge site (m)	2 × b
b	Recharge/discharge separation distance (m)	Calculated
g	Gravity (m s^{-1})	9.8 m s^{-1}
H_s	Seamount height (m)	Calculated
ξ	Ratio of seamount height to basal radius	0.21 [c]
R_b	Seamount basal radius (m)	Calculated
τ	Timescale of variation in off-axis seamounts production (Myrs)	20 Myrs [c]
n_0	Density of seamounts with zero size (m^{-3})	2.4 x 10^{-11} m^{-3} [c]
β_0	Characteristic seamount scale at $t = t0$ (m^{-1}). The inverse is a characteristic height of seamounts at $t = t0$.	4.4 x 10^{-3} m^{-1} [c]
$\beta\infty$	Characteristic seamount scale at $t\rightarrow\infty$ (m^{-1}). The inverse is a characteristic height of seamounts at $t\rightarrow\infty$.	3.2 x 10^{-3} m^{-1} [c]
t	Time (Myrs)	
x, y	Horizontal spatial coordinates (m)	

a. Goff, 1991; Goff et al., 1993, 1995; Neumann and Forsyth, 1995; Goff et al., 1997
b. Stein and Stein, 1994
c. Smith and Jordan, 1988

2.2.1. Synthetic bathymetry

The bathymetry of the oceanic crust is affected by abyssal hills and seamounts, which control the distribution of topographic highs and lows. Abyssal hills form at mid-ocean ridges, whereas seamounts form over a range of crustal ages. Synthetic bathymetry is advantageous to this study because, when coupled with the sedimentation model, it allows a probabilistic study of outcrop distributions for any set of basement parameters, including those representing locations where high-resolution bathymetric data are unavailable. Additionally, the effects of abyssal hills and seamounts on the sediment distribution can be studied separately.

2.2.1.1. Abyssal hills

Synthetic abyssal hills are generated using the model of Goff and Jordan [1988] to represent the initial, unsedimented seafloor. Synthetic abyssal hill bathymetry grids can be generated by a stochastic process from parameters describing the amplitude, characteristic width, characteristic length and fractal dimension of the abyssal hill seafloor. The abyssal hill amplitude, characteristic width and characteristic length are correlated with mid-ocean ridge spreading rate [*Goff*, 1991]. These parameters have been inverted from dozens of bathymetric tracks near the global mid-ocean ridge system where sediment is generally thin or absent owing to the young crustal age [*Goff*, 1991; *Goff et al.*, 1993, 1995, 1997; *Neumann and Forsyth*, 1995].

For each model run in this study, a full spreading rate of <30 km $Myrs^{-1}$ (slow-spreading), 30 – 60 km $Myrs^{-1}$ (intermediate-spreading) or >60 km $Myrs^{-1}$ (fast-spreading) was selected at random from the area-weighted distribution of seafloor spreading rates [*Muller et al.*, 2008]. The abyssal hill amplitude, width, and length parameters were selected randomly from the Gaussian distributions for that spreading

rate (Table 2.1), and a synthetic abyssal hill grid was generated for these parameters. The fractal dimension (D) varies little with spreading rate [*Goff*, 1991], and is assumed to have a constant value of 2.2.

The synthetic bathymetric grids used in this study have a cell resolution of 150 m × 150 m which is sufficiently fine to resolve outcrops at the scale of those identified in hydrogeological studies of seafloor hydrothermal systems (>~0.25 km^2 surface area [*Wheat and Fisher*, 2008; *Fisher and Wheat*, 2010]). The grids represent overall dimensions of 100 km × 100 km. This size is sufficiently large to minimize boundary effects and to represent hydrological connectivity between modelled outcrops as distal as those known to interact hydrologically in nature (up to 52 km apart [*Fisher et al.*, 2003]) while not becoming too computationally expensive. Additionally, limited testing of larger grids (up to 150 km x 150 km) shows that these give similar results.

2.2.1.2. Seamounts

Many of the known outcrops where off-axis focused fluid exchange occurs between the ocean and the crustal aquifer are seamounts [*Fisher et al.*, 2003; *Hutnak et al.*, 2008]. Satellite altimetry has revealed a global population of ~14,000 seamounts taller than approximately 1.5 km [*Wessel*, 2001]. Because the average sediment thickness on the abyssal seafloor is much less than 1.5 km [*Divins*, 2011], even small seamounts can potentially breach the sediment and act as outcrops. Jordan et al. [1983] and Smith and Jordan [1988] manually identified seamounts in the Pacific using wide beam sounding data, allowing them to assess seamount populations over a greater size range than is possible with satellite altimetry, albeit based on only partial coverage of the basin. They found the cumulative height distribution of Pacific seamounts decays

exponentially over heights (H_s) 400 m – 2500 m. Extrapolation of the exponential size relationship suggests there may be an average of ~5500 seamounts taller than 100 m per 10^6 km^2 of Pacific oceanic crust. Hillier and Watts [2007] used a computer algorithm to scan a much larger collection of wide-beam sounding data, automatically identifying probable seamounts taller than 100 m. Extrapolation of their results suggests there may be an average of ~9500 seamounts taller than 100 m per 10^6 km^2 of global oceanic crust. The more conservative estimate of Smith and Jordan [1988] is used here because of the inherent uncertainty in automation of seamount identification, although this choice has only a small impact on the results (see Section 2.3.4).

Smith and Jordan [1988] extended their exponential seamount height-abundance model to a height-abundance-crustal age model. They estimated the number of seamounts per 10^6 km^2 in the incremental height range H_s to H_s+dH_s at time t as:

$$n(H_s,t) = n_0 e^{-\beta(t)H_s} \qquad (2.1)$$

where n_0 is the intercept of an exponential graph of the number of seamounts (per 10^6 km^2) vs. seamount height (H_s) with the height of zero, and the function $\beta(t)$ is the temporal behavior of the seamount scale distribution, approximated by:

$$\beta(t) = (\beta_0 - \beta_\infty)e^{-t/\tau} + \beta_\infty \qquad (2.2)$$

The inverse of the parameter β_0 is the characteristic height of seamounts formed near the axis (crustal age $t < t_0$, where t_0 is assumed to be 5 Myrs), the inverse of β_∞ is the (extrapolated) characteristic height of seamounts at $t = \infty$, and τ is the characteristic timescale of variation in off-axis seamount formation. The estimated production rate (per 10^6 km^2) of off-axis Pacific seamounts taller than H_s at time t is given by:

$$p(H_s,t) = n(H_s,t)(\beta_0 - \beta_\infty)H_s\tau^{-1}e^{-t/\tau} \qquad (2.3)$$

Equation 2.3 was re-derived to correct a typographical error in Eq. 19 from Smith and Jordan [1988]. This model predicts that the majority of seamounts are formed on young crust near the ridge axis. The seamount production model (Eq. 2.3) is assumed to be globally appropriate, and is used to probabilistically add seamounts to random locations on the synthetic abyssal hill bathymetry. Values for β_0, β_∞, τ and n_0 are from estimates by Smith and Jordan [1988] (see Table 2.1).

A simple geometrical approximation is used for seamount shapes (Figure 2.3). Seamounts are assumed to be radially symmetrical cones with a sharp decrease in the flank slope near the summit. This is a variation on the flat-topped seamount approximation [*Jordan et al.*, 1983], and is used in preference to that model because with perfectly flat-topped seamounts the post-depositional sediment transport model (Section 2.2.2.2) does not allow seamount summits to shed sediment. Such a result would be contrary to the observation that seamounts are generally covered with less sediment than the surrounding seafloor [e.g., Hutnak et al., 2008]. It is assumed that the slope change occurs at height $0.9H_s$, consistent with visual inspection of seamount profiles, although the exact height of the slope break does not significantly affect the sediment distribution or the conclusions of this study. The basal radius (R_b) is related to the height (H_s) by:

$$H_s = \xi R_b \qquad (2.4)$$

where the height-to-radius ratio (ξ) is assumed to have a value of 0.21 based on the dimensions of well-surveyed seamounts [*Jordan et al.*, 1983; *Smith and Jordan*, 1988]. Between the base of the seamount and a height of $0.9H_s$, a constant flank slope of s_1=17° is assumed [*Smith and Jordan*, 1988; *Smith and Cann*, 1990; *Kleinrock and Brooks*,

1994; *Magde and Smith*, 1995; *Scheirer et al.*, 1996], giving a radius at the height of the slope break (R_t) of:

$$R_t = R_b - \frac{0.9H_s}{Tan(s_1)} \qquad (2.5)$$

For the remaining height to the summit a reduced slope (s_2) is assumed:

$$s_2 = \tan^{-1}\left[\frac{H_s - 0.9H_s}{R_t}\right] (\sim= 4°) \qquad (2.6)$$

For each model run, a random population of seamounts, their sizes, and their ages of formation were chosen probabilistically based on Eq. 2.3. The positions of the seamounts on the synthetic abyssal hill bathymetry are randomly distributed.

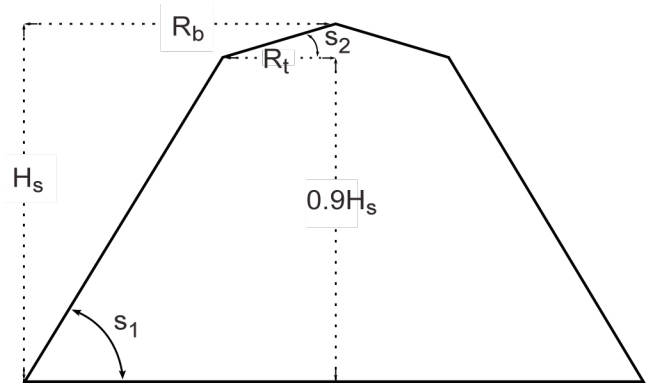

Figure 2.3. A cross section of the geometry of the axisymmetric synthetic seamounts used in this study. Symbols are: R_b = basal radius, R_t = radius at the height of the slope change, H_s = seamount height, s_1 = flank slope, s_2 = upper slope.

2.2.2. Sedimentation model

To estimate the distribution of outcrops, and the variability in this distribution with time, a numerical model of pelagic sediment supply and post-depositional transport [*Webb and Jordan*, 1993, 2001a, 2001b] is used to model sedimentation, and thus sediment thickness, as a function of time and space over a simulation area.

2.2.2.1. Pelagic sediment supply

The sedimentation model assumes that new sediment is supplied vertically from the water column at rain rate *F*. Johnson and Pruis [2003] estimated the global average sediment rain rate to be 4 - 6.5 m $Myrs^{-1}$ from global sediment thickness and crustal age digital grids. The same approach is applied in the present study, using updated digital grids of average sediment thickness [*Divins*, 2011] and seafloor age [*Muller et al.*, 2008]. Because the objective of this study is to investigate outcrop-to-outcrop hydrothermal flow in the oceanic crust in *abyssal* settings, continental margins were excluded from this analysis. For each intersecting grid cell of the global grids, the average sediment supply rate was computed as sediment thickness divided by crustal age. Continental margins are assumed to be seafloor locations in which the average seafloor depth estimated from satellite altimetry [*Smith and Sandwell*, 1997] is >10% shallower than the depth predicted by the GDH1 parameterization of the plate model [*Stein and Stein*, 1992] with 2600 m used as the initial water depth. The value of 10% was chosen because it provides a good visual representation of continental margins. This approach is imperfect, eliminating numerous anomalously shallow regions of the ocean basins in addition to continental margins. Nevertheless, the residual area provides a fair estimate of the global range of pelagic sediment supply rates (Figure 2.4).

The median rain rate of 3.5 m $Myrs^{-1}$ is lower than the global rain rate estimate of Johnson and Pruis [2003] due to the exclusion from this study of continental margins, which have thicker sediment in general. Rain rates of 1 m $Myrs^{-1}$ and 10 m $Myrs^{-1}$ represent the 10% and 80% percentiles. For the sedimentation models, values for the sediment rain rate parameter (*F*) were randomly drawn from this distribution.

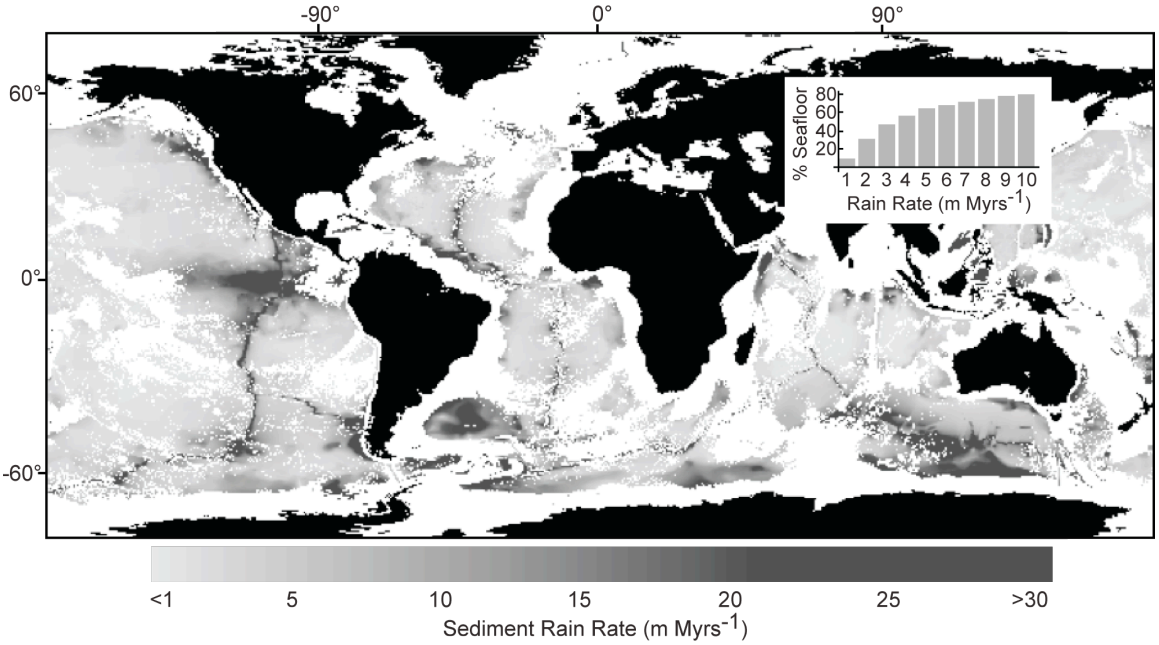

Figure 2.4. Average abyssal sediment rain rates determined from the global, digital plate age [*Müller et al.*, 2008] and sediment thickness [*Divins*, 2011] grids. For each grid cell, the average sediment rain rate is computed as sediment thickness divided by plate age. Areas considered continental margins, and areas where either sediment thickness or plate age data are unavailable, were excluded (excluded areas are white). The residual area is representative of the abyssal seafloor. Continental margins are identified as locations where the depth [*Smith and Sandwell*, 1997] is more than 10% shallower than predicted by the GDH1 lithosphere thermal model [*Stein and Stein*, 1992]. The inset shows the cumulative percentage of abyssal seafloor by sediment rain rate.

2.2.2.2. Post-depositional sediment redistribution

Following its initial deposition, sediment may be redistributed by processes such as mass wasting, interaction with bottom currents and bioturbation. Here, the post-depositional redistribution of sediment is approximated by the diffusion equation, such that the down-slope sediment flux (S) at any given location is proportional to the local topographic gradient [*Webb and Jordan*, 1993]:

$$S(x,y,t) = \kappa \nabla U(x,y,t) \qquad (2.7)$$

where the apparent diffusivity (κ) represents the net effect of environmental conditions that may affect down-slope sediment transport (such as the velocity of bottom currents, the amount of bioturbation and particle cohesion), and U is the height of the sediment-covered seafloor at location (x,y) and time t. Equation 2.7 is solved numerically using the algorithm given in the appendix of Webb and Jordan [2001a], subject to the condition that the sediment flux is not permitted to exceed the available sediment. Topographic gradients are affected by both the basement bathymetry and the changing thickness of overlying sediment. Each sedimentation simulation uses an apparent diffusivity drawn at random from a uniform distribution between 0.007 – 0.34 m^2 yr^{-1}, based on studies of various regions in the ocean with different sediment rain rates, sediment types, and bottom currents [*Webb and Jordan*, 1993, 2001b; *Mitchell*, 1995, 1996].

2.2.2.3. Sediment type

Sediment type is an input to the model because it is used to determine an appropriate formula for calculation of the hydraulic impedance of a given thickness of sediment, which is used to identify potential outcrops (see Section 2.2.3.1). It is assumed that all sediment in the model's spatial domain is of the same type and remains constant with time, although the sediment type may differ between model runs. The sediment type for each model run is selected at random from an area-weighted distribution of surface sediment type for the global abyssal seafloor [*Spinelli et al.*, 2004].

The primary abyssal sediment types, occurring away from continental margins, are calcareous ooze, siliceous ooze, and pelagic clay. Calcareous ooze is derived from biogenically-produced calcium carbonate tests, and siliceous ooze is derived from biogenically-produced amorphous silica. The distribution of these biogenic sediments on

the seafloor is controlled by the balance between biological productivity in the surface water and the rate of dissolution in the water column [*Archer et al.*, 1993]. Calcareous ooze commonly dominates the sediment near the mid-ocean ridge axis where the seafloor is shallower than the carbonate compensation depth (CCD) [*Barron and Whitman*, 1981]. Siliceous ooze dominates the sediment in the deep ocean where there is high biological productivity (notably the equatorial Pacific and the southern ocean) [*Rea et al.*, 1991]. Pelagic clay is sourced from wind-blown dust [*Rea*, 1994], and dominates the sediment where biogenic sediment supply or preservation are very low.

2.2.3. Focused aquifer-ocean fluid exchange

Crustal aquifer overpressures or underpressures (relative to hydrostatic) cause pressure gradients across the sediment that drive vertical fluid exchange between the ocean and the crustal aquifer [*Davis and Becker*, 2004]. Where the sediment distribution is not uniform, there is spatial variability in the hydraulic impedance of the sediment blanket. This variability is critical to understanding the distribution of potential aquifer-ocean fluid exchange sites because fluid will channel through paths of least impedance [*Moreno and Tsang*, 1994].

2.2.3.1. Identifying outcrops

Sedimentation atop basement bathymetry results in a spatially variable distribution of sediment thickness, as affected by slopes on the seafloor, the sediment rain rate, and the apparent diffusivity of the sediment. A simple model is used to determine the distribution of outcrops based on the distribution of sediment in the simulation area. Model locations with no sediment are assumed to be outcrops. Additionally, some locations with a sediment thickness >0 may be identified as outcrops as follows: the

hydraulic properties of the modelled sediment type (pelagic clay, calcareous ooze or siliceous ooze) are represented by the sediment burial depth-porosity and porosity-permeability relationships summarized in Spinelli et al. [2004] (their Table 6.2). For each sediment type, these relationships are combined into a sediment permeability vs. sediment burial depth relationship, $k_s(z)$. The function $k_s(z)$ and the sediment thickness (h_s) are used to determine the hydraulic impedance (I) and bulk vertical permeability (k_{bulk}) of sediment overlying each grid cell in the sedimentation model using [*Spinelli et al.*, 2004]:

$$I = \int_0^{h_s} \frac{dz}{k_s(z)} \qquad (2.8)$$

$$k_{bulk} = \frac{h_s}{I} \qquad (2.9)$$

Using the sediment bulk vertical permeability determined for each grid cell, Darcy's law is applied to estimate the potential magnitude of vertical fluid specific discharge (Q_v) across the grid cell's sediment:

$$Q_v = \frac{k_{bulk}}{\mu} \frac{dP}{h_s} \qquad (2.10)$$

where μ is the fluid's dynamic viscosity and dP is the pressure differential across the sediment. For this calculation, sediment thickness (h_s) is determined by the sedimentation model for each grid cell, and dP is assumed to be equal for each grid cell. The assumption of a spatially uniform dP is clearly incompatible with the notion of lateral fluid flow between outcrops (which requires lateral pressure differences), but allows a first approximation of where the majority of fluid exchange between the ocean and the crustal aquifer is likely to occur. Locations where calculated flow rates across the

sediment are too slow to be thermally significant (defined here by a Peclet number of 1, representing the ratio of advective to conductive heat loss vertically) are eliminated from consideration as potential outcrops. Using the remaining vertical fluid flux estimates from the simulation region, the threshold sediment thickness through which 90% of the calculated potential ocean-aquifer fluid exchange occurs is determined. Groups of adjoining grid cells with sediment thinner than this threshold value are considered to be outcrops. The choice of 90% is arbitrary, but is reasonable because values of 75-99% give similar results – in all cases, outcrops tend to be identified as locations with less than a few metres of sediment (until no such locations exist). The distribution of outcrops is evaluated each 5 Myrs of model time.

2.2.3.2. Partitioning outcrops into recharge and discharge sites

In off-axis oceanic hydrothermal systems, outcrops may act as sites of fluid recharge into the crustal aquifer or sites of fluid discharge from the crustal aquifer [*Fisher et al.*, 2003; *Hutnak et al.*, 2008]. There is also evidence that a single seamount may host both fluid recharge and discharge from different parts of the edifice [*Hutnak et al.*, 2008], and outcrops could exist that do not act as hydrological conduits between the aquifer and the ocean.

Previous studies have investigated the controls that determine whether a particular outcrop will act as a recharge site or discharge site. Harris et al. [2004] and Kawada et al. [2011] performed numerical simulations of fluid circulation driven by lithospheric heat within isolated seamounts, finding that edifice size and shape are important parameters controlling convection within the edifice and the underlying aquifer. In isolation, large seamounts (height > 1 km) with height-to-radius ratios similar to those used for synthetic

seamounts in this study (ξ=0.21), can theoretically support internal cellular convection sustained by lithospheric heat (i.e., recharge and discharge within a single edifice). Such convection removes crustal heat and cools the edifice and aquifer locally [*Kawada et al.*, 2011]. Neither Harris et al. [2004] nor Kawada et al. [2011] modelled flow patterns within small seamounts (height < 1 km) or within abyssal hill outcrops. Within groups of outcrops, there is empirical evidence that the larger edifices act as recharge sites, and the smaller edifices act as discharge sites [*Fisher et al.*, 2003; *Hutnak et al.*, 2008]. This may be because small features experience more concentrated heat supply when subjected to a fixed flow of rising warm fluid, sustaining them as high temperature (low pressure) regions [*Davis and Becker*, 2004]. An additional theoretical constraint on the hydrological role of outcrops is that proximal outcrops may collectively behave as either recharge sites or as discharge sites. This is because the lateral pressure gradients that drive outcrop-to-outcrop flow are a function of both outcrop separation distance and fluid temperature difference, so fluid from any given recharge site may preferentially flow towards an outcrop which is *not* the most proximal. Therefore, the more proximal outcrop would share the hydrological role of one of its neighbors.

For this modelling, each outcrop is assumed to be recharge only or discharge only (none host both recharge and discharge, and none are zero-flow outcrops). The outcrops are classified as recharge or discharge sites by the following steps. First, proximal outcrops are grouped into clusters using an agglomerative clustering algorithm [*Fränti et al.*, 2006]. Outcrops within a given cluster are assumed to be either all recharge or all discharge. Initially each outcrop is considered to be its own cluster. The two nearest clusters are successively merged until no clusters are nearer than a given “cluster

distance" (d_c). Cluster distances of 0 - 5 km are evaluated because the upper bound of this range represents the approximate length scale of fluid warming due to lateral flow (Figure 2.5), and lateral pressure gradients will diminish for larger distances. A cluster distance of zero represents the case where each outcrop acts separately. Uncertainty in the value of this parameter will have the greatest impact on young crust due to the high density of outcrops, but has diminished effect as the seafloor accumulates sediment and outcrops become more widely separated. Second, 50% of the clusters with the largest surface area of outcrop are considered recharge, and the remainder are considered discharge. To test the appropriateness of this method of recharge/discharge classification, an alternative method was also evaluated. In the alternative method, the two nearest clusters that have not yet been classified are assigned opposite hydrological roles (recharge and discharge), and this process is repeated until all clusters have been classified. This alternative method of recharge/discharge classification had little effect on the results of the hydrological modelling, so results are only presented for the case where the largest clusters are recharge sites and the smallest are discharge sites.

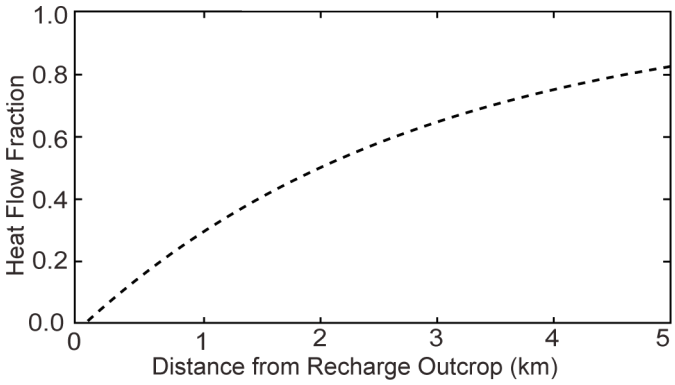

Figure 2.5. Example of the length scale of fluid warming in a well mixed aquifer (Eq. 2.13). Cool fluid enters the crust through a recharge outcrop ($x = 0$), and steady-state fluid flow drives the fluid laterally towards a discharge outcrop ($x = b$). The fluid receives lithospheric heat from below, causing the fluid to warm as it travels. Parameter values used are: $F = 3.5$ m Myrs^{-1}, $t = 10$ Ma, $\lambda_s = 1.2$ W m^{-1} K^{-1}, $b = 10$ km, $k = 10^{-9.5}$ m^2, $h_a = 300$ m. As thermal boundary conditions, there are isothermal columns of 0°C (cool) fluid at the recharge outcrop, and fluid that has warmed to thermal equilibrium with the sediment-basement interface at the discharge outcrop. The driving force of the fluid flow was calculated from the difference between the recharge site's "cold hydrostatic" pressure and the discharge site's "warm hydrostatic" pressure at the base of the aquifer (Eq. 2.16).

For each model simulation, grouping of outcrops into hydrologically related clusters, and assignment of those clusters as either recharge or discharge, is reevaluated each time outcrops are identified from the sediment distribution (after each 5 Myrs of model time). As such, an outcrop may switch clusters or change between recharge and discharge over the course of the simulation, as governed by the cluster distance and the outcrop distribution at each time step.

2.2.4. Outcrop-to-outcrop fluid flow and heat exchange in the crustal aquifer

Because hydrothermal systems redistribute crustal heat, the global heat flow data are influenced by the geometry of hydrothermal systems. As such, hydrological models

for the oceanic crust can be tested for consistency with the global heat flow data. To test whether outcrop-to-outcrop flow is consistent with the global heat flow data, models of outcrop-to-outcrop lateral fluid flow and heat exchange in the upper crust are applied to globally representative outcrop distributions predicted by the models described in Sections 2.2.1 to 2.2.3. Initially, a simple one-dimensional, analytical aquifer model is applied representing an idealized geometry of outcrop-to-outcrop flow in a hydrothermal system. This model is then extended to two dimensions, and applied numerically to explore the effects of more accurately representing the geometry of these systems. The two dimensional numerical model is used to determine whether there are any conditions under which model-predicted seafloor heat flow, as affected by outcrop-to-outcrop flow, is consistent with the global heat flow data.

2.2.4.1. Heat flow data

On average, globally measured conductive heat flow is suppressed relative to theoretical predictions of lithospheric heat loss for crust younger than ~65 Myrs [*Stein and Stein*, 1994]. This heat flow deficit is attributed to advective heat loss [e.g., *Anderson et al.*, 1977; *Fisher et al.*, 1990; *Langseth et al.*, 1988; *Lister*, 1972; *Sclater et al.*, 1974]. Trends in heat flow suppression with age are independent of ocean basin (a proxy for spreading rate) [*Stein and Stein*, 1994], and of sediment type overlying the crustal aquifer. As such, to test the viability of outcrop-to-outcrop flow as a globally important process, a single global data set of heat flow measurements is used to constrain all hydrological models of this process. The conductive heat flow data used here are based on the global compilation of Stein and Stein [1994], excluding continental margin data so that the subset represents abyssal seafloor data only. The data are then grouped

into 5 Myr crustal age bins, and the heat flow average and standard deviation are determined for each bin.

2.2.4.2. Idealized one-dimensional aquifer model

An idealized one-dimensional model of outcrop-to-outcrop flow [*Langseth and Herman*, 1981] is applied to provide a baseline with which to compare the enhanced two-dimensional aquifer model developed for this study (Section 2.2.4.3). The idealized one-dimensional model describes steady-state lateral fluid flow through a crustal aquifer in the uppermost basement between one recharge site and one discharge site, and the corresponding effect on conductive heat flow out the top of the aquifer (Figure 2.2). A deeper aquifer has been previously modelled [*Rosenberg et al.*, 2000], but an aquifer in the uppermost crust is preferred for this global study because low temperature alteration is generally concentrated in the uppermost basement [e.g., *Alt*, 2004; *Gillis and Robinson*, 1990], and permeability generally decreases with crustal depth [e.g., *Fisher et al.*, 2008]. The idealized one-dimensional outcrop-to-outcrop flow model is described here because it is the basis for the enhanced two-dimensional model. The one-dimensional model assumes temperature within the aquifer is constant with depth due to vertical mixing but varies laterally from recharge (cold) to discharge (warm). The fluid temperature difference (and thus, the density difference) between recharge and discharge gives rise to the pressure gradient driving outcrop-to-outcrop flow [*Fisher and Becker*, 2000]. The one-dimensional aquifer model is based on the thermal energy flux balance of the crustal aquifer [*Langseth and Herman*, 1981]:

$$h_a Q \rho c \frac{dT}{dx} - q_m + q_L = 0 \qquad (2.11)$$

where the term $h_a Q \rho c \frac{dT}{dx}$ represents the net lateral advective flux of heat into an increment of aquifer, q_L is the conductive heat flow into the base of the aquifer increment, and q_m is the conductive heat flow out the top of the aquifer increment through the overlying sediment. Lateral heat diffusion is not included. The parameter Q is the fluid's specific discharge, h_a is the aquifer thickness, ρ is the fluid's density, c is the fluid's specific heat capacity, T is the aquifer temperature, and x is the distance from a recharge site. Aquifer temperature T is related to conductive heat flow through the sediment (q_m) by:

$$q_m = \lambda_s \frac{T}{h_s} \qquad (2.12)$$

where λ_s is the sediment thermal conductivity, and h_s is the sediment thickness. With the boundary condition $T = 0$ºC at $x = 0$ (i.e., recharge fluid temperature is equal to the approximate present-day bottom seawater temperature), and assuming ρ, c, q_L, h_s and h_a are uniform with distance away from the recharge outcrop, the solution to equation 2.11 is [*Fisher and Becker*, 2000]:

$$f = \frac{q_m}{q_L} = 1 - \exp\left[\frac{-\lambda_s x}{Q h_s h_a \rho c}\right] \qquad (2.13)$$

where f is the heat flow fraction along the flow path. The average heat flow fraction (f_{avg}) along the flow path between recharge and discharge is:

$$f_{avg} = \frac{1}{b}\int_0^b \left(1 - \exp\left[\frac{-\lambda_s x}{Q h_s h_a \rho c}\right]\right) dx \qquad (2.14)$$

where b is the distance between recharge and discharge sites and Q is the specific discharge. Specific discharge (Q) is related to aquifer permeability (k) through Darcy's Law:

$$Q = \frac{k}{\mu}\nabla P_L \qquad (2.15)$$

where ∇P_L is the average lateral pressure gradient between recharge and discharge [*Fisher and Becker*, 2000]:

$$\nabla P_L = \frac{\Delta\rho g(h_s + h_a)}{b} \qquad (2.16)$$

The value of $\Delta\rho$ is the density difference between recharge and discharge fluids (the discharge fluid is assumed to have reached thermal equilibrium with the aquifer).

2.2.4.3. Two dimensional numerical aquifer model

The idealized one-dimensional aquifer model is extended to two horizontal dimensions so that it may be applied directly to predicted spatial distributions of sediment and outcrops. For any given spatial distribution of recharge and discharge clusters, each cluster is assigned a pressure field representing the perturbation to aquifer pressure around that site due to steady-state fluid recharge or discharge (Thiem's equation) [*Thiem*, 1906]. The pressure fields are represented by:

$$P(x,y) = P_0 \frac{\ln\left(\frac{\sqrt{(x-x_1)^2+(y-y_1)^2}}{r_e}\right)}{\ln\left(\frac{r_0}{r_e}\right)} \qquad (2.17)$$

where r_0 is the radius through which fluid recharges or discharges, r_e is the radius of pressure influence, (x_1, y_1) is the Cartesian coordinate of the recharge or discharge cluster's center, and P_0 is the pressure relative to a background value at r_0 due to a

column of cold aquifer recharge fluid or warm discharge fluid. The derivation of Eq. 2.17 and further discussion of its parameters is provided in Appendix A. Each pressure field is axi-symmetric and, therefore, two-dimensional. The pressure fields from all recharge and discharge clusters are summed to produce a combined pressure field representative of the two-dimensional (plan view) aquifer in the simulation area.

The two-dimensional area is discretized into a grid for numerical computation. Pressure gradients within the crustal aquifer are determined between adjacent grid cells (to the north, south, east, and west) and, from this, fluid fluxes are determined using Darcy's Law (Eq. 2.15). As with the idealized analytical model, it is assumed as a boundary condition that the aquifer fluid temperature at recharge sites is 0°C. The aquifer fluid temperatures into and out of each remaining grid cell are determined by numerically solving the energy balance of Eq. 2.11, beginning with cells adjacent to the recharge sites, and progressively solving for cells adjacent to those with temperatures already determined. For each grid cell, the conductive heat flow out the top of the aquifer is approximated by:

$$q_m = -\lambda_s \frac{T_{in}}{h_s} \qquad (2.18)$$

where T_{in} is the temperature of aquifer fluid entering the grid cell from an adjacent cell. The heat flow into the base of the aquifer is estimated with the GDH1 parameterization of the plate model [*Stein and Stein*, 1992]. These calculations lead to predictions of aquifer fluid temperatures and conductive heat flow through the overlying sediment for each grid cell of the two-dimensional area. The crustal permeability is iteratively adjusted, and the above numerical calculations are repeated, until the average predicted heat flow fraction

fits the global abyssal heat flow fraction for the corresponding crustal age bin (Section 2.2.4.1).

This numerical aquifer model has several advantages over the idealized one-dimensional analytical model [*Langseth and Herman*, 1981] (Section 2.2.4.2). Firstly, a quantitative description of fluid flow in two dimensions may be more representative of flow in natural hydrothermal systems. Secondly, the spatial distribution of recharge and discharge sites predicted by sedimentation/outcrop modelling may be fully represented in the coupled fluid flow and heat exchange calculations. This is preferable to modelling the geometry of the hydrothermal system as an idealized recharge/discharge pair separated by some representative distance, as Fisher and Becker [2000] did. Thirdly, the spatial variability of sediment thickness can be accounted for in these calculations rather than assuming constant sediment thickness. Fourthly, complete statistics of conductive heat flow through the sediment predicted for outcrop-to-outcrop flow in the simulation region can be used to provide a second test of how well the model fits the global heat flow data.

2.3. Results

A series of one hundred model simulations were performed. In these models sedimentation was simulated atop synthetic basement bathymetry, with outcrop identification, recharge/discharge classification, and aquifer energy balance calculations performed every 5 Myrs of model time. For each model run, the initial bathymetry (spreading rate) and values for sediment rain rate, sediment apparent diffusivity, sediment type, cluster distance and aquifer thickness are selected at random from distributions

representing global ranges. The distributions used for each parameter are discussed in Section 2.2 or listed in Table 2.1. Collectively, these model runs represent a global range of bathymetric, sedimentary and aquifer environments. To evaluate the representativeness of the one hundred model runs presented here, the statistics of interest were determined first for a random subset of 50 model runs. As the remaining model runs were incrementally included in the statistics, the average and standard deviation of recharge/discharge separation distance (Section 2.3.1) vary within ±10% of the fifty-sample statistics, and the average and standard deviation of aquifer log permeability (Section 2.3.4) vary within ±15%. These uncertainties in the model predictions are much smaller than uncertainties in the available data, so the one hundred model runs is considered to provide a reasonably representative result.

2.3.1. Recharge and discharge site distributions

For each model run, the distance between each recharge site and the nearest discharge site is determined at each 5 Myr model time step. The average and standard deviation of this characteristic recharge/discharge separation distance were determined over all model runs (Figure 2.6). The models predict that, on average, recharge and discharge sites globally may be 40-50% closer together than previously estimated [*Fisher and Becker*, 2000] (Figure 2.6).

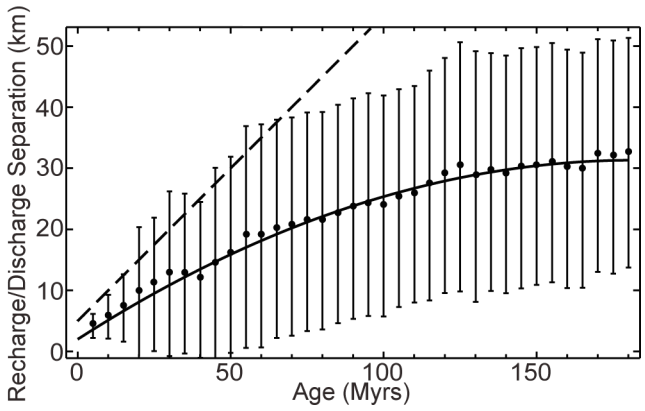

Figure 2.6. Prediction of the distance between recharge and discharge sites averaged over one hundred sedimentation model runs with all sediment, bathymetry, and outcrop parameters randomly chosen from global distributions (see text). Black dots are average distances between recharge sites and the nearest discharge site, and vertical bars are 1 standard deviation after each 5 Myrs of model time. Fit line is $b = -0.00088t^2 + 0.322t + 2$ (b in km, t in Myrs). Dashed line is another estimate of the separation distance between recharge and discharge sites: $b = 5 + 0.5t$ [*Fisher and Becker*, 2000].

The sediment rain rate and the seafloor bathymetry are of primary importance in the distribution of outcrops, with low rain rates and high relief abyssal hills (slow-spreading crust) contributing to greater outcrop density. As modelled, the sediment type only affects the distribution of outcrops when there are no locations with sediment thinner than a few metres. In this case, the relative impedance of different sediment types is more important than the permeability contrast between sediment and basement. Uncertainty in the cluster distance parameter in the range of 0-5 km has a relatively small effect on the average recharge/discharge separation distance. For example, in the case where each outcrop acts separately (i.e., cluster distance is zero), the average recharge/discharge separation distance decreases by 2.6 ± 0.7 km (average and one standard deviation).

Seamounts are significant to the distribution of outcrops where abyssal hill relief is low (fast-spreading crust) because they greatly increase the proportion of prominent topographic highs, but seamounts have a diminished effect where abyssal hill relief is high, as on crust formed at slow-spreading ridges (Figure 2.7).

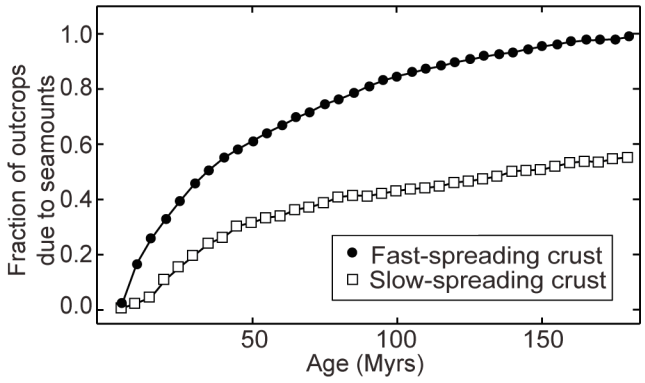

Figure 2.7. The predicted fraction of outcrops due to seamounts (as opposed to abyssal hill crests) for fast- and slow-spreading crust.

2.3.2. Onset of outcrop-to-outcrop fluid flow in the oceanic crustal aquifer

Steady-state outcrop-to-outcrop flow requires sufficient sediment cover to hydraulically seal some portions of the basement (at least partially), so outcrop-to-outcrop flow is unlikely to be the primary geometry of seafloor hydrothermal systems on very young seafloor. Before applying the quantitative hydrological models of outcrop-to-outcrop flow, I first consider the earliest age at which these models may become appropriate.

A simple model of the driving lateral and vertical forces of off-axis hydrothermal circulation is used to assess the onset of outcrop-to-outcrop flow. Lateral pressure gradients drive outcrop-to-outcrop flow. The lateral pressure gradient within the aquifer is a function of both recharge/discharge separation distance and fluid temperature difference. Temperature is relevant because it affects fluid density, and therefore also affects the pressure within the aquifer. Fluid buoyancy is the primary vertical force

encouraging fluid to discharge before significant lateral movement. In a simple model these forces control the balance between outcrop-to-outcrop flow and vertical discharge through the sediment. The average lateral pressure gradient between recharge and discharge sites was determined from Eq. 2.16. In this calculation an average simulated recharge/discharge separation distance was assumed (Figure 2.6), and $\Delta\rho$ is calculated based on the fluid temperature difference between 0°C recharge fluid and discharge fluid in thermal equilibrium with lithospheric heat flow at the sediment-basement interface. In natural systems the fluid may reach thermal equilibrium with lithospheric heat flow before discharging [e.g. *Fisher et al.*, 2003], but this is not the case everywhere [e.g. *Hutnak et al.*, 2008]. The assumption of fully warmed fluid leads to an upper bound on the lateral pressure gradient. The sediment thickness (h_s) is assumed to be the regional average (rain rate × crustal age). The buoyancy-driven vertical pressure gradient is determined from:

$$\nabla P_V = \frac{\Delta\rho g}{h_s} \qquad (2.19)$$

For a 300 m thick aquifer (h_a=300 m), and using h_s determined as a function of time for a rain rate of 3.5 m Myrs^{-1} (the median abyssal rain rate), the lateral pressure gradient is estimated to overtake the vertical gradient within a few Myrs of crustal formation (Figure 2.8). This result is insensitive to the choice of cluster distance (d_c) within the range evaluated (0-5 km). Because the permeability of sediment is lower than that of the aquifer, outcrop-to-outcrop fluid flux will overtake vertical fluid flux even sooner than predicted by this model.

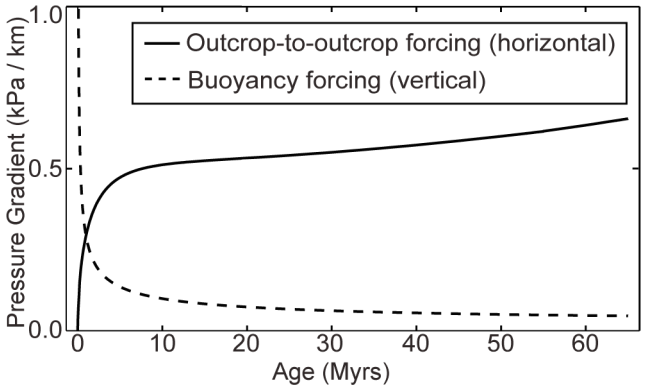

Figure 2.8. Comparison of estimated horizontal pressure gradients between outcrops and vertical pressure gradients due to buoyancy. A first approximation for the timing of the onset of outcrop-to-outcrop flow is the age at which the horizontal forcing first exceeds the vertical forcing (within a few Myrs). The average horizontal pressure gradient (dP/dx) is calculated with $dP = \Delta\rho g(h_s+h_a)$ based on the density difference between recharge and discharge fluid (assuming discharge fluid has reached thermal equilibrium with the aquifer), and with dx from the estimated average recharge/discharge separation distance (Figure 2.6). The vertical pressure gradient through the sediment due to buoyancy is calculated as $\Delta\rho g/h_s$.

Aquifer pressures predicted by this modelling are generally within ±7.5 kPa of hydrostatic pressure, leading to pressure differentials between recharge and discharge sites generally less than 15 kPa (Appendix B). For comparison, pressures relative to hydrostatic measured in the upper crust in ODP Holes 504B, 1024C, 1025C, 1026B, 1027C were -11 kPa, -3 kPa, +3 kPa, +18 kPa and -26 kPa respectively [Davis et al., 2004; Davis and Becker, 2002]. These holes were all drilled into young crust (<7 Ma) that experienced much more rapid sediment supply than the global mean sediment rain rate. These conditions result in an anomalously warm aquifer, so it is not surprising that the magnitude of super- and sub-hydrostatic pressures measured in some of the above drill holes exceeds the values predicted by this more globally representative modelling.

2.3.3. The role of enhanced model complexities

The present study builds on the idealized model of outcrop-to-outcrop fluid flow and aquifer heat exchange applied by *Fisher and Becker* [2000] by: (i) developing new estimates of the separation distance between outcrops globally, (ii) numerically modelling aquifer fluid flow in two horizontal dimensions, (iii) representing predicted spatial distributions of outcrops instead of an idealized recharge-discharge pair, and (iv) accounting for variability in sediment thickness. These enhancements all affect model predictions of conductive heat flow out the top of the aquifer due to outcrop-to-outcrop fluid flow within the aquifer, and therefore also affect the conditions in which the models fit the global heat flow data.

To illustrate the effects of the model enhancements on conductive heat flow out of the top of the aquifer, the idealized one-dimensional aquifer model is run as a base case, followed by runs that incrementally add in the modifications introduced in this study. For this comparison of models, no attempt is made to fit the global heat flow data. I simply compare the average heat flow vs. age predicted by the different models for a fixed set of parameter values. The following parameters are held constant for all models: $F = 3.5$ m Myrs^{-1}, $\kappa = 0.1$ m^2 yr^{-1}, $h_a = 300$ m, $k = 10^{-9.5}$ m^2, and $d_c = 5000$ m. Additionally, heat flow into the base of the aquifer is defined by the GDH1 parameterization of the plate model [*Stein and Stein*, 1992], and the initial bathymetry represents crust formed at an intermediate spreading rate. The incremental effects of the model modifications on the predicted average conductive heat flow out the top of the aquifer are shown in Figure 2.9 and explained below.

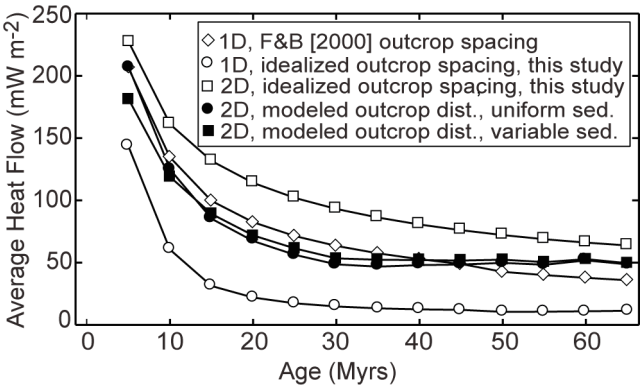

Figure 2.9. The effects of sedimentation and hydrological model changes introduced in this study on the prediction of average conductive heat flow over the model's spatial domain between recharge and discharge sites. Parameter values: F = 3.5 m Myrs^{-1}, κ = 0.1 m^2 yr^{-1}, h_a = 300 m, k = 10$^{-9.5}$ m^2, d_c = 5 km, and the initial bathymetry represents crust formed at an intermediate spreading rate.

As a base case, the idealized one-dimensional aquifer model is evaluated (Eq. 2.14, Figure 2.2) with the characteristic recharge/discharge distance (b) estimated by Fisher and Becker [2000], and a uniform sediment thickness (h_s) equal to sediment rain rate × age. To evaluate the effect of the new predictions of outcrop distribution on average heat flow, the same model was evaluated again, but setting b to the global average distance between a recharge site and the nearest discharge site estimated in this study (Figure 2.6). The new estimate of the global average recharge/discharge separation is smaller than the previous estimate [*Fisher and Becker*, 2000], so with all other parameters held constant this leads to larger pressure gradients and faster fluid flow extracting more heat (i.e., lower conductive heat flow at the seafloor). The effects of changing from a one-dimensional analytical aquifer model to a two-dimensional numerical aquifer model were assessed by calculating average heat flow over a two-dimensional area with a distribution of equally-spaced recharge and discharge sites

(separated by a distance of *b*, as per Figure 2.6). The two-dimensional model predicts higher average heat flow than the one-dimensional model (Figure 2.9). This is because there is greater area weighting for the locations distal from recharge, and the distal locations have higher heat flow because the aquifer fluid will have warmed as it travelled there. Using the actual predicted spatial distribution of recharge and discharge sites, instead of an average separation distance (*b*), reduces the average heat flow (Figure 2.9). This results from a non-linear scaling of average heat flow with recharge/discharge separation distance, so closely spaced recharge/discharge pairs have a greater effect on reducing the average heat flow than widely separated recharge/discharge pairs have on increasing the average heat flow. Using the model-predicted, spatially variable sediment thickness in the heat flow calculations, as opposed to assuming uniform sediment of a thickness equal to the regional average, has only a minor effect on the average heat flow relative to the other changes noted above (Figure 2.9). Nevertheless, modelling the variability in sediment thickness is useful to this study because it permits a meaningful determination of heat flow variability over the simulation region.

2.3.4. Conditions in which the global heat flow data are consistent with outcrop-to-outcrop flow

Seafloor heat flow predictions as a function of time were made using the two-dimensional numerical model of aquifer fluid flow and heat exchange (Section 2.2.4.3) for the predicted sediment and outcrop distributions of each model run (where each run is based on parameters randomly drawn from global distributions). The spatial variability in sediment thickness and the predicted spatial distribution of recharge and discharge outcrops are both represented in this modelling. For each model run the aquifer permeability was adjusted at each 5 Myr time step until the model-predicted average heat

flow fraction fit the global data for the corresponding age bin (Section 2.2.4.1). The required permeability for outcrop-to-outcrop flow to explain the global average heat flow deficit, averaged over all model runs in the globally representative suite, decreases from $\sim 10^{-9}$ to 10^{-11} m^2 over the duration of the average global heat flow deficit (~65 Myrs) (Figure 2.10). The permeability is relatively insensitive to the cluster distance parameter. For example, in the case where each outcrop acts separately (i.e., cluster distance is zero), the log permeability required to fit the global heat flow data decreases by 0.09 ± 0.06 m^2 (average and one standard deviation). Crustal ages beyond 65 Myrs are not explored because the average oceanic heat flow deficit, assumed equivalent to the average advective heat loss, decreases to zero by this age. By implication, the average rate of ocean-aquifer fluid exchange is thermally insignificant, and therefore the heat flow data in combination with the present model provide no constraint on aquifer permeability.

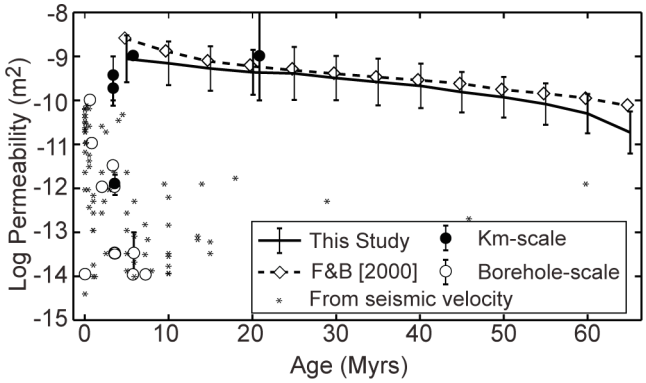

Figure 2.10. Permeability average and one standard deviation required for average heat flow predicted by the two-dimensional numerical model of outcrop-to-outcrop flow to fit the global heat flow data [*Stein and Stein*, 1994]. The best fitting permeability average and standard deviation were determined from a suite of one hundred model runs in which sediment, bathymetry, outcrop and hydrological parameters were randomly chosen from global distributions (see text). Other estimates of borehole-scale and km-scale permeability are shown for comparison [*Davis et al.*, 2000; *Fisher and Becker*, 2000; *Davis et al.*, 2001; *Davis and Becker*, 2002; *Becker and Davis*, 2003; *Davis et al.*, 2004; *Fisher*, 2005; *Hutnak et al.*, 2008; *Fisher et al.*, 2008]. Also shown are permeabilities estimated from seismic P-wave velocities [*Carlson*, 1998] using the velocity-permeability relationship of Carlson [2011]: log(k) = -(7.5 + 1.3 * velocity in km/s). Parameters for Fisher and Becker [2000] (diamonds) are F = 3.5 m Myrs^{-1} and h_a = 300 m.

The standard deviation of model-predicted heat flow was also determined as a function of time for the best-fitting average heat flow fraction (Figure 2.11). The model-predicted standard deviation of heat flow does not fit the data for the parameters required to fit the average heat flow (Figure 2.11). This may reflect a sampling bias in the heat flow data. Because heat flow probes can be damaged by encountering bedrock, heat flow measurements are preferentially taken away from locations known to have patchy or thin sediment. It is difficult to quantify this sampling bias, but I note that if a sampling bias is represented in the model by determining the average and standard deviation of model-

predicted heat flow only from locations with sediment thicker than 5 m, then the modelled heat flow distribution changes such that the modelled heat flow average and standard deviation can simultaneously fit the global data (Figure 2.11). The permeability required for the modelled average heat flow fraction to fit the data shifts by up to 20% depending on whether the average heat flow is calculated for the full simulation area, or just for the subset with at least 5 m of overlying sediment (i.e., the change is small relative to other uncertainty in aquifer permeability). In summary, the required change in aquifer permeability is simultaneously consistent with the measured heat flow average and variability if it is assumed that there is a sampling bias in the global heat flow data. If there is a sampling bias in the global heat flow data, then the model results here suggest the hydrothermal heat flux should not be estimated from the apparent heat flow deficit without accounting for the bias, otherwise the hydrothermal heat flux may be overestimated.

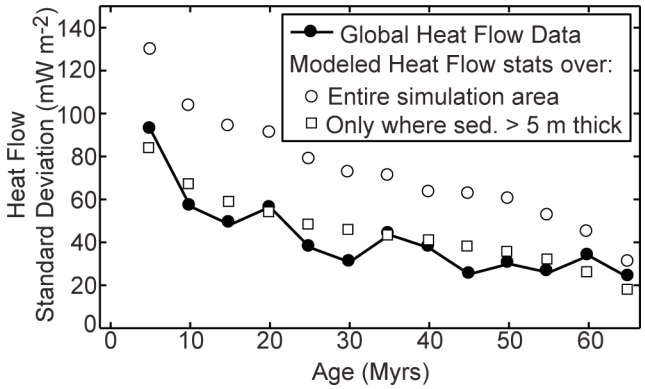

Figure 2.11. The standard deviation of model-predicted heat flow for models in which the average heat flow has been fit to the global data (by adjusting aquifer permeability). When heat flow statistics are calculated over the entire simulation area, the standard deviation and average of heat flow cannot simultaneously fit the global data. Calculating the statistics of model-predicted heat flow only over the subset of the simulation area with sediment thicker than 5 m (to simulate the sampling bias in the global data) allows the modelled heat flow standard deviation and average to simultaneously fit the data.

Also evaluated was the sensitivity of these results to uncertainty in the global seamount population and in the number of outcrops that are hydrologically active. For models with twice as many seamounts, consistent with the global seamount population estimated by Hillier and Watts [2007], the required log permeability decreases by 0.15 ± 0.05 m^2. This is a relatively minor effect because seamounts are not the only source of outcrops in the model. The fraction of all outcrops globally that are hydrologically active is a more significant uncertainty. In this modelling, a random selection of outcrops can be "turned off" by excluding them as possible recharge or discharge sites. Doing so demonstrates that log permeability increases approximately linearly with the fraction of hydrologically active outcrops, such that if only 10% of the outcrops are hydrologically active, then the aquifer must be about an order of magnitude more permeable.

2.4. Is outcrop-to-outcrop flow the dominant mode of hydrothermal heat loss from the oceanic crust

The model of outcrop-to-outcrop flow is only consistent with the global heat flow data if the average aquifer permeability decreases from approximately 10^{-9} m^2 to 10^{-11} m^2 over the duration of the average global heat flow deficit (~65 Myrs, Figure 2.10). To assess whether the permeabilities required by outcrop-to-outcrop flow are reasonable, these results are compared to other permeability estimates of the upper oceanic crust.

The average permeabilities required by outcrop-to-outcrop flow, as predicted in this study, represent a spatial scale of multiple kilometres. Four of the five estimates of upper crustal permeability at the kilometre scale (for 3.5 – 20 Ma crust) are within one standard deviation of the permeability required for outcrop-to-outcrop flow to explain the global heat flow data (Figure 2.10). The permeabilities required by outcrop-to-outcrop

flow are higher than most small-scale estimates of upper crustal permeability (from measurements in individual boreholes and estimates from seismic velocities [*Carlson*, 2011], Figure 2.10). This is consistent with observations that permeability is strongly scale dependant [*e.g., Becker et al.*, 2004], but requires that there exist spatially rare, high permeability channels within the crust as suggested by Fisher and Becker [2000]. The geological processes responsible for such high-permeability channels are not well understood.

The rate of reduction in permeability required by outcrop-to-outcrop flow is approximately two orders of magnitude over 65 Myrs. Too few estimates of permeability at a similar scale to this study (km-scale) are available to directly assess the reasonableness of this rate. Small-scale upper crustal permeability decreases by 3-4 orders of magnitude over the first 10 Myrs of crustal age. This suggests that if outcrop-to-outcrop flow is the dominant mode of off-axis hydrothermal circulation then the spatially rare high-permeability channels must experience a more gradual reduction in permeability than the smaller scale rock formation.

The average permeabilities required by outcrop-to-outcrop flow appear to be consistent with other permeability estimates and measurements, supporting outcrop-to-outcrop flow as being the primary mode of off-axis hydrothermal circulation globally provided that there are high permeability channels that survive in the upper crust. Nevertheless, other models may also be plausible and, in fact, may dominate if such channels do not exist. The global importance of local circulation within individual seamounts [*Harris et al.*, 2004; *Kawada et al.*, 2011] and of vertical fluid seepage through sediments to advective heat and chemical fluxes between the ocean and the

crustal aquifer remain open questions. If outcrop-to-outcrop flow is the dominant mode of off-axis hydrothermal circulation, then the gradual decline in the heat flow deficit over 65 Myrs is due to decreasing crustal permeability, increasing distance between outcrops, and waning lithospheric heat loss. Together these processes overwhelm the effects of thickening sediment which increases peak aquifer temperatures and hence lateral pressure differences.

2.5. Conclusions

The proposition that outcrop-to-outcrop flow is a globally important means of hydrothermal heat extraction is tested using numerical models and a global data set of heat flow measurements. Models of seafloor bathymetry and sedimentation are used to estimate the distribution of basement outcrops in abyssal settings globally. Outcrops are classified as recharge sites or discharge sites in a manner consistent with empirical data. A numerical model of fluid flow and heat exchange through the crustal aquifer, between recharge and discharge sites, is developed and used to determine the conditions in which outcrop-to-outcrop fluid flow in abyssal settings globally is consistent with the global compilation of heat flow measurements. This modelling results in four primary conclusions: (1) It is predicted that basement outcrops globally are 40-50% closer than previously estimated (Figure 2.5), implying pressure gradients within the crust may be higher than previously estimated. (2) The onset of outcrop-to-outcrop flow may occur within a few Myrs of crustal formation on average globally. (3) The modelled heat flow only fits the global data if the probable sampling bias in the global heat flow data is simulated in the modelled heat flow statistics. (4) The average upper crustal permeability must decrease from ~10^{-9} m^2 to ~10^{-11} m^2 between 5-65 Myrs for the average and

standard deviation of modelled heat flow to fit the global heat flow data. This range of permeability is consistent with outcrop-to-outcrop flow being the dominant mode of seafloor hydrothermal circulation.

3. A hydrologic model for the uppermost oceanic crust constrained by temperature estimates from carbonate minerals

3.1. Introduction

The heat released by the cooling of the oceanic lithosphere drives the entire volume of the global ocean through the oceanic crust every few hundred thousand years [*Parsons and Sclater*, 1977; *Mottl and Wheat*, 1994; *Johnson and Pruis*, 2003]. The fluid passing through the crust is believed to be concentrated in the most permeable upper few hundred metres of the oceanic crust (the aquifer), as supported by permeability estimates from a suite of drill hole pumping tests [*Fisher*, 2005] and observations that oxidative alteration, and hence low-temperature fluid flux, are concentrated in the upper igneous extrusive rocks [e.g., *Alt et al.*, 1986a, 2010; *Gillis and Robinson*, 1990]. The majority of the global hydrothermal fluid flux passes through the oceanic crust in off-axis settings [e.g., *Mottl and Wheat*, 1994]. This hydrothermal circulation is an important mechanism of heat loss from the oceanic crust. It also helps to support a crustal biosphere and leads to globally significant chemical fluxes between the crust and the ocean.

A fundamental question for quantifying the thermal, chemical and biological effects of hydrothermal circulation globally is how fluid enters and leaves the crust in off-axis settings, and its flow paths therein. Spatial patterns in seafloor heat flow measurements in multiple settings are consistent with models of a process in which ingress into, and egress from the crustal aquifer occur through discrete seafloor basement exposures ("outcrops"), with lateral fluid flow through the aquifer connecting these recharge and discharge zones [e.g., *Baker et al.*, 1991; *Fisher et al.*, 2003; *Hutnak et al.*, 2008; *Langseth and Herman*, 1981; *Langseth et al.*, 1984, 1992]. Using statistical constraints

from the global data set of seafloor heat flow measurements, it has been proposed that outcrop-to-outcrop flow may be characteristic of off-axis, hydrothermal systems globally [*Fisher and Becker*, 2000]. Anderson et al. [2012] extended the study of Fisher and Becker [2000] by coupling a model of lateral fluid flow and heat exchange in the aquifer with a probabilistic model of the global outcrop distribution, finding that outcrop-to-outcrop flow is consistent with global heat flow data if regional scale aquifer permeability decreases, on average, from 10^{-9} to 10^{-11} m^2 over the duration of the heat flow deficit (65 Myrs).

A common assumption in hydrologic models representing outcrop-to-outcrop flow is that there is efficient vertical heat advection in the aquifer, which homogenizes temperatures with depth (i.e., the aquifer is thermally "well mixed") [e.g., *Anderson et al.*, 2012; *Baker et al.*, 1991; *Davis et al.*, 1999; *Fisher and Becker*, 2000; *Langseth and Herman*, 1981; *Langseth et al.*, 1992; *Lucazeau et al.*, 2006; *Rosenberg et al.*, 2000]. Support for the assumption of a thermally well mixed aquifer comes largely from hydrologic models constrained by heat flow measurements [e.g., *Davis et al.*, 1997; *Fisher and Von Herzen*, 2005]. Temperature logging within Deep Sea Drilling Project (DSDP)/Ocean Drilling Program (ODP) Holes 504B and 896A, however, reveals temperature gradients in the upper basement [*Becker et al.*, 2004], suggesting the aquifer at these locations is not thermally well mixed. The rock record can provide additional insight into thermal mixing within the aquifer. Crustal rocks that experience off-axis hydrothermal circulation are altered by the interaction of fluid circulating within the aquifer. As such, thermal models of the crustal aquifer can be tested for consistency with temperature proxies from minerals that formed at different depths in the crust as a result

of off-axis hydrothermal circulation.

In this study, a compilation of previously published O-isotope data from crustal carbonate minerals picked from ten DSDP/ODP/Integrated Ocean Drilling Program (IODP) drill holes (representing seven discrete locations) are used as proxies for temperatures in the crustal aquifer, and are tested for consistency with temperatures predicted by models of fluid flow and heat exchange in an aquifer experiencing outcrop-to-outcrop flow. At three drilling locations the estimated formation temperatures of the carbonates are consistent with outcrop-to-outcrop flow in a well mixed aquifer. At the other four drilling locations the estimated carbonate formation temperatures are too high to be explained by a well mixed aquifer at any crustal age. It is found that the carbonate data from these locations can be reconciled with a model of outcrop-to-outcrop flow, but only in an aquifer that experiences less efficient vertical heat advection (i.e., a poorly mixed aquifer).

3.2. Crustal carbonate oxygen isotope data

Carbonate minerals, such as calcite and aragonite, form as secondary minerals in the oceanic crust as a result of fluid-rock reactions. Petrological evidence suggests that carbonates generally form after many of the other secondary phases associated with ridge flank hydrothermal circulation [e.g., *Alt and Honnorez*, 1984; *Staudigel et al.*, 1981]. When carbonate minerals precipitate, oxygen isotopes are fractionated between the mineral and the water in a way that is temperature-dependent [e.g., *Kim and O'Neil*, 1997; *O'Neil et al.*, 1969]. This study uses previously published O-isotope compositions ($\delta^{18}O$) of crustal carbonates (Figure 3.1) recovered by drilling in the uppermost 100 - 600 m of igneous crust at ten DSDP/ODP/IODP drill holes to constrain the carbonate

formation temperatures, and thus temperatures experienced by the crustal aquifer. Because aquifer temperatures are influenced by the pelagic sediment supply rate, basement roughness (largely reflecting differences in spreading rate), and crustal age [*Anderson et al.*, 2012], the drilling locations selected for this study represent ranges in these parameters.

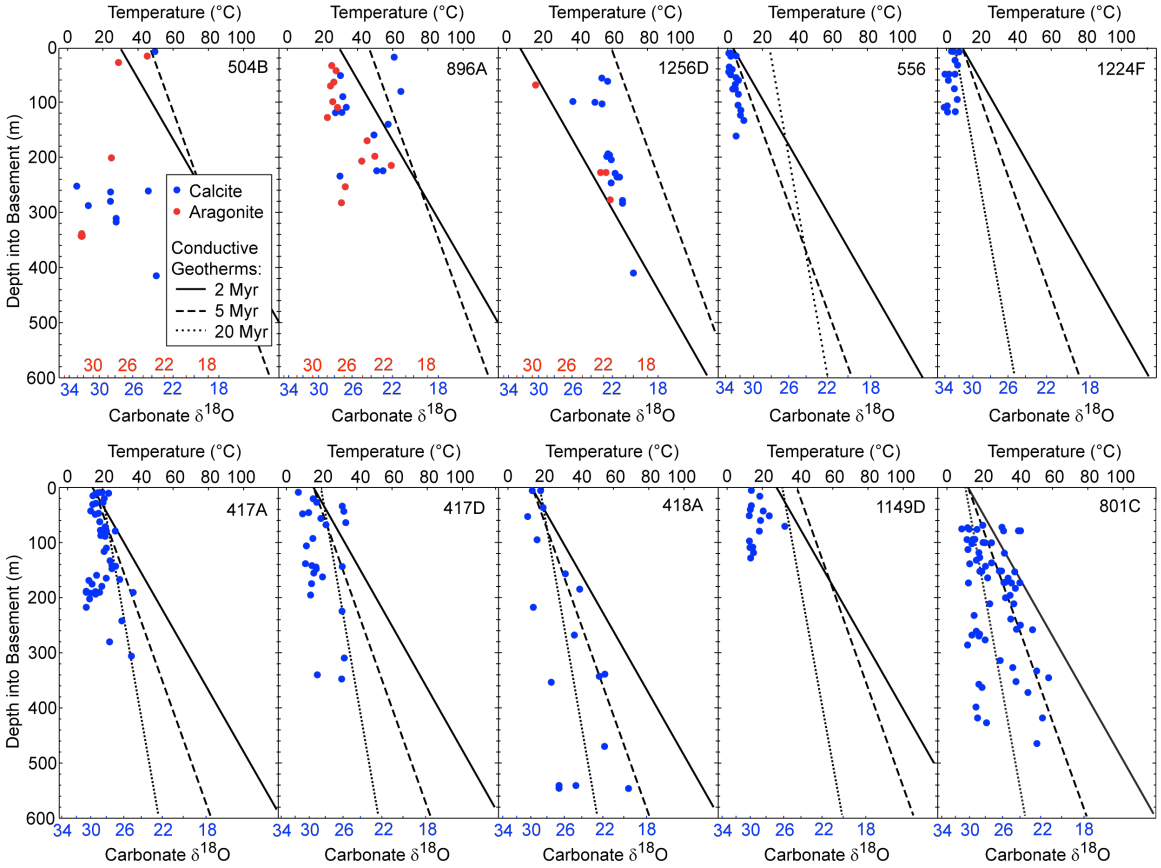

Figure 3.1. Crustal carbonate $\delta^{18}O$ data for the DSDP/ODP/IODP holes used in this study. Formation temperatures presented in this figure are estimated using the calcite-water O-isotope thermometer of Kim and O'Neil [1997], with a 0.7‰ offset for aragonite [*Grossman and Ku*, 1986]**. It is assumed that all carbonates formed in equilibrium with seawater. Fluid $\delta^{18}O$ (SMOW) is assumed to be 0‰, -0.5‰ and -1‰ for crustal ages <20 Ma, 20-55 Ma and >55 Ma, respectively** [*Coggon et al.*, 2010]**. See the main text for a discussion of the uncertainties inherent in these assumptions. Conductive geotherms through the aquifer are calculated based on the estimated thickness of overlying sediment after 2, 5, and 20 Myrs. Data sources are listed in Appendix J, Supplementary Table S3.1.**

The carbonate $\delta^{18}O$ data from the drill holes used in this study suggest that temperatures of the aquifer in off-axis hydrothermal systems are typically 0-60ºC (Figure 3.1). Data from about half of the drill holes show a trend of decreasing $\delta^{18}O$ with depth (Figure 3.1). There are three possible explanations for this trend: (i) the deep fluid in the aquifer was depleted in ^{18}O relative to the shallow fluid, (ii) the deep carbonates formed at times when the combination of lithospheric heat flow and sediment thickness made the entire aquifer warmer than when the shallow carbonates formed, or (iii) aquifer temperatures increased with depth during the period when the carbonates formed.

Model (i) can be rejected using a back-of-the-envelope mass balance calculation. Assuming the $\delta^{18}O$ of fresh aquifer rock is 5.8‰ [e.g., *Muehlenbachs and Clayton*, 1972], and using a $\delta^{18}O$ of altered aquifer rock of < 10‰ [*Hoernes and Friedrichsen*, 1978; *Friedrichsen and Hoernes*, 1980; *Alt et al.*, 1986a; *Alt and Teagle*, 2000, 2003], and water-rock mass ratios of >10 even in the deepest aquifer [e.g., *Alt et al.*, 1986b], then plausible shifts in $\delta^{18}O$ of the deep fluid relative to seawater are < 0.5‰. Such shifts in the fluid composition would decrease calculated formation temperatures of the deep carbonate minerals (Figure 3.1) by only a few degrees Celsius at most. This means the depth trend in the carbonate $\delta^{18}O$ data (Figure 3.1) likely represents a trend of increasing carbonate formation temperature with depth. The modelling presented in Section 3.5 shows that, irrespective of the timing of carbonate formation, model (ii) cannot explain all of the data. As such, the carbonate data at some of the drill holes require model (iii), an aquifer in which vertical advection is not efficient enough to homogenize temperatures across the thickness of the aquifer (i.e., an aquifer which is not thermally well mixed).

3.3. Poorly mixed aquifer model

Since some of the carbonate data require an aquifer that is not thermally well mixed (Section 3.2), a poorly mixed aquifer model is developed which can represent inefficient vertical advection within the aquifer and, thus, a temperature gradient across the thickness of the aquifer. A poorly mixed aquifer implies higher temperatures deeper in the aquifer than can be explained by a well mixed aquifer and is the only way in which the high-temperature carbonate minerals at some of the drilling locations are consistent with outcrop-to-outcrop flow. This model is used to explore those conditions under which the carbonate data are consistent with outcrop-to-outcrop flow.

The poorly mixed aquifer is mathematically represented as a stack of well mixed hydrologic layers overlain by a layer of impermeable sediment (Figure 3.2). The aquifer layers do not necessarily represent discrete lithological sections (although they could). In this study the layers are used to represent gradual changes in properties with depth. Each aquifer layer experiences steady-state lateral fluid flow and heat exchange, but fluid does not mix across layer boundaries; vertical heat transport across layer boundaries is purely conductive. Horizontal heat transport within each aquifer layer is purely advective. For reasonable thermal conductivities within the aquifer, this results in a stepped vertical temperature gradient across the full thickness of the aquifer. The energy balance for each layer is:

$$-\rho c L v \frac{dT}{dx} + q_{in} - q_{out} = 0 \qquad (3.1)$$

The first term in this equation represents heat transport by lateral advection, where ρ is the fluid density, c is the fluid heat capacity, L is the thickness of the layer, v is the specific discharge, and dT/dx is the lateral temperature gradient. The symbols q_{in} and

q_{out} represent conductive heat flow into the base of the layer and out of the top of the layer respectively. Conductive heat flow into the base of the bottom layer is assumed to be lithospheric, taken from the global heat flow model GDH1 [*Stein and Stein*, 1992]. Because each layer is well mixed, and there is a temperature step between adjacent layers, vertical conductive heat flow between aquifer layers is approximated by the product of aquifer thermal conductivity and the temperature difference between adjacent layers divided by the layer thickness.

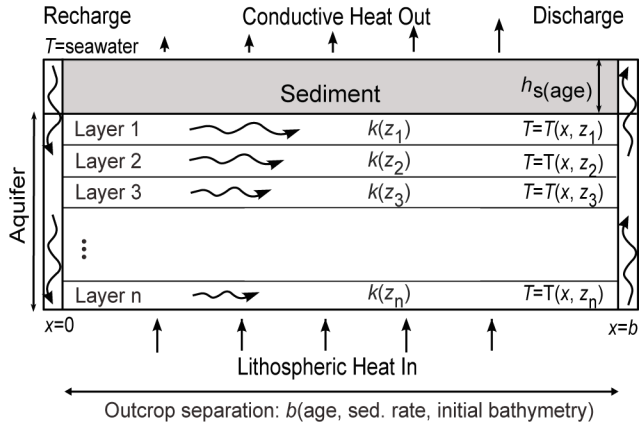

Figure 3.2. A schematic diagram of the layered aquifer model. The aquifer is represented as a vertical stack of permeable layers, each of which may have a discrete representation of permeability (k). Overlying the aquifer is an impermeable layer of sediment with uniform thickness (h_s). Vertical heat transport between aquifer layers is purely conductive, and lateral heat transport is purely advective. In this model cold fluid enters the crust at a recharge zone ($x = 0$), and travels laterally within one of the aquifer layers towards a discharge zone (at $x = b$). As the fluid travels it warms to a maximum temperature defined by the purely conductive geotherm. As a result, deeper aquifer layers experience higher temperatures.

The layered aquifer model is implemented numerically. The results described herein were produced using a horizontal and vertical resolution of 50 m. Tests of models with higher resolution demonstrated that 50 m provides sufficient accuracy. For

example, heat flow out of the top layer is generally within a few mW of the value predicted by a model with 5 m resolution (i.e., within the uncertainty in the global heat flow data). Due to each layer being well mixed, the largest error in temperature as a function of depth occurs at the base of each layer, where the temperature is underestimated by up to a few degrees (i.e., within the uncertainty in the estimated carbonate formation temperatures, discussed in Section 3.4.1).

3.3.1. Pressure differences driving lateral flow in the aquifer

The driving force of outcrop-to-outcrop flow is thought to result from a difference in pressure beneath columns of cool recharge fluid and warmer discharge fluid [*Fisher and Becker*, 2000]. The pressure difference (*dP*) available to drive lateral fluid flow has been approximated by Fisher and Becker [2000] as:

$$dP = \Delta\rho_0 g(h_s + h_a) \qquad (3.2)$$

where $\Delta\rho_0$ is the difference in fluid density between cold recharge fluid and warmer discharge fluid, g is gravity, h_s is the sediment thickness and h_a is the aquifer thickness. This approximation assumes that both the recharge and discharge columns extend from the top of the sediment to the base of the aquifer. In nature, outcrops might typically be topographic highs that extend above the top of the sediment. The height of the outcrop above the location of sediment overlap is excluded from the calculation of *dP* because this detail has little bearing on estimates of aquifer permeability (discussed in Section 3.3.3), and because it is unclear whether an unsedimented outcrop summit could maintain temperatures significantly different from seawater. The column of recharge fluid is assumed to be uniformly of bottom seawater temperature. This assumption is consistent with fluid fluxes estimated through outcrops on the Cocos plate [*Hutnak et al.*, 2008] and

the eastern flank of the Juan de Fuca Ridge [*Fisher et al.*, 2003]. For example, 1 litre s^{-1} of recharge fluid flux [*Fisher et al.*, 2003] through a circular outcrop of 500 m radius into an aquifer 100-600 m thick gives a Peclet number (the ratio of vertical advection to conduction) of a few hundred, which is sufficient to produce a nearly isothermal condition at the recharge zone. The column of discharge fluid is different for the well mixed and poorly mixed cases. If it is assumed that fluid in the aquifer has reached thermal equilibrium with lithospheric heat flow before discharging, then in a well mixed aquifer the discharge column has a uniform fluid temperature equal to the equilibrium temperature at the sediment-basement interface. In a poorly mixed aquifer, fluid near the discharge zone that has reached thermal equilibrium with the aquifer rocks will have a temperature profile equivalent to the purely conductive geotherm. Although vertical advection (mixing of fluid between layers) is restricted along the entire lateral flow path in a poorly mixed aquifer, fluid from each layer must ascend (and mix) at the discharge zone. Therefore, in the poorly mixed aquifer model it is assumed that the discharge column has a uniform temperature equal to the average discharge temperature of each model layer weighted by the volumetric fluid flux within that layer. Because a poorly mixed aquifer can achieve warmer discharge zone temperatures than a well mixed aquifer, and because fluid density is a function of temperature, the driving lateral pressure differences (Eq. 3.2) are greater in a poorly mixed aquifer than a well mixed aquifer (Figure 3.3). The difference in *dP* between the two models is greatest for a thick aquifer in which deep, warm fluid contributes to the weighted average temperature of the discharge column. In a poorly mixed aquifer the driving lateral pressure difference initially decreases with time as waning lithospheric heat flux reduces vertical temperature

gradients in the upper crust, and therefore also reduces the maximum temperatures in the aquifer. As the rate of change in the vertical temperature gradient slows and the aquifer becomes buried by increasingly thick sediment (which increases aquifer temperatures), the driving lateral pressure differences are predicted to begin increasing again (Figure 3.3). Thin, poorly mixed aquifers are predicted to experience only a few Myrs of decreasing lateral pressure difference before the inflection point, while thick aquifers may experience up to 30 Myrs of decreasing lateral pressure difference before the inflection point (Figure 3.3). Well mixed aquifers do not experience decreasing lateral pressure differences because the effects of thickening sediment overwhelm the effects of decreasing lithospheric heat flux.

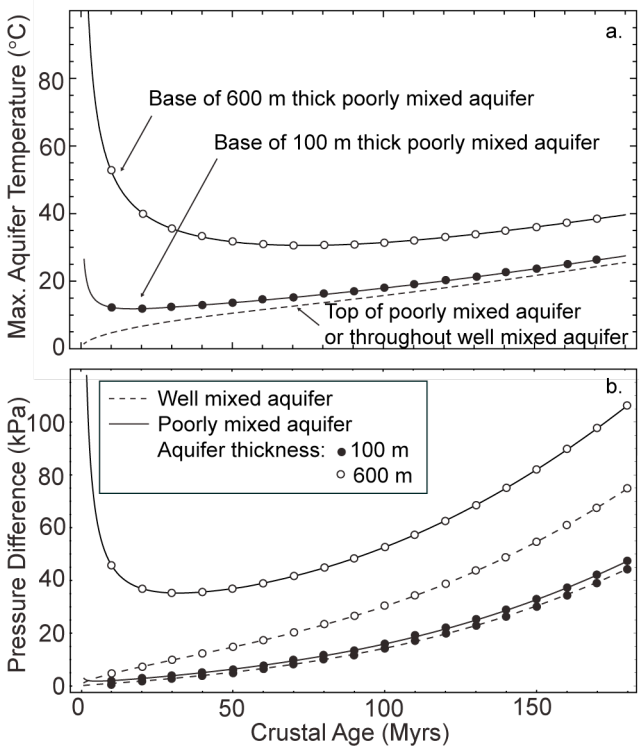

Figure 3.3. (a) Maximum aquifer temperatures and (b) lateral pressure differences available to drive outcrop-to-outcrop flow in well mixed and poorly mixed aquifers as functions of time. The lateral pressure difference available to drive fluid flow is the difference between the pressure beneath a column of cold recharge fluid and a column of warmer discharge fluid (Eq. 3.2). It is assumed that the fluid approaching the discharge zone has reached thermal equilibrium with lithospheric heat flow, and fluid densities at recharge and discharge zones are functions of temperature calculated using the seawater equation of state (TEOS-10). Time-dependent parameters affecting aquifer temperatures are sediment thickness and lithospheric heat flow. The sediment thickness is the product of the global average sediment accumulation rate (3.5 m Myrs^{-1}) and crustal age. Lithospheric heat flow is based on GDH1 [*Stein and Stein*, 1992]**.**

3.3.2. Heat transport in the aquifer

In a well mixed aquifer heat transport from the base to the top of the aquifer is rapid due to efficient vertical heat advection. In a poorly mixed aquifer, vertical heat advection is less efficient, so thermal energy entering the base of the aquifer takes more

time to propagate upwards. As a consequence, temperatures in the uppermost part of the aquifer have a longer length scale of warming in a poorly mixed aquifer relative to a well mixed aquifer (Figure 3.4). This is relevant to inversions of aquifer properties from measurements of conductive heat flow through seafloor sediments because heat flow through the sediment is controlled by the temperature at the sediment-basement interface.

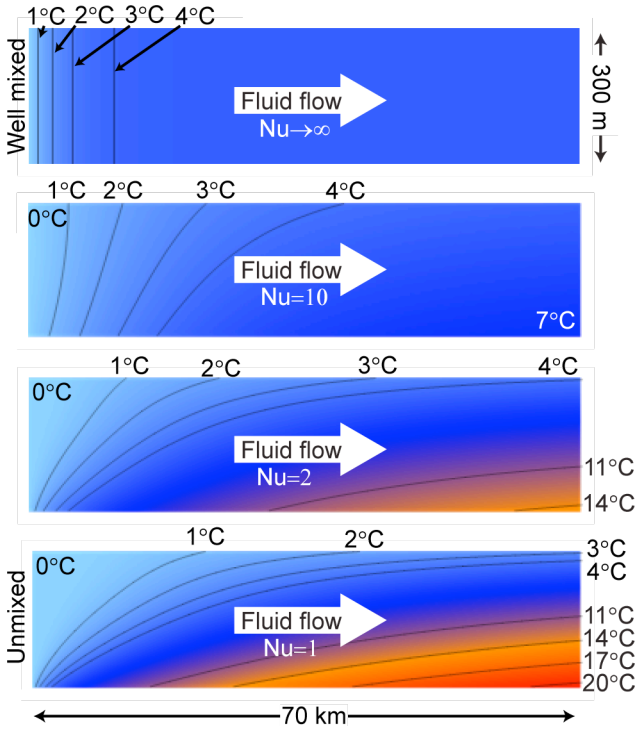

Figure 3.4. Comparison of temperatures in a well mixed aquifer (Nu→∞) to temperatures in a poorly mixed aquifer (Nu=10, 2, 1) under steady-state fluid flow. Parameter values are: crustal age = 10 Myrs, heat flow into the base of the aquifer is GDH1 [*Stein and Stein*, 1992]**, the pressure gradient driving the fluid flow assumes the recharge/discharge outcrop separation function given in Figure 2.6, sediment thickness (h_s) is calculated from the abyssal median sediment accumulation rate (3.5 m Myrs^{-1}) (Chapter 2), aquifer thickness (h_a) is 300 m, aquifer permeability (k) is $10^{-9.5}$ m^2, sediment thermal conductivity (λ_s) is 1.2 W m^{-1} K^{-1}, aquifer thermal conductivity (λ_a) is 2.0 W m^{-1} K^{-1}.**

Although vertical heat advection is not physically represented in the poorly mixed aquifer model (i.e., the model represents an aquifer that is completely unmixed), the

effects of vertical heat advection can be simulated using elevated thermal conductivities. This is achieved using a Nusselt number (*Nu*, the ratio of total heat flow to conductive heat flow). Thus, partial mixing within the aquifer can be explored using $Nu > 1$. The end-member of infinitely high *Nu* is equivalent to a well mixed aquifer. It is found that Nusselt numbers > 10 approximate thermal conditions in a well mixed aquifer (Figure 3.4). Lower Nusselt numbers imply slower vertical advection within the aquifer, which (if all else is equal) allows warmer temperatures in the deep aquifer, extends the length scale of warming of the uppermost layer and reduces the average heat flow through the sediment. Two dimensional numerical simulations of forced fluid flow and heat transport in the crustal aquifer have revealed a similar relationship between the efficiency of vertical advection and thermal conditions in the aquifer [*Davis et al.*, 1999; *Stein and Fisher*, 2003].

The ability of a fluid's thermal buoyancy to overcome viscous resistance within the aquifer, and therefore to develop cellular convection leading to thermal mixing, can be explored using the appropriate Rayleigh number (*Ra*) [*Wang*, 2004]:

$$Ra = \frac{k_v g \alpha h_a \Delta T_a}{\kappa \upsilon} \qquad (3.3)$$

where k_v is the vertical permeability of the aquifer, g is the gravitational acceleration, α is the thermal expansivity, h_a is the total thickness of the aquifer, ΔT_a is the temperature difference between the upper and lower boundaries of the aquifer, κ is the thermal diffusivity of the fluid-saturated rock matrix, and υ is the kinematic viscosity of the fluid. The efficiency of vertical heat transport via mixing, relative to the conductive heat flux (i.e., the Nusselt number) can be estimated from the ratio of the Rayleigh number (*Ra*) to the critical Rayleigh number (Ra_c) at which free convection commences. While the exact

form of this relationship depends on the details of the system (e.g., Fig 12.5 in Wang [2004]) a rough estimate can be obtained from [*Bejan*, 2013]:

$$Nu = \frac{Ra}{Ra_c} \qquad (3.4)$$

Combining equations 3.3 and 3.4, and assuming Ra_c is 40 [*Straus and Schubert*, 1977], α is 0.257 x 10^{-3} K^{-1}, h_a is between 100 and 600 m, κ is 4.76 x 10^{-7} m^2 s^{-1}, υ is 1 x 10^{-6} m^2 s^{-1}, and ΔT_a is as prescribed by the 5 Myr conductive geotherm, then an unmixed aquifer (Nu = 1) requires vertical permeability (k_v) of about 10^{-11} to $10^{-12.5}$ m^2 (depending on the aquifer thickness) to prevent convective mixing. A Nusselt number of 10 requires k_v of about $10^{-10.5}$ to 10^{-12} m^2, depending on the aquifer thickness. The vertical permeability estimates for Nu = 10 are 1.5 to 2.5 orders of magnitude lower than the horizontal permeability estimates for young crust from previous studies that extracted permeability from the global heat flow deficit [*Fisher and Becker*, 2000; *Anderson et al.*, 2012]. This requirement for a substantial difference between horizontal and vertical permeability in the poorly mixed aquifer model is returned to later.

3.3.3. Estimating average horizontal permeability in a poorly mixed aquifer from the global heat flow data

As a first investigation of the poorly mixed aquifer model, the global average horizontal aquifer permeability required to explain the age-binned global heat flow data by outcrop-to-outcrop flow is determined for the well mixed ($Nu \rightarrow \infty$) and unmixed (Nu = 1) aquifer end members (Figure 3.5). Well mixed and unmixed aquifer models were run with globally representative parameters: aquifer thickness (h_a) is 300 m, sediment thickness (h_s) is the product of crustal age (t, in Myrs) and the median abyssal sediment accumulation rate of 3.5 m $Myrs^{-1}$ (Figure 2.4), the distance between recharge and

discharge outcrops as a function of time is from Figure 2.6, and the lateral driving pressure difference is based on Eq. 3.2. The horizontal permeability as a function of time required for the aquifer model to fit the 5 Myr age-binned average global heat flow data [*Stein and Stein*, 1994] is determined.

Assuming horizontal permeability is uniform with depth, then in a well mixed aquifer the global average horizontal permeability required to fit the global heat flow decreases from $10^{-9.5}$ to 10^{-11} m^2 over the duration of the heat flow deficit (65 Myrs). In an unmixed aquifer the global average horizontal permeability required to fit the global heat flow is approximately uniform at 10^{-11} m^2 over the first 30 Myrs, then decreases to approximately 10^{-12} m^2 by 65 Myrs (Figure 3.5). The slight increase in permeability predicted for a unmixed aquifer within young crust may not be real, and cannot be resolved within uncertainty in the global heat flow [*Stein and Stein*, 1994].

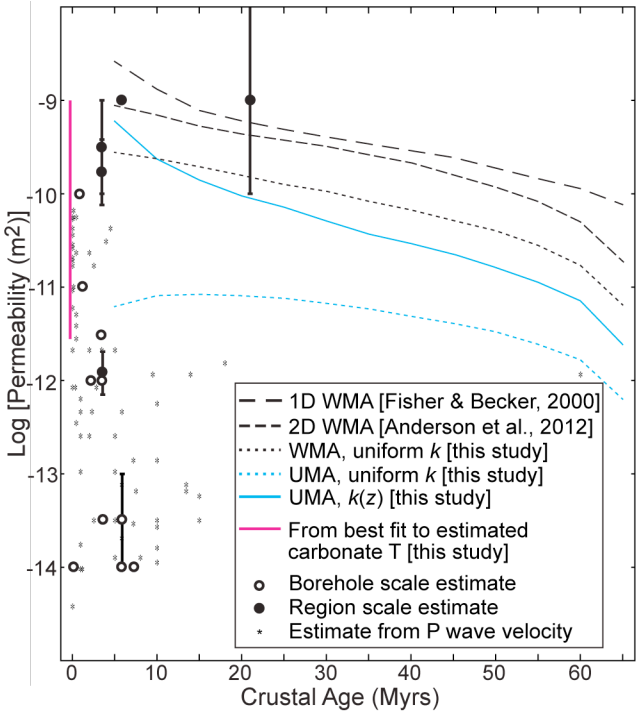

Figure 3.5. Aquifer permeability (*k*) estimates. The curves predicting *k* changing with time are based on fits of modelled conductive heat flow out the top of well mixed aquifers (WMAs) or unmixed aquifers (UMAs) to age-binned global heat flow data. For the fits to global heat flow, aquifer thickness (h_a) is assumed to be 300 m, and the sediment thickness (h_s) is the product of crustal age and the median abyssal sediment accumulation rate (3.5 m Myrs^{-1}). The pink line is the range of initial permeabilities of the uppermost aquifer required by the location-specific aquifer models in this study to best fit the carbonate data. Filled circles are region-scale estimates of permeability, and open circles are borehole-scale estimates of permeability [*Davis et al.*, 2000, 2001, 2004; *Davis and Becker*, 2002; *Becker and Davis*, 2003; *Fisher*, 2005; *Fisher et al.*, 2008; *Hutnak et al.*, 2008]**. Permeabilities estimated from seismic P-wave velocities are from Carlson [1998].**

The assumption that the recharge zone is uniformly of seawater temperature (Section 3.3.1) was tested *a posteriori* by calculating Peclet numbers for the recharge zone from the fluid fluxes predicted by the modelling. The unmixed aquifer models that best fit the global heat flow data require an average specific discharge of 10^{-7} to 10^{-8} m s^{-}

[1]. Assuming fluid recharges the aquifer through outcrops of a few hundred metres radius, vertical heat transport at the recharge zone can be described with Peclet numbers no lower than about 10. This is sufficiently high to maintain the recharge zone at an average temperature within 10% of seawater temperature, and justifies the simplifying assumption of an isothermal recharge zone at seawater temperature.

The globally averaged horizontal permeability estimates for a well mixed aquifer from this study are about 0.5 orders of magnitude lower than estimates from other well mixed aquifer modelling based on fits to the global heat flow (Chapter 2 and [*Fisher and Becker*, 2000]). The reason for the difference is this study assumes outcrops are closer than predicted by Fisher and Becker [2000] (as determined by a model of sediment and outcrop distribution), and because the model used in this study represents fluid and heat transport in one horizontal dimension, whereas the model in Chapter 2 represents transport in two horizontal dimensions. Chapter 2 investigated the effects of these model differences on predictions of conductive heat flow out of the top of an aquifer. It was found that a one dimensional model predicts a lower average conductive heat flow out of the aquifer because in one dimension there is less weighting on the high heat flow zones distal from a recharge site. As such, the permeability required to fit the global heat flow data is lower for the one dimensional model.

Borehole hydrological testing in numerous ODP holes shows that permeability tends to decrease with depth in the upper oceanic crust [e.g., Fisher, 2005]. The downward-decreasing abundance of secondary oxidative minerals as well as depth trends in bulk rock alkali and H_2O^+ content [e.g., *Alt et al.*, 1986, 2010; *Gillis and Robinson*, 1990; *Staudigel et al.*, 1981] also generally suggest that fluid flux, and therefore

permeability, decrease downwards in the upper oceanic crust. As such, the effect of changes in horizontal permeability with depth are also explored. It is found that if horizontal permeability in an unmixed aquifer decreases with depth by 2.5 orders of magnitude per 300 m (an upper limit on the plausible variation), then the entire aquifer must lose about 2 orders of magnitude of permeability over 65 Myrs, with the permeability of the uppermost part of the aquifer decreasing from $10^{-9.5}$ to $10^{-11.5}$ m^2. This is comparable to the prediction of temporal variation in permeability within a well mixed aquifer in which permeability is uniform with depth (Figure 3.5).

For crustal ages less than a few tens of Myrs, the *horizontal* permeability estimated for an unmixed aquifer (Figure 3.5) is higher than the *vertical* permeability estimated for an unmixed aquifer (Section 3.3.2). This is consistent with the modelling of Fisher and Becker [1995] which suggests that permeability in the crust near ODP Hole 504B (6.9 Ma) must be greater in the horizontal direction than the vertical direction in order to laterally transport sufficient heat to explain regional heat flow patterns. Fisher and Becker [1995] predicted that without such permeability anisotropy low aspect convection cells would develop within the aquifer, thereby restricting lateral heat transport. A plausible physical basis for such anisotropy would be laterally contiguous low permeability lithological units (such as massive flows) intermixed with laterally contiguous higher permeability units (such as pillows and breccias). Because horizontal permeability is predicted to decrease with crustal age (Figure 3.5) such that it eventually overlaps with the estimate of vertical permeability (Section 3.3.2), anisotropy of permeability may diminish with time.

3.4. Thermal evolution at the drilling locations predicted by the well mixed and poorly mixed aquifer models

In this study, thermal conditions as a function of time in well mixed and poorly mixed aquifers experiencing outcrop-to-outcrop flow are modelled for the drilling locations with carbonate O-isotope data (Section 3.2). For each drilling location, the conditions under which these models are consistent with formation temperatures estimated for the crustal carbonates and also with seafloor heat flow measurements where available (only available at three of the seven drilling locations), are identified and used as tests of outcrop-to-outcrop flow in well mixed and poorly mixed aquifers.

3.4.1. Carbonate formation temperatures

Traditionally the formation temperatures of crustal carbonates are estimated using an O-isotope thermometer parameterized with a fractionation factor determined between the carbonate mineral and the fluid from which the mineral formed. It is typically assumed that the O-isotope composition of the aquifer fluid is equivalent to that of seawater (which is generally a fair assumption, as noted in Section 3.2), although this assumption leads to two principal difficulties. First, there is uncertainty in the O-isotope composition of seawater which has varied through time between about -1 and 0‰ (SMOW) [*Veizer et al*., 1999], and second, the timing of carbonate formation is debated. Competing hypotheses suggest that either carbonates form within a few tens of Myrs of crustal accretion [*Staudigel et al.*, 1981a; *Staudigel and Hart*, 1985; *Gillis and Coogan*, 2011] or that they continually form over the life span of a plate [*Alt and Teagle*, 2003; *Jarrard*, 2003]. These uncertainties result in a 4-6ºC uncertainty in the carbonate temperature estimate. Another complication stems from comparing carbonate formation temperatures to aquifer temperatures estimated with a hydrologic model. This is because

hydrologic models cannot predict *absolute* aquifer temperatures without setting a boundary condition for the temperature of bottom seawater that recharges the aquifer. The temperature of bottom seawater is another parameter with considerable uncertainty as a function of time.

To minimize uncertainties in the O-isotope composition of bottom seawater and in the temperature of bottom seawater, this study estimates crustal carbonate formation temperatures *relative to* the formation temperatures of contemporaneous deep-sea benthic shell calcites. This relative temperature estimate is based on the extensive record of benthic shell calcite O-isotope variation throughout the Cenozoic (largely for foraminifera of the genus *Cibicidoides*) [*Zachos et al.*, 2001, 2008], and a more limited record during the Cretaceous [*Huber et al.*, 2002]. It is assumed that contemporaneously formed crustal carbonate minerals and benthic shell calcites precipitated from fluid having the same O-isotope composition, which allows a relative O-isotope thermometer to be developed that is independent of $\delta^{18}O_{water}$. The relative thermometer is based on a linear fit through an oxygen isotope thermometer for inorganic calcite and water over 0-60ºC [*Kim and O'Neil*, 1997]:

$$T = -5.09(1000 \ln \alpha) + 167.63 \qquad (3.5)$$

where α is the fractionation factor and T is the formation temperature (°C). The error introduced by this linear approximation is ±2°C. The value of $1000\ln\alpha$ is then approximated by the difference between the $\delta^{18}O$ of the calcite and the water, and separate formulations of Eq. 3.5 for the benthic carbonates and the crustal carbonates are subtracted to determine the difference between their formation temperatures (ΔT):

$$\Delta T \approx -5.09\left(\delta^{18}O_{crustalcarbonate} - \delta^{18}O_{benthiccarbonate} + A - B\right) \qquad (3.6)$$

The term *A* is a correction for the difference in fractionation of calcite and aragonite [*Grossman and Ku*, 1986]. This term is zero for calcite, and 0.7‰ for aragonite (Figure 3.6). The term *B* is a correction to account for the different relationship between O-isotope fractionation and temperature for the biogenic calcite in *Cibicidoides* benthic shells relative to the inorganic crustal carbonates [*Bemis et al.*, 1998]. The correction for biogenic calcite in the benthic shells (*B*) is 1.0‰ (Figure 3.6).

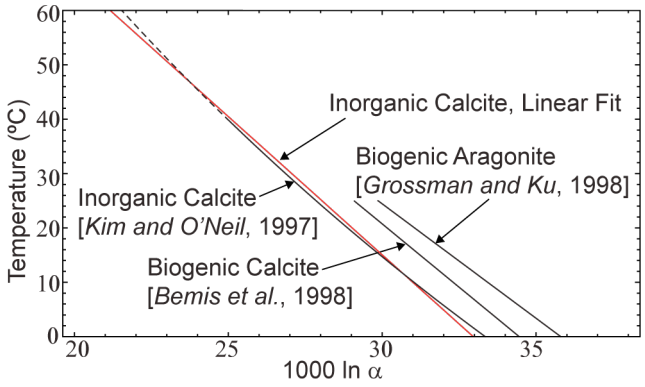

Figure 3.6. Comparison of oxygen isotope thermometers for inorganic calcite, biogenic calcite, and biogenic aragonite. Equation 3.6 uses constant correction terms based on this plot to account for the different types of calcium carbonate being compared in the present study (see main text for details).

The timing of formation of all the crustal carbonates used in this study is unknown. The uncertainty in formation timing presents a difficulty because $\delta^{18}O_{benthic\ carbonate}$ varies within the approximate range of -1 to +5‰ (PDB) between the Cretaceous and the present, resulting in an approximately 15-20°C uncertainty in ΔT. In this study, no *a priori* assumption is made about the timing of formation. Instead, for each sample, the possible formation temperatures are determined over all crustal ages (at 1 Myr intervals) from 1 Myr after the time of crustal accretion until the present day based on variation in $\delta^{18}O_{benthic\ carbonate}$ with time. The Cenozoic $\delta^{18}O_{benthic\ carbonate}$ record is based on a

5 Myr moving average through the data of Zachos et al. [2001], and a value of -1‰ (PDB) is assumed for older benthic carbonate shells [*Huber et al*., 2002]. The hydrologic models are tested by determining whether the crustal carbonate formation temperatures at any time are consistent with modelled aquifer temperatures at each drilling location.

3.4.2. Modelling the temperature evolution at each drilling location

To estimate the thermal conditions that the aquifer drilled at each location could have experienced over its history if subjected to outcrop-to-outcrop flow, models of sediment and outcrop distributions and outcrop-to-outcrop flow in well mixed and poorly mixed aquifers as a function of time were run for each drilling location. The parameters used for each drilling location are listed in Supplementary Table S3.1 of Appendix J.

Synthetic abyssal hill seafloor representing initial, sediment-free oceanic basement bathymetry is generated for each drilling location using the stochastic Gaussian model of Goff and Jordan [1988]. Parameters for this model (abyssal hill height, length, width and fractal dimension) are correlated with mid-ocean ridge spreading rate [*Goff*, 1991; *Neumann and Forsyth*, 1995; *Goff et al.*, 1997], so values for these parameters were chosen based on the spreading rate at which the crust of each drilling location formed. Numerous random initial bathymetry grids were generated for each drilling location. All bathymetry grids have dimensions of 100 km x 100 km and have a 150 m resolution. Where two-dimensional seismic reflection data are available to constrain the true basement depth, only those synthetic grids that misfit the seismic basement reflector, on average, by less than one standard deviation of the seismic basement depth, are kept. Where three-dimensional seismic reflection data are available, these data are used to interpolate the basement depth at the drilling location. Because the three-dimensional

seismic data only cover small areas, this interpolated initial bathymetry is then "stitched" into the center of several larger grids of random synthetic bathymetry representative of the appropriate spreading rate (as above). Approximately 50 initial bathymetric grids were kept for each drilling location and used in the modelling discussed below.

Sediment supply and post-depositional transport as functions of time are then simulated on all basement representations for each drilling location. As model time elapses, synthetic seamounts are inserted onto the initial basement bathymetry at random locations with sizes and formation times based on the global seamount population (Chapter 2). A globally representative seamount distribution covering a range of seamount sizes (100 m and taller) is used for this study because location-specific seamount distributions are generally only known for seamounts taller than 1-2 km [*Wessel and Lyons*, 1997], but not for small seamounts, which are more abundant globally and, as such, are more important to the distribution of outcrops. The net sediment accumulation rate (due to new sediment supply from the water column plus or minus post-depositional transport) is constrained by the biostratigraphic record from each drill hole. In the sedimentation model, however, the pelagic sediment supply rate and the post-depositional transport rate are separate parameters. For those drilling locations with multiple drill holes, the pelagic supply rate as a function of time is approximated by the average net accumulation rate inferred from biostratigraphic interpretations of the holes. Where there is only one drill hole in the area, or where biostratigraphy is only available for one hole in the area, the pelagic supply rate is assumed to equal the net accumulation rate. A diffusion model is used to represent post-depositional sediment transport as a function of topographic gradient [*Webb and Jordan*, 2001a]. The apparent diffusivity of

lateral sediment transport is generally unknown for the drilling locations, so a globally representative range of values is evaluated for most locations ($0.007 – 0.7$ m^2 yr^{-1}). At the location of Holes 504B/896A three-dimensional seismic reflection data constraining sediment thickness permitted a location-specific inversion of this parameter. For this location sediment supply and post depositional transport were modelled atop a basement bathymetric grid interpolated from the basement seismic reflectors [*Swift et al.*, 1998]. Variability in the modelled sediment thickness is consistent with variability in sediment thickness estimated from seismic reflection data [*Swift et al.*, 1998] for apparent diffusivities of lateral sediment transport in the range of $0.05 – 0.09$ m^2 yr^{-1}.

At each 1 Myr time step in the location-specific sedimentation models, the distribution of sediment is used to calculate a distribution of outcrops that could act as zones of recharge or discharge in an outcrop-to-outcrop hydrothermal regime. Here, outcrop identification, and classification of those outcrops as recharge or discharge zones, follows the procedure described in Section 2.2.3. Statistics of modelled sediment thickness and the recharge/discharge outcrop separation distance are recorded as functions of time and used as input to the location-specific aquifer thermal models.

The poorly mixed aquifer model applied in this study does not account for the spatial variability in the sediment thickness, yet this is an important parameter in controlling temperatures in the aquifer. To determine how best to approximate the thermal effects of a variable sediment blanket in a model of uniform sediment thickness I first evaluate the aquifer thermal conditions predicted by the two-dimensional well mixed aquifer thermal model described in Section 2.2.4 which fully represents the spatial variability in sediment thickness. For this modelling a globally representative set of

sediment and aquifer parameters was applied to synthetic bathymetry representative of crust formed at slow-, intermediate-, and fast-spreading ridges (Table 3.1). The distance between recharge and discharge zones as a function of time was estimated following the procedure described in Section 2.2. It was found that the aquifer temperature beneath 95% of the seafloor in the model domain is less than the conductive equilibrium temperature beneath the region's thickest sediment (more than one standard deviation thicker than the modelled average sediment thickness). This implies that fluid generally does not reach the conductive equilibrium temperature beneath the thickest sediment because fluid cannot generally flow slowly enough to fully warm beneath those zones (which are of limited spatial extent). It is assumed that the aforementioned findings for a well mixed aquifer overlain by a variable thickness sediment blanket also apply, to a first approximation, to a poorly mixed aquifer. Therefore, the maximum temperature in an aquifer overlain by non-uniform sediment is approximated by assuming a uniform thickness of sediment that is one standard deviation thicker than the true average. This upper bound aquifer temperature can then be tested for consistency with estimated carbonate temperatures.

Table 3.1. Sediment and aquifer parameters used to explore thermal conditions in a well mixed aquifer overlain by a sediment blanket of spatially variable thickness.

Parameter	Value
Diffusivity of lateral sediment transport	0.05 m^2 yr^{-1}
Sediment accumulation rate	3.5 m $Myrs^{-1}$
Sediment thermal conductivity	1.2 W m^{-1} K^{-1}
Aquifer thickness	300 m
Aquifer permeability	Log-linear decrease from 10^{-9} to 10^{-11} m^2 over 65 Myrs
Abyssal hill height	Fast-spreading: 58.7 m Intermediate-spreading: 85 m Slow-spreading: 235 m
Abyssal hill length	Fast-spreading: 2.9 km Intermediate-spreading: 3.8 km Slow-spreading: 8.2 km
Abyssal hill width	Fast-spreading: 13.7 km Intermediate-spreading: 15 km Slow-spreading: 24.7 km

One-dimensional well mixed and poorly mixed aquifer models are run for each drilling location to predict upper bound aquifer temperatures as a function of crustal age. The primary hydrologic parameters in these models are the aquifer thickness and horizontal permeability. The thickness of the aquifer at each location is estimated from the thickness of the zone of low-temperature alteration in the drill core (inferred from the distributions of celadonite, iron oxyhydroxides, carbonate minerals and bulk rock alkali concentrations; Appendix J, Supplementary Table S3.1). For holes with only shallow penetration into the igneous crust, the base of the aquifer cannot be identified, so a range of aquifer thicknesses is investigated (100 – 600 m). Within the aquifer, the horizontal permeability is assumed to decrease with depth at a rate of one order of magnitude per 300 m, and beneath the aquifer the crust is assumed to be impermeable. The rate of decrease in permeability with depth is an approximate average from borehole permeability tests globally [*Fisher et al.*, 2008]. Permeability at all depths in the aquifer is assumed to decrease with time by two orders of magnitude over 65 Myrs (Figure 3.5).

The aquifer permeability is assumed to remain constant thereafter. The initial permeability at the top of the aquifer at the time of crustal accretion is unknown, so a range of values from 10^{-8} to 10^{-14} m^2 is evaluated. Assuming the heat capacity of hydrothermal fluid is constant over the range of temperatures in off-axis hydrothermal systems, the aquifer models can predict temperatures relative to bottom seawater temperature. These relative model temperatures can be compared to the relative carbonate temperatures estimated with Eq. 3.6, which are also differences between the temperature of bottom seawater and the aquifer. As such, it is not necessary to know the temperature of bottom seawater entering the crust.

Temperatures in well mixed and poorly mixed aquifers are sensitive to the thermal conductivity of the sediment. The modern value for this parameter is well constrained at most of the drilling locations from shipboard measurements on the drill core (Appendix J, Supplementary Table S3.1). For locations without sediment thermal conductivity data, a conservatively low value of 0.8 W m^{-1} K^{-1} [*Pribnow et al.*, 2000] is used to ensure the aquifer models predict an upper bound on aquifer temperature. For drilling locations in which heat flow surveys were conducted, model parameterizations are discarded if the predicted average heat flow through the sediment (at the model time representing present-day conditions) is not within one standard deviation of the average measured heat flow. For models representing a poorly mixed aquifer, the modelled maximum temperature in each 50 m aquifer layer is compared to the estimated carbonate formation temperatures (for samples corresponding to the same depth range) at all times from crustal accretion to the present. For each drill hole, the model parameterizations that best fit the carbonate data are identified. The measure of "fit" between the models

and the data is based on the number of carbonate samples in which the estimated formation temperature is less than the modelled upper bound aquifer temperature (at the corresponding aquifer depth) at any time. A similar approach is taken for the well mixed aquifer, except the carbonate mineral temperatures are compared to the depth-independent aquifer temperature. Detailed results of estimated carbonate formation temperatures and aquifer thermal conditions as a function of time and depth for two representative example drill holes (Holes 556 and 418A) are given in Figures 3.7 and 3.8. Results for the remaining drill holes are included in Appendix C, and a summary of the best fitting parameterizations for each drill hole is presented in Table 3.2.

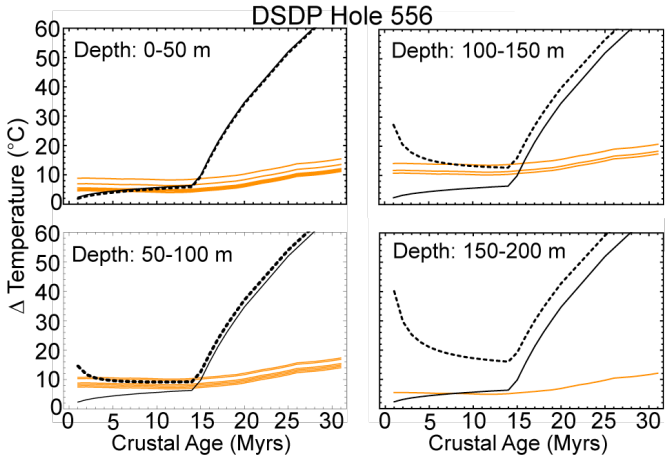

Figure 3.7. Estimated formation temperatures relative to bottom seawater (ΔT) of carbonate minerals from Hole 556 (orange lines) compared to maximum temperatures achievable along the lateral flow path in a well mixed aquifer (solid black line) and an unmixed aquifer (dashed line). Because the timing of carbonate formation is unknown, each orange line represents estimates of the formation temperature for one carbonate sample depending on when it formed. Possible formation temperatures for each sample are estimated with Eq. 3.6 from $\delta^{18}O_{\text{crustal carbonate}}$ (Figure 3.1), and $\delta^{18}O_{\text{benthic carbonate}}$ [*Zachos et al.*, 2001, 2008]**. For a given carbonate sample to be consistent with modelled aquifer temperatures, its orange line must lie below the model temperature curve at any point in time. Parameters used for the aquifer models are listed in Appendix J, Supplementary Table S3.1. The rapid increase in aquifer temperatures after 15 Myrs reflects a change in the sediment accumulation rate at this time. Results for the other drill holes discussed in this study are included in the supplementary material.**

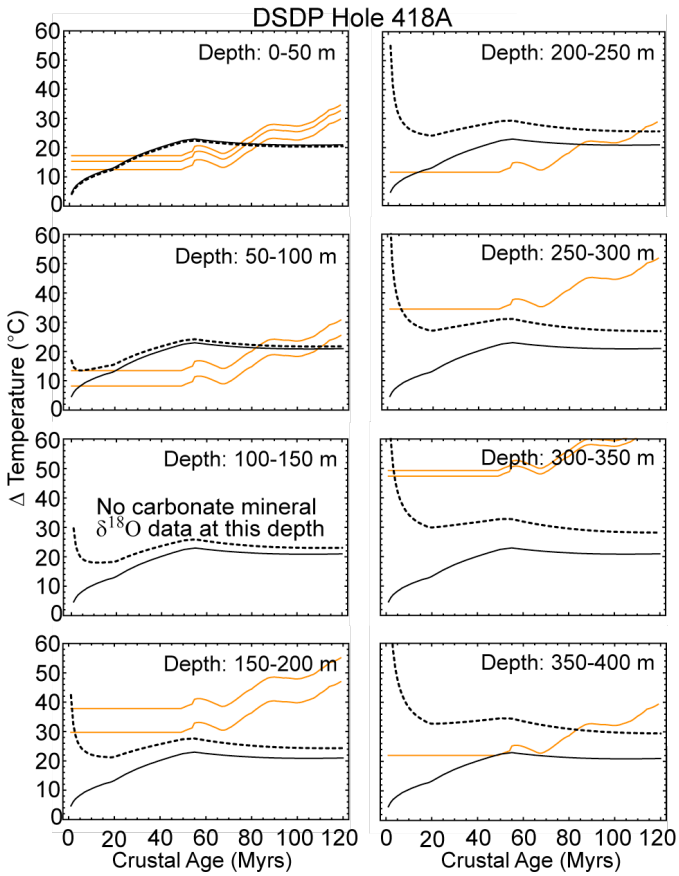

Figure 3.8. Estimated formation temperatures relative to bottom seawater (ΔT) of carbonate minerals from Hole 418A (orange lines) compared to maximum temperatures achievable along the lateral flow path in a well mixed aquifer (solid black line) and an unmixed aquifer (dashed line) as in Figure 3.7. Results for the other drill holes discussed in this study are included in the supplementary material.

Table 3.2. Percentages of the carbonate mineral samples having $\delta^{18}O$ that is consistent with temperatures in end-member well mixed and unmixed aquifers.

Hole	Well mixed aquifer ($Nu \rightarrow \infty$)			Unmixed aquifer ($Nu = 1$)		
	% carbonate samples consistent [a]	Best fit log [k (m^2)] [b]	Best fit h_a (m) [b]	% carbonate samples consistent [a]	Best fit log [k (m^2)] [b]	Best fit h_a (m) [b]
504B	100	-10	300	100	-10	300
896A	76	-10 [c]	300	92	-10 [c]	300
1256D	26	-11	400	100	-11	400
556	100	-10	200	100	-9.5	200
1224F	100	-9	200	100	-9	200
417A	86	-10	400	100	-11	400
417D	73	-9.5	400	88	-11	400
418A	42	-9	400	100	-11	400
1149D	100	-10	200	100	-10	200
801C	49	-10	500	94	-11.5	500

[a] The percentage of the carbonate samples with estimated crystallization temperatures that are less than or equal to the maximum temperature modelled for a well mixed aquifer or an unmixed aquifer at the depth the carbonate was recovered and at any time in the crust's history.

[b] The initial log permeability (k) of the uppermost aquifer and the minimum total aquifer thickness (h_a) required by the best fitting aquifer models. Lower permeabilities or thicker aquifers along with lower permeabilities can fit the carbonate data equally well.

[c] Excluding the two shallow, high temperature carbonates which are presumed to have formed at a discharge zone.

3.5. Are the carbonate $\delta^{18}O$ data consistent with outcrop-to-outcrop flow?

Some of the drill holes selected for this study are in close proximity (Holes 504B and 896A are 1 km apart in the Eastern Equatorial Pacific; Holes 417A and 417D are 0.5 km apart in the Western Atlantic, with Hole 418A about 8 km away from the pair). Because outcrop-to-outcrop flow is a regional scale process, data from these proximal holes are considered together as a test of outcrop-to-outcrop flow for the same region.

The remaining drill holes (Holes 1256D, 556, 1224F, 1149D and 801C) are considered to be individually representative of discrete regions. This section considers whether the estimated carbonate formation temperatures from the drill holes within each region are consistent with the aquifer temperatures modelled for these regions.

3.5.1. Regions in which carbonate mineral $\delta^{18}O$ are consistent with outcrop-to-outcrop flow in either a well mixed or poorly mixed aquifer

At three of the seven drilling locations analyzed (Holes 556, 1224F and 1149D), the estimated formation temperatures of all the carbonate samples are within the range of temperatures achievable by either a well mixed or a poorly mixed aquifer. All the carbonate samples from Holes 556 and 1224F formed at temperatures low enough to be achievable in an outcrop-to-outcrop flow system under a wide variety of conditions. The carbonate minerals from Hole 1149D formed under warmer conditions (ΔT = 10 to 55 °C), but because the crust at this location was rapidly sedimented at a young age, even a well mixed aquifer could reach sufficiently warm temperatures to be consistent with all the carbonate data from this hole. Although both models can explain the carbonate data, a poorly mixed aquifer can achieve warm temperatures at a younger age. Therefore, secondary carbonates could potentially form earlier in a poorly mixed aquifer than in a well mixed aquifer.

3.5.2. Regions in which carbonate mineral $\delta^{18}O$ suggest a poorly mixed aquifer

The four regions represented by Holes 504B/896A, 1256D, 417A/417D/418A and 801C contain carbonates that crystallized at higher temperatures than can be explained by a well mixed aquifer (Table 3.2). At these locations, crystallization temperatures of only 26-86% of the carbonate can be attained in a well mixed aquifer but a poorly mixed

aquifer model can explain 88-100% of the carbonate crystallization temperatures. Nevertheless, the poorly mixed aquifer is still unable to explain up to 12% of the data at some holes without considering special circumstance for a small proportion of the carbonate samples (discussed below).

3.5.2.1. Holes 504B and 896A

Holes 504B and 896A were drilled ~1 km apart into oceanic crust in the Eastern Equatorial Pacific that formed at an intermediate spreading rate approximately 6.9 Myrs ago. This region has experienced a rapid rate of sedimentation (38 m $Myrs^{-1}$ on average) of largely calcareous sediment [*Fisher et al.*, 1990]. Hole 896A was drilled into a local maximum in the basement topography, so this location may have remained sediment-free for longer than the surrounding area. Extensive seismic surveys have been conducted near these drill holes and three-dimensional maps of basement topography and sediment thickness are available over an approximately 25 km x 25 km area [*Swift et al.*, 1998]. There may be an active discharge zone a few kilometres from Holes 504B and 896A where a local heat flow maximum exists above a thinly sedimented basement high [*Davis et al.*, 2004]. There are no known recharge outcrops in the well-surveyed region, although there may be distant outcrops that participate in outcrop-to-outcrop flow.

The estimated formation temperatures of carbonate minerals from Hole 504B are consistent with a well mixed aquifer or a poorly mixed aquifer under a wide range of conditions, and do not constrain the hydrology of the crust at this location. The estimated formation temperatures of carbonate minerals from Hole 896A, however, are more consistent with a poorly mixed aquifer than a well mixed aquifer (Table 3.2). At this hole, temperatures estimated for 92% of the carbonate samples are consistent with

temperatures attainable along the lateral flow path in a poorly mixed aquifer compared to only 76% being consistent with a well mixed aquifer model; this is consistent with hydrological studies that demonstrate that the present-day aquifer is not well mixed [*Becker et al.*, 2004]. In Hole 896A there are two carbonate minerals with estimated formation temperatures 5-8ºC higher than temperatures achievable in either a well mixed or poorly mixed the aquifer model (samples 896A-8R1-45-48 and 896A-1R1-59-63). These temperature discrepancies are larger than the uncertainty in the relative O-isotope thermometer. Because Hole 896A was drilled into a maximum in the basement topography, it is possible that this site was a discharge zone [*Teagle et al.*, 1996]. Although there is limited vertical advection in a poorly mixed aquifer along most of the flow path between a recharge and discharge zone, fluid from depth must ascend and leave the crust at the discharge zone. This must cause mixing between deep, warm fluid and shallow, cooler fluid, thereby allowing the uppermost aquifer to achieve warmer temperatures than is possible along the lateral flow path. Plausible discharge zone temperatures, calculated as the flux-weighted average temperature across all aquifer depths for fluid that has reached thermal equilibrium with lithospheric heat flow, can explain these carbonate crystallization temperatures provided that $Nu < 10$.

3.5.2.2. Hole 1256D

Hole 1256D was drilled into oceanic crust in the Eastern Pacific that formed at a fast spreading rate approximately 15 Myrs ago. The location experienced rapid sediment accumulation (45 m $Myrs^{-1}$) for the first 4 Myrs of its history, and reduced sediment accumulation (3 to 10 m $Myrs^{-1}$) thereafter. The uppermost basement rock recovered from Hole 1256D (and the nearby Hole 1256C) is a massive flow unit several tens of

metres thick, suggesting the location was initially a bathymetric low infilled by a lava flow. The uppermost massive unit is less altered than the underlying extrusive units, suggesting it experienced less fluid flux [*Alt et al.*, 2010]. As such, the crust drilled at Hole 1256D was likely not a recharge or discharge zone. If this location experienced outcrop-to-outcrop flow, it must have been along the lateral flow path between recharge and discharge zones. All of the estimated carbonate formation temperatures from Hole 1256D are consistent with temperatures in a poorly mixed aquifer, but only 26% of the carbonate data are consistent with temperatures in a well mixed aquifer.

3.5.2.3. Holes 417A, 417D and 418A

Holes 417A, 417D and 418A were drilled into oceanic crust in the Western Atlantic that formed at a slow spreading rate approximately 120 Myrs ago. The sediment at this location is mainly pelagic clay that accumulated at a relatively slow average rate of 2.5 m $Myrs^{-1}$. The basement drilled at Hole 417A is a basement topographic high, whereas Holes 417D and 418A were drilled into basement topographic lows that are approximately 150 m deeper. The deepest sedimentary unit from Holes 417D and 418A is not present at Hole 417A, suggesting the crust at Hole 417A remained exposed to seawater for several million years longer than the crust at the other holes [*Donnelly et al.*, 1980b].

The estimated carbonate mineral formation temperatures for Holes 417A, 417D and 418A are all more consistent with a poorly mixed aquifer than a well mixed aquifer (Table 3.2). This result is most apparent at Hole 418A where 100% of the carbonate data are consistent with a poorly mixed aquifer, but only 42% are consistent with a well mixed aquifer (Figure 3.8). The well mixed aquifer is unable to explain the apparently high

temperature carbonate at depth in Hole 418A. One carbonate mineral sample from Hole 417A (sample 417A-31R3-91-93) has an estimated formation temperature a couple of degrees higher than can be achieved in a well mixed or poorly mixed aquifer, but this temperature discrepancy is within uncertainty in the relative O-isotope thermometer.

Three samples from the upper 100 m of Hole 417D (samples 417D-27R5-16-19, 417D-28R7-8-10, 417D-31R1-94-96) are inconsistent with both the well mixed and poorly mixed aquifer models without considering special circumstances. Estimated formation temperatures for the anomalous samples from this hole are 10 - 20ºC higher than the modelled aquifer temperatures, depending on the timing of formation. The high temperatures of the anomalous samples from Hole 417D can be reconciled with models of outcrop-to-outcrop flow if the sediment accumulation rate at Hole 417D was higher than modelled. For example, if an additional 35 m of sediment had accumulated within 2 Myrs of crustal accretion, the upper aquifer would have been sufficiently warm to explain these samples. Some uncertainty is inherent in the biostratigraphic interpretation of the cored sediment on which our estimate of the sediment accumulation rate was based [*Donnelly et al.*, 1980a], but probably not enough to account for the full discrepancy. Early deposition of carbonate sediment followed by subsequent partial dissolution is a possibility [*Berger*, 1972]. The CCD in the Atlantic 120 Myrs ago was approximately 3500 m deep [*Van Andel*, 1975]. The crust at Hole 417D may have been above the CCD, and therefore had a positive net accumulation rate of carbonate sediment, for perhaps a few Myrs of its early history. Provided that much of the early sediment at Hole 417D was carbonate (modern Mid-Atlantic ridge sediment at similar latitudes is 80-85%

$CaCO_3$ [*Marks*, 1981]), some of the sediment could have dissolved after the crust subsided below the CCD.

3.5.2.4. Hole 801C

Hole 801C was drilled into oceanic crust in the Western Pacific. The uppermost igneous unit recovered from this hole is 60 m of alkalic sills that intruded into sediments off axis about 157 Myrs ago. Underlying this unit is normal tholeiitic mid-ocean ridge basalt estimated to have formed about 168 Myrs ago at a fast-spreading mid-ocean ridge [*Pringle*, 1992]. It has been proposed that the magmatic heat associated with the sills may have contributed to a unique thermal evolution of the upper crust at this location [*Alt et al.*, 1992]. The sediment at Hole 801C is primarily siliceous and has accumulated at a rate of 3 m $Myrs^{-1}$ on average, slightly below the median global abyssal accumulation rate (Figure 2.4).

The complex early history of this location presents modelling challenges. The aquifer models used herein cannot represent an additional heat source associated with the late-forming sills, and probably do not suitably represent the hydrology of the sills. As such, carbonate minerals from the alkalic sills are excluded from this analysis. Carbonate minerals from the tholeiitic section could have been affected by the additional magmatic heat if they formed after the late volcanism occurred, but before the heat from this magmatic event had dissipated. Because the timing of carbonate mineral formation is unknown, all of the carbonates from the tholeiitic section are included in this analysis. To model the sediment and hydrological environment at this location it is assumed that the basement topography and the sediment sequence are unchanged as a result of the off-axis magmatism. This is considered to be a fair approximation because the alkalic unit is

relatively thin, the sediment accumulation rate is relatively low, and an alternative model in which the upper alkalic unit is treated as sediment leads to the same conclusions.

In Hole 801C, 92% of the estimated carbonate mineral formation temperatures are consistent with a poorly mixed aquifer, but only 49% are consistent with a well mixed aquifer. The five carbonate minerals that are inconsistent with the poorly mixed aquifer model (samples 801C-6R1-26A, 801C-6R1-26B, 801C-6R1-26C, 801C-6R1-26D and 801C-10R3-86) are from massive flows within the upper 150 m of the tholeiitic section [*Alt and Teagle*, 2003]. The apparently high formation temperatures of these minerals can be explained by an aquifer experiencing outcrop-to-outcrop flow if: (a) they formed during a period when the upper tholeiitic section was re-heated (by about 20°C) by the off-axis volcanism, (b) the carbonate temperatures were overestimated because the anomalous samples did not form in equilibrium with seawater, or (c) the location experienced more rapid early sediment accumulation than is suggested by the recovered stratigraphic record.

3.5.3. Aquifer permeability at the drilling locations

The aquifer models that best fit the carbonate data provide an upper bound on the initial horizontal permeability at each of the drilling locations. These models assume the horizontal permeability decreases downwards by one order of magnitude per 300 m. Only an upper bound on the horizontal permeability is constrained because this is generally the permeability that allows the fluid to fully warm to match the conductive geotherm (or nearly so) before discharging, resulting in the largest possible range of temperatures achievable in the aquifer and the best fit to the carbonate data. Lower permeabilities cannot produce aquifer temperatures any higher than those of a purely

conductive system and therefore are equally consistent with the carbonate data. Upper bound initial horizontal permeabilities of the uppermost aquifer of 10^{-9} to $10^{-11.5}$ m^2 are found for the drilling locations analyzed in this study (Table 3.2, Figure 3.5). Most of these estimates are slightly lower than initial permeability estimated from fitting a well mixed aquifer model to the global heat flow (Chapter 2, [*Fisher and Becker*, 2000]). The new estimates fall within the range of permeabilities estimated from regional scale analyses of permeability on the eastern flank of the Juan de Fuca Ridge [*Davis et al.*, 2000; *Davis and Becker*, 2002], and are also within the range of borehole-scale estimates [*Fisher et al.*, 2008].

3.6. Conclusions

Oxygen isotope thermometry was used to estimate formation temperatures of secondary carbonate minerals from ten DSDP/ODP/IODP drill holes representing seven discrete locations. These formation temperatures are compared to thermal conditions predicted by location-specific well mixed and poorly mixed aquifer thermal models. It is found that carbonate data from three of the seven locations (Holes 556, 1224F and 1149D) are consistent with temperatures in either a well mixed or a poorly mixed aquifer. Carbonate data from the other four locations (Holes 504B/896A, 1256D, 417A/417D/418A and 801C) are inconsistent with temperatures in a well mixed aquifer, and are more consistent with a poorly mixed aquifer. A small proportion of the samples from Holes 896A, 417D and 801C are not consistent with either model without considering crystallization under special circumstances (e.g., at a discharge zone, out of equilibrium with seawater, or within crust that was reheated by off-axis volcanism). Because a poorly mixed aquifer can achieve warm temperatures earlier than a well mixed

aquifer, the secondary carbonates that crystalized at relatively high temperatures could have formed significantly earlier if the aquifer was poorly mixed aquifer than if it was well mixed. These results are generally supportive of the proposition that outcrop-to-outcrop flow is the dominant mode of off-axis hydrothermal circulation globally. The location-specific poorly mixed aquifer models that best fit the carbonate O-isotope data require initial horizontal permeabilities of the uppermost aquifer to be in the range of 10^{-9} to $10^{-11.5}$ m^2. The global average horizontal permeability of the uppermost oceanic crust required for a poorly mixed aquifer to fit the global heat flow data is predicted to decrease from 10^{-9} to $10^{-11.5}$ m^2 over 65 Myrs.

4. Fluid seepage rates through marine sediments, constrained by a global compilation of interstitial water SO_4^{2-}, Mg^{2+} and Ca^{2+} profiles

4.1. Introduction

The entire volume of the ocean circulates through the oceanic crust every few hundred thousand years [e.g., *Johnson and Pruis*, 2003], driven by the thermal energy released by the cooling lithosphere. This process is responsible for globally-significant heat and chemical fluxes between the crust and the ocean, and supports a deep biosphere [*Stein and Stein*, 1994; *Alt*, 2004; *Huber and Johnson*, 2006].

The majority of the hydrothermal fluid flux through the oceanic crust occurs on ridge flanks [*Mottl and Wheat*, 1994] where volcanic crust is generally covered by marine sediments. Marine sediments of all types are less permeable than the underlying volcanic crust [*Spinelli et al.*, 2004], so the distribution of sediment from local to global scales is believed to be an important control on the locations of fluid ingress into and egress out of the oceanic crust [e.g., *Langseth and Herman*, 1981]. Topographic highs in the basement, such as seamounts and abyssal hills, generally remain free of sediment for longer than the surrounding seafloor [*Webb and Jordan*, 2001b]. It has been proposed that fluid exchange between the ocean and the crust globally may be primarily focused through these "outcrops", either through local circulation within isolated outcrops [*Harris et al.*, 2004; *Kawada et al.*, 2011], or by a process in which fluid flows laterally through the uppermost volcanic crust between recharge and discharge outcrops that are separated by hydraulically resistive sediment [*Anderson et al.*, 2012; *Fisher and Becker*, 2000; *Fisher et al.*, 2003, *Langseth and Herman*, 1981]. In Chapter 2 a probabilistic model of

sedimentation and outcrop distribution was used to predict that lateral forces supporting outcrop-to-outcrop flow will generally not overcome vertical buoyancy forces until after a few Myrs of sediment accumulation. This suggests that outcrop-to-outcrop flow is not the dominant mode of ridge flank circulation in young crust, although the importance of outcrop-to-outcrop flow relative to isolated circulation within individual outcrops in older crust is unknown. Outcrop-centric models of hydrothermal circulation imply that only a small proportion of the total hydrothermal fluid flux passes through sediments. Because fluid fluxes through sediments globally have not been rigorously quantified, the importance of fluid fluxes through outcrops relative to sediments remains somewhat uncertain. In addition, although ridge flank chemical fluxes are significant to global geochemical cycles [*Mottl and Wheat*, 1994; *Brady and Gíslason*, 1997; *Staudigel*, 2003; *Wheat and Fisher*, 2008; *Coogan and Gillis*, 2013], it is unknown whether chemical fluxes due to transport across the sediment are significant [*Brady and Gíslason*, 1997; *Coogan and Gillis*, 2013].

Fluid seepage through marine sediments covering igneous basement has been investigated in numerous previous studies. McDuff [1981] used the geochemistry of interstitial waters from sediments collected during the first 53 Deep Sea Drilling Project (DSDP) legs to identify locations with chemical gradients across the sediment. McDuff [1981] modelled basement fluid composition as a function of vertical diffusion across the sediment, *downward* advection through the sediment and reactivity within the basement. Lateral advection within the basement and reactivity within the sediment were not modelled as controls on the basement fluid composition. Based on this modelling, McDuff [1981] suggested that 100-150 m of sediment is sufficient to effectively stop

advection through sediments, thereby allowing the basement fluid composition to become dominated by basement reactivity such that vertical chemical gradients across the sediment can develop. It is now known that advection within basement and chemical reactions within sediments can affect sediment and basement fluid chemistry, so more recent studies have taken a different approach. Rates of vertical fluid seepage have been estimated in several locations through various thicknesses and types of sediment by fitting transport-reaction models to interstitial water concentrations of various species, including Mg^{2+}, Ca^{2+}, SO_4^{2-}, Mn^{2+} and chlorinity [*Maris et al.*, 1984; *Gieskes*, 1986; *Langseth et al.*, 1988, 1992; *Mottl*, 1989; *Wheat and Mottl*, 1994; *Wheat and McDuff*, 1995; *Rudnicki et al.*, 2001; *Wheat and Fisher*, 2008]. Unlike the model of McDuff [1981], these models make no *a priori* assumptions about the processes controlling the composition of basement fluid. Instead, boundary concentrations at the top and bottom of the sediment are estimated from measured values and held constant for models in which advection, diffusion and reaction within the sediment control sediment interstitial water concentrations. Typically the seepage rate is estimated by adjusting a model parameter for the rate of vertical advection (seepage), and sometimes also parameters describing reactivity within the sediment, until the modelled interstitial water chemical profile closely fits the measured profile. Another line of evidence for seepage through sediments is curvature in temperature profiles measured in surface sediments [e.g., *Becker and Von Herzen*, 1983; *Noel*, 1985]. Vertical seepage rates estimated in the studies noted above are generally in the range of 100-10000 m Myr^{-1} (0.01 - 1 cm yr^{-1}). Integrated globally, such seepage could support significant chemical fluxes between the volcanic section of the oceanic crust, the overlying sediment, and the ocean. Seepage

may also play important roles in sediment diagenesis and in supporting metabolic activity within the sediment. Seepage through sediments at the above noted rates, however, would not contribute significantly to the total advective heat loss from the oceanic lithosphere [e.g., *Stein and Stein*, 1994].

The objectives of this study are to estimate rates of vertical seepage through sediments at many locations, most of which have no previous seepage rate estimates, and to use the new seepage rate estimates, along with previously published estimates, to quantify fluid and chemical fluxes through sediments globally. Seepage rates are estimated at 140 ocean drill holes by fitting a model of chemical advection, diffusion and reaction within the sediment to measured interstitial water SO_4^{2-}, Mg^{2+} and Ca^{2+} profiles. This work greatly expands the quantity and spatial distribution of seepage rate estimates globally (see Appendix J, Supplementary Table S4.1 for a compilation of previous estimates), and investigates the connection between seepage rate and sedimentary environments (e.g., sediment type, thickness and crustal age). It is found that vertical seepage through sediments at the holes analyzed in this study generally occur at specific discharges < 500 m $Myrs^{-1}$. At these rates, integrated globally, seepage through sediments is estimated to represent only a small proportion of total hydrothermal fluid and chemical fluxes.

4.2. Data

Sediment interstitial water concentrations of SO_4^{2-}, Mg^{2+} and Ca^{2+} were compiled for ocean drill holes from Deep Sea Drilling Project (DSDP), Ocean Drilling Program (ODP) and Integrated Ocean Drilling Program (IODP) initial reports (Appendix J,

Supplementary Table S4.2). Sulfate, Mg^{2+} and Ca^{2+} ions were chosen because they are major ions in seawater, and thus can be accurately measured in interstitial waters, and also because previous studies have shown each of these ions to be sensitive indicators of transport and reaction processes within the sediment [e.g., *Gieskes*, 1986; *Langseth et al.*, 1992; *Wheat and McDuff*, 1994; *Rudnicki et al.*, 2001]. As this study focuses on seepage and reactivity of interstitial waters through mid-ocean ridge flank sediments, drill holes from continental margins, marginal basins and subduction zone settings are excluded. Additionally, holes having sparse interstitial water chemical data (fewer than 4 downhole measurements) are excluded. Some of the interstitial water samples do not have concentration data for all three species investigated in this study. These samples are still used to constrain the models provided that the suite of samples from that hole does include some concentration data for each species.

The transport-reaction model used herein is sensitive to the basement fluid concentrations of the ions. This is assumed to be the same as the deepest measured interstitial fluid composition provided that the deepest sample collected was within the bottom 15% of the sediment pile. Basement fluid composition is often chemically different from seawater due to reactions in the basement [e.g., *McDuff and Gieskes*, 1976], and it does not vary systematically as a function of sediment type, thickness or crustal age (Figure 4.1). Basement fluid chemistry is probably controlled primarily by basement temperature and time within basement, but these parameters are governed by the geometry of the local hydrothermal systems, which are not well known. This means that basement fluid composition cannot be predicted from the available data, and thus holes in which there are no data for interstitial water composition near the base of the

sediment (defined as within the lower 15% of the sediment) are excluded from the modelling.

Additional parameters for each hole were also compiled, including total sediment thickness, sediment porosity and sediment type as functions of depth below the seafloor, and sediment accumulation rate as a function of time. Crustal age for each hole was estimated using the global oceanic plate age grid of Muller et al. [2008]. The sediment thickness at each hole was determined from the drilling depth to basement, or is estimated from a nearby drill hole or from seismic data if drilling did not reach basement. The rate of sediment accumulation as a function of time is based on published bio- or magnetostratographic interpretations of the cored sediment. If the sediment accumulation rate as a function of time has not been previously determined, a uniform rate is assumed based on the total sediment thickness divided by the crustal age. Sediment accumulation rates are not adjusted for compaction. For holes in which sediment porosity has not been determined, a porosity-depth relationship representative of the dominant sediment type in the hole is assumed (from Table 6.2 in Spinelli et al. [2004]). For holes without sediment thermal conductivity measurements, the approximate global average value of 1.0 W m^{-1} K^{-1} is assumed [*Pribnow et al.*, 2000].

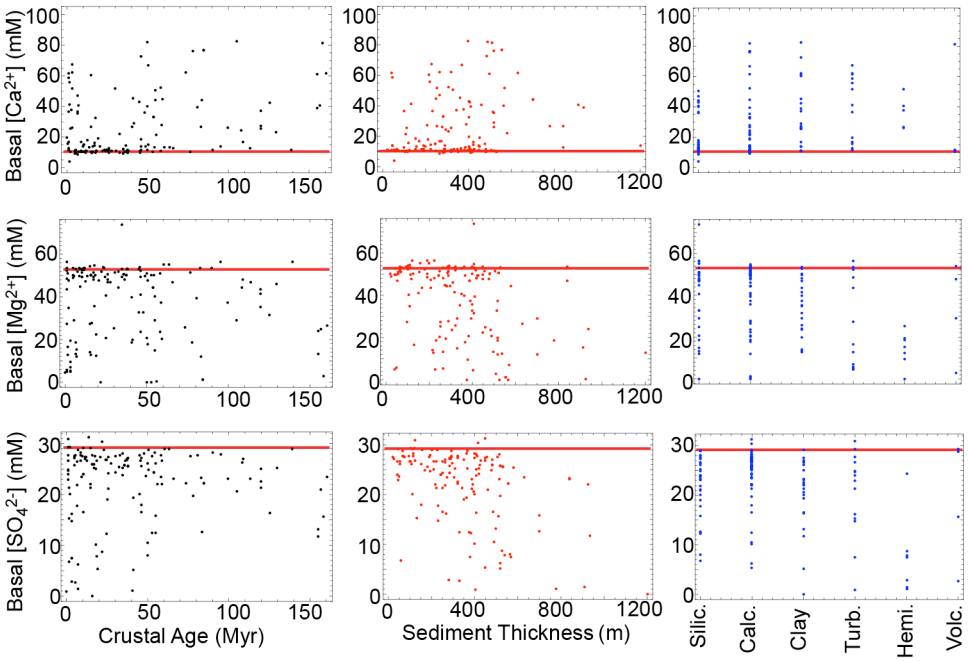

Figure 4.1. Concentrations of interstitial water SO_4^{2-}, Mg^{2+} and Ca^{2+} near the sediment-basement interface (within 15% of the total sediment thickness) plotted as functions of crustal age, sediment thickness and sediment type. Sediment type abbreviations are silic=siliceous, calc=calcareous, turb=turbidite, hemi=hemipelagic and volc=volcanogenic. Modern seawater concentrations are shown as red lines [*Millero*, 2014].

The final compilation includes 140 holes with sufficient data to model interstitial water transport and reaction for SO_4^{2-}, Mg^{2+} and Ca^{2+} (Figure 4.2). These holes represent ranges of crustal ages, sediment types, sediment accumulation rates, and sediment thicknesses (Figure 4.3). Interstitial water data from these drill holes are presented in Appendix J, Supplementary Table S4.2, and the other parameter values are presented in Appendix J, Supplementary Table S4.3.

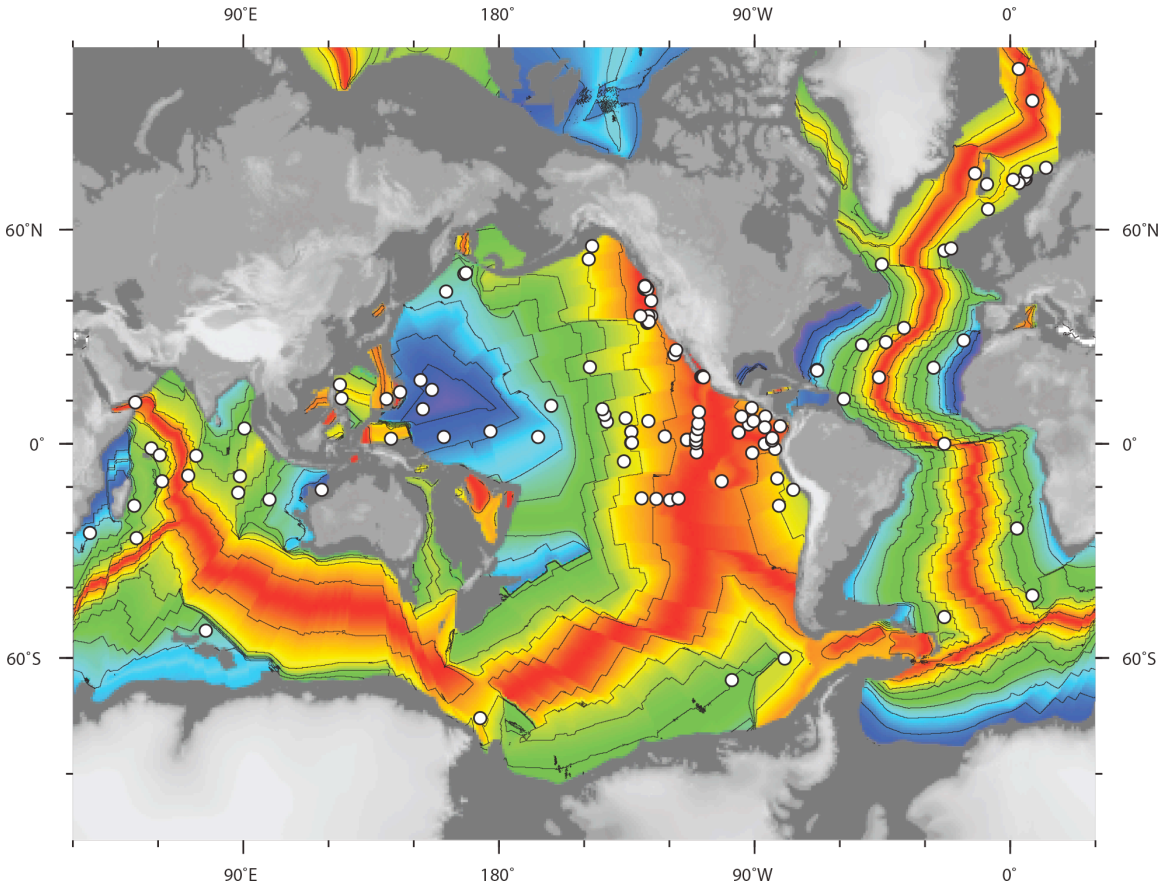

Figure 4.2. Locations of the drill holes analyzed in this study shown over a crustal age base map [*Muller et al.*, 2008] **with 20 Myr isochrons (red is young crust and blue is old crust).**

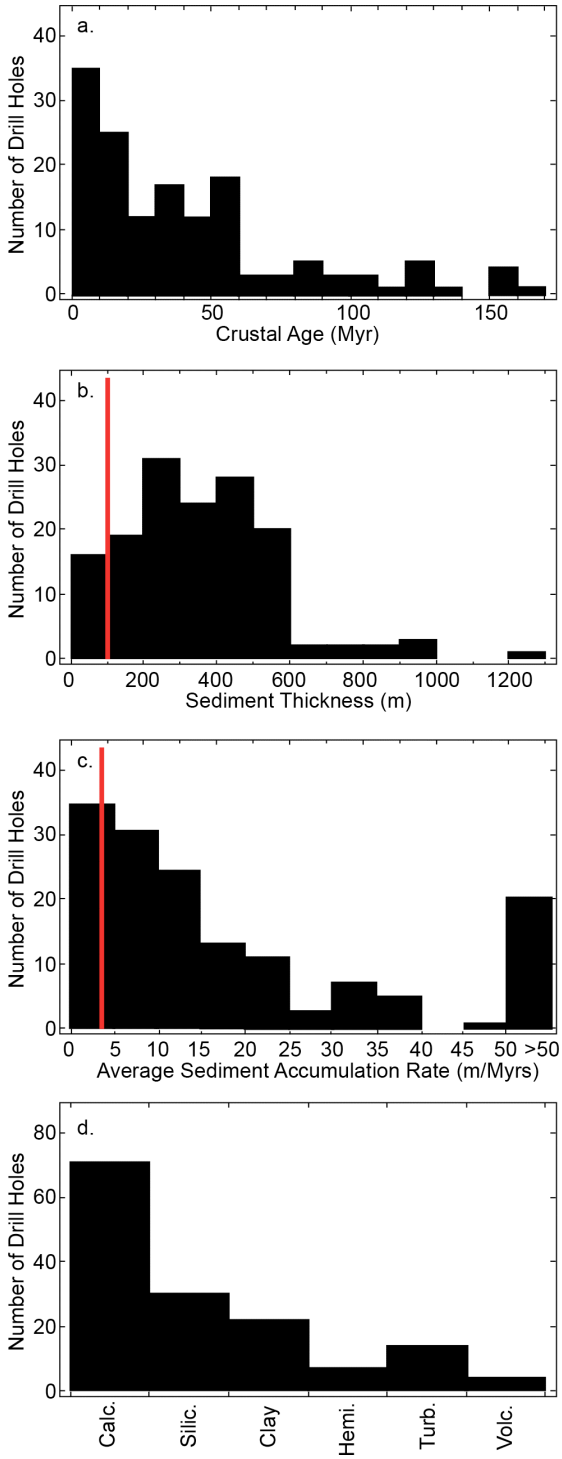

Figure 4.3. Summary of the deep sea environments represented by the drill holes used in this modelling. The histograms show the proportions of drill holes by: (a) crustal age, (b) sediment thickness, (c) sediment accumulation rate and (d) sediment type. Sediment abbreviations as in Figure 4.1. Red lines are global medians for abyssal seafloor calculated from sediment thickness [*Divins*, 2011] **and crustal age** [*Muller et al.*, 2008] **digital grids.**

4.3. Physical model for extracting seepage rates from interstitial water compositions

The one dimensional conservation equation for advection, diffusion and reaction of interstitial water is [*Richter and DePaolo*, 1987]:

$$\frac{\partial C}{\partial t} = D_c \frac{\partial^2 C}{\partial z^2} - v_v \frac{\partial C}{\partial z} + R \qquad (4.1)$$

where the first term on the right hand side of Eq. 4.1 represents diffusion, the second term represents advection, and R is a place holder for an appropriate reaction term (such as R_{SO4}, R_{Mg} or R_{Ca} defined in Section 4.4). The symbol C is the concentration of an ion in solution, v_v is the vertical average linear velocity of seepage (positive upward), t is time, and z is vertical distance which is positive upwards from the base of the sediment. The variable D_c is the diffusion coefficient of the ion in solution (D) corrected for tortuosity (θ) [*Li and Gregory*, 1974]:

$$D_c = \frac{D}{\theta^2} \qquad (4.2)$$

where tortuosity is estimated from the sediment porosity (ϕ) by [*Boudreau*, 1996]:

$$\theta^2 = 1 - \ln(\phi^2) \qquad (4.3)$$

Diffusion through the solid is considered negligible on the timescales of interest to this study. The temperature-dependent diffusion coefficients (D) for SO_4^{2-}, Mg^{2+} and Ca^{2+} are listed in Table 4.1. The temperature profile across the sediment is assumed to be equivalent to the conductive geotherm, and this temperature profile is used to estimate values for the diffusion coefficients with depth in the sediment. The average linear velocity of vertical seepage is related to the specific discharge (V_v) and sediment porosity by:

$$V_v = \phi v_v \qquad (4.4)$$

Hereafter the term "seepage rate" is used to refer to the average linear velocity of seepage (v_v), or is used when the distinction between average linear velocity and specific discharge is not important. All references to the specific discharge (V_v) are made explicitly.

Table 4.1. Diffusion coefficients used in the interstitial water transport reaction modelling.

Ion	Diffusion Coefficient (D, $cm^2\ s^{-1}$) *
SO_4^{2-}	$(4.88 + 0.232\ T) \times 10^{-6}$
Mg^{2+}	$(3.43 + 0.144\ T) \times 10^{-6}$
Ca^{2+}	$(3.60 + 0.179\ T) \times 10^{-6}$

* From *Boudreau* [1997], where temperature (T) is in °C.

Steady-state solutions to Eq. 4.1 have been applied to model reactive transport through sediment in some settings [e.g., Berner, 1978; Wheat and McDuff, 1994], although a time dependent solution is necessary to model interstitial water if the sediment thickness changes significantly on timescales over which transport occurs. To assess the importance of changes to the sediment column for the holes in this study relative to the timescale of vertical advection, it is assumed that the typical vertical seepage rate is on the order of hundreds of metres per Myrs [e.g., *Rudnicki et al.*, 2001]. Because about half of the drill holes have an average sediment accumulation rate >10 m $Myrs^{-1}$, the sediment thickness might change on the order of 10% over the time it takes fluid to pass through the sediment. As such, a time dependent solution was chosen for this study. Equation 1 is approximated numerically with a centred finite difference equation [*Fantle and DePaolo*, 2006]:

$$\frac{C_j^{n+1} - C_j^{n-1}}{2\Delta t} = \frac{D_c}{(\Delta z)^2}\left[C_{j+1}^n + C_{j-1}^n - C_j^{n+1} - C_j^{n-1}\right] - v_v \frac{C_{j+1}^n - C_{j-1}^n}{2\Delta z} + R \qquad (4.5)$$

and solved for C_j^{n+1} (Appendix D) which represents the new concentration of the j^{th} element in the depth dimension after each time increment (Δt). The symbol Δz is the depth increment (the thickness of sediment represented by each grid cell), n is the current model time increment, and j is the current depth increment (i.e., j x Δz is depth, and n x Δt is model time elapsed). To achieve a model spatial resolution comparable to that of the interstitial water data, the value of Δz is set to 2 m where $h_s < 100$ m, 5 m where $100 < h_s < 300$ m, and 10 m for $h_s > 300$ m. Model stability is achieved when $\Delta t \frac{D_c}{(\Delta z)^2} \leq 0.5$ [*Lasaga*, 1998], so an appropriate Δt is determined for each drill hole by estimating an upper bound on D_c assuming a temperature of the sediment-basement interface under conductive conditions.

It is not necessary to start the interstitial water reactive transport models from the time of crustal accretion because, in general, fluid is only expected to take a few Myrs to pass through the sediment. For example, at the minimum detectable seepage rate ($v_v \approx$ 100 m Myrs^{-1}, [*Spinelli et al.*, 2004]), a packet of fluid would pass through 300 m of sediment in 3 Myrs. The model time before present that the reactive transport modelling is started, t_s (Myrs), is calculated as present day sediment thickness in metres divided by the minimum detectible seepage rate of 100 m Myrs^{-1}. The initial sediment pile at t_s has a thickness defined by the sediment accumulation rate since crustal accretion.

To assess the sensitivity of the model results to the choice of concentrations of SO_4^{2-}, Mg^{2+} and Ca^{2+} in fluids throughout the initial sediment pile, different initial concentrations of these ions were tested, including uniform seawater values, uniform basement values, and a linear gradient between the seawater and basement values. It was found that the final interstitial water concentrations of SO_4^{2-}, Mg^{2+} and Ca^{2+} throughout

the sediment are insensitive to the initial concentrations at t_s. Thus, for the model results presented here the initial concentrations were set as linear gradients between the upper and lower boundary concentrations; this is approximately what the profiles would be under purely diffusive conditions. Modern seawater concentrations of SO_4^{2-}, Mg^{2+} and Ca^{2+} [*Millero*, 2014] are assumed at the upper sediment boundary, and measured concentrations near the base of the sediment are assumed as the lower boundary condition.

In natural systems vertical advection across the sediment is driven by super- or sub-hydrostatic pressure within the aquifer (discussed further in Section 4.7), and also by compaction of the sediment. Advection driven by compaction has been explicitly included in some interstitial water transport-reaction models [e.g., Richter and DePaolo, 1987; Rudnicki et al., 2001], but is considered negligible in other models [e.g., Fantle and DePaolo, 2006; Wheat and McDuff, 1995]. The importance of flow driven by compaction can be assessed with a fluid conservation equation [*Richter and DePaolo*, 1988]:

$$\frac{\partial \phi}{\partial t} = -\frac{\partial (\phi v_v)}{\partial z} \qquad (4.6)$$

An estimate of the *maximum* vertical seepage rate due to compaction can be made assuming a rapid change in porosity due to rapid deposition of sediment. For example, if 100 m of sediment is deposited within 1 Myrs, which is much more rapid than the global median sediment accumulation rate of 3.5 m $Myrs^{-1}$[*Anderson et al.*, 2012]), and if the sediment compacts such that there is a loss in porosity of the deepest sediment relative to the surface sediment such that $\partial\phi = 0.3$, then the upward seepage rate due to compaction is on the order of 30 m $Myrs^{-1}$. For a sediment column with an average porosity of 0.5,

this corresponds to an upward seepage rate of about 60 m $Myrs^{-1}$ (Eq. 4.4), which is less than the minimum detectible seepage rate (about 100 m $Myrs^{-1}$). As such, advection driven by compaction is considered to be negligible in general, and is not included in the modelling. All parameters for this modelling are defined in Table 4.2.

Table 4.2. Parameter definitions for Chapter 4

Parameter	Definition
A	Constant used to calculate the sulfate reaction rate, k_{SO4}
C	Interstitial water concentration of a given ion
D	Diffusion coefficient of a given ion in solution
D_c	Diffusion coefficient of a given ion in solution, corrected for tortuosity of the sediment
dP_v	Difference in non-hydrostatic pressure between the top and bottom of the sediment
G	The concentration of metabolizable organic carbon in the sediment. G_0 is the initial concentration at $t = t_s$.
h_s	Sediment thickness
$k`_{sp}$	Apparent solubility product for $CaCO_3$. Related to the true solubility product through Eq. 4.15
k_{CaCO3}	Calcium carbonate reaction rate
k_{Mg}	Magnesium reaction rate
k_{SO4}	Sulfate reaction rate
k_v	Vertical permeability of sediment
L	Stoichiometric constant (= 0.5) representing the charge balance between carbon and sulfate in Eq. 4.7.
M	Mass ratio of solid sediment to interstitial fluid
R	Placeholder for a term representing the chemical reaction for a specific ion (e.g., R_{SO4}, R_{Mg}, R_{Ca})
t	Time
t_s	Model start time before present.
V_v	The specific discharge of vertical seepage through sediment.
v_v	The average linear velocity of vertical seepage through sediment.
z	Depth below sediment surface
ϕ	Sediment porosity
μ	Dynamic viscosity of sediment interstitial water
θ	Tortuosity of the sediment
ω	Sediment accumulation rate

4.4. Chemical reactions

4.4.1. Sulfate and organic carbon

Sulfate is removed from sediment interstitial waters primarily by sulfate reducing bacteria [*Berner*, 1978], a reaction which is described by Toth and Lerman [1977] as:

$$2CH_2O + SO_4^{2-} \leftrightarrow H_2S + 2HCO_3^- \qquad (4.7)$$

The fractional rate of sulfate reduction in abyssal sediments (k_{SO4} in yr^{-1}) has been found to be dependent on the square of the sediment accumulation rate (ω, in cm yr^{-1}) [*Toth and Lerman*, 1977; *Berner*, 1978]:

$$k_{SO4} = A\omega^2 \qquad (4.8)$$

where A is a proportionality constant. The dependence on sedimentation rate is because slowly buried organic matter is likely to be destroyed by aerobic organisms near the seafloor, but rapidly buried material is more likely to persist until it reaches anoxic sediment where sulfate reduction can occur [*Berner*, 1978]. Here, the rate of interstitial water sulfate removal due to organic matter degradation (R_{SO4}) is represented by [*Boudreau and Westrich*, 1984; *Rudnicki et al.*, 2001]:

$$R_{SO4} = \frac{-MLk_{SO4}G[SO_4^{2-}]}{K_s + [SO_4^{2-}]} \qquad (4.9)$$

The parameter L (=0.5) is a stoichiometric constant representing the charge balance between carbon and sulfate in Eq. 4.7, G is the concentration of metabolizable organic carbon in the sediment (mM kg^{-1}), and M is the mass ratio of solid sediment to interstitial fluid, which is defined based on porosity and the solid and fluid densities, ρ_s and ρ_f respectively:

$$M = \frac{\rho_s(1-\phi)}{\rho_f\phi} \qquad (4.10)$$

The Monod kinetic saturation constant (K_s) is the sulfate concentration at which the rate of sulfate reduction is half of its asymptotic value, and a value of K_s = 1 mM kg^{-1} is used following Boudreau and Westrich [1984]. For each drill hole newly deposited sediment is assumed to have a metabolizable organic carbon concentration of $G = G_0$ where G_0 is a

free parameter that is fit during the modelling. It is assumed that organic carbon is degraded by sulfate reducing bacteria at a rate (R_G) of [*Rudnicki et al.*, 2001]:

$$R_G = \frac{-k_{SO4} G[SO_4^{2-}]}{K_s + [SO_4^{2-}]} \qquad (4.11)$$

The final interstitial water SO_4^{2-} profile is sensitive to the value of G_0 for sediment deposited within the most recent few million years, although it is insensitive to the initial profile of metabolizable organic carbon throughout the sediment at t_s. This is because the models are started early enough before the present day to "flush" any assumptions about G in old sediment out of the system. The proportionality constant in the rate of sulphate reduction, A, and the concentration of metabolizable organic carbon in newly deposited sediment (G_0) are initially unknown values which are determined along with the seepage rate through the modelling (Section 4.5).

4.4.2. Magnesium

Interstitial water Mg^{2+} is known to be reactive in some sediment types, including continent-sourced sediments [e.g., *Rudnicki et al.*, 2001] and sediments containing volcanic material (e.g., ODP Leg 129, [*Lancelot and Larson*, 1990]), where dissolved Mg may be consumed by the formation of smectites [*Gieskes and Lawrence*, 1981]. Dolomite recrystallized from calcite or aragonite may also be a sink for magnesium in carbonate sediments [*Matter et al.*, 1975; *Sayles and Manheim*, 1975], and dissolving dolomite may be a source of Mg to interstitial waters. In addition, Mg adsorbed to sediment particles may be released to the fluid by exchange with NH_4^+ [*Breymann and Suess*, 1988]. For the purpose of estimating seepage rates, distinguishing the relative importance of these processes in any given sediment is unnecessary. Here the rate of the

Mg^{2+} reaction (R_{Mg}) is approximated as a first order process dependent only on the interstitial water Mg^{2+} concentration:

$$R_{Mg} = k_{Mg}[Mg^{2+}] \qquad (4.12)$$

This model is not a physical representation of the specific sources and sinks of Mg^{2+} within the sediment, but it does capture the net effect of the above-noted processes on Mg^{2+} exchange between the sediment and interstitial water. Because the value of the first order rate constant k_{Mg} is unknown for each drill hole, and because the parameter may vary by sediment composition, k_{Mg} is adjusted for each drill hole to determine a value that best fits the interstitial water chemical data (see Section 4.5 for a discussion of the modelling methodology).

4.4.3. Calcium and carbonate alkalinity

Dissolution and precipitation of calcium carbonate is an important process in controlling the Ca^{2+} concentration in sediment interstitial waters [*Sayles and Manheim*, 1975]. As such, the behavior of calcium depends on the saturation state of the fluid with respect to $CaCO_3$, which is determined by the fluid Ca^{2+} and CO_3^{2-} concentrations and the pressure/temperature dependence of calcite or aragonite solubility [e.g., *Morse*, 1978; *Keir*, 1980]. In addition, the concentration of CO_3^{2-} is controlled by the pH and dissolved inorganic carbon (DIC) of the fluid. Because pH and DIC data are not available for all drill holes, the CO_3^{2-} concentration is uncertain. I follow the approach of Rudnicki et al. [2001] and model the saturation state of the fluid (Ω) with respect to $CaCO_3$ as a function of carbonate alkalinity (CA), and an apparent solubility product ($k`_{sp}$).

$$\Omega = 1 - \frac{[Ca^{2+}][CA]}{k`_{sp}} \qquad (4.13)$$

where carbonate alkalinity is:

$$[CA] = 2[CO_3^{2-}] + [HCO_3^-] \qquad (4.14)$$

and the apparent solubility product is an unknown determined by adjusting this parameter while fitting the downhole measurements of $[Ca^{2+}]$. The apparent solubility product ($k`_{sp}$) is related to the true calcium carbonate solubility product (k_{sp}) by [*Rudnicki et al.*, 2001]:

$$k`_{sp} = k_{sp}\left(\frac{[CO_3^{2-}]}{[CA]}\right)\overline{\Omega} \qquad (4.15)$$

where $\overline{\Omega}$ is the average saturation state of the fluid with respect to $CaCO_3$. The $CaCO_3$ dissolution/precipitation reaction is assumed to be first order with Ω. The reaction terms for Ca^{2+} and CA are based on the equations used by Rudnicki et al. [2001]:

$$R_{Ca} = k_{CaCO3}\Omega \qquad (4.16)$$

$$R_{CA} = 2k_{CaCO3}\Omega - 2R_{SO4} \qquad (4.17)$$

where k_{CaCO3} is a reaction rate constant. In the carbonate alkalinity reaction (Eq. 4.17), the first term describes the production/removal of CO_3^{2-}, and the second term describes the production of HCO_3^- associated with sulfate reduction (Eq. 4.7). The carbonate alkalinity of interstitial waters in newly deposited sediment is set to the modern seawater value. The value of the rate constant k_{CaCO3} is an unknown, and is fit as part of the transport-reaction modelling (Section 4.5).

4.5. Methodology to estimate seepage rates

The interstitial water transport-reaction model described in Section 4.3 is applied to each of the drill holes to determine the seepage rate (v_v) that best fits the measured downhole interstitial water concentrations of SO_4^{2-}, Mg^{2+} and Ca^{2+}. The misfit is

calculated as a Mean Square Weighted Deviation (MSWD) across SO_4^{2-}, Mg^{2+} and Ca^{2+} simultaneously:

$$MSWD = \frac{1}{N}\sum_{i=1}^{N}\frac{\left(C^{i}_{measured} - C_{modeled}\right)^2}{\sigma_i^2} \qquad (4.18)$$

where $C^{i}_{measured}$ is the measured concentration of a given ion in the sediment interstitial water and $C_{modelled}$ is the modelled concentration for the same ion at the depth of the measurement, N is the total number of concentration measurements for SO_4^{2-}, Mg^{2+} and Ca^{2+} combined, and σ_i is the analytical uncertainty of the measurement. Analytical accuracies for measured concentrations of SO_4^{2-}, Mg^{2+} and Ca^{2+} are estimated to be 2%, with precisions of 0.5% for SO_4^{2-} and 0.2% for both Mg^{2+} and Ca^{2+} [*Gieskes*, 1974].

The models are run in two stages. In the first stage, for all drill holes, the reaction term in Eq. 4.1 is neglected so only the processes of diffusion and advection affect the modelled interstitial water SO_4^{2-}, Mg^{2+} and Ca^{2+} profiles. In this modelling, the seepage rate is the only unknown parameter for each drill hole, and its value is incrementally adjusted until a minimum total misfit is found, or until it becomes apparent that the calculated total misfit is insensitive to the value of v_v. The minimum misfit is determined by testing seepage rates in the range of -10^4 to $+10^4$ m $Myrs^{-1}$. Models are considered insensitive to v_v when the misfit changes by < 10% for seepage rates within ±2000 m $Myrs^{-1}$ from the best fitting value.

After the first stage of no-reaction models, those holes in which the best fitting model produces a "good fit" to the measured ion concentrations are determined. Based on a visual inspection of the measured and modelled interstitial water concentrations, holes from the first stage modelling having MSWD misfits < 5 are considered to fit the data well without modelling diagenetic reactions. For the 31 holes that meet this criteria

the best fitting seepage rate from the first stage of modelling is a reasonable estimate and no further modelling with chemical reactions is conducted. Clay, calcareous or siliceous sediments dominate at these holes. At 13 of these holes there are insufficient chemical gradients across the sediment to constrain the seepage rates. Estimated seepage rates for the remaining 18 holes that are well fit by no-reaction models are within a few hundred m $Myrs^{-1}$. To invert the seepage rates at the 111 holes that could not be well fit without modelling chemical reactions, a second stage of modelling is performed which includes diagenetic reactions for SO_4^{2-}, Mg^{2+} and Ca^{2+}. In the second stage of modelling the following parameters are unknown and are iteratively adjusted to find the best fitting combination: the constant (A) used to estimate the sulphate reduction rate constant, the initial metabolizable organic carbon (G_0), the rate constant for magnesium reactivity (k_{Mg}), the rate constant for calcium carbonate dissolution/precipitation (k_{CaCO3}), the apparent calcium carbonate solubility product ($k`_{sp}$), and the seepage rate (v_v). The ranges evaluated for each parameter are listed in Table 4.3.

Table 4.3. Range of values tested for the diagenetic reaction parameters.

	Range Tested		
Parameter	**Minimum**	**Maximum**	**Reference**
A (yr^1 cm^{-2})	0.01	0.08	[*Toth and Lerman*, 1977; *Berner*, 1978]
G_0 (mM kg^{-1})	0	2000	[*Müller and Suess*, 1979; *Emerson and Hedges*, 1988]
k_{Mg} (Ma^{-1})	-10	10	[*Rudnicki et al.*, 2001]
k_{CaCO3} (mM Ma^{-1})	0	2000	[*Rudnicki et al.*, 2001]
k'_{sp} (mM^{-2})	1	3000	[*Rudnicki et al.*, 2001]

4.6. Results

4.6.1. Seepage rates

The results of the modelling for each drill hole are included in Appendix J, Supplementary Table S4.3. Measured and modelled concentration profiles for the best fitting parameterizations are graphed in Appendix E, and representative example profiles for two of the drill holes (Hole 1020B and 1039B) in which chemical reactions within the sediment are important are shown in Figure 4.4. The best fitting seepage rates, converted to specific discharges based on the average sediment porosity (using Eq. 4.4), are summarized in Figure 4.5. Both upper and lower bounds on the magnitude of seepage

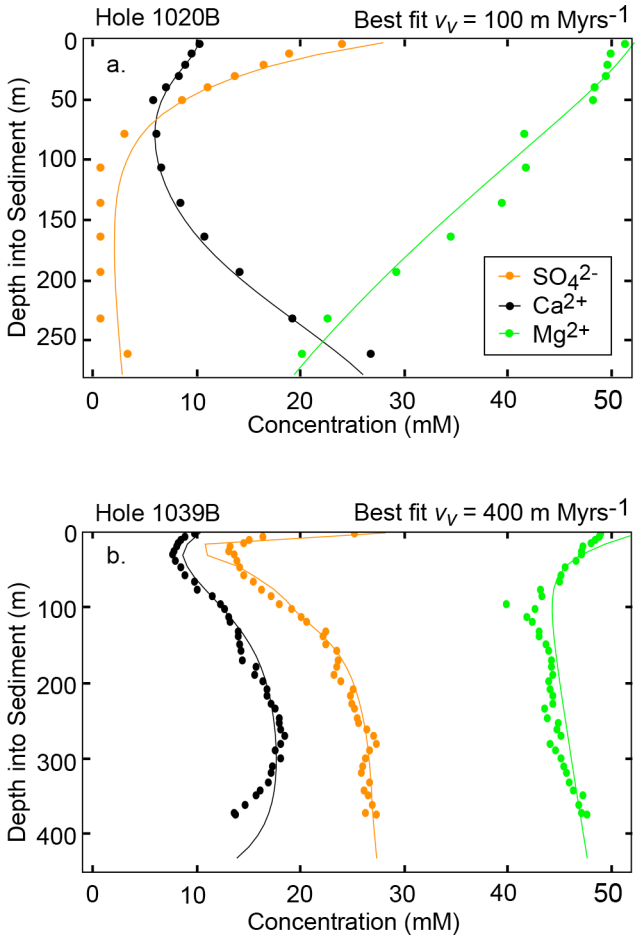

Figure 4.4. Representative examples of measured and best-fitting model profiles of interstitial water SO_4^{2-}, Mg^{2+} and Ca^{2+} for Holes 1020B and 1039B. Profiles for the other drill holes in which the seepage rate is constrained are graphed in Appendix E.

are constrained at 85% of all holes, lower bounds only are constrained at 9% of the holes, upper bounds only are constrained at 1% of the holes, and there is no constraint on the seepage rate at 5% of the holes. Those holes in which the seepage rate is unconstrained have no gradient in SO_4^{2-}, Mg^{2+} and Ca^{2+} profiles within uncertainty in the data (i.e., the concentrations are approximately that of seawater across the thickness of the sediment). Of the holes in which the seepage rate is constrained, the best fitting seepage rate suggests that 52% host upward flow, 20% host downward flow, and 28% have no

resolvable seepage. The average magnitude of the specific discharge is 200 m $Myrs^{-1}$ (0.02 cm yr^{-1}), and the specific discharge is slower than 500 m $Myrs^{-1}$ (0.05 cm yr^{-1}) at approximately 90% of the holes.

4.6.2. Uncertainties

The misfits between measured and modelled concentrations of interstitial water SO_4^{2-}, Mg^{2+} and Ca^{2+} are the result of both analytical uncertainty and uncertainty in the model. The MSWD (Eq. 4.18) is ≤ 1 when the misfit is within analytical uncertainty. Only four holes have a MSWD misfit below this value, meaning that model uncertainty is relevant at most of the drill holes. The distribution of misfits for the best fitting models is non-Gaussian. The best misfits range from 0.08 – 28000, and approximately 90% of the holes have best misfits < 500. The models tend to fit best at holes with approximately linear gradients in the measured concentrations (i.e. those holes that can be well explained by advection and diffusion without reactivity), suggesting the primary sources of model uncertainty are the simplifying assumptions in the model representations of chemical reactions (Section 4.4) and/or the assumption that reaction parameters are uniform throughout the sediment at any given drill hole. The range of seepage rates at each hole that produce MSWD within 15% of the best fit value is used to approximate the total uncertainty in seepage rate at each hole (Figure 4.5). At those holes in which both an upper and lower bound on the seepage rate are constrained, the average range of uncertainty in the specific discharge is about 300 m $Myrs^{-1}$, which is slightly larger than the average magnitude of the best fitting specific discharge (200 m $Myrs^{-1}$).

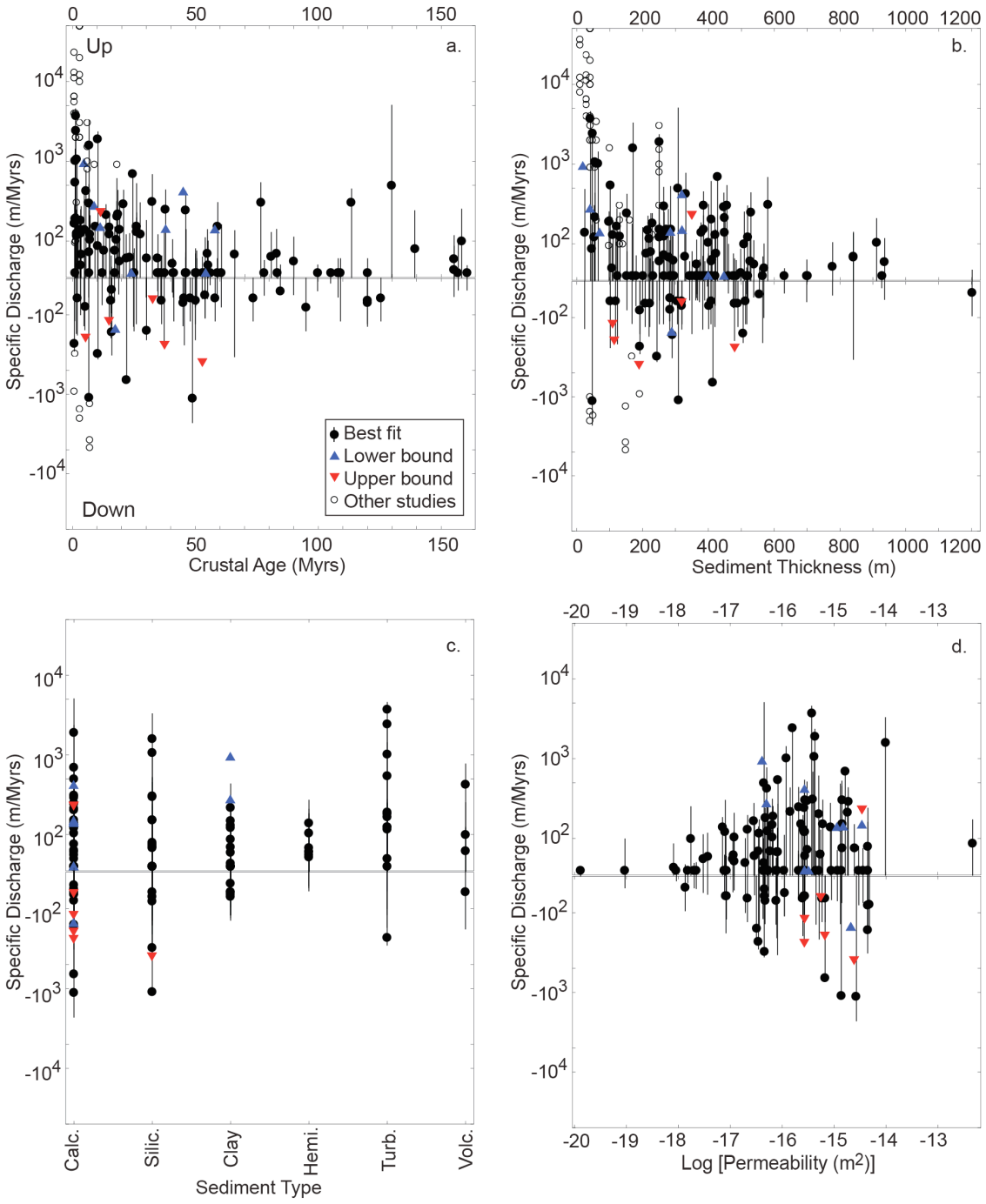

Figure 4.5. Specific discharge through sediment plotted against a) crustal age, b) sediment thickness, c) sediment type and d) sediment bulk permeability. Sediment bulk permeability is estimated for the appropriate sediment type and thickness using the porosity-permeability functions of Spinelli et al. [2004] (their Table 6.2). Uncertainty on each seepage rate is approximated as the range of modelled seepage rates that fit the data with a MSWD within 15% of the best fit. Sediment abbreviations as in Figure 4.1.

4.6.3. Comparison of seepage rates to other studies

Twelve drill holes analyzed in this study have been previously analyzed to determine seepage rates (Appendix F). Rudnicki et al. [2001] and Giambalvo et al. [2002] estimated seepage rates at two drill holes (Holes 1030B and 1031A) on the Juan de Fuca plate using fits of numerical transport-reaction models to SO_4^{2-} and Mg^{2+} profiles, respectively. For both holes Rudnicki et al. [2001] and Giambalvo et al. [2002] estimated upward specific discharge of thousands of m $Myrs^{-1}$, which are in good agreement with estimates from this study (Appendix F). Rudnicki et al. [2001] investigated seepage rates at six additional holes on the Juan de Fuca plate (Holes 1023A, 1024B, 1025B, 1026C, 1028A and 1029A). For these holes the discrepancies between seepage rates estimated in this study compared to those from Rudnicki et al., [2001] are of similar magnitude to the best fitting seepage rates themselves (generally a few hundred m $Myrs^{-1}$). The largest discrepancy between seepage rates from this study and those of Rudnicki et al. [2001] is for Hole 1023A. At this hole Rudnicki et al. [2001] identified two discrete specific discharge rates that gave clear minimum misfits to SO_4^{2-} data (approximately -910 and -250 m $Myrs^{-1}$). Although their models with V_v = -910 m $Myrs^{-1}$ result in a slightly better fit to SO_4^{2-} only, the other minimum at V_v = -250 m $Myrs^{-1}$ is in better agreement with our estimate of roughly -150 to -300 m $Myrs^{-1}$. The primary differences between the models and methodologies of this study and Rudnicki et al. [2001] are: i) in this study the reactive transport model is simultaneously fit to SO_4^{2-}, Mg^{2+} and Ca^{2+}, while Rudnicki et al. [2001] only fit to SO_4^{2-}, and ii) this study assumes there is no seepage due to compaction, while Rudnicki et al. [2001] account for compaction. There is very little change in porosity with depth in the sediment at these eight holes [*Davis et al.*, 1997b], and therefore the component of seepage due to

compaction is negligible. If the model developed for this study is fit only to SO_4^{2-} then the best fitting seepage estimates are in closer agreement, suggesting the primary cause of the discrepancies is that this study fits to concentrations of three ions instead of one. Other seepage rate estimates have been made for DSDP Holes 598 and 599 in the south Pacific [*Gieskes*, 1986] using a model of steady-state Ca^{2+} advection and diffusion (but no reaction), and at ODP Holes 677A and 678B in the equatorial Pacific [*Mottl*, 1989] using models of steady-state Ca^{2+} and Mg^{2+} advection and diffusion (but no reaction). In these cases, our estimates of the direction and magnitude of seepage are in agreement with the previous estimates (Appendix F).

4.6.4. Correlations between seepage rates and environmental parameters

In this section the estimated seepage rates at the drill holes modelled in this study are analyzed with respect to site-specific crustal ages and properties of the sediments to determine whether any correlations exist. Estimated specific discharges are plotted against crustal age, sediment thickness, primary sediment type and estimated sediment permeability (Figure 4.5). Permeability is a fundamental hydrologic property of porous media which influences the rate of fluid flow, but this property was not measured directly in the sediment sections at most of the drill holes analyzed in this study. As such, an estimate of the bulk vertical permeability of the sediment (k_v) is made for each drill hole based on the primary sediment type and the measured sediment porosity as a function of depth in the sediment using the porosity-permeability relationships of Spinelli et al. [2004]. The specific discharge through sediment (V_v) is dependent on the bulk vertical permeability of the sediment as described by Darcy's Law:

$$V_v = \frac{k_v}{\mu}\frac{dP_v}{h_s} \qquad (4.19)$$

where h_s is the sediment thickness, dP_v is the pressure difference across the sediment, and μ is the dynamic viscosity of the fluid. The specific discharge estimated for the drill holes analyzed in this study show no correlation with estimated permeability, sediment type or sediment thickness individually (Figure 4.5). This is likely because it is the combination of these parameters (sediment type only indirectly), as well as the driving pressure difference, which control the specific discharge (Eq. 4.19). The driving pressure difference at most of the drill holes is not known *a priori*, and probably cannot be predicted with sufficient accuracy by models of crustal hydrothermal circulation (discussed further in Section 4.7) to test this relationship. The fastest specific discharge rates identified in this study (2000-4000 m $Myrs^{-1}$) occur through thin sediment (< 50 m) overlying young crust (< 5-10 Myrs), and the maximum specific discharges generally decrease with sediment thickness and crustal age.

Correlations between seepage direction and heat flow have been previously reported in numerous settings. For example Maris et al. [1984] and Langseth et al. [1988] found downward seepage in low heat flow areas and upward seepage in high heat flow areas. None of the drill holes analyzed in this study had down-hole temperature measurements taken sufficiently long after drilling ceased to represent natural conditions and thus do not allow heat flow to be directly determined. Seafloor heat flow measurements have been made near to many of the drill holes (tens to hundreds of metres away). To determine whether these nearby measurements can be considered representative of the drill holes themselves, differences between nearby measurements from the global heat flow data set [*Hasterok et al.*, 2011] were compared to the distances

separating the measurement locations (Appendix G). No clear relationship exists between the difference in heat flow measured at two locations and the distance separating those locations. As such, heat flow measured within tens or hundreds of metres of the drill holes are not considered reliable predictors of heat flow at the drill holes, and it is not possible to investigate a correlation between heat flow and seepage rate or direction.

4.6.5. Reaction constants

For each drill hole analyzed, the parameters representing SO_4^{2-} reactivity (A and G_0), Mg^{2+} reactivity (k_{Mg}) and Ca^{2+} reactivity (k_{CaCO3} and $k`_{sp}$) were varied for each seepage rate tested. There is only one combination of these parameters that best fits the interstitial water chemical data for each hole (see Appendix J, Supplementary Table S4.3), but in some cases other values can fit the data similarly well. To investigate uncertainty in the reaction parameters, the subset of all parameterizations resulting in a fit within 15% of the best fitting parameterization are collected. The minimum and maximum values for each reaction parameter from within this subset of parameterizations is determined, and reported in Appendix J, Supplementary Table S4.3. These ranges approximate uncertainty in the parameter values. No clear correlation exists between the best fitting values for each reaction parameter and uncertainty in the other reaction parameters (for example, between the best fitting k_{CaCO3} and uncertainty in $k`_{sp}$ as shown in Appendix H). For many of the drill holes, the magnitude of uncertainty in one or more of the reaction parameters is comparable to the range of values that were tested during the modelling. The poorly constrained reaction parameters (defined here as those in which the range of uncertainty is >20% of the range of tested values) are excluded from any

further analysis. Values for the SO_4^{2-} proportionality constant (A) and the initial organic carbon concentration (G_0) are the least well constrained at most holes, with a wide range of values resulting in similarly good fits to the SO_4^{2-} interstitial water chemical data. Of the parameter values that are well constrained, there are no clear correlations with the primary sediment type (Appendix I). The lack of correlation between the reaction parameters and the primary sediment type is surprising but may be because many of the holes have inter-layered sediments of different types, or because fluid-sediment reactions earlier in the history of each site affected the reactivity over the most recent few Myrs (the period of time that was modelled).

4.7. Pressures in the crust

Fluid flow within the sediment and the igneous crust can occur where there are gradients in non-hydrostatic pressure. There are limited direct measurements of pressures in the oceanic crust, but those which do exist suggest that pressures relative to hydrostatic in the uppermost igneous crust are ± a few tens of kPa [*Davis and Becker*, 2002]. Super-hydrostatic pressures in the crust drive upward seepage through the sediment, and sub-hydrostatic pressures drive downward seepage. Previous numerical modelling based on coupled heat and Darcy flow equations has also been used to make predictions of crustal pressure, temperature, fluid fluxes, and paths of fluid circulation within basement and the overlying sediment. Fisher et al. [1994], Davis et al. [1997a] and Wang et al. [1997] applied finite element models representing the crustal aquifer as a high permeability layer sandwiched between low permeability basement and low permeability sediment. These models were used to identify the conditions in which hydrothermal circulation at two

locations (near to DSDP/ODP Site 504 and on the eastern flank of the Juan de Fuca ridge) are consistent with patterns of conductive heat flow measurements and the direction of seepage across sediment (previously inferred from interstitial water chemical data). These numerical models assumed steady-state fluid and heat transport and a flat sediment-ocean interface with a sinusoidal sediment-basement interface (i.e., variable sediment thickness). For boundary conditions, these models assumed constant heat flow into the lower boundary, constant temperature and pressure at the top boundary, and no fluid flux across any edge. Fluid was permitted to cross the boundaries between layers such that fluid fluxes are subject to buoyancy forces developing in the aquifer and the permeability of the layers. Outcrops were not represented. Under these conditions the models predict that convection cells can develop to transport fluid through all model layers, including both upward and downward flow across the sediment.

The parameterizations of these models that best match observables from the respective survey areas require super-hydrostatic crustal pressure at buried basement peaks, and sub-hydrostatic pressure at basement troughs. Basement bathymetry stimulates circulation because igneous rocks and sediments conduct heat at different rates, resulting in lateral temperature gradients (and thus pressure gradients) even under conductive conditions. These models predict that the sediment-basement interface is pressurized within ± a few tens of kPa of hydrostatic, which is similar to the measured crustal pressures. Other modelling representative of the eastern flank of the Juan de Fuca ridge demonstrates that convective circulation within basement and across the sediment can also develop in the absence of basement topography, although sufficiently low

permeability sediment can reduce fluid fluxes across the sediment to near zero [*Snelgrove and Forster*, 1996].

Stein and Fisher [2003] modelled time-dependent convective circulation in the basement and sediment in the presence of a lateral driving force to simulate lateral flow between outcrops. Outcrops are represented in the model, but basement topography is flat and sediment thickness is uniform away from the outcrops. This modelling predicted that secondary convection cells develop and overprint the net lateral flow such that the convection cells migrate in the direction of the lateral flow. Under this scenario, pressures at any given location in the aquifer are subject to change with time, although super- and sub-hydrostatic pressures at the base of the sediment are within ± 20 kPa. In summary, hydrologic models of the oceanic crust suggest pressures at the sediment-basement interface are within a few tens of kPa of hydrostatic. Pressures at any given location in the crust are difficult to predict with any more precision than this because the models are sensitive to assumptions about basement topography and sediment thickness in the surrounding area, and steady vs. non-steady-state circulation.

The non-hydrostatic pressure difference across the sediment (dP_v) can be estimated independently at each drill hole from the specific discharge (V_v) using Darcy's Law (Eq. 4.19). For this calculation the dynamic viscosity (μ) is determined using the approach of Millero [1974] based on the estimated average temperature within the sediment assuming equilibrium with lithospheric heat flow, and the bulk vertical permeability of the sediment (k_v) is estimated as described in Section 4.6.4. The upper and lower bound specific discharge rates estimated for each hole are used to estimate a range of uncertainty in dP_v (Figure 4.6; Appendix J, Supplementary Table S4.3). In

general, holes in which the sediment is estimated to have low bulk vertical permeability (k_v) provide very poor constraints on dP_v. For example, at Hole 249 in 125 Myr old crust with 400 m of sediment (having k_v of 10^{-17} m^2) and an estimated specific discharge

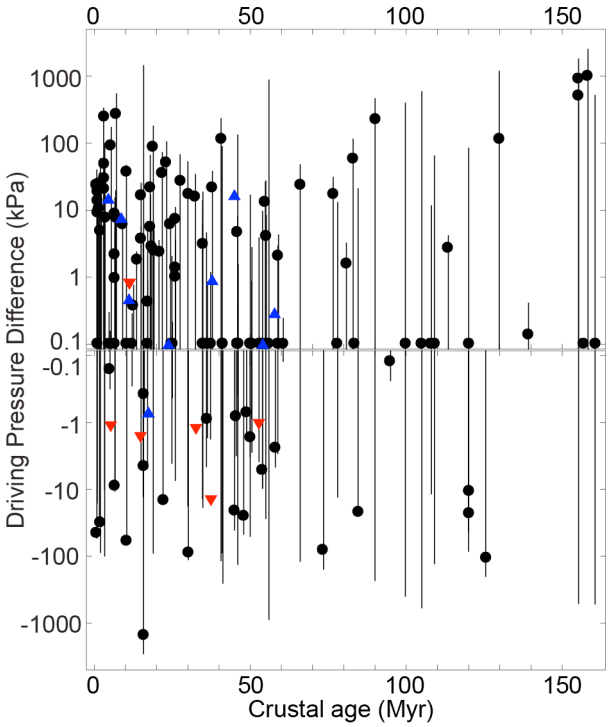

Figure 4.6. Vertical driving pressure (dP_v) across the sediment required to match the calculated seepage rate estimated for each drill hole from Darcy's Law (Eq. 4.19). The dP_v error bars correspond to the ranges of uncertainty in seepage rates.

of 0 to 120 m $Myrs^{-1}$ downward, *dPv* is estimated to be in the range of 0 to -200 kPa (negative indicating sub-hydrostatic pressure in the basement). In this scenario, because of the low bulk vertical permeability of the thick sediment, even slow downward seepage at a specific discharge of 120 m $Myrs^{-1}$ requires a dP_v that is an order of magnitude larger than previously measured and modelled values. In cases such as this, where a seepage rate requires an unrealistically large driving pressure difference, either the actual rate of seepage is smaller than the estimated upper bound or the sediment permeability was

underestimated. Although there is substantial uncertainty in dP_v at many of the drill holes, the pressure differences corresponding to the best fitting seepage rates are generally within a few tens of kPa of hydrostatic, which is broadly in agreement with previous measurements and model predictions.

Four of the drill holes considered here (Holes 1024B, 1025B, 1026C and 1027B) have been instrumented with pressure sensors to measure non-hydrostatic pressures in the upper basement ([*Davis and Becker*, 2002], Table 4.4). Because there is substantial uncertainty in the pressure differences across the sediment estimated in this study, comparison between our estimates and non-hydrostatic pressures measured in the crust is not especially revealing. At all four holes, driving pressure differences estimated from the seepage rates, within uncertainty, are consistent with the measured non-hydrostatic pressures in the upper basement (Table 4.4).

Table 4.4. Pressure differences available to drive vertical fluid seepage through sediments.

	Vertical *dP* (kPa)	
Hole	**This Study ***	[*Davis and Becker*, 2002] **
1024B	0 (-16 to 24)	-3
1025B	9 (0 to 13)	3
1026C	30 (-10 to 40)	18
1027B	50 (-100 to 100)	-26

* Calculated *dP* from the best fit seepage rate using Eq. 4.19. The range of *dP* for seepage rates in which misfit is within 15% of the best fit is in parentheses.
** Pressure in the uppermost igneous crust relative to the geotherm hydrostat

4.8. Global fluid and chemical fluxes through sediment

In this section the rates of seepage through sediments at the drill holes analyzed in this study are extrapolated to a global scale to estimate the total fluid and chemical fluxes through marine sediments. The proportion of drill holes hosting upward flow (52%) is

larger than that hosting downward flow (20%), and the average seepage rate is similar for upward and downward flow, so an upper bound on the global fluid flux through sediments can be estimated from the assumed seafloor area hosting upward flow only. Of those sites hosting upward flow, the average specific discharge is 320 m $Myrs^{-1}$ (0.032 cm yr^{-1}), and about 90% of these holes have seepage < 500 m $Myrs^{-1}$ (0.05 cm yr^{-1}). These rates are at the low end of the range estimated in other studies (roughly 0.01 – 1 cm yr^{-1}, Appendix J, Supplementary Table S4.1). Assuming upward seepage occurs through 50% of the seafloor at 500 m $Myrs^{-1}$ (a conservatively high estimate), the global fluid flux from sediments into the ocean is estimated to be 7.5 x 10^{10} m^3 yr^{-1}. Estimates of the total ridge flank hydrothermal fluid flux are in the range of 2.5 - 7.3 x 10^{12} m^3 yr^{-1} [*Mottl and Wheat*, 1994; *Elderfield and Schultz*, 1996; *Johnson and Pruis*, 2003]. The global fluid flux through sediment estimated in this study has a magnitude equivalent to a few percent of the ridge flank hydrothermal flux estimated from thermal data.

To estimate global chemical fluxes through sediments, differences between hole top concentrations of SO_4^{2-}, Mg^{2+} and Ca^{2+} (measured in the upper 5 m of the holes) and corresponding seawater concentrations were determined for all holes where upward seepage was predicted. There is significant scatter in the differences between hole top and seawater concentrations, and the distribution is non-Gaussian, so the first and third quartiles are used to approximate the range of uncertainty (Table 4.5). Nevertheless, the product of these concentration differences and the estimated global seepage fluid flux suggests advective fluxes of SO_4^{2-}, Mg^{2+} and Ca^{2+} through sediments that are only a few percent of the global river input (Table 4.6). Rivers are a major source of SO_4^{2-}, Mg^{2+} and Ca^{2+} to the ocean, and because seepage of these ions through sediments is small

relative to riverine fluxes, seepage through sediments is probably only of minor importance to the respective global geochemical cycles. Diffusive fluxes of these ions across the sediment globally are at least an order of magnitude smaller than the estimated advective fluxes.

Global chemical fluxes of various species between the ocean and the crust in ridge flank settings have been previously investigated from fluid and rock chemistry [*Mottl and Wheat*, 1994; *Wheat et al.*, 2000; *Staudigel*, 2003; *Wheat and Fisher*, 2008]. Estimates of the chemical fluxes vary widely, although ridge flank hydrothermal fluxes of SO_4^{2-}, Mg^{2+} and Ca^{2+} may be of similar magnitude to riverine fluxes [*Mottl and Wheat*, 1994; *Staudigel*, 2003; *Wheat and Fisher*, 2008]. The present study is not in a position to refine estimates of total ridge flank hydrothermal chemical fluxes, except to suggest that the majority of the ridge flank SO_4^{2-}, Mg^{2+} and Ca^{2+} fluxes probably occurs through outcrops.

Table 4.5. Statistics of hole top concentrations of SO_4^{2-}, Mg^{2+} and Ca^{2+}relative to the corresponding seawater concentration for those holes in which upward seepage was predicted.

	Concentration differences between hole top* interstitial water and seawater (mM).				
	Minimum	**Maximum**	**First Quartile**	**Median**	**Third quartile**
SO_4^{2-}	-11.64	2.16	-2.34	-1.04	0.31
Mg^{2+}	-32.13	0.21	-3.2	-1.84	-1.08
Ca^{2+}	-1.41	29.06	-0.28	0.02	0.58

* Within the upper 5 m of sediment.

Table 4.6. Estimated chemical fluxes through sediments globally.

	Advective Fluxes through sediment (this study, 10^{12} mol yr^{-1}) *		
	Minimum	**Maximum**	**River flux (10^{12} mol yr^{-1}) ****
SO_4^{2-}	-0.18	0.02	3.5
Mg^{2+}	-0.24	-0.08	4.8
Ca^{2+}	-0.02	0.04	11.7

* Calculated as the product of the estimated global upward fluid flux through sediment (7.5 x 10^{10} m^3 yr^{-1}) and the first or third quartile hole top concentrations of SO_4^{2-}, Mg^{2+} and Ca^{2+} relative to the corresponding seawater concentration (Table 4.5).
** Calculated as the product of the global river fluid flux [*Palmer and Edmond*, 1989] and mean chemical concentrations of river water [*Meybeck*, 2003].

4.9. Conclusions

Models of SO_4^{2-}, Mg^{2+} and Ca^{2+} advection, diffusion and reaction in sediment interstitial waters were fit to interstitial water chemical data from sediments at 140 DSDP, ODP and IODP drill holes representing a range of crustal ages and sedimentary environments globally. It was found that the specific discharge through sediments is generally slower than 500 m $Myrs^{-1}$ (0.05 cm yr^{-1}). Assuming this compilation of seepage rates is globally representative, only a few percent of the total ridge flank fluid flux passes through sediments (the remainder must enter or leave basement through outcrops). Based on the estimated global fluid flux through sediments, and the difference between seawater and hole-top concentrations of SO_4^{2-}, Mg^{2+} and Ca^{2+}, fluxes of these ions through sediment likely only represent a few percent of global riverine inputs, and thus are only of minor importance to their respective global geochemical cycles.

5. A model of off-axis hydrothermal circulation and future research objectives

This section collects the findings of Chapters 2 – 4, along with findings from previous studies, into a unified conceptual model of off-axis hydrothermal circulation and crustal hydrology. The principal uncertainties with respect to this model are highlighted and specific studies designed to address these uncertainties are proposed for future research.

5.1. Conceptual model of off-axis hydrothermal circulation and crustal hydrology

The conceptual model of off-axis hydrothermal circulation and crustal hydrology that emerges from this dissertation is one in which >90% of the fluid passing through the crustal aquifer enters and leaves the crust through basement rocks outcropping through marine sediment. This is consistent with relatively slow seepage through marine sediments globally (Chapter 4), with estimates of sediment permeability [*Spinelli et al.*, 2004] relative to basement permeability [*Fisher*, 2005], and with other studies that have identified specific outcrops as focused ingress or egress locations [*Fisher et al.*, 2003; *Hutnak et al.*, 2008]. Models of off-axis hydrothermal circulation in which fluid travels laterally within the upper igneous crust, between outcrops separated by kilometres or tens of kilometres (outcrop-to-outcrop flow), are consistent with the global heat flow data (Chapter 2, [*Fisher and Becker*, 2000]) and with detailed hydrological studies in a small number of locations [*Fisher et al.*, 2003; *Hutnak et al.*, 2008]. This evidence supports the proposition that outcrop-to-outcrop flow is the dominant mode of hydrothermal

circulation over most of the seafloor, although local convective circulation within isolated outcrops is also possible [*Harris et al.*, 2004; *Kawada et al.*, 2011].

It is predicted in Chapter 2 that lateral driving forces will not overcome vertical buoyancy forces in the aquifer until sufficient sediment has accumulated (a few Myrs after crustal accretion on average), so local convective circulation (i.e., not between outcrops) is probably the norm in crust less than a few Myrs old. Hydrothermal circulation in young crust represents a significant proportion of the total advective heat loss. For example, the heat flow deficit (Figure 1.2) suggests that approximately 40-50% of the total hydrothermal heat flux occurs in crust younger than 4 Myrs (representing about 5% of the seafloor) [*Stein and Stein*, 1994]. This suggests that local convective circulation (i.e., not between outcrops) is a globally important process in young crust, but it is unclear whether this mode of circulation is also common within isolated outcrops in older crust.

The distribution of seafloor outcrops is principally controlled by the pelagic sediment supply rate, local post-depositional sediment transport processes (such as bottom currents and bioturbation), and basement roughness which varies with mid-ocean ridge spreading rate (Chapter 2). Crust formed at slow spreading rates is rougher than that formed at fast spreading rates [e.g., *Goff*, 1991], so if all else is equal, outcrops will be more abundant on slow spreading crust. Probabilistic modelling of sediment and outcrop distribution globally suggests that, on average, outcrops in crust a few Myrs old will be a couple kilometres apart, increasing to tens of kilometres apart over tens of Myrs (Figure 2.6).

The O-isotopic composition of secondary carbonate minerals such as calcite and aragonite recovered from the crustal aquifer have been used to estimate the crystallization temperatures of these minerals, and thus temperatures experienced by the aquifer. Chapter 3 investigated crystallization temperatures of carbonates from seven discrete drilling locations, finding that the carbonate temperatures, in some cases, constrain the amount of mixing experienced within the aquifer due to local cellular convection. At four of the drilling locations analyzed, the highest temperature carbonates are most consistent with an aquifer that was thermally poorly mixed (i.e., Nusselt numbers close to 1). At the other three locations, the estimated carbonate crystallization temperatures are sufficiently low so as to provide no constraint on the vigor of local convective mixing (i.e., in these cases carbonate data alone cannot distinguish between a thermally well mixed and a poorly mixed aquifer). Davis et al. [1997a] used a numerical model of aquifer fluid and heat transport constrained by heat flow and sediment thickness data from the eastern flank of the Juan de Fuca ridge to infer that the aquifer at that location *is* thermally well mixed (Nusselt number > 25). Together, these studies suggest that the amount of thermal mixing within the aquifer is variable by location, and is likely affected by the local permeability structure.

The most permeable zones of the oceanic crust likely coincide, in general, with pillow lavas and volcanic rubble. Numerous studies have shown that permeable zones may be laterally contiguous for multiple kilometres or tens of kilometres [e.g., *Fisher et al.*, 2003, 2008; *Becker et al.*, 2013]. Although hypotheses exist for the controls on lateral permeability and anisotropy of lateral permeability (e.g., vertical offsets of permeable zones due to initial volcanism or subsequent faulting), these controls have not

been rigorously tested and lateral permeability anisotropy has yet to be fully quantified. The degree of lateral contiguity of permeable zones within the igneous crust is probably strongly dependant on the mid-ocean ridge spreading rate at which the crust formed because spreading rate affects both volcanism and tectonics [e.g., *Macdonald*, 1982]. There may also be anisotropy between horizontal and vertical permeability. Vertical permeability must be lower than horizontal permeability in some settings to explain apparently high temperature carbonate minerals at depth in the crustal aquifer (Chapter 3). A plausible physical basis for the reduced vertical permeability is laterally contiguous flow units (having low permeability) interlayered with higher permeability pillows and rubble.

The permeability of the crustal aquifer is also predicted to decrease as the crust ages (Chapters 2 and 3), probably primarily due to loss of porosity by infilling from secondary minerals. The timescale of loss of permeability, however, is unclear, because hydrothermal mineral formation is estimated to occur mostly within 20 Myrs [*Staudigel et al.*, 1981b; *Gillis and Coogan*, 2011], changes in seismic velocities in the upper crust (a proxy for permeability) suggest most permeability is lost within 10 Myrs [*Carlson*, 1998], and models of outcrop-to-outcrop flow fit to the global heat flow data suggest permeability may continually decline (by about two orders of magnitude) over at least 65 Myrs (Chapter 2, [*Fisher and Becker*, 2000]). A conceptual model of off-axis hydrothermal circulation that may reconcile the apparent discrepancy between the timescales of hydrothermal *circulation* and crustal *alteration* is as follows: most igneous basement experiences local convective circulation during the first few Myrs after crustal accretion (on average globally) when much of the seafloor remains uncovered by

sediment. During this period the young crust experiences widespread hydrothermal alteration including the formation of secondary minerals and a corresponding loss of porosity/permeability. After this time, once a few tens of m of sediment have accumulated and there are scattered outcrops, outcrop-to-outcrop flow or circulation within isolated outcrops becomes the dominant mode of circulation (Figure 5.1). Only crust within outcrops or on the flow path between outcrops will continue to experience significant fluid flux, chemical and mineralogical alteration and loss of porosity/permeability. Circulation within or between outcrops will continue until the hydrologically active outcrops become sealed by sediment. Crust that is off the primary flow path will experience restricted fluid flux and a lesser degree of continued hydrothermal alteration. This is, for example, consistent with the greater abundance of carbonate minerals at the basement high drilled at ODP Hole 896A compared to the nearby basement low at Hole 504B [*Alt et al.*, 1996b]. The crust drilled at Hole 896A may have been a discharge outcrop for part of its history [*Teagle et al.*, 1996], and as such experienced greater fluid flux and chemical alteration than Hole 504B which was covered by sediment from a young age. This model suggests that the timescale of vigorous off-axis hydrothermal circulation is controlled by the local distributions of outcrops and basement permeability. Therefore, the degree of crustal alteration is expected to be highly variable from location to location and some discrepancy is expected when comparing the timing of alteration estimated from data with different spatial distributions, sample sizes and determined from different proxies. The crust near DSDP Sites 417 and 418 is a unique location where both the timing of hydrothermal mineral formation and the duration of hydrothermal circulation can be independently

estimated. Geochemical evidence suggests alteration minerals at this site generally formed within 10-20 Myrs of crustal accretion, [*Hart and Staudigel*, 1980; *Staudigel et al.*, 1981b; *Gillis and Coogan*, 2011]). The topographic high drilled at Hole 417A remained free of sediment for about 20 Myrs [*Donnelly et al.*, 1980a], and if this is representative of the timescale of local hydrothermal circulation, then the timing of circulation and secondary mineral formation are roughly in agreement at this location.

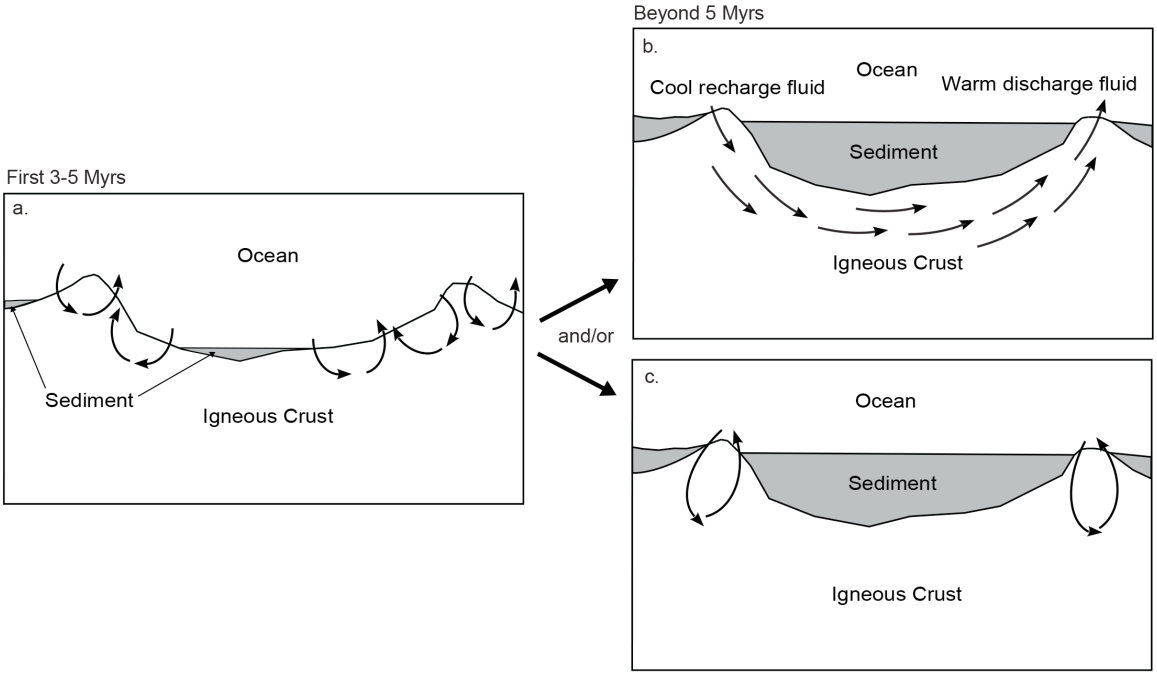

Figure 5.1. Conceptual model of off-axis hydrothermal circulation. (a) In young crust, local convective circulation is widespread through unsedimented seafloor. After a few Myrs of sedimentation, ingress and egress are restricted primarily to basement outcrops, and circulation within basement occurs either by (b) lateral flow between outcrops or by (c) local convection within isolated outcrops and the underlying basement.

5.2. Future research objectives

Future research into off-axis hydrothermal circulation and crustal hydrology should:

a. Quantify the importance of outcrop-to-outcrop flow relative to local circulation within isolated outcrops on total hydrothermal heat and fluid fluxes. Local convective circulation is probably important in crust where sediment cover is lacking (generally crust younger than a few Myrs old), but the relative importance of these modes of hydrothermal circulation is not known for older crust that represents most of the seafloor area.
b. Collect new measurements of upper crustal permeability for crustal ages in which data are presently lacking. Use these data to ground truth theoretical models of temporal changes in aquifer permeability, and to clarify the timescale of hydrothermal alteration.
c. Investigate the proportion of basement outcrops globally that are hydrologically active, and also the proportions that host fluid ingress and egress. Determine the physical properties that controls these.
d. Quantify lateral permeability anisotropy of the crustal aquifer, and identify the principal controls on this anisotropy.

The remainder of this section proposes specific studies to address the research objectives suggested above.

A modelling study should be conducted to investigate the importance of convective circulation within isolated outcrops to global hydrothermal fluxes (objective a) Because hydrothermal circulation transports and removes heat from the oceanic crust, the global database of seafloor heat flow measurements [*Hasterok et al.*, 2011] may constrain which models of off-axis circulation are globally important. Quantitative models of fluid and heat exchange within an aquifer experiencing outcrop-to-outcrop

flow have been shown to be consistent with the global heat flow data (Chapter 2), so the next step is to determine whether the alternative model of convective circulation within isolated outcrops is also consistent with global heat flow. Convective circulation within large seamounts, and the corresponding effects on seafloor heat flow have been previously modelled [*Harris et al.*, 2004]. Because convective circulation patterns are known to be sensitive to edifice shape [*Kawada et al.*, 2011], this work should be extended to include outcrops associated with smaller seamounts and also abyssal hills.

To investigate outcrop hydrology and the timescale of hydrothermal alteration (objectives b and c), co-located bathymetric and heat flow surveys should be conducted on crust representing typical abyssal settings. The most important environment parameters in selecting a study site are crustal spreading rate and sedimentation rate because both control the distribution of sediment and outcrops. Studies should target crust formed at the most common spreading rate (approximately 5-7 cm yr^{-1}, full rate) that has experienced primarily pelagic sediment supply at a rate close to the global median of 3.5 m $Myrs^{-1}$. Hydrological testing of the oceanic crust has been generally limited to crust younger than 11 Myrs old (excepting one detailed hydrologic survey on 18-24 Ma crust [*Hutnak et al.*, 2008], and one drill hole pumping test in ~160 Ma crust [*Larson et al.*, 1993]), so new hydrologic surveys should target the gaps in crustal age. Crust 12-17 Myrs old and 30-35 Myrs old would be ideal targets for new studies for two reasons. First, these ages are well within the duration of the average heat flow deficit (65 Myrs) and the crust is therefore likely to host active hydrothermal systems supporting significant fluid, heat and possibly chemical fluxes. Second, the younger of these age ranges (12-17 Myrs) is within the time frame of hydrothermal mineral formation

estimated elsewhere (20 Myrs [e.g., *Staudigel et al.*, 1981b; *Gillis and Coogan*, 2011]), and the older age range (30-35 Myrs) is beyond that time frame, so targeting both for hydrologic studies will help test the timing of hydrothermal alteration. For each selected study site, a bathymetric survey (with a resolution finer than 100 m) should be conducted over an area of comparable size to the surveys on the Juan de Fuca and Cocos plates (~20000 km^2) [*Fisher et al.*, 2003; *Hutnak et al.*, 2007]. Topographic highs in the bathymetry should be identified as possible outcrops, and be targeted for further study. Detailed conductive heat flow surveys should be conducted within a radius of a few kilometres around selected outcrops. The heat flow surveying should target outcrops of different size because outcrop size is believed to control local temperatures and thus control whether the outcrop hosts fluid ingress or egress. Suppressed or elevated heat flow (relative to predicted lithospheric heat flow) will indicate which outcrops are hydrologically active, and can be used to estimate whether fluid is recharging or discharging. A quantitative model of fluid and heat exchange in the aquifer, similar to those used by Fisher et al. [2003] and Hutnak et al. [2008], can be fit to local heat flow data to estimate permeability and fluid fluxes through the local aquifer. Comparing the new estimates of permeability in crust aged 12-17 Myrs and 30-35 Myrs to existing models of temporal changes in aquifer permeability (e.g., Figure 3.5) will provide a valuable test of these models.

Anisotropy of lateral permeability (objective d) can be investigated with a hydrologic pumping test in the oceanic crust. The test will require three oceanic drill holes separated by several kilometres and oriented in a "L" shape (on a plan view map). Because faulting is potentially an important control on lateral contiguity of the aquifer,

the distance between holes should be at least as wide as the average abyssal hill. Fluid should be pumped into a sealed interval in the upper few hundred metres of igneous crust at the middle hole, and pressure sensors should monitor changes in pressure at the other holes. The pressure records can be used to estimate the aquifer permeability in perpendicular directions following a technique similar to Fisher et al. [2008]. It would be ideal if the drill holes used for the permeability anisotropy test were located in the same area as the above-recommended bathymetry/heat flow survey.

This dissertation has shown evidence that basement outcrops play a fundamental role in off-axis hydrothermal systems. The future research recommended here will clarify the flow paths of fluid through outcrops and elsewhere in the oceanic crust, and also the timescale of hydrothermal alteration. Conclusions from this work will be paramount in selecting sites for crustal drilling, fluid sampling and other data collection needed to investigate chemical fluxes and crustal biology associated with off-axis seafloor hydrothermal circulation.

Bibliography

Alt, J. C. (2004), Alteration of the upper oceanic crust: mineralogy, chemistry, and processes, edited by E. E. Davis and H. Elderfield, pp. 495–533, Cambridge University Press, Cambridge, UK.

Alt, J. C., and J. Honnorez (1984), Alteration of the upper oceanic crust, DSDP site 417: mineralogy and chemistry, *Contributions to Mineralogy and Petrology*, *87*(2), 149–169.

Alt, J. C., and D. A. H. Teagle (2000), Hydrothermal alteration and fluid fluxes in ophiolites and oceanic crust, in *Ophiolites and Oceanic Crust: New Insights from Field Studies and the Ocean Drilling Program*, edited by Y. Dilek, E. M. Moores, D. Elthon, and A. Nicolas, pp. 273–282, Boulder, Colorado.

Alt, J. C., and D. A. H. Teagle (2003), Hydrothermal alteration of upper oceanic crust formed at a fast-spreading ridge: mineral, chemical, and isotopic evidence from ODP Site 801, *Chemical Geology*, *201*(3-4), 191–211.

Alt, J. C., K. Muehlenbachs, and J. Honnorez (1986a), An oxygen isotopic profile through the upper kilometer of the oceanic crust, DSDP Hole 504B, *Earth and Planetary Science Letters*, *80*, 217–229.

Alt, J. C., J. Honnorez, C. Laverne, and R. Emmermann (1986b), Hydrothermal alteration of a 1 km section through the upper oceanic crust, DSDP Hole 504B: The mineralogy, chemistry, and evolution of seawater-basalt interactions, *Journal of Geophysical Research*, *91*(10), 10309–10335.

Alt, J. C., C. France-Lanord, P. A. Flyod, P. Castillo, and A. Galy (1992), Low-temperature hydrothermal alteration of Jurassic oceanic crust, site 801, in *Proceedings of the Ocean Drilling Program, Scientific Results*, vol. 129, edited by Y. Larson, R. L., Lancelot.

Alt, J. C., H. Kinoshita, and L. B. Stokking (1993), *Proceedings of the Ocean Drilling Program, Initial Reports, vol. 148*, Ocean Drilling Program, College Station, TX.

Alt, J. C. et al. (1996a), Hydrothermal alteration of a section of upper oceanic crust in the eastern equatorial Pacific: A synthesis of results from site 504 (DSDP legs 69,70, and 83, and ODP legs 111, 137,140, and 148), in *Proceedings of the Ocean Drilling Program, Scientific Results*, vol. 148, edited by J. C. Alt, H. Kinoshita, L. B. Stokking, and P. J. Michael, pp. 417–434, Ocean Drilling Program, College Station, TX.

Alt, J. C., D. A. H. Teagle, C. Laverne, D. A. Vanko, W. Bach, H. Jose, K. Becker, M. Ayadi, and P. A. Pezard (1996b), Ridge flank alteration of the uppe oceanic cust in

the easten pacific: systhesis of results for volcanic rocks for holes 504B and 896A in a ridge flank convection cell, in *Proceedings of the Ocean Drilling Program, Scientific Results, Vol. 148*, edited by J. C. Alt, H. Kinoshita, L. B. Stokking, and P. J. Michael, pp. 435–450, Ocean Drilling Program, College Station, TX.

Alt, J. C., C. Laverne, R. M. Coggon, D. A. H. Teagle, N. R. Banerjee, S. Morgan, C. E. Smith-Duque, M. Harris, and L. Galli (2010), Subsurface structure of a submarine hydrothermal system in ocean crust formed at the East Pacific Rise, ODP/IODP Site 1256, *Geochemistry Geophysics Geosystems*, *11*(10), Q10010, doi:10.1029/2010GC003144.

Van Andel, T. H. (1975), Mesozoic/Cenozoic calcite compensation depth and the global distribution of calcareous sediments, *Earth and Planetary Science Letters*, *26*, 187–194.

Anderson, B. W., L. A. Coogan, and K. M. Gillis (2012), The role of outcrop-to-outcrop fluid flow in off-axis oceanic hydrothermal systems under abyssal sedimentation conditions, *Journal of Geophysical Research*, *117*(B5), B05103, doi:10.1029/2011JB009052.

Anderson, B. W., K. M. Gillis, and L. A. Coogan (2013), A hydrologic model for the uppermost oceanic crust constrained by temperature estimates from carbonate minerals, *Journal of Geophysical Research*, *118*, 3917–3930.

Anderson, R. N., M. G. Langseth, and J. G. Sclater (1977), The Mechanisms of Heat Transfer Through the Floor of the Indian Ocean, *Journal of Geophysical Research*, *82*(23), 3391–3409, doi:10.1029/JB082i023p03391.

Archer, D., M. Lyle, K. Rodgers, and P. Froelich (1993), What Controls Opal Preservation in Tropical Deep-Sea Sediments?, *Paleoceanography*, *8*(1), 7–21, doi:10.1029/92PA02803.

Baker, P. A., P. M. Stout, M. Kastner, and H. Elderfield (1991), Large-scale lateral advection of seawater through oceanic crust in the central equatorial Pacific, *Earth and Planetary Science Letters*, *105*(4), 522–533.

Barron, E. J., and J. M. Whitman (1981), Ocean sediments in space and time, in *The Oceanic Lithosphere*, edited by C. Emiliani, pp. 689–731, Wiley, New York.

Becker, K., and E. E. Davis (2003), New evidence for age variation and scale effects of permeabilities of young oceanic crust from borehole thermal and pressure measurements, *Earth and Planetary Science Letters*, *210*(3-4), 499–508.

Becker, K., and R. P. Von Herzen (1983), Heat transfer through the sediments of the mounds hydrothermal area, Galapagos Spreading Center at 86 W, *Journal of Geophysical Research*, *88*(B2), 995–1008.

Becker, K., R. H. Morig, and E. E. Davis (1994), Permeabilities in the Middle Valley Hydrothermal System Measured with Packer and Flowmeter Experiments, in *Proceedings of the Ocean Drilling Program, Scientific Results, Vol. 139*, edited by M. J. Mottl, E. E. Davis, A. T. Fisher, and J. F. Slack, pp. 613–626, Ocean Drilling Program, College Station, TX.

Becker, K., E. E. Davis, F. N. Spiess, and C. P. Demoustier (2004), Temperature and video logs from the upper oceanic crust, Holes 504B and 896A, Costa Rica Rift flank: implications for the permeability of upper oceanic crust, *Earth and Planetary Science Letters*, *222*(3-4), 881–896.

Becker, K., A. T. Fisher, and T. Tsuji (2013), New packer experiments and borehole logs in upper oceanic crust: Evidence for ridge-parallel consistency in crustal hydrogeological properties, *Geochemistry Geophysics Geosystems*, *14*(8), 2900–2915, doi:10.1002/ggge.20201.

Bejan, A. (2013), *Convection Heat Transfer*, Fourth Edi., Wiley, New York.

Bemis, E. B., H. J. Spero, J. Bijma, and D. W. Lea (1998), Reevaluation of the oxygen isotopic composition of planktonic foraminifera: Experimental results and revised paleotemperature equations, *Paleoceanography*, *13*(2), 150–160.

Berger, W. H. (1972), Deep sea carbonates: dissolution facies and age-depth constancy, *Nature*, *236*, 392–395.

Berner, R. A. (1978), Sulfate reduction and the rate of deposition of marine sediments, *Earth and Planetary Science Letters*, *37*, 492–498.

Boudreau, B. (1996), The diffusive tortuosity of fine-grained unlithified sediments, *Geochimica et Cosmochimica Acta*.

Boudreau, B., and J. Westrich (1984), The dependence of bacterial sulfate reduction on sulfate concentration in marine sediments, *Geochimica et Cosmochimica Acta*.

Boudreau, B. P. (1997), *Diagenetic models and their implementation: modelling transport and reactions in aquatic sediments*, Springer, Berlin.

Brady, P., and S. Gíslason (1997), Seafloor weathering controls on atmospheric CO 2 and global climate, *Geochimica et Cosmochimica Acta*, *61*(5), 965–973.

Breymann, M. Von, and E. Suess (1988), Magnesium in the marine sedimentary environment: Mg - NH 4 ion exchange, *Chemical geology*, *70*(4), 359–371.

Bryant, W., A. Deflache, and P. Trabant (1974), Consolidation of marine clays and carbonates, in *Deep-sea sediments: Physical and Mechanical Properties*, edited by A. L. Inderbitzen, pp. 209–244, Plenum Press, New York.

Cannat, M. (1996), How thick is the magmatic crust at slow spreading oceanic ridges?, *Journal of Geophysical Research*, *101*(B2), 2847–2857.

Carbotte, S. M., and D. S. Scheirer (2004), Variability of ocean crustal structure created along the global mid-ocean ridge, in *Hydrogeology of the Oceanic Lithosphere*, edited by E. E. Davis and H. Elderfield, pp. 59–107, Cambridge University Press, New York.

Carlson, R. L. (1998), Seismic velocities in the uppermost oceanic crust: Age dependence and the fate of layer 2 A, *Journal of Geophysical Research*, *103*, 7069–7077.

Coggon, R. M., D. A. H. Teagle, C. E. Smith-Duque, J. C. Alt, and M. J. Cooper (2010), Reconstructing past seawater Mg/Ca and Sr/Ca from mid-ocean ridge flank calcium carbonate veins, *Science*, *327*, 1114–1117.

Coogan, L. A., and K. M. Gillis (2013), Evidence that low-temperature oceanic hydrothermal systems play an important role in the silicate-carbonate weathering cycle and long-term climate regulation, *Geochemistry, Geophysics, Geosystems*, *14*(6), doi:10.1002/ggge.20113.

Davis, E., and C. Lister (1977), Heat flow measured over the Juan de Fuca Ridge: Evidence for widespread hydrothermal circulation in a highly heat transportive crust, *Journal of Geophysical Research*, *82*(30), 4845–4860.

Davis, E., K. Wang, and J. He (1997a), An unequivocal case for high Nusselt number hydrothermal convection in sediment-buried igneous oceanic crust, *Earth and Planetary Science Letters*, *146*, 137–150.

Davis, E. E., and K. Becker (2002), Observations of natural-state fluid pressures and temperatures in young oceanic crust and inferences regarding hydrothermal circulation, *Earth and Planetary Science Letters*, *204*(1-2), 231–248.

Davis, E. E., and K. Becker (2004), Observations of temperature and pressure: constraints on ocean crustal hydrologic state, properties, and flow, in *Hydrogeology of the Oceanic Lithosphere*, edited by E. E. Davis and H. Elderfield, pp. 225–271, Cambridge University Press, Cambridge.

Davis, E. E., and H. Elderfield (Eds.) (2004), *Hydrogeology of the Oceanic Lithosphere*, Cambridge, UK.

Davis, E. E., and C. Lister (1974), Fundamentals of Ridge Crest Topography, *Earth and Planetary Science Letters*, *21*, 405–413.

Davis, E. E., A. T. Fisher, and et al. Firth, J.V. (1997b), *Proc. ODP, Init. Repts., 168*, Ocean Drilling Program, College Station, TX.

Davis, E. E., D. S. Chapman, K. Wang, H. Villinger, A. T. Fisher, S. W. Robinson, J. Grigel, D. Pribnow, J. Stein, and K. Becker (1999), Regional heat flow variations across the sedimented Juan de Fuca Ridge eastern flank: Constraints on lithospheric, *Journal of Geophysical Research*, *104*(B8), 17675–17688.

Davis, E. E., K. Wang, K. Becker, and R. E. Thomson (2000), Formation-scale hydraulic and mechanical properties of oceanic crust inferred from pore pressure response to periodic seafloor loading, *Journal of Geophysical Research*, *105*(B6), 13423–13435.

Davis, E. E., K. Wang, R. E. Thomson, K. Becker, and J. F. Cassidy (2001), An episode of seafloor spreading and associated plate deformation inferred from crustal fluid pressure transients, *Journal of Geophysical Research*, *106*(B10), 21953–21.

Davis, E. E., K. Becker, and J. He (2004), Costa Rica Rift revisited: constraints on shallow and deep hydrothermal circulation in young oceanic crust, *Earth and Planetary Science Letters*, *222*(3-4), 863–879.

DeLaughter, J., S. Stein, and C. a. Stein (1999), Extraction of a lithospheric cooling signal from oceanwide geoid data, *Earth and Planetary Science Letters*, *174*(1-2), 173–181, doi:10.1016/S0012-821X(99)00247-2.

Dezileau, L., G. Bareille, J. L. Reyss, and F. Lemoine (2000), Evidence for strong sediment redistribution by bottom currents along the southeast Indian ridge, *Deep Sea Research I*, *47*, 1899–1936.

Divins, D. L. (2011), NGDC Total Sediment Thickness of the World's Oceans & Marginal Seas,

Doin, M. P., and L. Fleitout (1996), Thermal evolution of the oceanic lithosphere: an alternative view, *Earth and Planetary Science Letters*, *142*(1-2), 121–136, doi:10.1016/0012-821X(96)00082-9.

Donnelly, T. W., J. Francheteau, W. Bryan, P. Robinson, M. Flower, and M. Salisbury (1980a), *Initial Reports of the Deep Sea Drilling Project, 51,52,53*, US Government Printing Office, Washington, DC.

Donnelly, T. W., G. Thompson, and M. H. Salisbury (1980b), The chemistry of altered basalts at site 417, Deep Sea Drilling Project Leg 51, in *Initial Reports of the Deep Sea Drilling Project*, vol. 51/52/53, pp. 1319–1330, U.S. Government Printing Office, Washington, D.C.

Elderfield, H., and A. Schultz (1996), Mid-ocean ridge hydrothermal fluxes and the chemical composition of the ocean, *Annual Review of Earth and Planetary Sciences*, *24*, 191–224.

Elderfield, H. F., C. G. Wheat, M. J. Mottl, C. Monnin, and B. Spiro (1999), Fluid and geochemical transport through oceanic crust: a transect across the eastern flank of the Juan de Fuca Ridge, *Earth and planetary science letters*, *172*(1-2), 151–165.

Emerson, S., and J. Hedges (1988), Processes controlling the organic carbon content of open ocean sediments, *Paleoceanography*, *3*(5), 621–634.

Fantle, M., and D. DePaolo (2006), Sr isotopes and pore fluid chemistry in carbonate sediment of the Ontong Java Plateau: Calcite recrystallization rates and evidence for a rapid rise in seawater Mg, *Geochimica et cosmochimica acta*.

Fisher, A. T. (1998), Permeability within basaltic oceanic crust, *Reviews of Geophysics*, *36*(2), 143–182.

Fisher, A. T. (2005), Marine hydrogeology: recent accomplishments and future opportunities, *Hydrogeology Journal*, *13*(1), 69–97.

Fisher, A. T., and K. Becker (1995), Correlation between seafloor heat flow and basement relief: Observational and numerical examples and implications for upper crustal permeability, *Journal of Geophysical Research*, *100*, 12641–12657.

Fisher, A. T., and K. Becker (2000), Channelized fluid flow in oceanic crust reconciles heat-flow and permeability data, *Nature*, *403*, 71–74.

Fisher, A. T., and R. P. Von Herzen (2005), Models of hydrothermal circulation within 106 Ma seafloor: Constraints on the vigor of fluid circulation and crustal properties, below the Madeira Abyssal Plain, *Geochemistry, Geophysics, Geosystems*, *6*(11), doi:10.1029/2005GC001013.

Fisher, A. T., and C. G. Wheat (2010), Seamounts as conduits for massive fluid, heat, and solute fluxes on ridge flanks, *Oceanography*, *23*(1), 74–87.

Fisher, A. T., K. Becker, I. T. N. Narasimhan, M. G. Langseth, and M. J. Mottl (1990), Passive, off-axis convection through the southern flank of the Costa Rica Rift, *Journal of Geophysical Research*, *95*(B6), 9343–9370.

Fisher, A. T., K. Becker, and T. N. Narasimhan (1994), Off-axis hydrothermal circulation: Parametric tests of a refined model of processes at Deep Sea Drilling Project/Ocean Drilling Program site 504, *Journal of Geophysical Research*, *99*(B2), 3097–3121.

Fisher, A. T., E. E. Davis, M. Hutnak, V. Spiess, L. Zühlsdorff, A. Cherkaoui, L. Christiansen, K. Edwards, R. Macdonald, and H. Villinger (2003), Hydrothermal recharge and discharge across 50 km guided by seamounts on a young ridge flank, *Nature*, *421*(6923), 618–621.

Fisher, A. T., E. E. Davis, and K. Becker (2008), Borehole-to-borehole hydrologic response across 2.4 km in the upper oceanic crust: Implications for crustal-scale properties, *Journal of Geophysical Research*, *113*(B7), B07106, doi:10.1029/2007JB005447.

Fränti, P., O. Virmajoki, and V. Hautamäki (2006), Fast Agglomerative Clustering Using a-Nearest Neighbor Graph, *IEEE transactions on pattern analysis and machine intelligence*, 1875–1881.

Friedrichsen, H., and S. Hoernes (1980), Oxygen and hydrogen isotope exchange reactions between sea water and oceanic basalts from legs 51 through 53, in *Initial Reports of the Deep Sea Drilling Project*, vol. 51/52/53, edited by T. W. Donnelly, J. Francheteau, and U. Bleil, pp. 1177–1182, Ocean Drilling Program, College Station, TX.

Furnes, H., and H. Staudigel (1999), Biological mediation in ocean crust alteration: how deep is the deep biosphere?, *Earth and Planetary Science Letters*, *166*(3-4), 97–103, doi:10.1016/S0012-821X(99)00005-9.

Giambalvo, E. R. G., C. I. Steefel, A. T. Fisher, N. D. Rosenberg, and C. G. Wheat (2002), Effect of fluid – sediment reaction on hydrothermal fluxes of major elements , eastern flank of the Juan de Fuca Ridge, *Geochimica et Cosmochimica Acta*, *66*(10), 1739–1757.

Gieskes, J. M. (1974), Interstitial Water Studies, Leg 25, in *Init. Rept. DSDP, 25*, pp. 361–394, US Government Printing Office, Washington, D.C.

Gieskes, J. M. (1976), Interstitial Water Studies, Leg 33, in *Init. Rept. DSDP, 33*, pp. 563–570.

Gieskes, J. M. (1986), Interstitial Water Studies, Leg 92, in *Init. Repts. DSDP, 9*, pp. 423–429, US Government Printing Office, Washington, D.C.

Gieskes, J. M., and J. R. Lawrence (1981), Alteration of volcanic matter in deep sea sediments: evidence from the chemical composition of interstitial waters from deep sea drilling cores, *Geochimica et Cosmochimica Acta*, *45*(10), 1687–1703.

Gillis, K., and P. Robinson (1988), Distribution of alteration zones in the upper oceanic crust, *Geology*, *16*, 262–266.

Gillis, K. M., and L. A. Coogan (2011), Secular variation in carbon uptake into the ocean crust, *Earth and Planetary Science Letters*, *302*(3-4), 385–392.

Gillis, K. M., and P. T. Robinson (1990), Patterns and Processes of Alteration in the Lavas and Dykes of the Troodos Ophiolite, Cyprus, *Journal of Geophysical Research*, *95*(B13), 21523–21548.

Goff, J. A. (1991), A global and regional stochastic analysis of near-ridge abyssal hill morphology, *Journal of Geophysical Research*, *96*(B13), 21713–21737.

Goff, J. A., and T. H. Jordan (1988), Stochastic modeling of seafloor morphology: Inversion of sea beam data for second-order statistics, *Journal of Geophysical Research*, *93*(B11), 13589–13608.

Goff, J. A., A. Malinverno, D. J. Fornari, and J. R. Cochran (1993), Abyssal hill segmentation: Quantitative analysis of the East Pacific Rise flanks 7 S–9 S, *Journal of Geophysical Research*, *98*(B8), 13851–13862.

Goff, J. A., B. E. Tucholke, J. Lin, G. E. Jaroslow, and M. C. Kleinrock (1995), Quantitative analysis of abyssal hills in the Atlantic Ocean: A correlation between inferred crustal thickness and extensional faulting, *Journal of Geophysical Research*, *100*(B11), 22509–22522.

Goff, J. A., Y. Ma, A. Shah, J. R. Cochran, and J. C. Sempéré (1997), Stochastic analysis of seafloor morphology on the flank of the Southeast Indian Ridge: The influence of ridge morphology on the formation of abyssal hills, *Journal of Geophysical Research*, *102*(B7), 15521–15534.

Grossman, E. L., and T. L. Ku (1986), Oxygen and carbon isotope fractionation in biogenic aragonite: temperature effects, *Chemical Geology: Isotope Geoscience Section*, *59*, 59–74.

Hamilton, E. (1976), Variations of density and porosity with depth in deep-sea sediments, *Journal of Sedimentary Research*, *46*(2), 280–300.

Harris, R. N., A. T. Fisher, and D. S. Chapman (2004), Fluid flow through seamounts and implications for global mass fluxes, *Geology*, *32*(8), 725–728.

Hart, S. R., and H. Staudigel (1980), Ocean crust-sea water interaction: Sites 417 and 418, in *Init. Rept. DSDP*, edited by T. Donnelly et al., pp. 1169–1176, U.S. Government Printing Office, Washington, DC.

Hasterok, D., D. Chapman, and E. Davis (2011), Oceanic heat flow: Implications for global heat loss, *Earth and Planetary Science Letters*, *311*, 386–395.

Henstock, T. J., A. W. Woods, and R. S. White (1993), The accretion of oceanic crust by episodic sill intrusion, *Journal of Geophysical Research*, *98*(B3), 4143, doi:10.1029/92JB02661.

Hillier, J. K., and A. B. Watts (2007), Global distribution of seamounts from ship-track bathymetry data, *Geophysical Research Letters*, *34*(13), L13304, doi:doi:10.1029/2007GL029874.

Hoernes, S., and H. Friedrichsen (1978), 18O/16O and D/H Investigations on Basalts Of Leg 46, in *Initial Reports of the Deep Sea Drilling Project*, vol. 46, edited by L. Dmitriev and J. Heirtzler, pp. 253–255, U.S. Government Priniting Office, Washington.

Honnorez, J., C. Laverne, H. Hubberten, R. Emmerman, and K. Muehlenbachs (1983), Alteration processes in layer 2 basalts from Deep Sea Drilling Project Hole 504B, Costa Rica Rift, in *Initial Rep., Deep Sea Drill. Proj. 691*, pp. 509–546, US Government Printing Office, Washington, D.C.

Huber, B. T., R. D. Norris, and K. G. MacLeod (2002), Deep-sea paleotemperature record of extreme warmth during the Cretaceous, *Geology*, *30*(2), 123–126.

Huber, J., and H. Johnson (2006), Microbial life in ridge flank crustal fluids, *Environmental Microbiology*, *8*(1), 88–99.

Hutnak, M., A. T. Fisher, L. Zühlsdorff, V. Spiess, P. H. Stauffer, and C. W. Gable (2006), Hydrothermal recharge and discharge guided by basement outcrops on 0.7–3.6 Ma seafloor east of the Juan de Fuca Ridge: observations and numerical models, *Geochemistry Geophysics Geosystems*.

Hutnak, M. et al. (2007), The thermal state of 18–24 Ma upper lithosphere subducting below the Nicoya Peninsula, northern Costa Rica margin, edited by T. Dixon and C. Moore, pp. 86–122, Columbia Univ. Press, New York.

Hutnak, M., A. T. Fisher, R. Harris, C. Stein, K. Wang, G. Spinelli, M. Schindler, H. Villinger, and E. Silver (2008), Large heat and fluid fluxes driven through mid-plate outcrops on ocean crust, *Nature Geoscience*, *1*(9), 611–614.

Ildefonse, B., D. K. Blackman, B. E. John, Y. Ohara, D. J. Miller, and C. J. MacLeod (2007), Oceanic core complexes and crustal accretion at slow-spreading ridges, *Geology*, *35*(7), 623, doi:10.1130/G23531A.1.

Jarrard, R. (2003), Subduction fluxes of water, carbon dioxide, chlorine, and potassium, *Geochemistry, Geophysics, Geosystems*, *4*(5), doi:10.1029/2002GC000392.

Johnson, H. P., and M. J. Pruis (2003), Fluxes of fluid and heat from the oceanic crustal reservoir, *Earth and Planetary Science Letters*, *216*(4), 565–574.

Jordan, T. H., H. W. Menard, and D. K. Smith (1983), Density and size distribution of seamounts in the eastern Pacific inferred from wide-beam sounding data, *Journal of Geophysical Research*, *88*(B12), 10508–10518.

Karson, J. A. (2002), Geologic Structure of the Uppermost Oceanic Crust Created At Fast- to Intermediate-Rate Spreading Centers, *Annual Review of Earth and Planetary Sciences*, *30*(1), 347–384, doi:10.1146/annurev.earth.30.091201.141132.

Kawada, Y., N. Seama, and T. Urabe (2011), The role of seamounts in the transport of heat and fluids: Relations among seamount size, circulation patterns, and crustal heat flow, *Earth and Planetary Science Letters*, *306*, 55–65.

Keir, R. (1980), The dissolution kinetics of biogenic calcium carbonates in seawater, *Geochimica et Cosmochimica Acta*, *44*, 241–252.

Kim, S. T., and J. R. O'Neil (1997), Equilibrium and nonequilibrium oxygen isotope effects in synthetic carbonates, *Geochimica et Cosmochimica Acta*, *61*(16), 3461–3475.

Kleinrock, M. C., and B. A. Brooks (1994), Construction and destruction of volcanic knobs at the Cocos-Nazca Spreading System near 95° W, *Geophysical Research Letters*, *21*(21), 2307–2310.

Lancelot, Y., and R. L. Larson (1990), *Proc. ODP, Init. Repts., 129*, Ocean Drilling Program, College Station, TX.

Langseth, M. G., and B. M. Herman (1981), Heat transfer in the oceanic crust of the Brazil Basin, *Journal of Geophysical Research*, *86*(B11), 10805–10819.

Langseth, M. G., X. Le Pichon, and M. Ewing (1966), Crustal Structure of the Mid-Ocean Ridges, *Journal of Geophysical Research*, *71*(22), 5321–5355.

Langseth, M. G., R. D. Hyndman, K. Becker, S. H. Hickman, and M. H. Salisbury (1984), The Hydrogeological Regime of Isolated Sediment Ponds in Mid-Oceanic Ridges, in *Initial Reports of the Deep Sea Drilling Project*, vol. 78B, pp. 825–837.

Langseth, M. G., M. J. Mottl, M. A. Hobart, and A. Fisher (1988), The distribution of geothermal and geochemical gradients near site 501/504: Implications for hydrothermal circulation in the oceanic crust, in *Proceedings of the Ocean Drilling Program, Initial Reports (Part A), Volume 111*, vol. 111, edited by H. Becker, K., Sakai, pp. 23–32, Ocean Drilling Program.

Langseth, M. G., K. Becker, R. P. Von Herzen, and P. Schultheiss (1992), Heat and fluid flux through sediment on the western flank of the Mid-Atlantic Ridge: A hydrogeological study of North Pond, *Geophysical Research Letters*, *19*(5), 517–520.

Larson, R. L., A. T. Fisher, R. D. Jarrard, K. Becker, and Ocean Drilling Program Leg 144 Shipboard Scientific Party (1993), Highly permeable and layered Jurassic oceanic crust in the western Pacific, *Earth and Planetary Science Letters*, *119*, 71–83.

Lasaga, A. C. (1998), *Kinetic Theory in the Earth Sciences*, Princeton University Press, Princeton, NJ.

Li, Y., and S. Gregory (1974), Diffusion of ions in sea water and in deep-sea sediments, *Geochimica et cosmochimica acta*, *38*(5), 703–714.

Lister, C. R. B. (1972), On the Thermal Balance of a Mid-Ocean Ridge, *Geophysical Journal of the Royal Astronomical Society*, *26*(5), 515–535.

Lucazeau, F., A. Bonneville, and J. Escartin (2006), Heat flow variations on a slowly accreting ridge: Constraints on the hydrothermal and conductive cooling for the Lucky Strike segment (Mid-Atlantic Ridge, 37° N), *Geochemistry Geophysics Geosystems*, *7*(7), doi:10.1029/2005GC001178.

Macdonald, K. (1982), Mid-ocean ridges: Fine scale tectonic, volcanic and hydrothermal processes within the plate boundary zone, *Annual Review of Earth and Planetary Sciences*, *10*, 155–190.

Macdonald, K. C., K. Becker, F. N. Speiss, and R. D. Ballard (1980), Hydrothermal heat flux of the "black smoker" vents on the East Pacific Rise, *Earth and Planetary …*.

Magde, L. S., and D. K. Smith (1995), Seamount volcanism at the Reykjanes Ridge: Relationship to the Iceland hot spot, *Journal of Geophysical Research*, *100*(B5), 8449–8468.

Maris, C. R. ., M. L. Bender, P. N. Froelich, R. Barnes, and N. A. Luedtke (1984), Chemical evidence for advection of hydrothermal solutions in the sediments of the Galapagos Mounds Hydrothermal Field, *Geochimica et Cosmochimica Acta*, *48*(11), 2331–2346.

Marks, N. S. (1981), Sedimentation on new ocean crust: the Mid-Atlantic Ridge at 37 N, *Marine Geology*, *43*, 65–82.

Matter, A., R. G. Douglas, and K. Perch-Nielsen (1975), Fossil preservation, geochemistry, and diagenesis of pelagic carbonates from Shatsky Rise, Northwest Pacific, in *Init. Rept. DSDP, 32*, pp. 891–921, U.S. Government Printing Office, Washington, D.C.

McDuff, R. E., and J. M. Gieskes (1976), Calcium and magnesium profiles in DSDP interstitial waters: Diffusion or reaction?, *Earth and Planetary Science Letters*, *33*(1), 1–10.

McKenzie, D. (1967), Some Remarks on Heat Flow and Gravity Anomalies, *Journal of Geophysical Research*, *72*(24), 6261–6273, doi:10.1029/JZ072i024p06261.

Meybeck, M. (2003), Global Occurange of Major Elements in Rivers, in *Treatise on Geochemistry*, edited by H. D. Holland and K. K. Turekian, pp. 207–223, Elsevier Pergamon, San Diego, CA.

Millero, F. J. (1974), Seawater as a multicomponent electrolyte solution, in *The Sea, Ideas and Observations*, vol. 5, edited by M. N. Hill, pp. 3–80, Wiley, New York.

Millero, F. J. (2014), Physico-Chemical Controls on Seawater, in *Treatise on Geochemistry*, vol. 8, edited by H. Holland and K. Turekian, pp. 1–18, Elsevier, Amsterdam.

Mitchell, N. C. (1995), Diffusion transport model for pelagic sediments on the Mid-Atlantic Ridge, *Journal of Geophysical Research*, *100*(B10), 19991–20009.

Mitchell, N. C. (1996), Creep in pelagic sediments and potential for morphologic dating of marine fault scarps, *Geophysical Research Letters*, *23*(5), 483–486.

Mitchell, N. C. (1998), Sediment accumulation rates from Deep Tow profiler records and DSDP Leg 70 cores over the Galapagos Spreading Centre, *Geological Society, London, Special Publications*, *131*, 199–209.

Moores, E., and F. Vine (1971), The Troodos Massif, Cyprus and other ophiolites as oceanic crust: evaluation and implications, *Philosophical Transactions of the Royal Society of London*, *264*, 443–467.

Moreno, L., and C. F. Tsang (1994), Flow channeling in strongly heterogeneous porous media: A numerical study, *Water resources research*, *30*(5), 1421–1430.

Morse, J. (1978), Dissolution kinetics of calcium carbonate in sea water: VI. The near-equilibrium dissolution kinetics of calcium carbonate-rich deep sea sediments, *Am. J. Sci.*, *278*, 344–353.

Mottl, M. (1989), Hydrothermal convection, reaction and diffusion in sediments on the Costa Rica rift flank: Pore-water evidence from ODP sites 677 and 678., in *Proceedings of the Ocean Drilling Program, Scientific Results, Volume 111*, vol. 111, edited by H. Becker, K., Sakai, pp. 195–213, Ocean Drilling Program.

Mottl, M. J. (2003), Partitioning of energy and mass fluxes between mid-ocean ridge axes and flanks at high and low temperature, in *Energy and Mass Transfer in Marine Hydrothermal Systems*, edited by P. E. Halbach, V. Tunnicliffe, and J. R. Hein, pp. 271–286, Dahlem University Press, Berlin.

Mottl, M. J., and C. G. Wheat (1994), Hydrothermal circulation through mid-ocean ridge flanks: Fluxes of heat and magnesium, *Geochimica et Cosmochimica Acta*, *58*(10), 2225–2237.

Muehlenbachs, K. (1980), The alteration and aging of the basaltic layer of the sea floor: Oxygen isotope evidence from DSDP/IPOD Legs 51. 52 and 53, in *Initial Reports of the Deep Sea Drilling Project*, vol. 51/52/53, edited by T. Donnelly, pp. 1159–1166, U.S. Government Priniting Office, Washington, DC.

Muehlenbachs, K., and R. N. Clayton (1972), Oxygen isotope studies of fresh and weathered submarine basalts, *Canadian Journal of Earth Sciences*, *9*(2), 172–184.

Müller, P., and E. Suess (1979), Productivity, sedimentation rate, and sedimentary organic matter in the oceans—I. Organic carbon preservation, *Deep Sea Research*, *26A*, 1347–1362.

Muller, R. D., M. Sdrolias, C. Gaina, and W. R. Roest (2008), Age, spreading rates, and spreading asymmetry of the world's ocean crust, *Geochemistry Geophysics Geosystems*, *9*(4), doi:10.1029/2007GC001743.

Neumann, G. A., and D. W. Forsyth (1995), High resolution statistical estimation of seafloor morphology: Oblique and orthogonal fabric on the flanks of the Mid-Atlantic Ridge, 34° 35.5° S, *Marine Geophysical Research*, *17*, 221–250.

Noel, M. (1985), Heat flow, sediment faulting and porewater advection in the Madeira Abyssal Plain, *Earth and planetary science letters*, *73*, 398–406.

O'Neil, J. R., R. N. Clayton, and T. K. Mayeda (1969), Oxygen isotope fractionation in divalent metal carbonates, *The Journal of Chemical Physics*, *51*, 5547–5558.

Palmer, M., and J. Edmond (1989), The strontium isotope budget of the modern ocean, *Earth and Planetary Science Letters*, *92*, 11–26.

Parsons, B., and J. Sclater (1977), An analysis of the variation of ocean floor bathymetry and heat flow with age, *Journal of Geophysical Research*, *82*(5), 803–827.

Peterson, C., R. Duncan, and K. F. Scheidegger (1986), Sequence ang Longevity of Basalt Alteration at Deep Sea Drilling Project Site 597, in *Initial Reports of the Deep Sea Drilling Project Vol. 92*, edited by M. Leinen and D. K. Rea, pp. 505–515, US Government Printing Office, Washington, D.C.

Phipps Morgan, J., and Y. J. Chen (1993), Magma Injection , Hydrothermal Circulation , and Crustal Flow, *Journal of Geophysical Research*, *98*(B4), 6283–6297.

Pribnow, D. F. C., M. Kinoshita, and C. A. Stein (2000), *Thermal Data Collection and Heat Flow Recalculations for ODP Legs 101-180*, Hannover, Germany.

Pringle, M. S. (1992), Radiometric ages of basaltic basement recovered at sites 800, 801, and 802, Leg 129, Western Pacific Ocean, in *Proceedings of the Ocean Drilling Program, Scientific Results*, vol. 129, edited by R. L. Larson and Y. Lancelot, pp. 389–404.

Quick, J. E., and R. P. Denlinger (1993), Ductile deformation and the origin of layered gabbro in ophiolites, *Journal of Geophysical Research*, *98*(B8), 14015–14027.

Rea, D. (1994), The paleoclimatic record provided by eolian deposition in the deep sea: The geologic history of wind, *Reviews of Geophysics*, *32*, 159–195.

Rea, D. K., N. G. Pisias, and T. Newberry (1991), Late Pleistocene Paleoclimatology of the Central Equatorial Pacific: Flux Patterns of Biogenic Sediments, *Paleoceanography*, *6*(2), 227–244.

Reid, I., and H. Jackson (1981), Oceanic spreading rate and crustal thickness, *Marine Geophysical Researches*, *5*, 165–172.

Richter, F., and D. DePaolo (1987), Numerical models for diagenesis and the Neogene Sr isotopic evolution of seawater from DSDP Site 590B, *Earth and Planetary Science Letters*.

Richter, F., and D. DePaolo (1988), Diagenesis and Sr isotopic evolution of seawater using data from DSDP 590B and 575, *Earth and Planetary Science Letters*.

Rosenberg, N. D., A. T. Fisher, and J. S. Stein (2000), Large-scale lateral heat and fluid transport in the seafloor: revisiting the well-mixed aquifer model, *Earth and Planetary Science Letters*, *182*(1), 93–101.

Rudnicki, M. D., H. Elderfield, and M. J. Mottl (2001), Pore fluid advection and reaction in sediments of the eastern flank, Juan de Fuca Ridge, 48 N, *Earth and Planetary Science Letters*, *187*(1-2), 173–189.

Sayles, F., and F. Manheim (1975), Interstitial solutions and diagenesis in deeply buried marine sediments: results from the Deep Sea Drilling Project, *Geochimica et cosmochimica acta*, *39*, 103–127.

Scheirer, D. S., K. C. Macdonald, D. W. Forsyth, and Y. Shen (1996), Abundant seamounts of the Rano Rahi seamount field near the Southern East Pacific Rise, 15° S to 19° S, *Marine Geophysical Research*, *18*, 13–52.

Sclater, J. G., and J. Francbeteau (1970), The Implications of Terrestrial Heat Flow Observations on Current Tectonic and Geochemical Models of the Crust and Upper Mantle of the Earth, *Geophysical Journal of the Royal Astronomical Society*, *20*, 509–542.

Sclater, J. G., R. P. Von Herzen, D. L. Williams, R. N. Anderson, and K. Klitgord (1974), The Galapagos Spreading Centre: Heat-flow low on the North Flank, *Geophysical Journal International*, *38*(3), 609–626.

Sclater, J. G., C. Jaupart, and D. Galson (1980), The heat flow through oceanic and continental crust and the heat loss of the Earth, *Reviews of Geophysics*, *18*(1), 269–311.

Sleep, N. H. (1974), Segregation of Magma from a Mostly Crystalline Mush, *Geological Society of America Bulletin*, *85*(8), 249–275, doi:10.1130/0016-7606(1974)85<1225.

Smith, D. K., and J. R. Cann (1990), Hundreds of small volcanoes on the median valley floor of the Mid-Atlantic Ridge at 24–30 N, *Nature*, *348*, 152–155.

Smith, D. K., and T. H. Jordan (1988), Seamount statistics in the Pacific Ocean, *Journal of Geophysical Research*, *93*(B4), 2899–2918.

Smith, W. H. ., and D. T. Sandwell (1997), Global sea floor topography from satellite altimetry and ship depth soundings, *Science*, *277*(5334), 1956.

Snelgrove, S., and C. Forster (1996), Impact of seafloor sediment permability and thickness on off-axis hydrothermal circulation: Juan de Fuca Ridge eastern flank, *Journal of geophysical research*, *101*(B2), 2915–2925.

Spinelli, G. A., E. R. Giambalvo, and A. T. Fisher (2004), Sediment permeability, distribution, and influence on fluxes in oceanic basement, in *Hydrogeology of the Oceanic Lithosphere*, edited by E. E. Davis and H. Elderfield, pp. 151–188, Cambridge Univ. Press, New York.

Staudigel, H. (2003), Hydrothermal alteration processes in the oceanic crust, *Treatise on geochemistry*, *3*, 511–535.

Staudigel, H., and S. R. Hart (1985), Dating of Oceanic Crust Hydrothermal Alteration: Strontium Isotope Ratios From Hole 504B Carbonates and a Reinterpretation of Sr Isotope Data From Deep Sea Drilling Project Sites 105, 332, 417, AND 418, in *Initial Reports of the Deep Sea Drilling Project*, vol. 83, edited by R. N. Anderson, J. Honnorez, and K. Becker, pp. 297–303, US Gov. Printing Office, Washington, DC.

Staudigel, H., K. Muehlenbachs, S. H. Richardson, and S. R. Hart (1981a), Agents of low temperature ocean crust alteration, *Contributions to Mineralogy and Petrology*, *77*(2), 150–157.

Staudigel, H., S. R. Hart, and S. H. Richardson (1981b), Alteration of the oceanic crust: processes and timing, *Earth and Planetary Science Letters*, *52*(2), 311–327.

Stein, C. A., and S. Stein (1992), A model for the global variation in oceanic depth and heat flow with lithospheric age, *Nature*, *359*(6391), 123–129.

Stein, C. A., and S. Stein (1994), Constraints on hydrothermal heat flux through the oceanic lithosphere from global heat flow, *Journal of Geophysical Research*, *99*(B2), 3081–3095.

Stein, J. S., and A. T. Fisher (2003), Observations and models of lateral hydrothermal circulation on a young ridge flank: numerical evaluation of thermal and chemical constraints, *Geochemistry Geophysics Geosystems*, *4*(3), 1026, doi:doi:10.1029/2002GC000415.

Straus, J., and G. Schubert (1977), Thermal convection of water in a porous medium: Effects of temperature□and pressure□dependent thermodynamic and transport properties, *Journal of geophysical research*, *82*(2), 325–333.

Swift, S. A., G. M. Kent, R. S. Detrick, J. A. Collins, and R. A. Stephen (1998), Oceanic basement structure, sediment thickness, and heat flow near Hole 504B, *Journal of Geophysical Research*, *103*(B7), 15377–15391.

Teagle, D. A. H., J. C. Alt, W. Bach, A. N. Halliday, and J. Erzinger (1996), Alteration of upper ocean crust in a ridge-flank hydrothermal upflow zone: mineral, chemical, and isotopic constraints from Hole 896A, in *Proceedings of the Ocean Drilling Program, Scientific Results*, vol. 148, edited by J. C. Alt, H. Kinoshita, L. B. Stokking, and P. J. Michael, pp. 119–150, Ocean Drilling Program, College Station, TX.

Todd, D. K. (1959), *Ground Water Hydrology*, Wiley, New York.

Toth, D., and A. Lerman (1977), Organic matter reactivity and sedimentation rates in the ocean, *American Journal of Science*, *277*, 465–485.

Tucholke, B., and V. Fry (1985), Basement structure and sediment distribution in Northwest Atlantic Ocean, *Am. Assoc. Pet. Geol., Bull.;(United States)*, *69*, 2077–2097.

Veizer, J. et al. (1999), 87Sr/86Sr, δ13C and δ18O evolution of Phanerozoic seawater, *Chemical Geology*, *161*(1-3), 59–88.

Von Herzen, R. P. (2004), Geothermal evidence for continuing hydrothermal circulation in older (>60 M.y.) ocean crust, in *Hydrogeology of the Oceanic Lithosphere*, edited by E. E. Davis and H. Elderfield, pp. 414–449, Cambridge University Press, Cambridge.

Von Herzen, R. P., and S. Uyeda (1963), Heat flow through the eastern Pacific Ocean floor, *Journal of Geophysical Research*, *68*(14), 4219–4250.

Wang, K. (2004), Applying fundamental principles and mathematical models to understand processes and estimate parameters, in *Hydrogeology of the Oceanic Lithosphere*, edited by H. Davis, E.E., Elderfield, pp. 376–413, Cambridge University Press.

Wang, K., J. He, and E. E. Davis (1997), Influence of basement topography on hydrothermal circulation in sediment-buried igneous oceanic crust, *Earth and Planetary Science Letters*, *146*(1-2), 151–164.

Webb, H. F., and T. H. Jordan (1993), Quantifying the distribution and transport of pelagic sediments on young abyssal hills, *Geophysical Research Letters*, *20*(20), 2203–2206.

Webb, H. F., and T. H. Jordan (2001a), Pelagic sedimentation on rough seafloor topography 1. Forward Model, *Journal of Geophysical Research*, *106*(B12), 30433–30449.

Webb, H. F., and T. H. Jordan (2001b), Pelagic sedimentation on rough seafloor topography 2. Inversion results from the North Atlantic Acoustic Reverberation Corridor, *Journal of Geophysical Research*, *106*(B12), 30451–30473.

Wessel, P. (2001), Global distribution of seamounts inferred from gridded Geosat/ERS-1 altimetry, *Journal of Geophysical Research*, *106*(B9), 19431–19441.

Wessel, P., and S. Lyons (1997), Distribution of large Pacific seamounts from Geosat/ERS-1: Implications for the history of intraplate volcanism, *Journal of Geophysical Research*, *277*, 802–805.

Wheat, C., and R. McDuff (1994), Hydrothermal flow through the Mariana Mounds: Dissolution of amorphous silica and degradation of organic matter on a mid-ocean ridge flank, *Geochimica et cosmochimica acta*, *58*(11), 2461–2475.

Wheat, C. G., and A. T. Fisher (2008), Massive, low-temperature hydrothermal flow from a basaltic outcrop on 23 Ma seafloor of the Cocos Plate: Chemical constraints and implications, *Geochemistry, Geophysics, Geosystems*, *9*, Q12O14, doi:10.1029/2008GC002136.

Wheat, C. G., and R. E. McDuff (1995), Mapping the fluid flow of the Mariana Mounds ridge flank hydrothermal system: Pore water chemical tracers, *Journal of Geophysical Research*, *100*(B5), 8115–8131.

Wheat, C. G., and M. J. Mottl (1994), Hydrothermal circulation, Juan de Fuca Ridge eastern flank: Factors controlling basement water composition, *Journal of geophysical research*, *99*(B2), 3067–3080.

Wheat, C. G., H. Elderfield, M. J. Mottl, and C. Monnin (2000), Chemical composition of basement fluids within an oceanic ridge flank: Implications for along-strike and across-strike hydrothermal circulation, *Journal of Geophysical Research*, *105*(B6), 13437–13447, doi:10.1029/2000JB900070.

Wheatcroft, R. A., P. A. Jumars, C. R. Smith, and A. R. M. Nowell (1990), A mechanistic view of the particulate biodiffusion coefficient: step lengths, rest periods and transport directions, *Journal of Marine Research*, *48*, 177–207.

Williams, D. L., and R. P. Von Herzen (1974), The Galapagos Spreading Centre: Lithospheric Cooling and Hydrothermal Circulation, *Geophysical Journal of the Royal Astronomical Society*, *38*, 587–608.

Zachos, J., M. Pagani, L. Sloan, E. Thomas, and K. Billups (2001), Trends, rhythms, and aberrations in global climate 65 Ma to present, *Science*, *292*(5517), 686–693.

Zachos, J. C., G. R. Dickens, and R. E. Zeebe (2008), An early Cenozoic perspective on greenhouse warming and carbon-cycle dynamics., *Nature*, *451*(7176), 279–283, doi:10.1038/nature06588.

Appendices

Appendix A – Derivation of pressure equation

This section provides a derivation of the pressure field equation used in the two dimensional well mixed aquifer model (Eq. 2.17). One form of Thiem's equation is [*Todd*, 1959]:

$$h(r) = h_B + (h_0 - h_B)\frac{\ln\left(\frac{r}{r_e}\right)}{\ln\left(\frac{r_0}{r_e}\right)} \qquad \text{(A1)}$$

where $h(r)$ is the hydraulic head at radius r from the recharge or discharge site, h_0 is the hydraulic head at the recharge or discharge site, which is assumed to have radius r_0, and r_e is the radius of pressure influence of the recharge or discharge site, beyond which head has a background value of h_B, and is unaffected by ingress or egress. Assuming that the elevation and velocity components of hydraulic head are negligible, hydraulic head is related to pressure (P) by:

$$h = \frac{P}{\rho g} \qquad \text{(A2)}$$

With this relationship, Theim's equation (A1) can be expressed in terms of pressure. Assuming h_B=0, the pressure field contributed by a given cluster of outcrops (relative to the background pressure) is:

$$P(r) = P_0 \frac{\ln\left(\frac{r}{r_e}\right)}{\ln\left(\frac{r_0}{r_e}\right)} \qquad \text{(A3)}$$

where P_0 is the pressure relative to background at r_0. A positive P_0 implies recharge and a negative value implies discharge. The parameter P_0 is defined from the following equations. The pressure relative to the seafloor at recharge sites is:

$$P_R = \rho_R g\left(h_a + h_s\right) \qquad \text{(A4)}$$

and at discharge sites is:

$$P_D = \rho_D g\left(h_a + h_s\right) \qquad \text{(A5)}$$

and the background pressure is:

$$P_B = \frac{P_R + P_D}{2} \qquad \text{(A6)}$$

The subscripts *R*, *D,* and *B* indicate "recharge", "discharge", and "background" respectively. It is assumed that ρ_R is the density of 0°C recharge fluid, and ρ_D is the density of fluid that has equilibrated in temperature with the aquifer rocks. The value of P_0 at recharge sites is:

$$P_0 = P_R - P_B \qquad \text{(A7a)}$$

and at discharge sites is:

$$P_0 = P_D - P_B \qquad \text{(A7b)}$$

The value of r_e is not well known, but the pressure field is not sensitive to this parameter, so a value of r_e=2b is assumed. To use this model, recharge and discharge sites must be approximated as circular features (in plan view). This geometry is not characteristic of some abyssal hill outcrops predicted by the sedimentation model, but it is a fair assumption for others and for outcrops resulting from seamounts. Outcrops are predicted in a variety of shapes and sizes, but fluid flux is unlikely to be uniform across the surface of any given outcrop, so it is assumed that the radius of recharge and discharge sites (r_0)

is half the numerical model's grid cell resolution (75 m). Equation A3 can be expressed in Cartesian coordinates by substituting:

$$r = \sqrt{(x - x_1)^2 + (y - y_1)^2} \qquad \text{(A8)}$$

where (x_1,y_1) is the Cartesian coordinate of the recharge or discharge site, giving:

$$P(x,y) = P_0 \frac{\ln\left(\frac{\sqrt{(x-x_1)^2+(y-y_1)^2}}{r_e}\right)}{\ln\left(\frac{r_0}{r_e}\right)} \qquad \text{(A9 and Eq. 2.17 in the main text)}$$

Appendix B – Example synthetic bathymetry

The figure below is a representative example of: (a) synthetic basement bathymetry corresponding to crust formed at a fast spreading rate, including a distribution of seamounts, (b) sediment thickness overlying the basement and outcrop distribution after 40 Myrs of sedimentation where the sediment supply rate (F) is 3.5 m/Myrs and the diffusion coefficient is 0.1 m^2/yr, and (c) the aquifer pressure distribution (relative to background) for an aquifer thickness (h_a) of 300 m. The pressure distribution assumes that all outcrops have been grouped into clusters using a cluster distance (d_c) of 5 km. The largest 50% of the clusters are assumed to be recharge, and the smallest 50% are assumed to be discharge. Each recharge cluster is assigned a positive pressure field, and each discharge cluster is assigned a negative pressure field as described in Section 2.2.4.3 of the main text. Under the conditions represented in this example, outcrops are generally more widely spaced than the cluster distance, so relatively few outcrops are grouped into clusters. Thus, any apparent grouping of recharge and discharge zones is unrelated to the cluster distance -- it is due only to the spatial distribution of large outcrops and small outcrops.

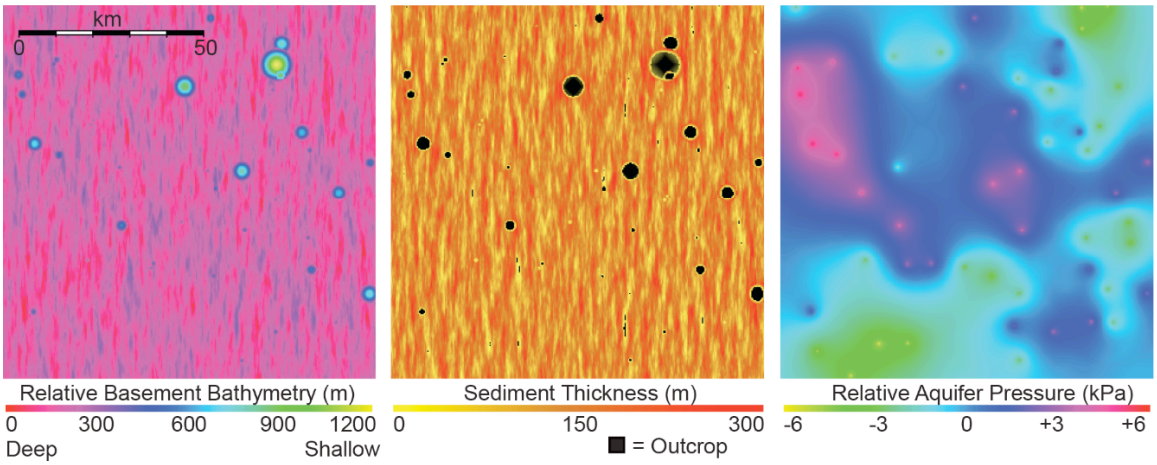

Appendix C – Model results for Chapter 3

This section show estimated formation temperatures relative to bottom seawater (delta T) of carbonate minerals (orange lines) compared to maximum temperatures achievable along the lateral flow path in a well mixed aquifer (solid black line) and an unmixed aquifer (dashed line). Because the timing of carbonate formation is unknown, each orange line represents estimates of the formation temperature for one carbonate sample depending on when it formed. Possible formation temperatures for each sample are estimated with Eq. 3.6 from $\delta^{18}O_{crustal\_carbonate}$ (Figure 3.1), and $\delta^{18}O_{benthic\_carbonate}$ [*Zachos et al.*, 2001, 2008]. For a given carbonate sample to be consistent with modelled aquifer temperatures, its orange line must lie below the model temperature curve at any point in time. Parameters used for the aquifer models are listed in Appendix J, Supplementary Table S3.1.

DSDP/ODP Hole 504B

Crustal Age: 6.9 Myrs

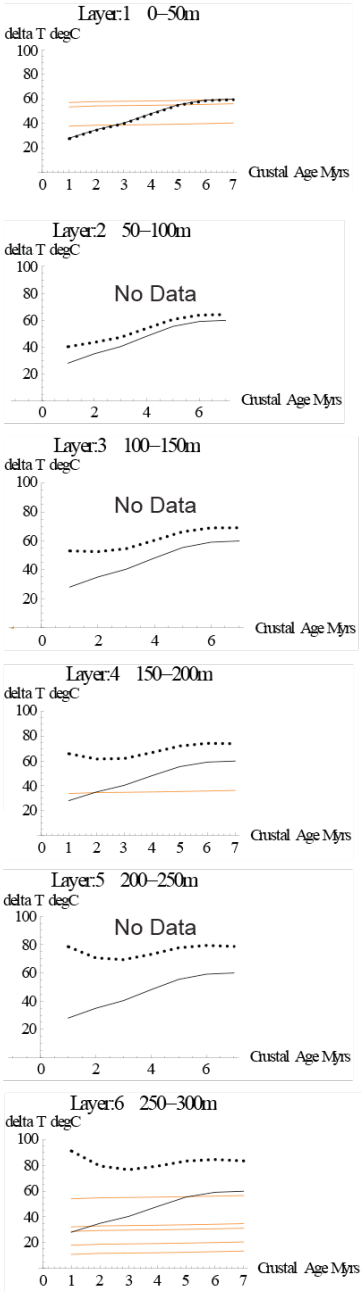

Carbonate

Best UMA ($Nu = 1$, $h_a = 300$ m, log $k = -10$) fits 100% of the carbonate samples

Best WMA ($Nu \to \infty$, $h_a = 300$ m, log $k = -10$) fits 100% of the carbonate samples

* models with lower log k fit equally well

ODP Hole 896A

Crustal Age: 6.9 Myrs

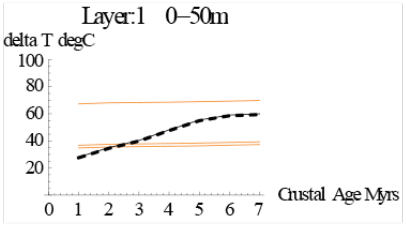

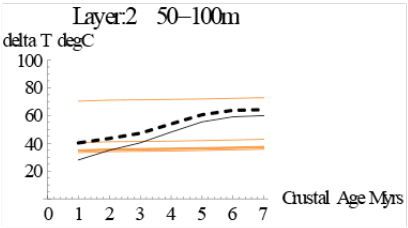

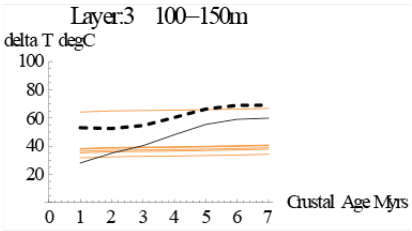

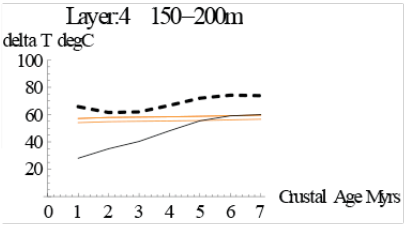

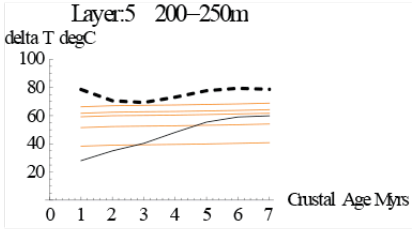

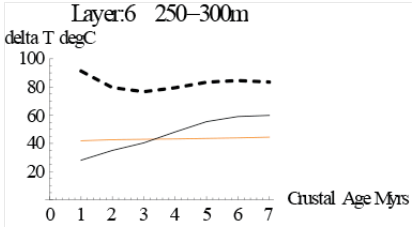

Carbonate

Best UMA ($Nu = 1$, $h_a = 300$ m, log $k = -10$) fits 92% of the carbonate samples

Best WMA ($Nu \to \infty$, $h_a = 300$ m log $k = -10$) fits 76% of the carbonate samples

* models with lower log k fit equally well

ODP Hole 1256D

Crustal Age: 15 Myrs

Carbonate

Best UMA ($Nu = 1$, $h_a = 400$ m, log $k = -11$) fits 100% of the carbonate samples

Best WMA ($Nu \to \infty$, $h_a = 400$ m, log $k = -11$) fits 26% of the carbonate samples

* models with lower log k fit equally well.

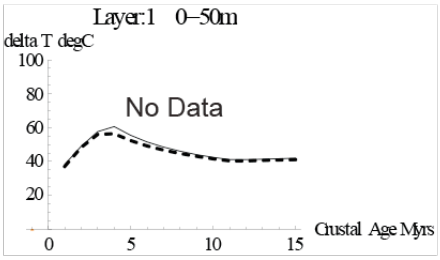

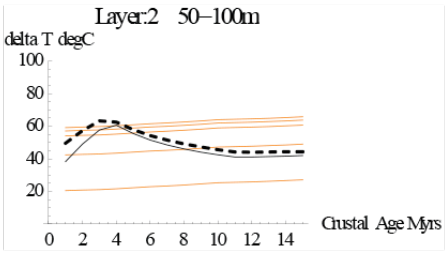

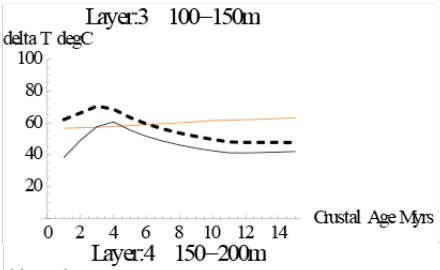

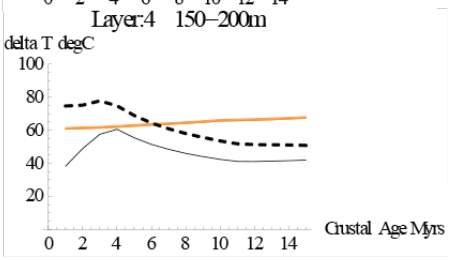

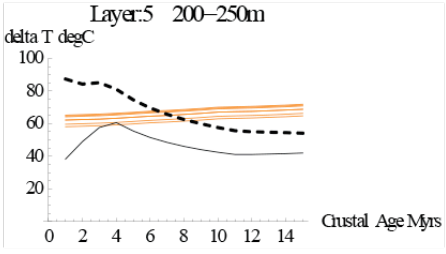

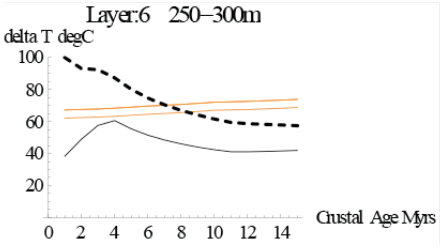

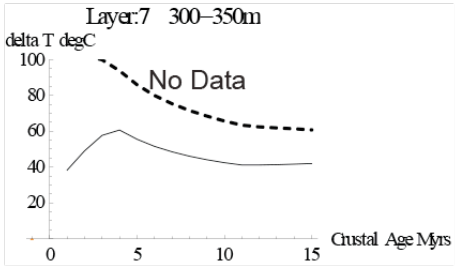

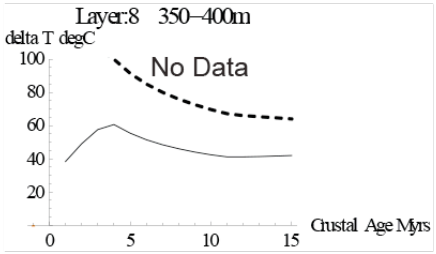

DSDP Hole 556

Crustal Age: 31 Myrs

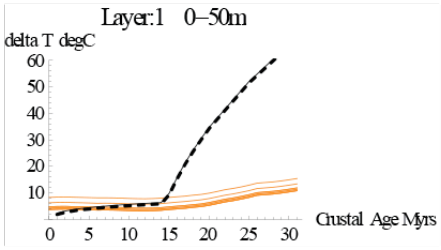

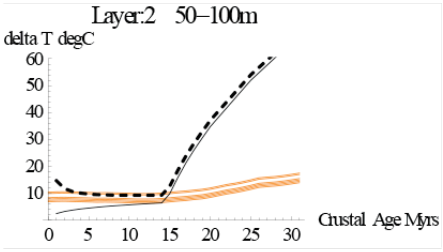

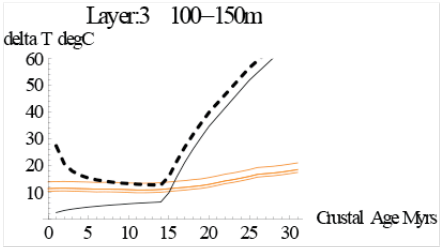

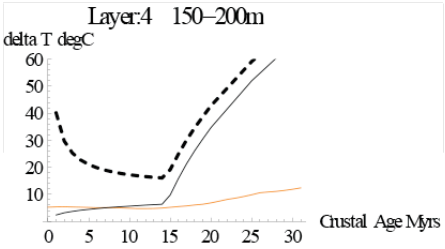

Carbonate

UMA (*Nu* = 1, h_a = 200 m, log *k* = -9.5) fits 100% of the carbonate samples

WMA (*Nu* -> ∞, h_a = 200 m, log *k* = -10) fits 100% of the carbonate samples

* models with lower log *k*, or higher h_a and lower log *k* fit equally well.

ODP Hole 1224F

Crustal Age: 45 Myrs

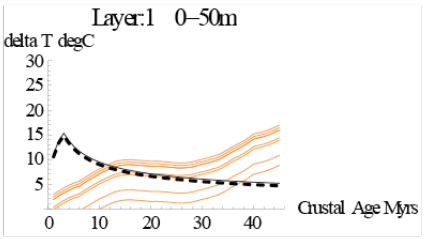

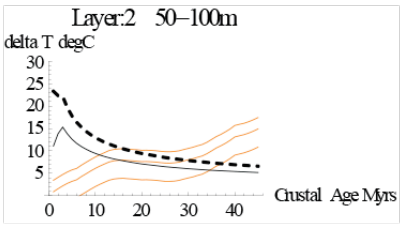

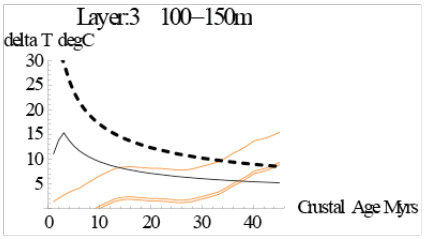

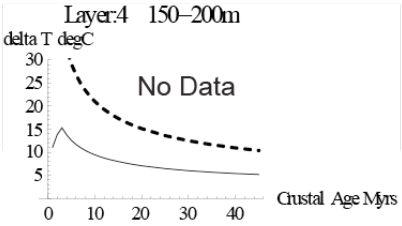

Carbonate

Best UMA ($Nu = 1$, $h_a = 200$ m, log $k = -9$) fits 100% of the carbonate samples

Best WMA ($Nu \to \infty$, $h_a = 200$ m, log $k = -9$) fits 100% of the carbonate samples

* models with lower log k, or higher ha and lower log k fit equally well.

DSDP Hole 417A

Crustal Age: 120 Myrs

Carbonate

Best UMA ($Nu = 1$, $h_a = 400$ m, log $k = -11$) fits 100% of the carbonate samples

Best WMA ($Nu \to \infty$, $h_a = 400$ m, log $k = -10$) fits 86% of the carbonate samples

* models with lower log k, or higher h_a and lower log k fit equally well

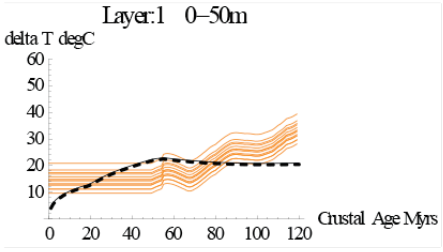

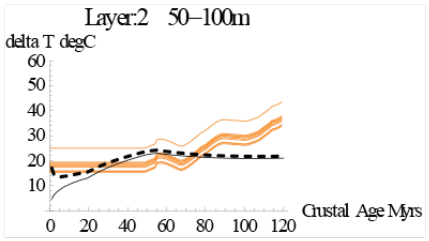

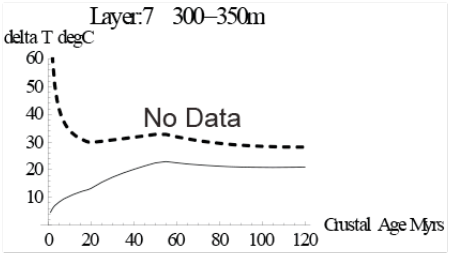

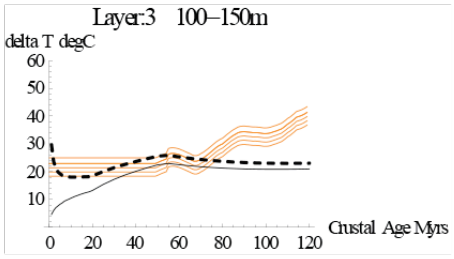

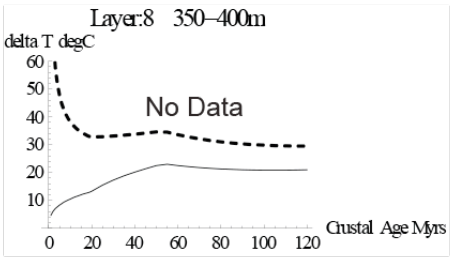

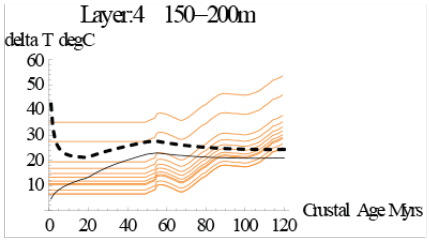

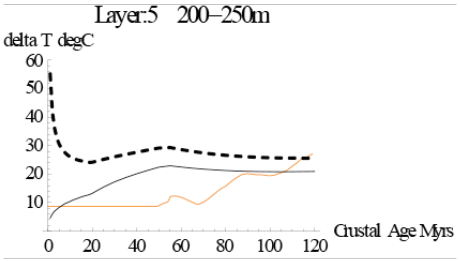

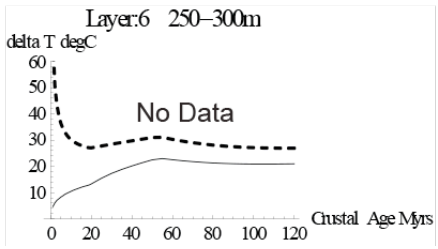

DSDP Hole 417D

Crustal Age: 120 Myrs

Carbonate

Best UMA ($Nu = 1$, $h_a = 400$ m, $\log k = -11$) fits 88% of the carbonate samples

Best WMA ($Nu \to \infty$, $h_a = 400$ m, $\log k = -9.5$) fits 73% of the carbonate samples

* models with lower $\log k$, or higher h_a and lower $\log k$ fit equally well

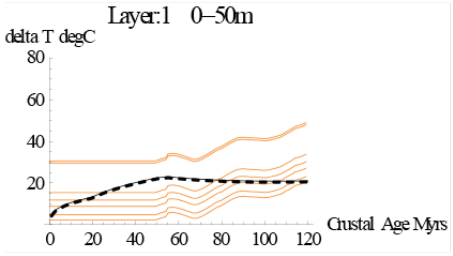

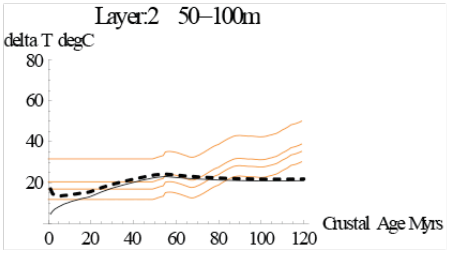

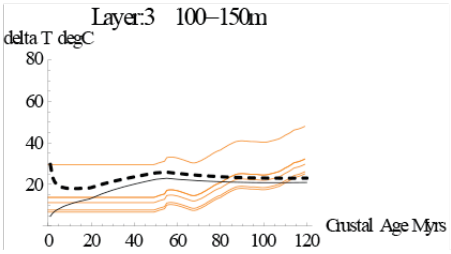

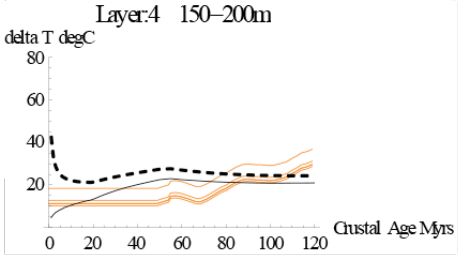

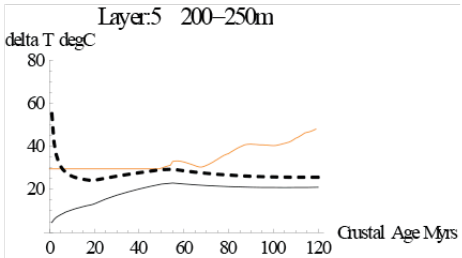

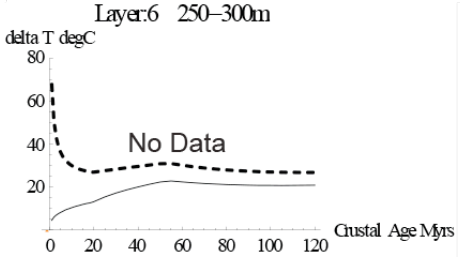

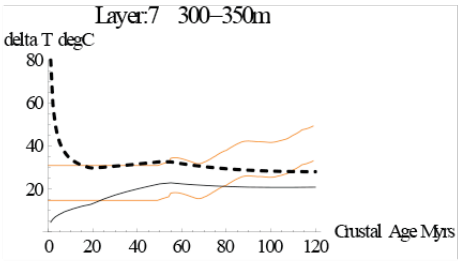

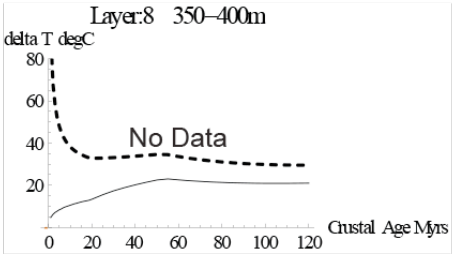

DSDP Hole 418A

Crustal Age: 120 Myrs

Carbonate

Best UMA ($Nu = 1$, $h_a = 400$ m, log $k = -11$) fits 100% of the carbonate samples

Best WMA ($Nu \to \infty$, $h_a = 400$ m, log $k = -9$) fits 42% of the carbonate samples

* models with lower log k, or higher h_a and lower log k fit equally well.

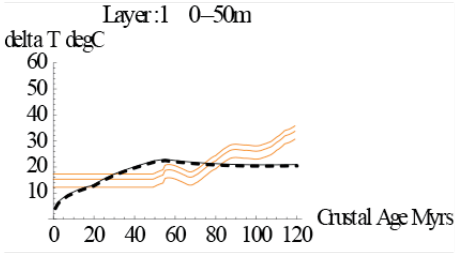

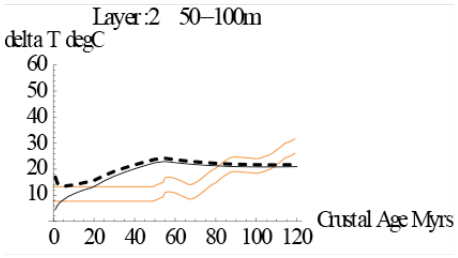

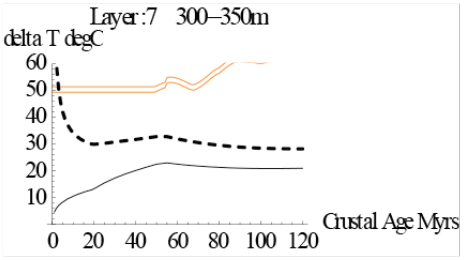

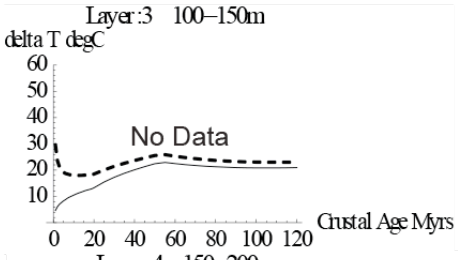

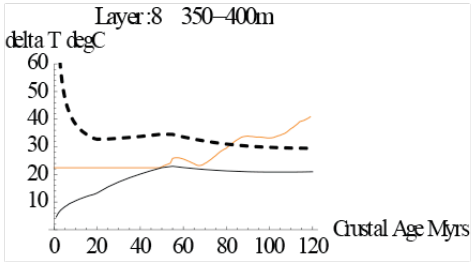

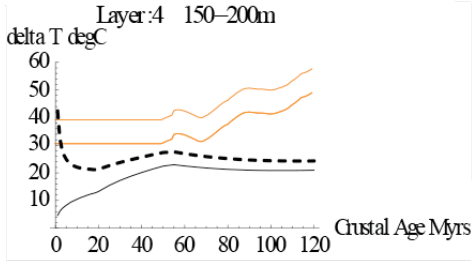

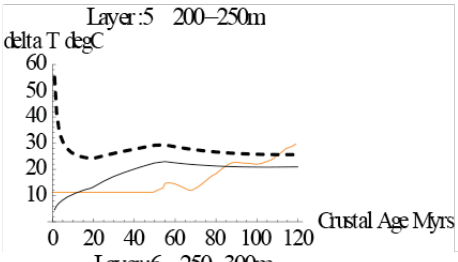

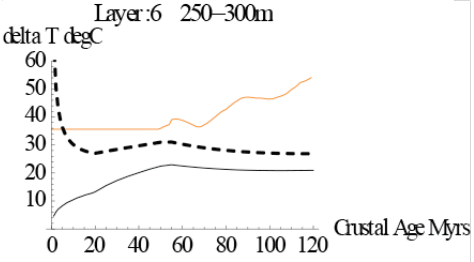

ODP Hole 1149D

Crustal Age: 132 Myrs

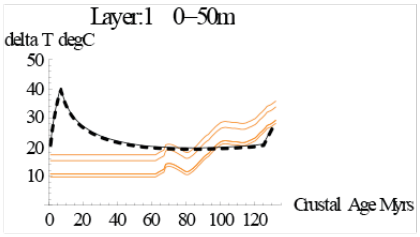

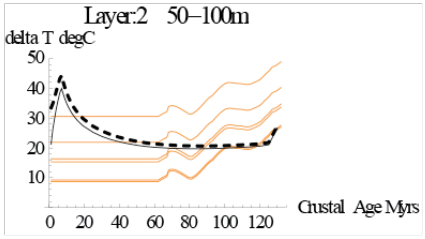

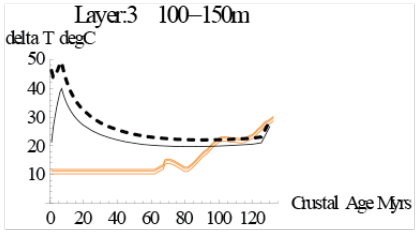

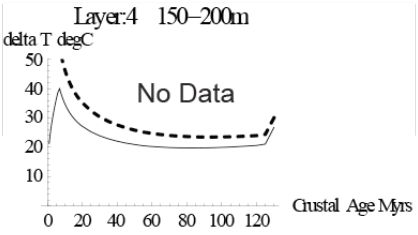

Carbonate

Best UMA ($Nu = 1$, $h_a = 200$ m, $\log k = -10$) fits 100% of the carbonate samples

Best WMA ($Nu \to \infty$, $h_a = 200$ m, $\log k = -10$) fits 100% of the carbonate samples

* models with lower $\log k$, or larger h_a and lower $\log k$ fit equally well

ODP Hole 801C

Crustal Age: 168 Myrs

Carbonate

Best UMA ($Nu = 1$, $h_a = 500$ m, log $k = -11.5$) fits 94% of the carbonate samples

Best WMA ($Nu \to \infty$, $h_a = 500$ m, log $k = -10$) fits 49% of the carbonate samples

* models with lower log k, or higher h_a and lower log k fit equally well.

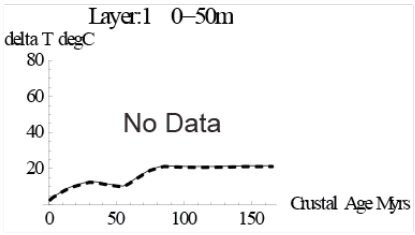

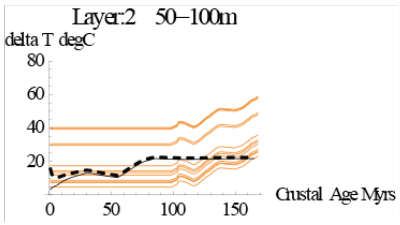

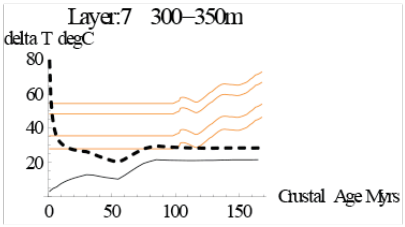

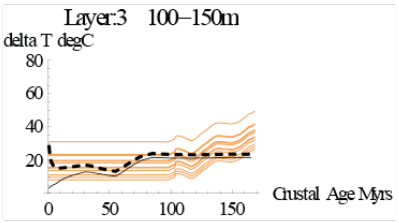

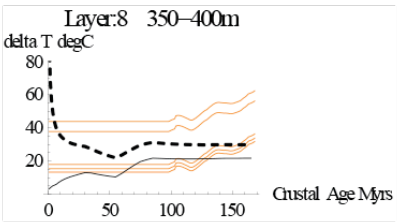

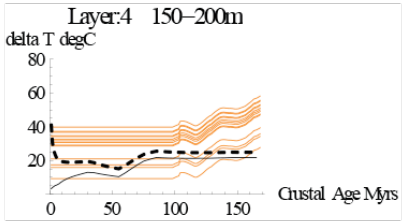

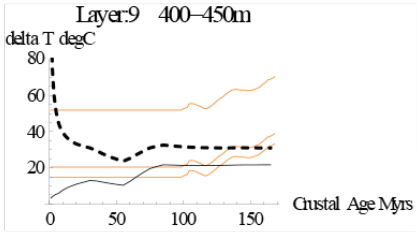

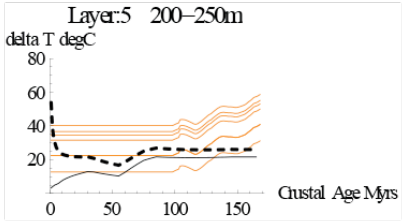

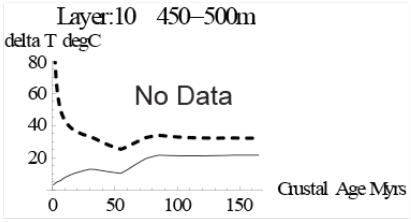

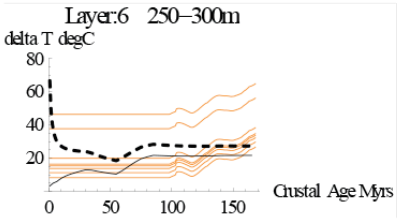

Appendix D – Finite difference equation for chemical transport and reaction in sediment interstitial water

The solution to Eq. 4.5 for the concentration (C) of a given ion at the j^{th} cell depth and the next time increment (n+1) is:

$$C_j^{n+1} = \frac{1}{D_c\Delta t + \Delta z^2}\begin{pmatrix} -2C_j^{n-1}D_c\Delta t + 2C_{j+1}^{n}D_c\Delta t + 2C_{j-1}^{n}D_c\Delta t + \\ C_j^{n-1}\Delta z^2 + 2\Delta t\Delta z^2 R - C_{j+1}^{n}\Delta t\Delta z v_v + C_{j-1}^{n}\Delta t\Delta z v_v \end{pmatrix}$$

Appendix E – Model Results for Chapter 4

This section shows graphs of measured and best-fitting model interstitial water concentrations for SO_4^{2-}, Mg^{2+} and Ca^{2+}. For holes in which only a lower bound seepage rate is constrained, the model parameterization corresponding to the lower bound seepage is plotted. Holes in which the seepage rate is not constrained (i.e., those in which the measured concentrations profiles are vertical) are not shown.

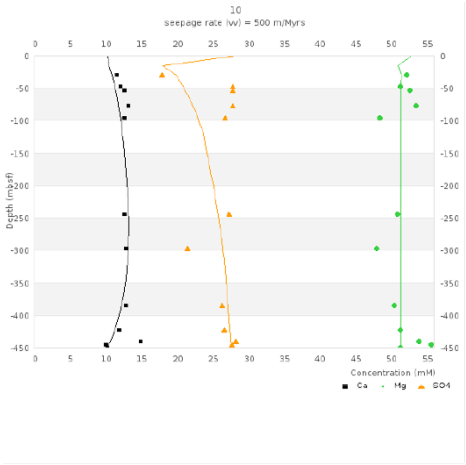
10
seepage rate (vv) = 500 m/Myrs
Depth (mbsf)
Concentration (mM)
Ca
Mg
SO4

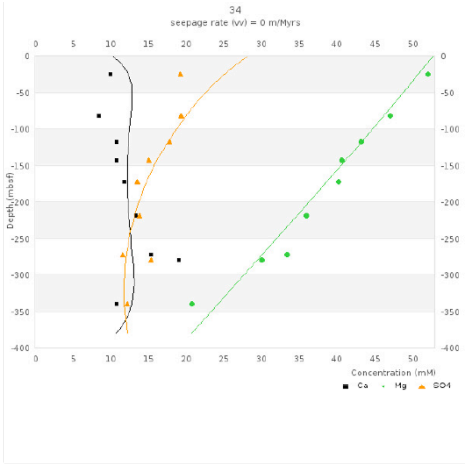
34
seepage rate (vv) = 0 m/Myrs
Depth (mbsf)
Concentration (mM)
Ca
Mg
SO4

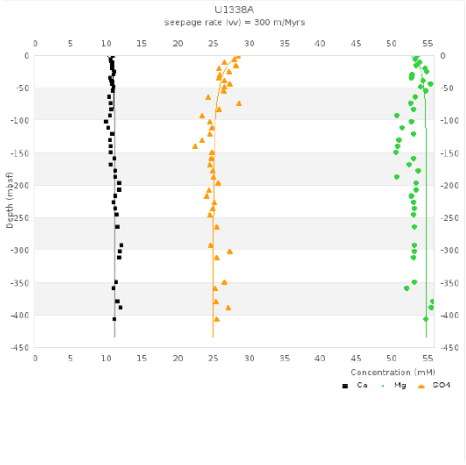
U1338A
seepage rate (vv) = 300 m/Myrs
Depth (mbsf)
Concentration (mM)
Ca
Mg
SO4

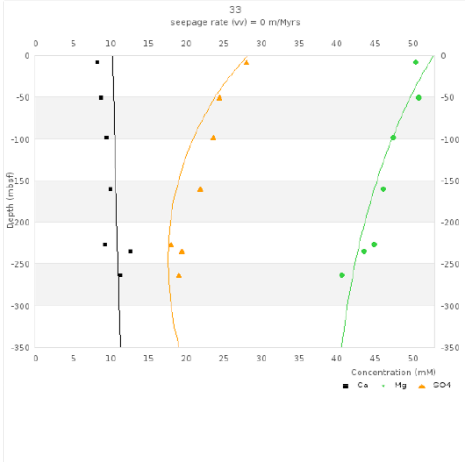
33
seepage rate (vv) = 0 m/Myrs
Depth (mbsf)
Concentration (mM)
Ca
Mg
SO4

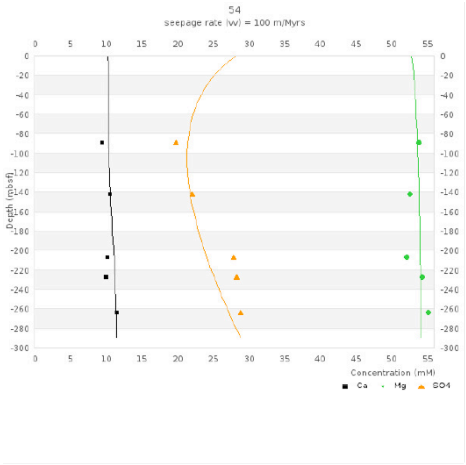
54
seepage rate (vv) = 100 m/Myrs
Depth (mbsf)
Concentration (mM)
Ca
Mg
SO4

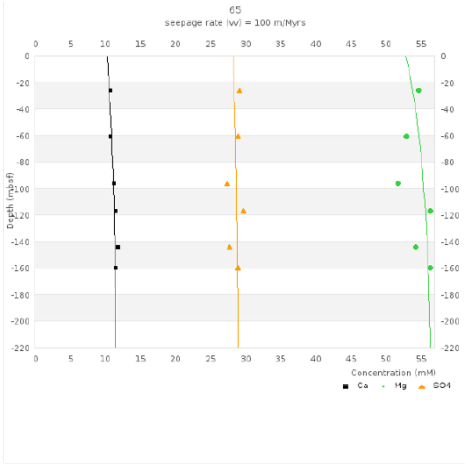
65
seepage rate (vv) = 100 m/Myrs
Depth (mbsf)
Concentration (mM)
Ca
Mg
SO4

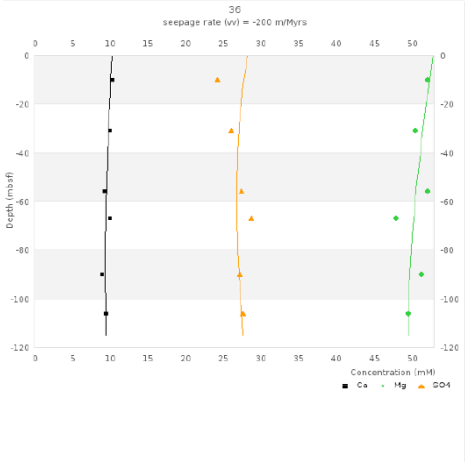
36
seepage rate (vv) = -200 m/Myrs
Depth (mbsf)
Concentration (mM)
Ca
Mg
SO4

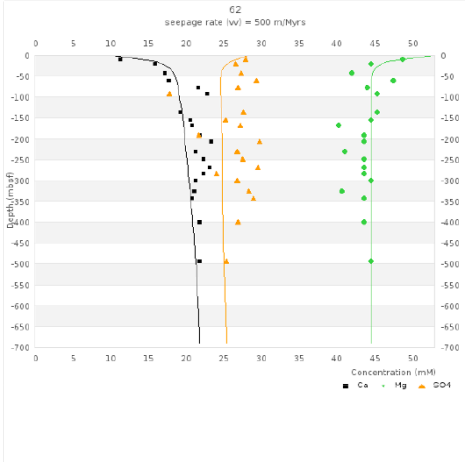
62
seepage rate (vv) = 500 m/Myrs
Depth (mbsf)
Concentration (mM)
Ca
Mg
SO4

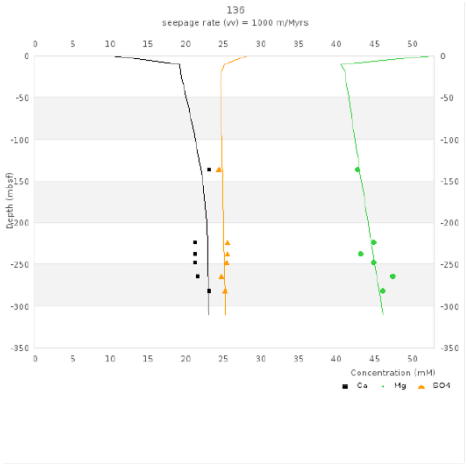
136
seepage rate (vv) = 1000 m/Myrs
Depth (mbsf)
Concentration (mM)
Ca
Mg
SO4

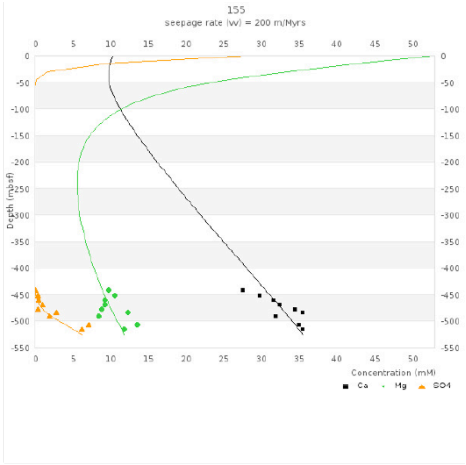
155
seepage rate (vv) = 200 m/Myrs
Depth (mbsf)
Concentration (mM)
Ca
Mg
SO4

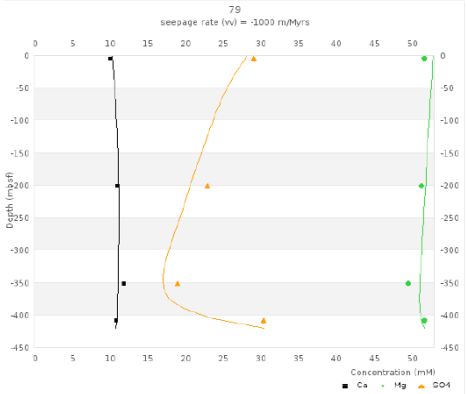
79
seepage rate (vv) = -1000 m/Myrs
Depth (mbsf)
Concentration (mM)
Ca
Mg
SO4

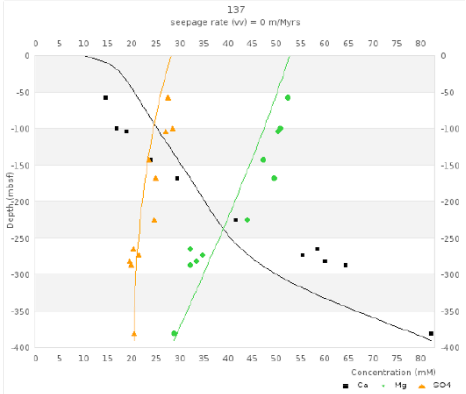
137
seepage rate (vv) = 0 m/Myrs
Depth (mbsf)
Concentration (mM)
Ca
Mg
SO4

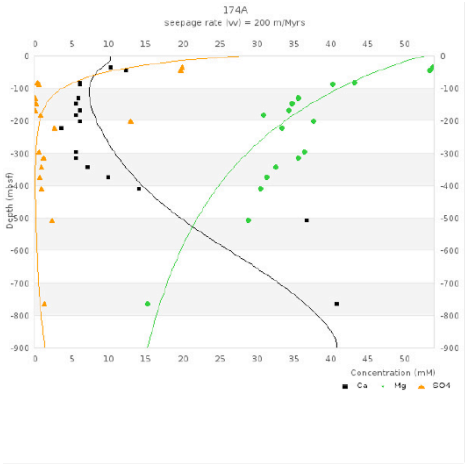
174A
seepage rate (vv) = 200 m/Myrs
Depth (mbsf)
Concentration (mM)
Ca
Mg
SO4

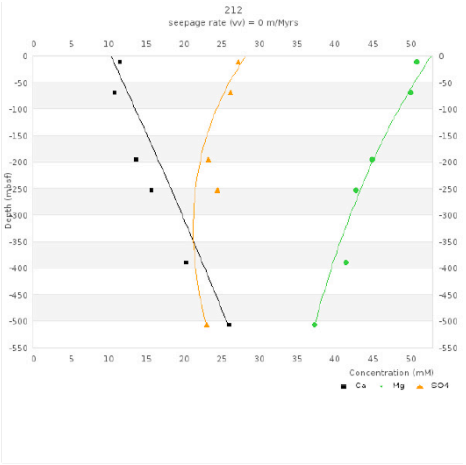
212
seepage rate (vv) = 0 m/Myrs
Depth (mbsf)
Concentration (mM)
Ca
Mg
SO4

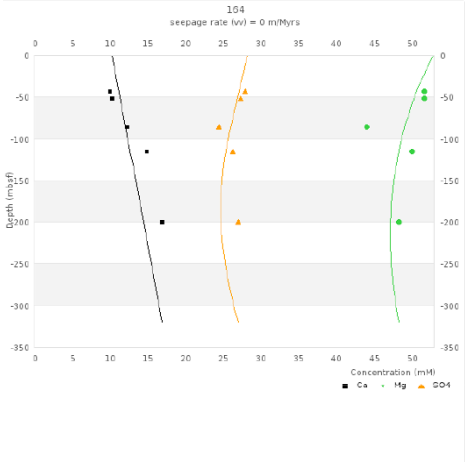
164
seepage rate (vv) = 0 m/Myrs
Depth (mbsf)
Concentration (mM)
Ca
Mg
SO4

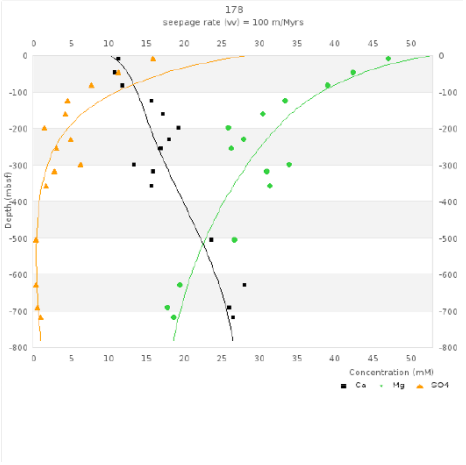
178
seepage rate (vv) = 100 m/Myrs
Depth (mbsf)
Concentration (mM)
Ca
Mg
SO4

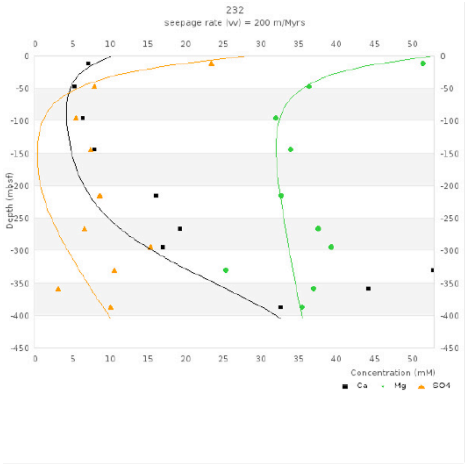
232
seepage rate (vv) = 200 m/Myrs
Depth (mbsf)
Concentration (mM)
Ca
Mg
SO4

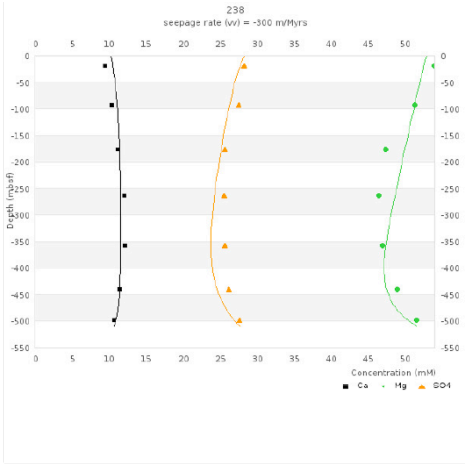
238
seepage rate (vv) = -300 m/Myrs
Depth (mbsf)
Concentration (mM)
Ca
Mg
SO4

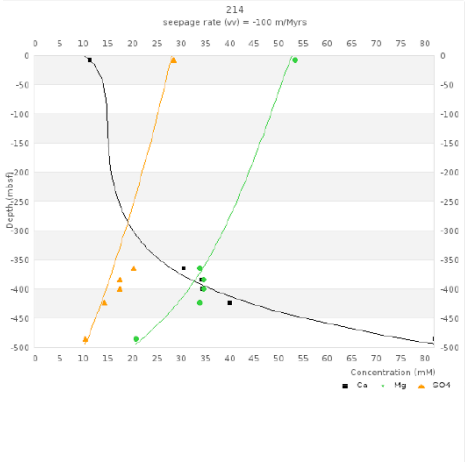
214
seepage rate (vv) = -100 m/Myrs
Depth (mbsf)
Concentration (mM)
Ca
Mg
SO4

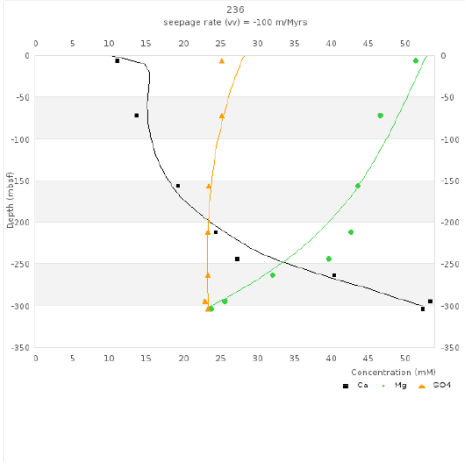
236
seepage rate (vv) = -100 m/Myrs
Depth (mbsf)
Concentration (mM)
Ca
Mg
SO4

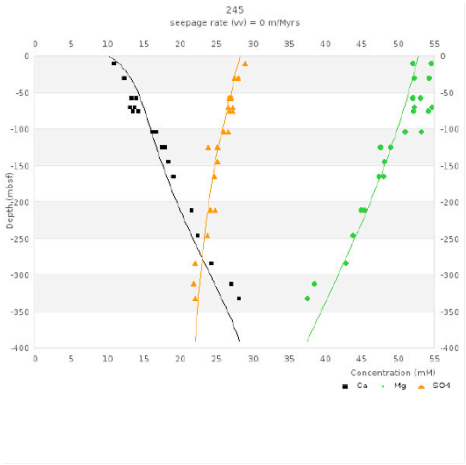
245
seepage rate (vv) = 0 m/Myrs
Depth (mbsf)
Concentration (mM)
Ca
Mg
SO4

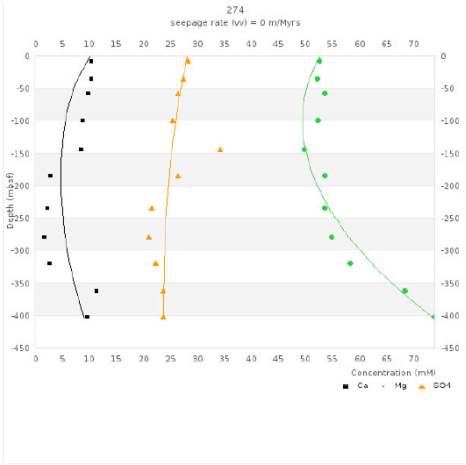
274
seepage rate (vv) = 0 m/Myrs
Depth (mbsf)
Concentration (mM)
Ca
Mg
SO4

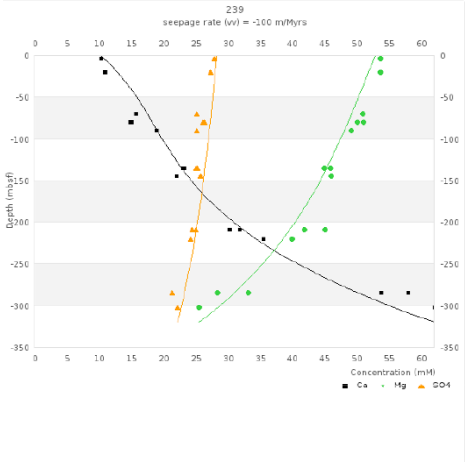
239
seepage rate (vv) = -100 m/Myrs
Depth (mbsf)
Concentration (mM)
Ca
Mg
SO4

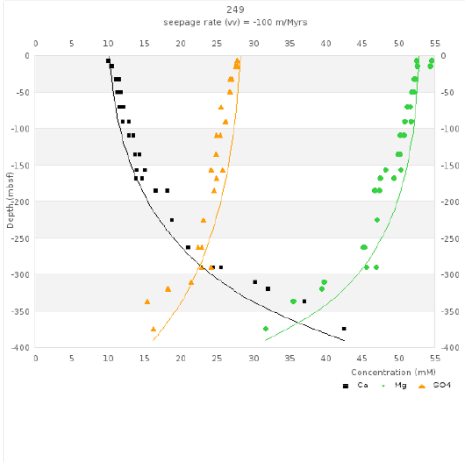
249
seepage rate (vv) = -100 m/Myrs
Depth (mbsf)
Concentration (mM)
Ca
Mg
SO4

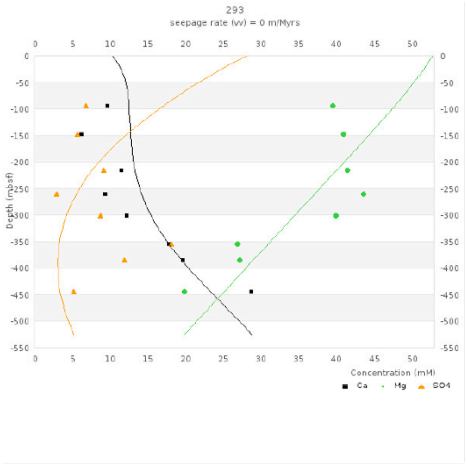
293
seepage rate (vv) = 0 m/Myrs
Depth (mbsf)
Concentration (mM)
Ca
Mg
SO4

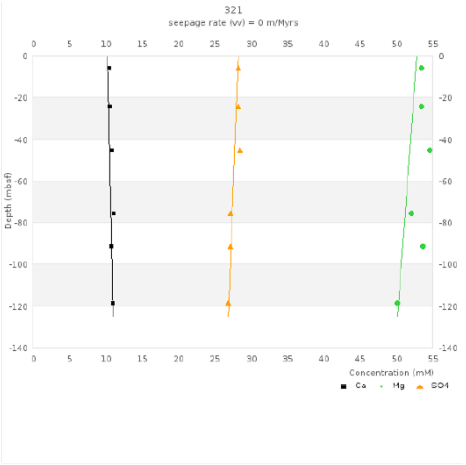
321
seepage rate (vv) = 0 m/Myrs
Depth (mbsf)
Concentration (mM)
Ca
Mg
SO4

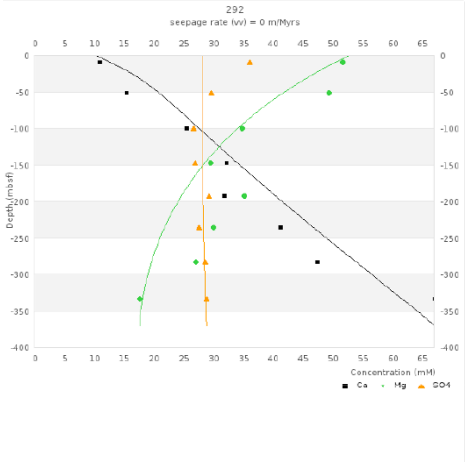
292
seepage rate (vv) = 0 m/Myrs
Depth (mbsf)
Concentration (mM)
Ca
Mg
SO4

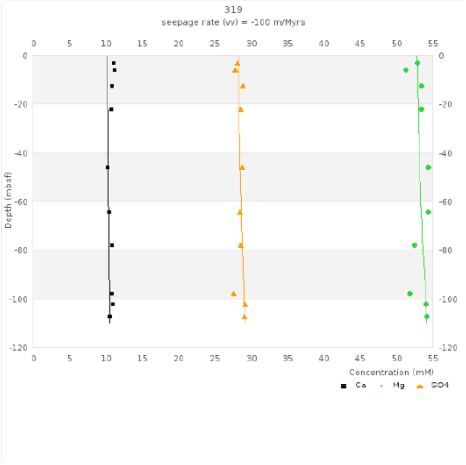
319
seepage rate (vv) = -100 m/Myrs
Depth (mbsf)
Concentration (mM)
Ca
Mg
SO4

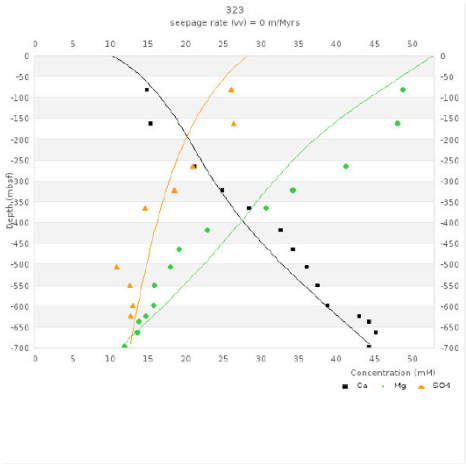
323
seepage rate (vv) = 0 m/Myrs
Depth (m b.s.f)
Concentration (mM)
Ca
Mg
SO4

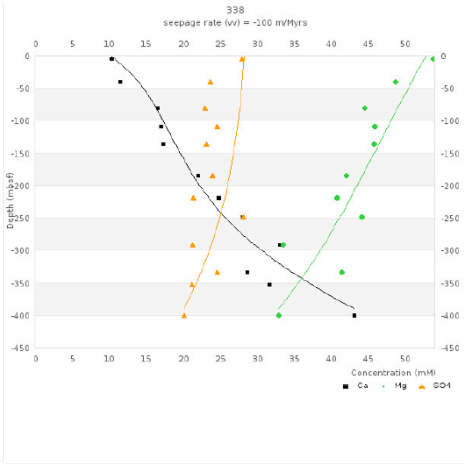
338
seepage rate (vv) = -100 m/Myrs
Depth (m b.s.f)
Concentration (mM)
Ca
Mg
SO4

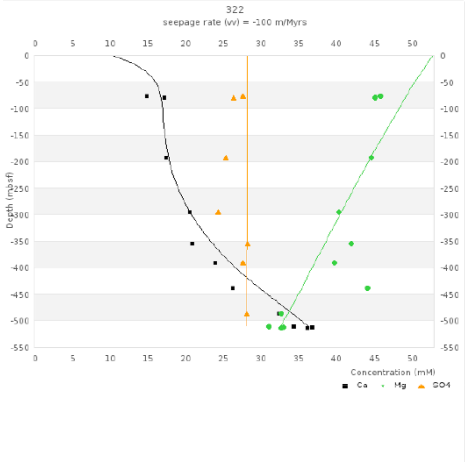
322
seepage rate (vv) = -100 m/Myrs
Depth (m b.s.f)
Concentration (mM)
Ca
Mg
SO4

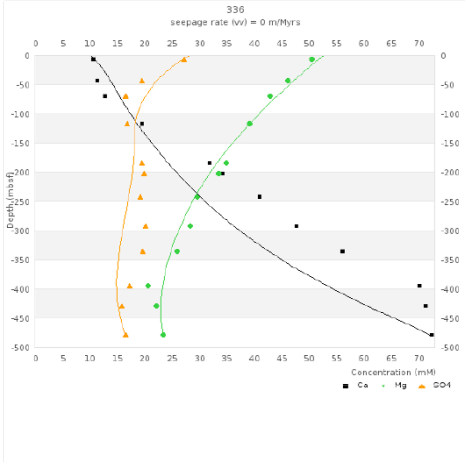
336
seepage rate (vv) = 0 m/Myrs
Depth (m b.s.f)
Concentration (mM)
Ca
Mg
SO4

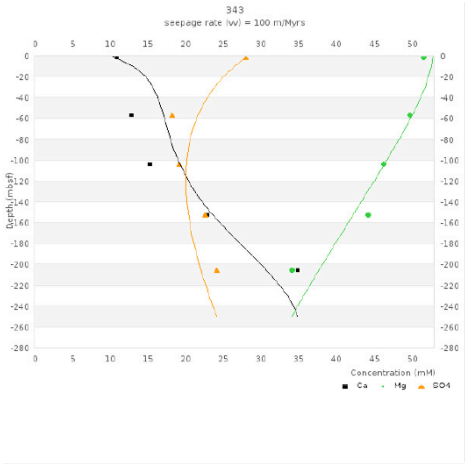
343
seepage rate (w) = 100 m/Myrs
Depth (mbsf)
Concentration (mM)
Ca
Mg
SO4

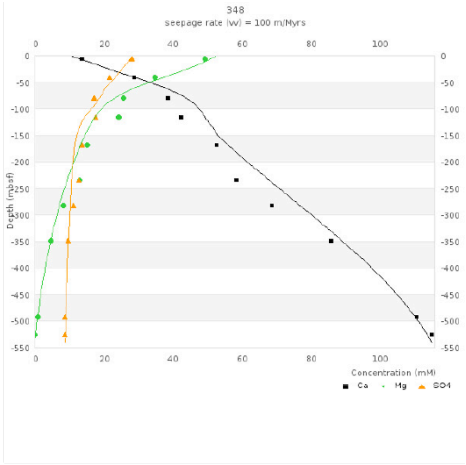
348
seepage rate (w) = 100 m/Myrs
Depth (mbsf)
Concentration (mM)
Ca
Mg
SO4

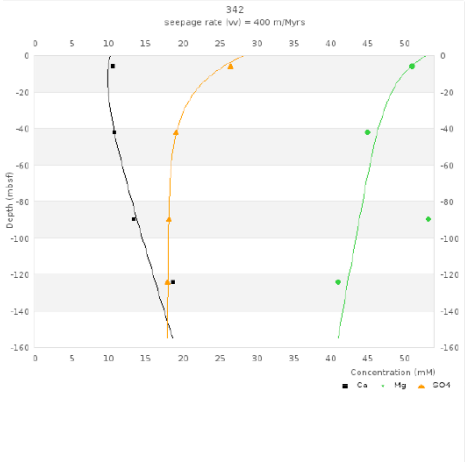
342
seepage rate (w) = 400 m/Myrs
Depth (mbsf)
Concentration (mM)
Ca
Mg
SO4

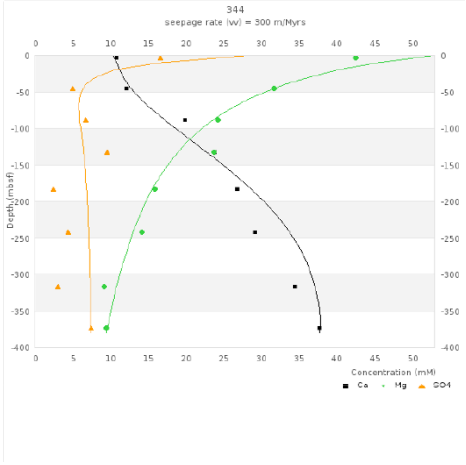
344
seepage rate (w) = 300 m/Myrs
Depth (mbsf)
Concentration (mM)
Ca
Mg
SO4

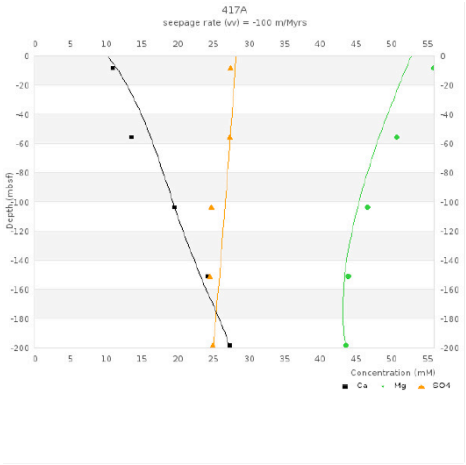
417A
seepage rate (vv) = -100 m/Myrs
Depth (mbsf)
Concentration (mM)
Ca
Mg
SO4

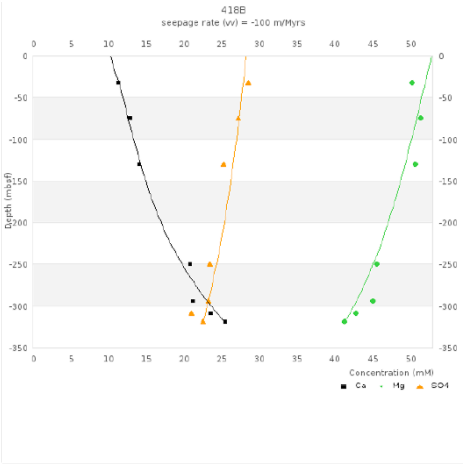
418B
seepage rate (vv) = -100 m/Myrs
Depth (mbsf)
Concentration (mM)
Ca
Mg
SO4

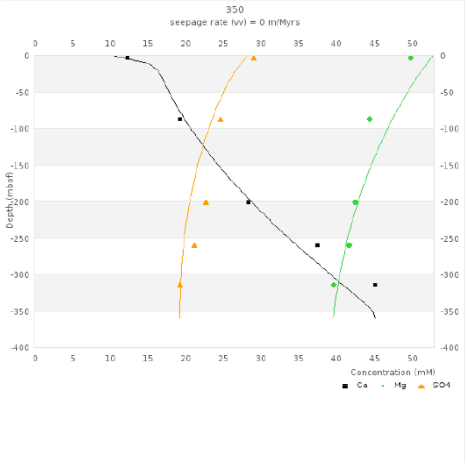
350
seepage rate (vv) = 0 m/Myrs
Depth (mbsf)
Concentration (mM)
Ca
Mg
SO4

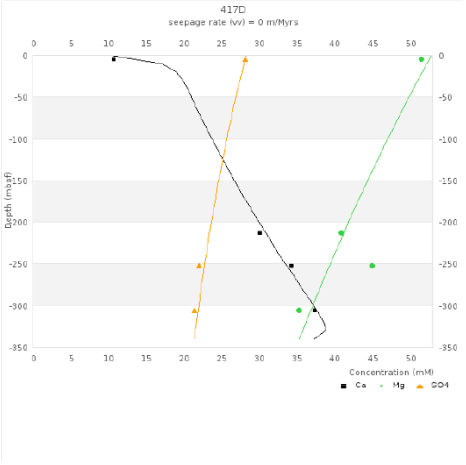
417D
seepage rate (vv) = 0 m/Myrs
Depth (mbsf)
Concentration (mM)
Ca
Mg
SO4

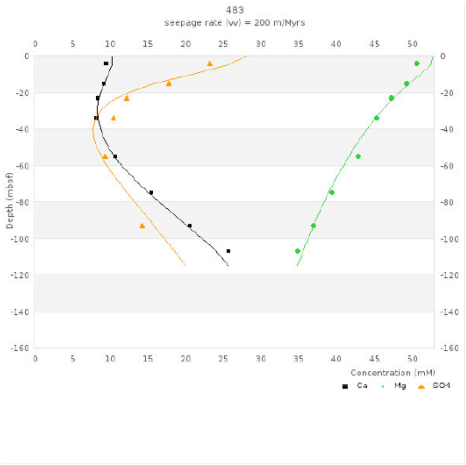
483
seepage rate (w) = 200 m/Myrs
Depth (mbsf)
Concentration (mM)
Ca
Mg
SO4

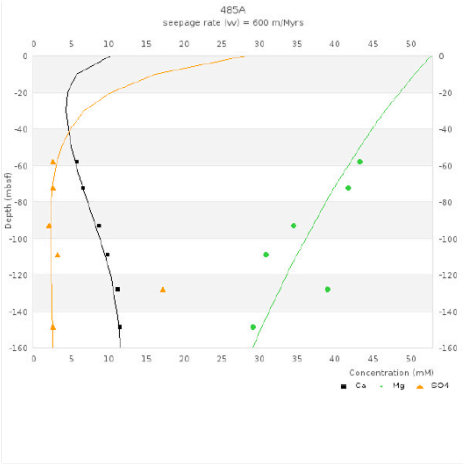
485A
seepage rate (w) = 600 m/Myrs
Depth (mbsf)
Concentration (mM)
Ca
Mg
SO4

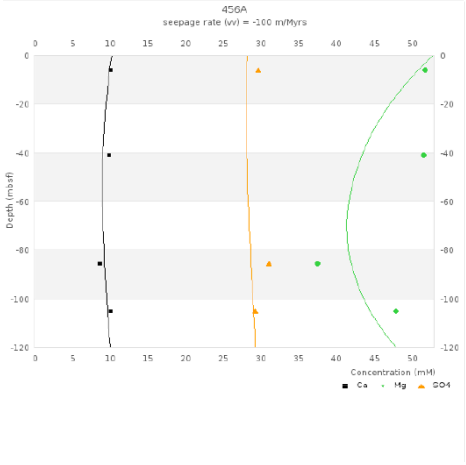
456A
seepage rate (w) = -100 m/Myrs
Depth (mbsf)
Concentration (mM)
Ca
Mg
SO4

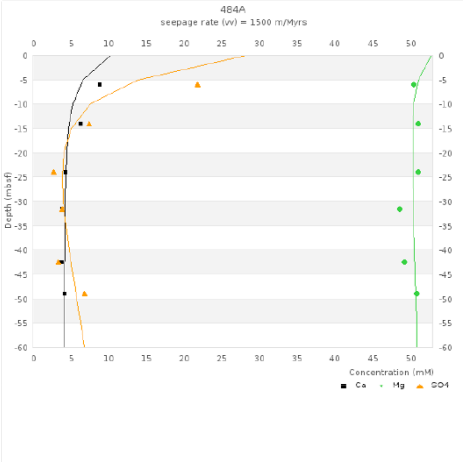
484A
seepage rate (w) = 1500 m/Myrs
Depth (mbsf)
Concentration (mM)
Ca
Mg
SO4

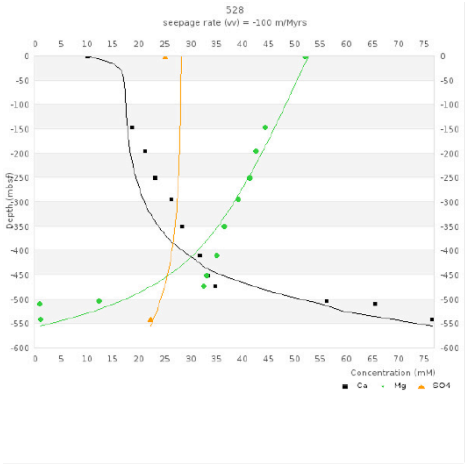
528
seepage rate (vv) = -100 m/Myrs
Depth (mbsf)
Concentration (mM)
Ca
Mg
SO4

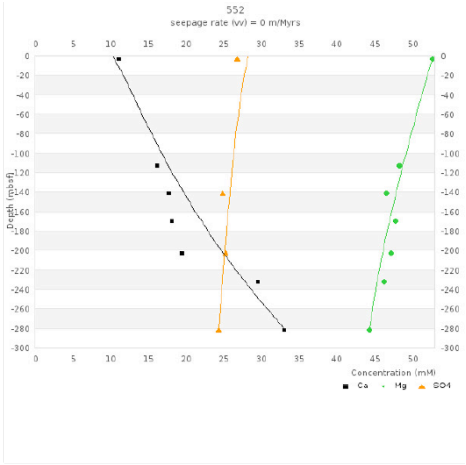
552
seepage rate (vv) = 0 m/Myrs
Depth (mbsf)
Concentration (mM)
Ca
Mg
SO4

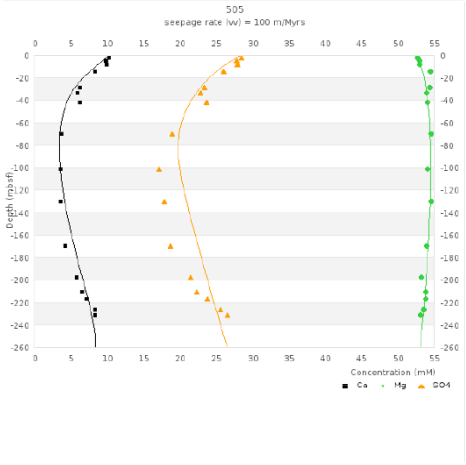
505
seepage rate (vv) = 100 m/Myrs
Depth (mbsf)
Concentration (mM)
Ca
Mg
SO4

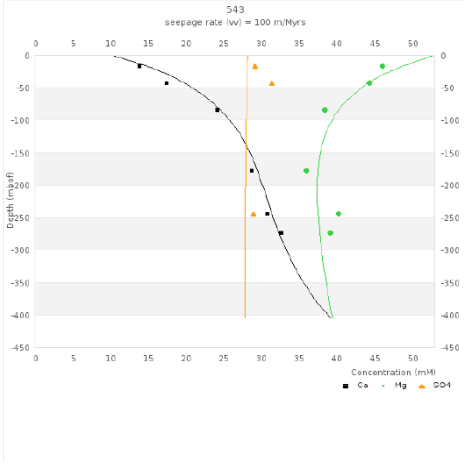
543
seepage rate (vv) = 100 m/Myrs
Depth (mbsf)
Concentration (mM)
Ca
Mg
SO4

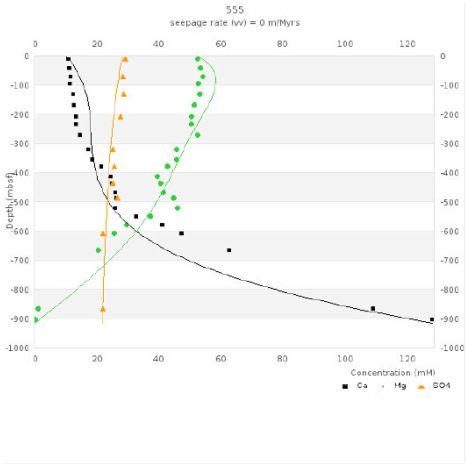
555
seepage rate (vv) = 0 m/Myrs
Depth (mbsf)
Concentration (mM)
Ca
Mg
SO4

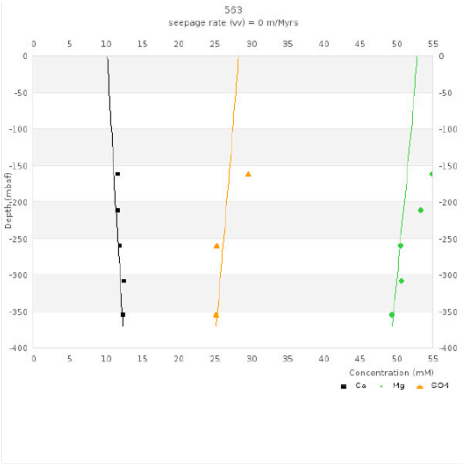
563
seepage rate (vv) = 0 m/Myrs
Depth (mbsf)
Concentration (mM)
Ca
Mg
SO4

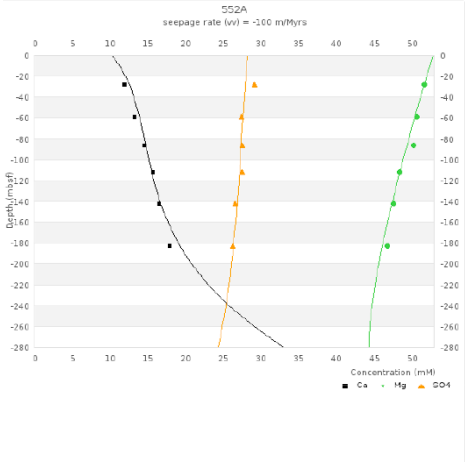
552A
seepage rate (vv) = -100 m/Myrs
Depth (mbsf)
Concentration (mM)
Ca
Mg
SO4

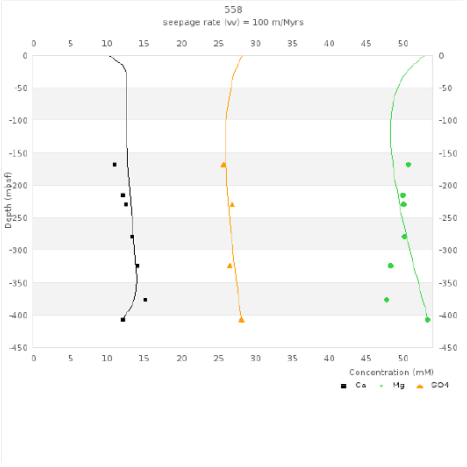
558
seepage rate (vv) = 100 m/Myrs
Depth (mbsf)
Concentration (mM)
Ca
Mg
SO4

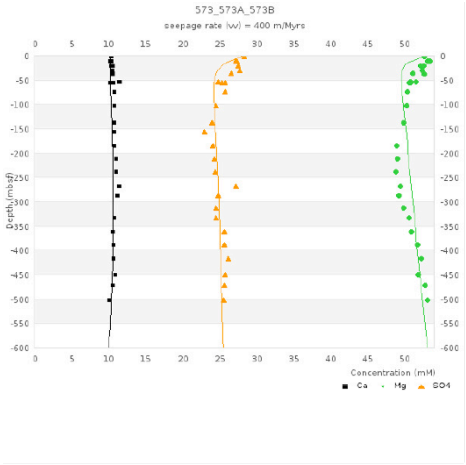
573_573A_573B
seepage rate (vv) = 400 m/Myrs
Depth (mbsf)
Concentration (mM)
Ca
Mg
SO4

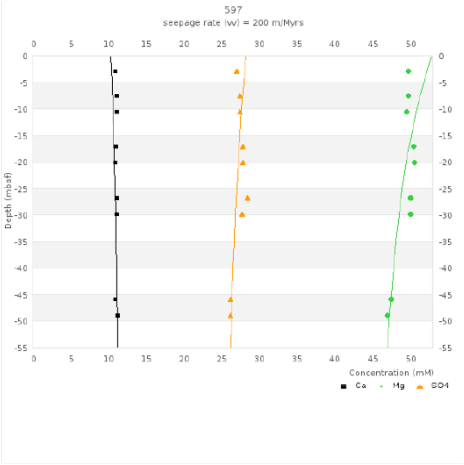
597
seepage rate (vv) = 200 m/Myrs
Depth (mbsf)
Concentration (mM)
Ca
Mg
SO4

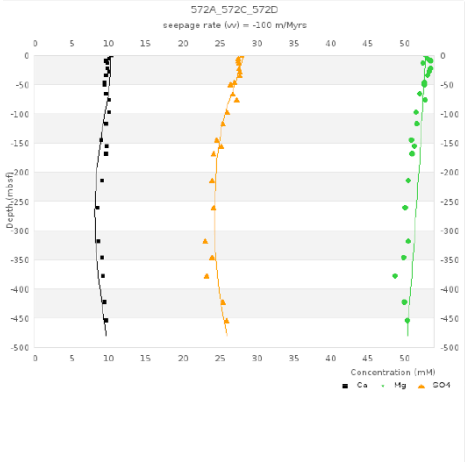
572A_572C_572D
seepage rate (vv) = -100 m/Myrs
Depth (mbsf)
Concentration (mM)
Ca
Mg
SO4

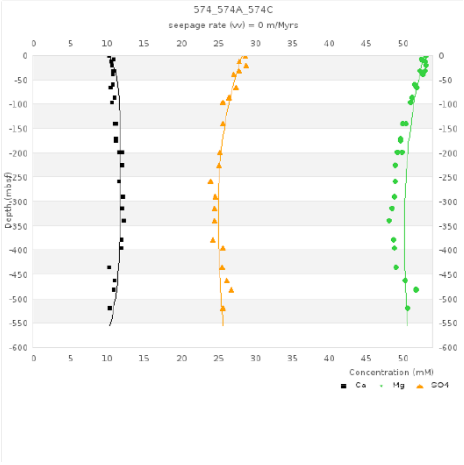
574_574A_574C
seepage rate (vv) = 0 m/Myrs
Depth (mbsf)
Concentration (mM)
Ca
Mg
SO4

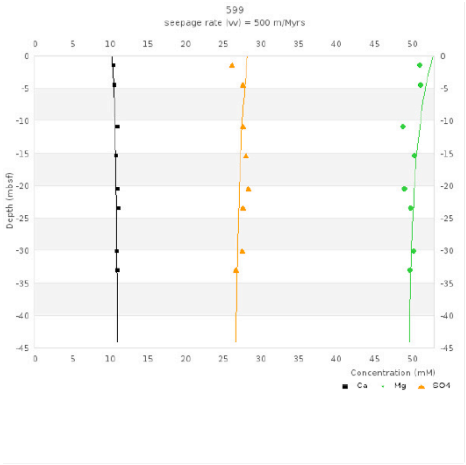
599
seepage rate (vv) = 500 m/Myrs
Depth (mbsf)
Concentration (mM)
Ca
Mg
SO4

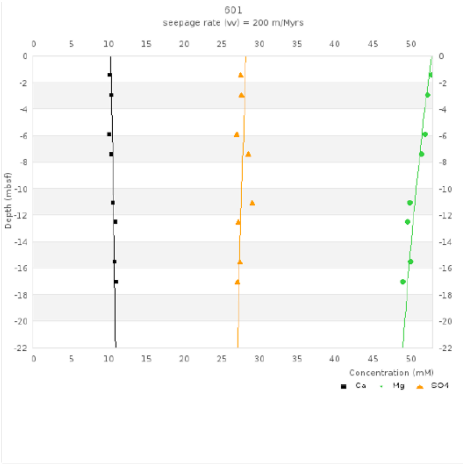
601
seepage rate (vv) = 200 m/Myrs
Depth (mbsf)
Concentration (mM)
Ca
Mg
SO4

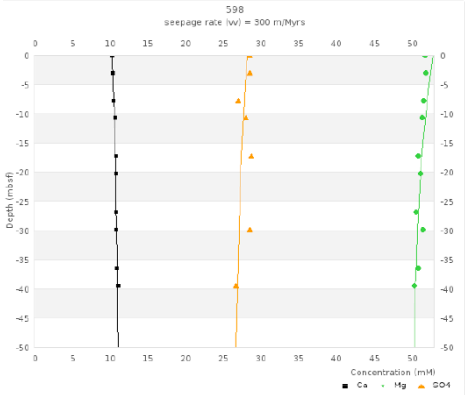
598
seepage rate (vv) = 300 m/Myrs
Depth (mbsf)
Concentration (mM)
Ca
Mg
SO4

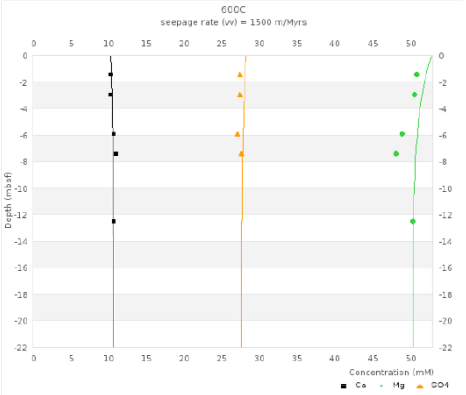
600C
seepage rate (vv) = 1500 m/Myrs
Depth (mbsf)
Concentration (mM)
Ca
Mg
SO4

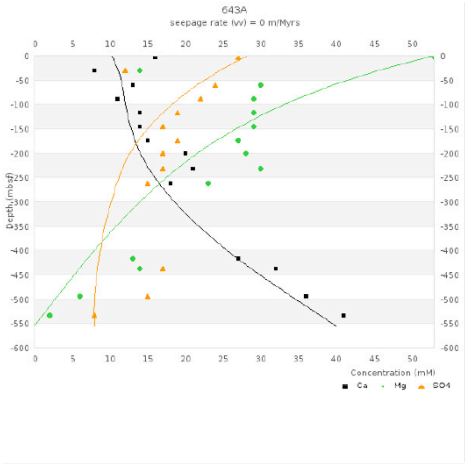
643A
seepage rate (vv) = 0 m/Myrs
Depth (mbsf)
Concentration (mM)
Ca
Mg
SO4

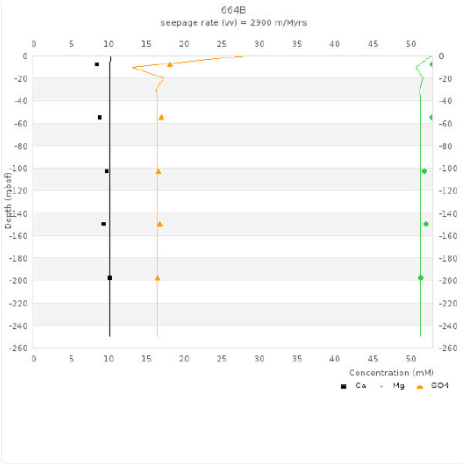
664B
seepage rate (vv) = 2900 m/Myrs
Depth (mbsf)
Concentration (mM)
Ca
Mg
SO4

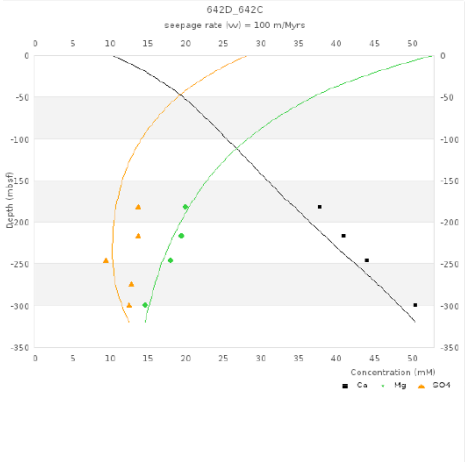
642D_642C
seepage rate (vv) = 100 m/Myrs
Depth (mbsf)
Concentration (mM)
Ca
Mg
SO4

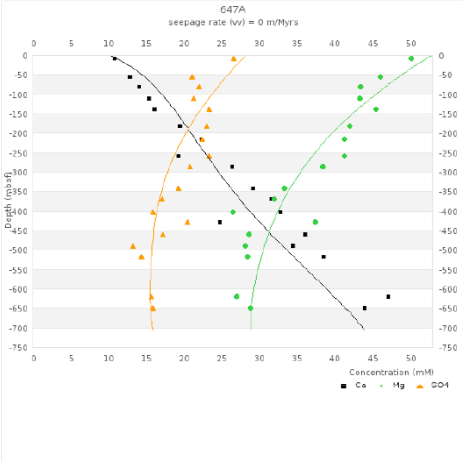
647A
seepage rate (vv) = 0 m/Myrs
Depth (mbsf)
Concentration (mM)
Ca
Mg
SO4

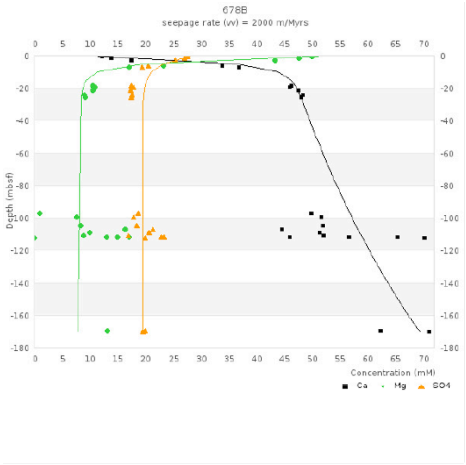
678B
seepage rate (vv) = 2000 m/Myrs
Depth (mbsf)
Concentration (mM)
Ca
Mg
SO4

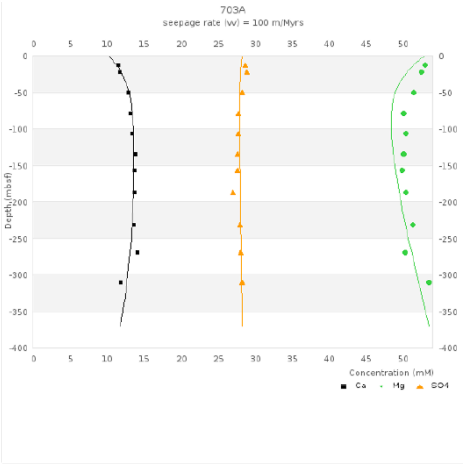
703A
seepage rate (vv) = 100 m/Myrs
Depth (mbsf)
Concentration (mM)
Ca
Mg
SO4

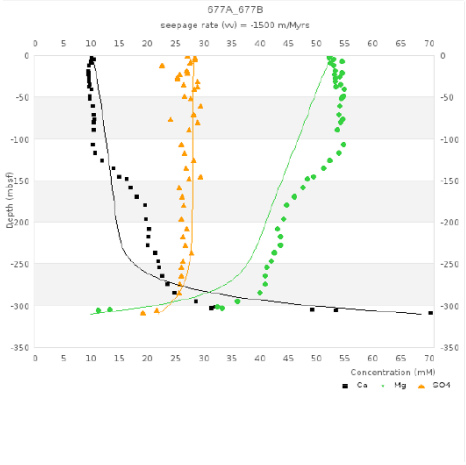
677A_677B
seepage rate (vv) = -1500 m/Myrs
Depth (mbsf)
Concentration (mM)
Ca
Mg
SO4

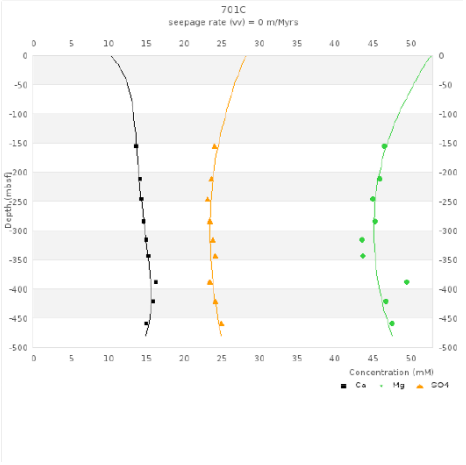
701C
seepage rate (vv) = 0 m/Myrs
Depth (mbsf)
Concentration (mM)
Ca
Mg
SO4

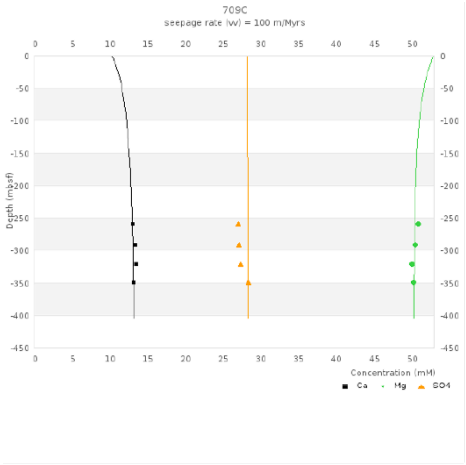
709C
seepage rate (vv) = 100 m/Myrs
Depth (mbsf)
Concentration (mM)
Ca
Mg
SO4

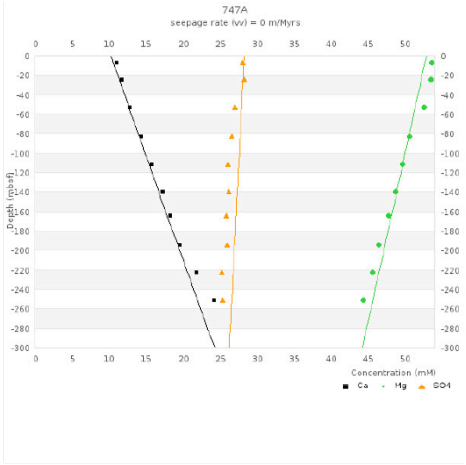
747A
seepage rate (vv) = 0 m/Myrs
Depth (mbsf)
Concentration (mM)
Ca
Mg
SO4

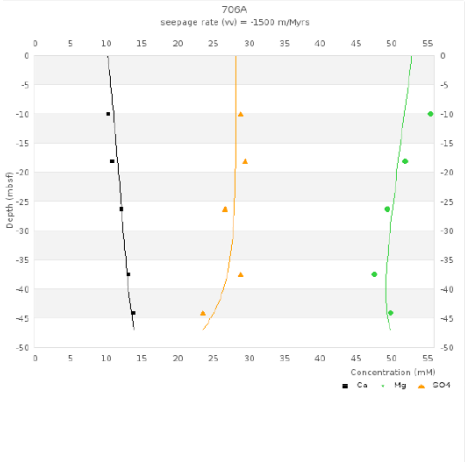
706A
seepage rate (vv) = -1500 m/Myrs
Depth (mbsf)
Concentration (mM)
Ca
Mg
SO4

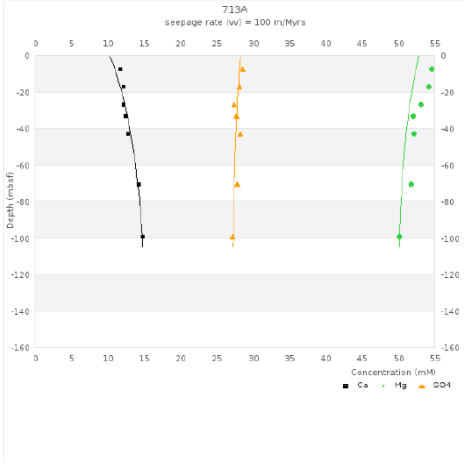
713A
seepage rate (vv) = 100 m/Myrs
Depth (mbsf)
Concentration (mM)
Ca
Mg
SO4

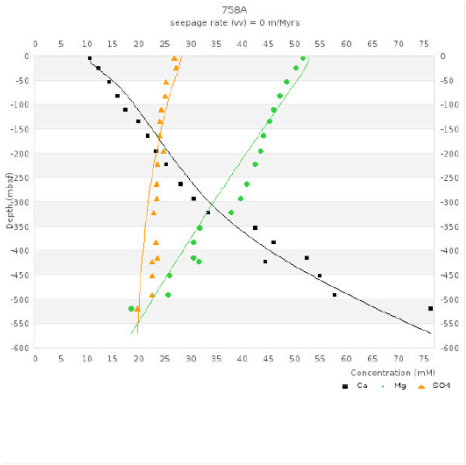
758A
seepage rate (w) = 0 m/Myrs
Depth (mbsf)
Concentration (mM)
Ca
Mg
SO4

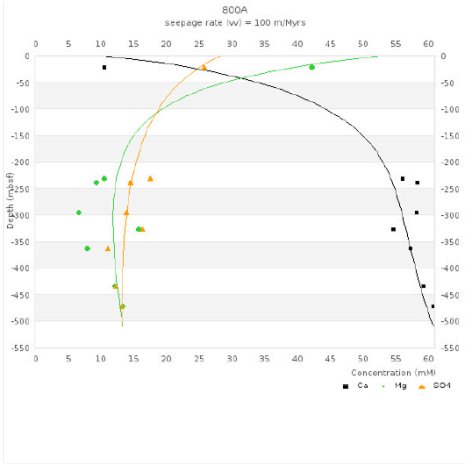
800A
seepage rate (w) = 100 m/Myrs
Depth (mbsf)
Concentration (mM)
Ca
Mg
SO4

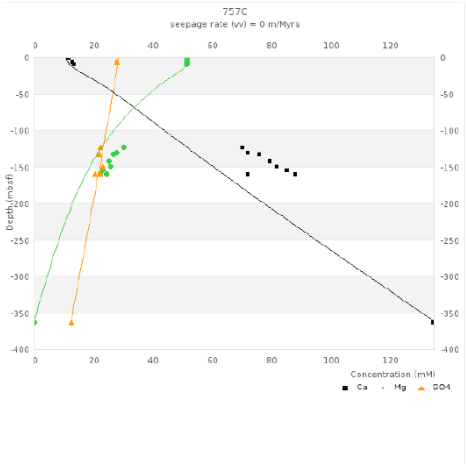
757C
seepage rate (w) = 0 m/Myrs
Depth (mbsf)
Concentration (mM)
Ca
Mg
SO4

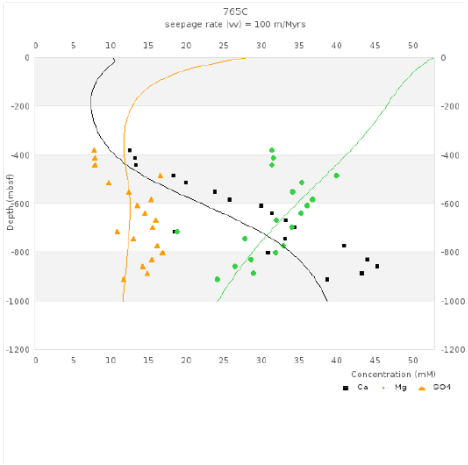
765C
seepage rate (w) = 100 m/Myrs
Depth (mbsf)
Concentration (mM)
Ca
Mg
SO4

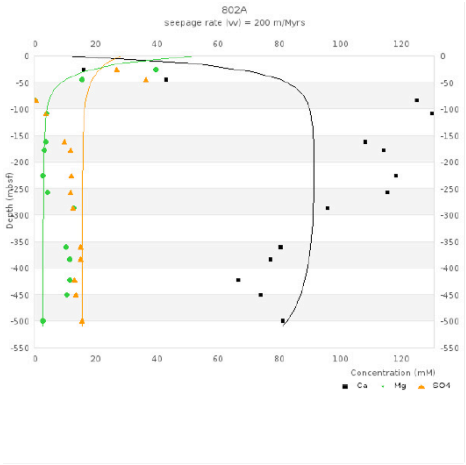
802A
seepage rate (vv) = 200 m/Myrs
Depth (mbsf)
Concentration (mM)
Ca
Mg
SO4

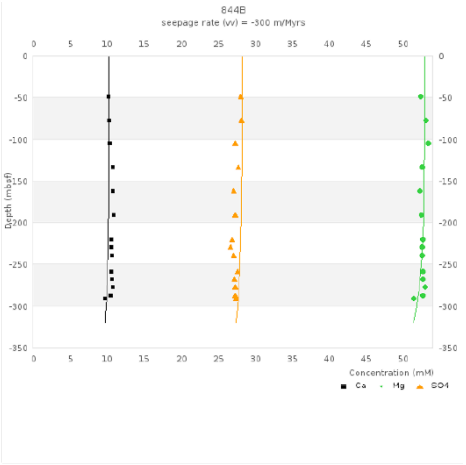
844B
seepage rate (vv) = -300 m/Myrs
Depth (mbsf)
Concentration (mM)
Ca
Mg
SO4

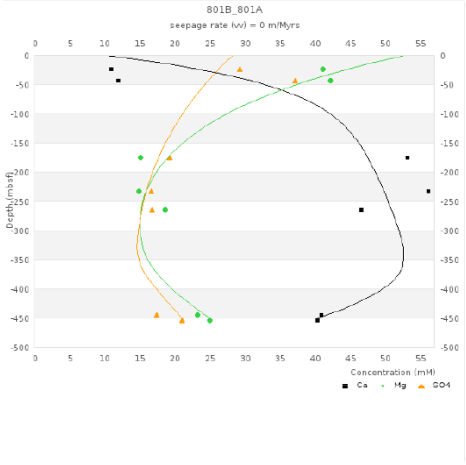
801B_801A
seepage rate (vv) = 0 m/Myrs
Depth (mbsf)
Concentration (mM)
Ca
Mg
SO4

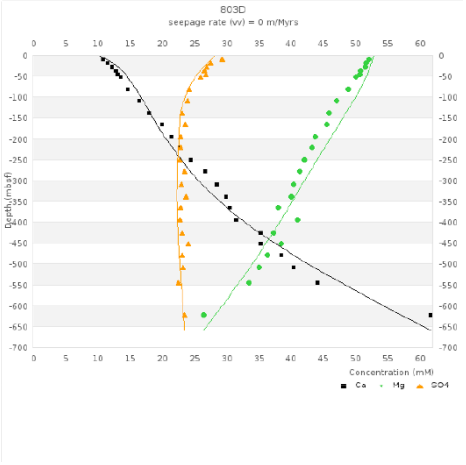
803D
seepage rate (vv) = 0 m/Myrs
Depth (mbsf)
Concentration (mM)
Ca
Mg
SO4

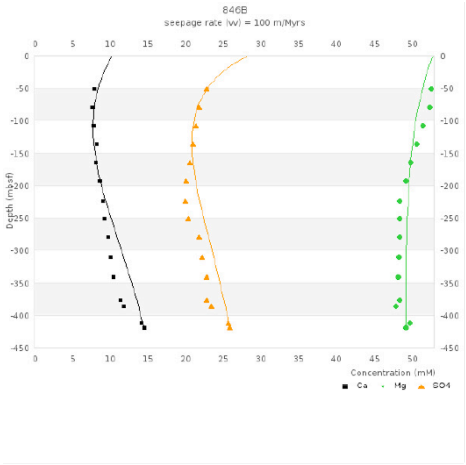
846B
seepage rate (vv) = 100 m/Myrs
Depth (mbsf)
Concentration (mM)
Ca
Mg
SO4

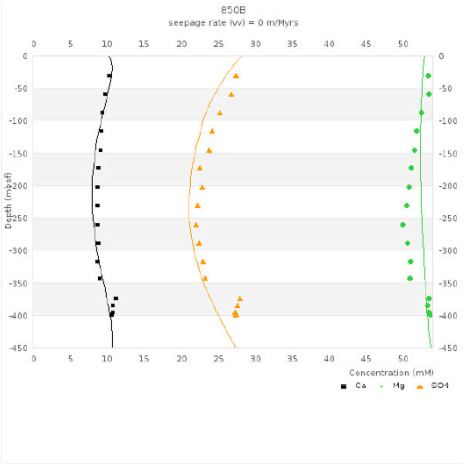
850B
seepage rate (vv) = 0 m/Myrs
Depth (mbsf)
Concentration (mM)
Ca
Mg
SO4

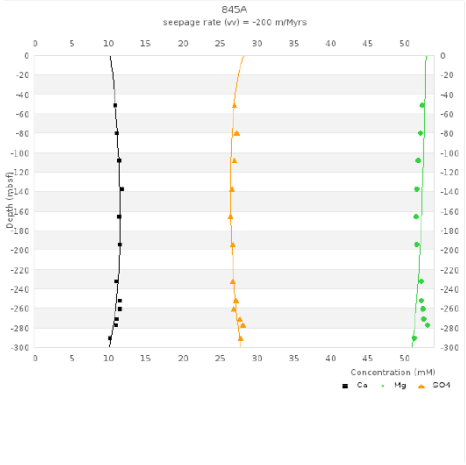
845A
seepage rate (vv) = -200 m/Myrs
Depth (mbsf)
Concentration (mM)
Ca
Mg
SO4

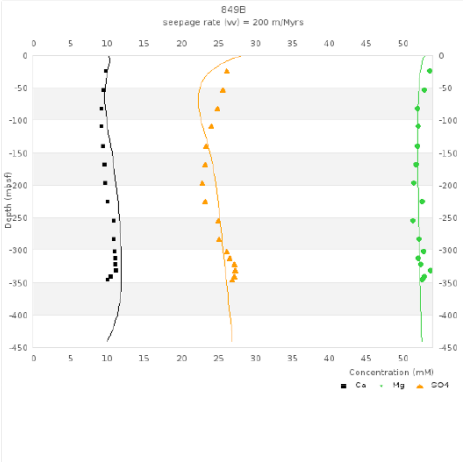
849B
seepage rate (vv) = 200 m/Myrs
Depth (mbsf)
Concentration (mM)
Ca
Mg
SO4

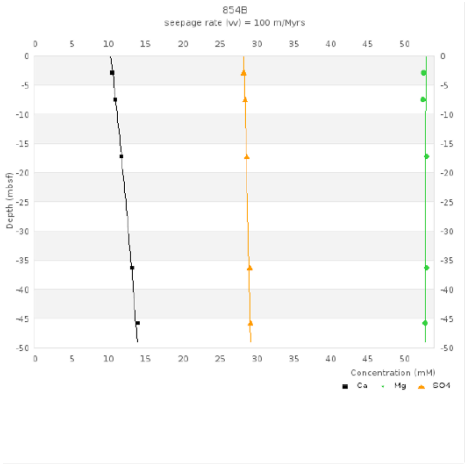
854B
seepage rate (w) = 100 m/Myrs
Depth (mbsf)
Concentration (mM)
Ca
Mg
SO4

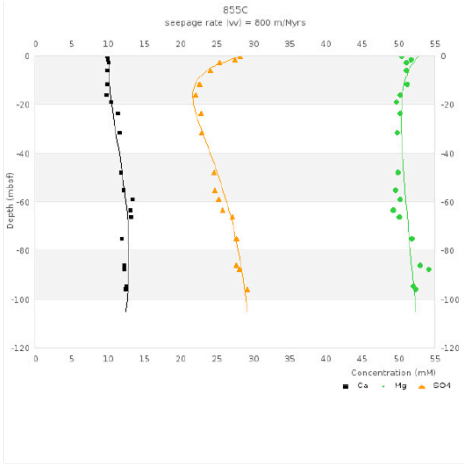
855C
seepage rate (w) = 800 m/Myrs
Depth (mbsf)
Concentration (mM)
Ca
Mg
SO4

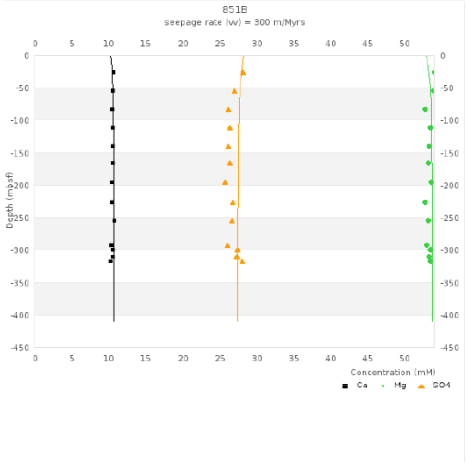
851B
seepage rate (w) = 300 m/Myrs
Depth (mbsf)
Concentration (mM)
Ca
Mg
SO4

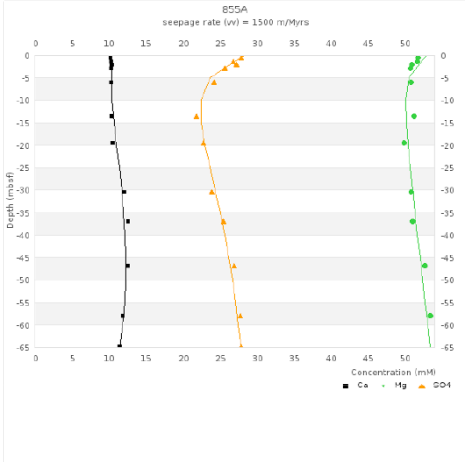
855A
seepage rate (w) = 1500 m/Myrs
Depth (mbsf)
Concentration (mM)
Ca
Mg
SO4

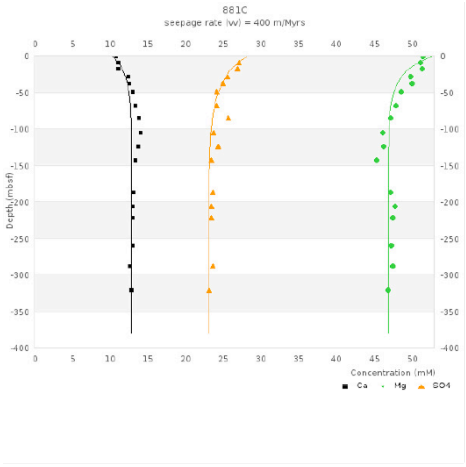
881C
seepage rate (w) = 400 m/Myrs
Depth (mbsf)
Concentration (mM)
Ca
Mg
SO4

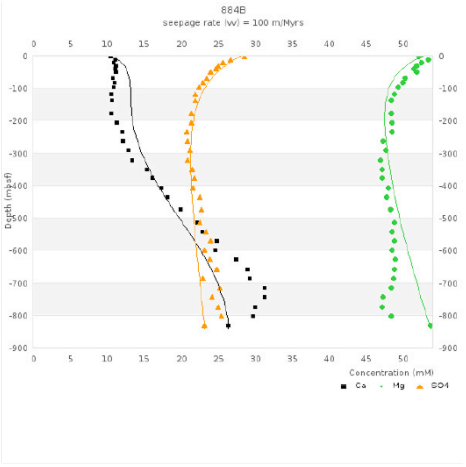
884B
seepage rate (w) = 100 m/Myrs
Depth (mbsf)
Concentration (mM)
Ca
Mg
SO4

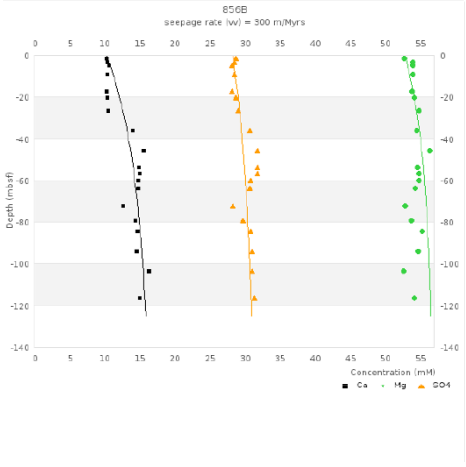
856B
seepage rate (w) = 300 m/Myrs
Depth (mbsf)
Concentration (mM)
Ca
Mg
SO4

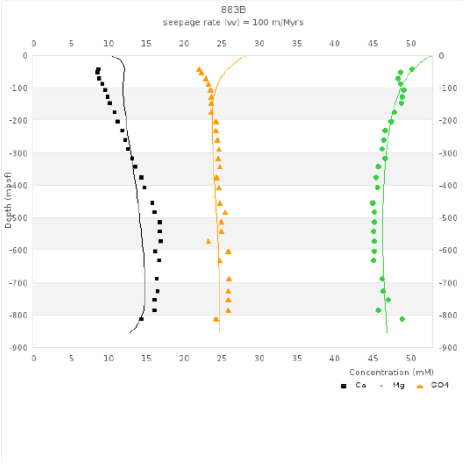
883B
seepage rate (w) = 100 m/Myrs
Depth (mbsf)
Concentration (mM)
Ca
Mg
SO4

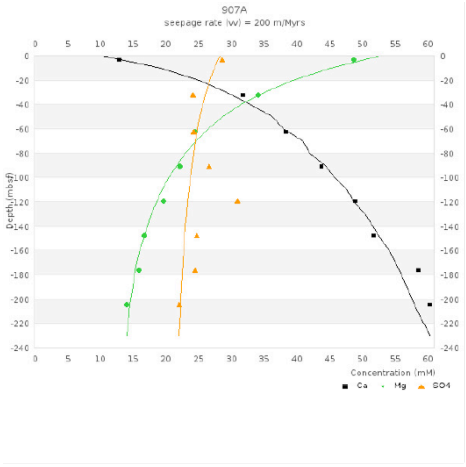
907A
seepage rate (w) = 200 m/Myrs
Depth (mbsf)
Concentration (mM)
Ca
Mg
SO4

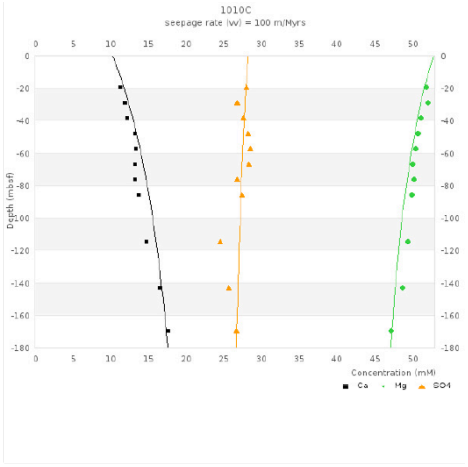
1010C
seepage rate (w) = 100 m/Myrs
Depth (mbsf)
Concentration (mM)
Ca
Mg
SO4

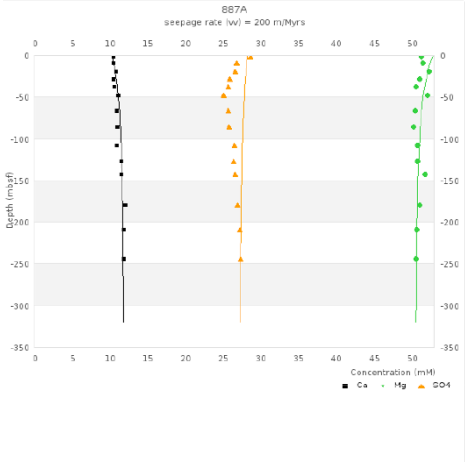
887A
seepage rate (w) = 200 m/Myrs
Depth (mbsf)
Concentration (mM)
Ca
Mg
SO4

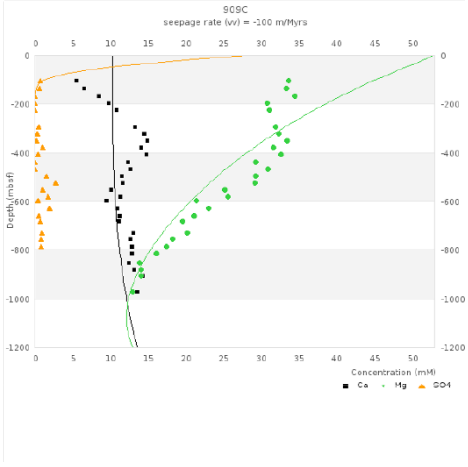
909C
seepage rate (w) = -100 m/Myrs
Depth (mbsf)
Concentration (mM)
Ca
Mg
SO4

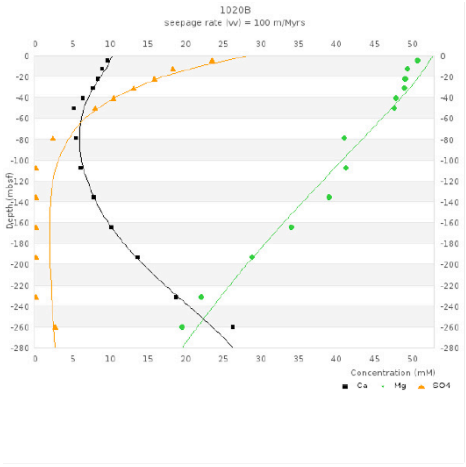
1020B
seepage rate (vv) = 100 m/Myrs
Depth (mbsf)
Concentration (mM)
Ca
Mg
SO4

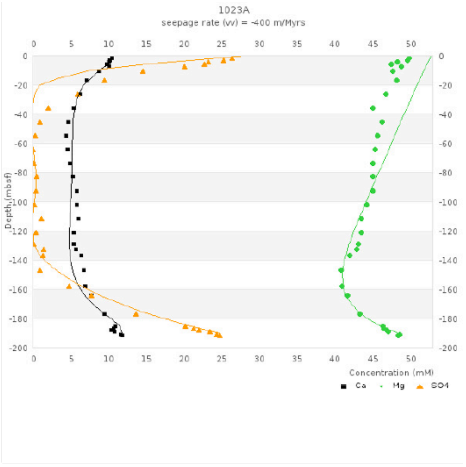
1023A
seepage rate (vv) = ~400 m/Myrs
Depth (mbsf)
Concentration (mM)
Ca
Mg
SO4

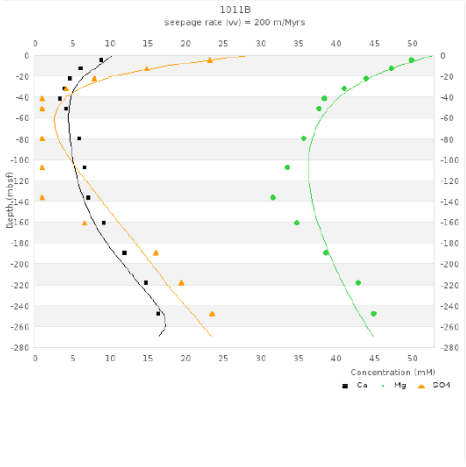
1011B
seepage rate (vv) = 200 m/Myrs
Depth (mbsf)
Concentration (mM)
Ca
Mg
SO4

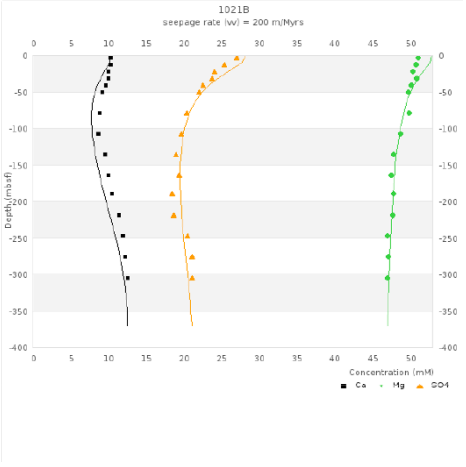
1021B
seepage rate (vv) = 200 m/Myrs
Depth (mbsf)
Concentration (mM)
Ca
Mg
SO4

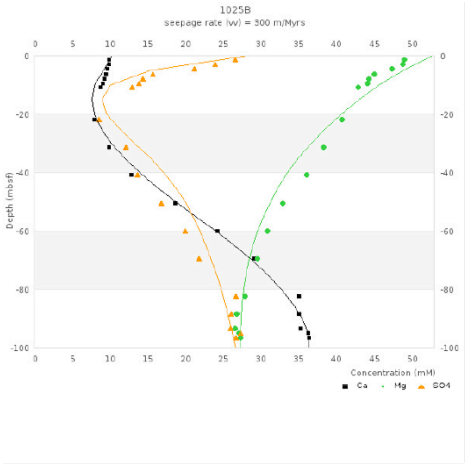
1025B
seepage rate (w) = 300 m/Myrs
Depth (mbsf)
Concentration (mM)
Ca
Mg
SO4

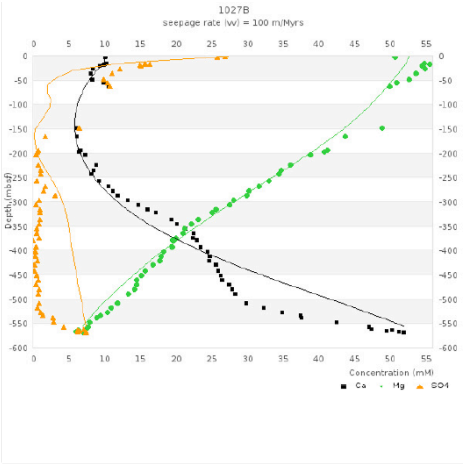
1027B
seepage rate (w) = 100 m/Myrs
Depth (mbsf)
Concentration (mM)
Ca
Mg
SO4

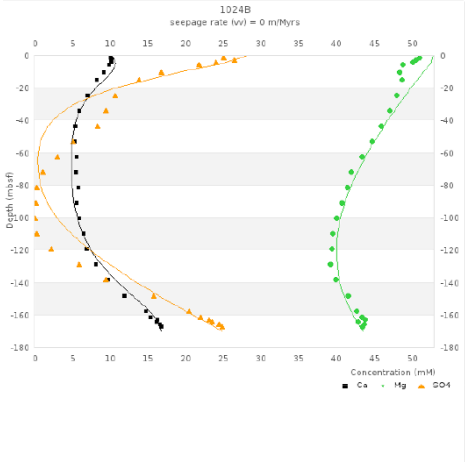
1024B
seepage rate (w) = 0 m/Myrs
Depth (mbsf)
Concentration (mM)
Ca
Mg
SO4

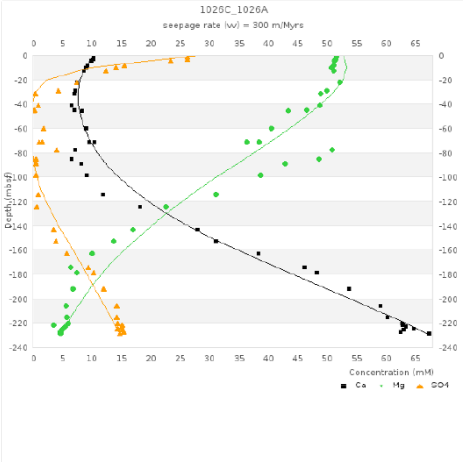
1026C_1026A
seepage rate (w) = 300 m/Myrs
Depth (mbsf)
Concentration (mM)
Ca
Mg
SO4

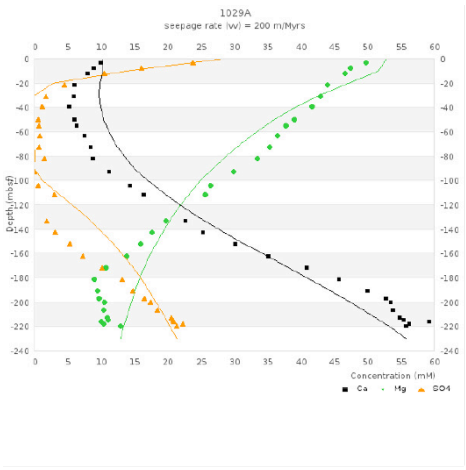
1029A
seepage rate (vv) = 200 m/Myrs
Depth (mbsf)
Concentration (mM)
Ca
Mg
SO4

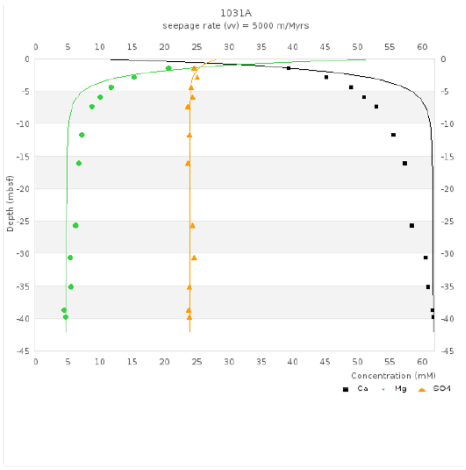
1031A
seepage rate (vv) = 5000 m/Myrs
Depth (mbsf)
Concentration (mM)
Ca
Mg
SO4

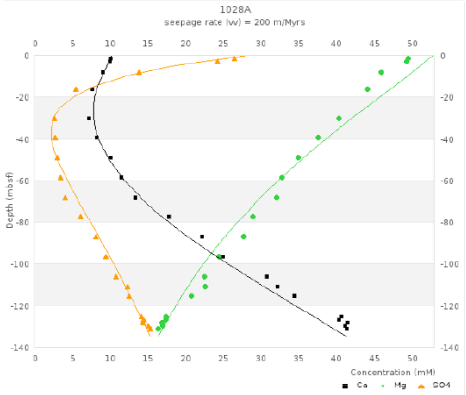
1028A
seepage rate (vv) = 200 m/Myrs
Depth (mbsf)
Concentration (mM)
Ca
Mg
SO4

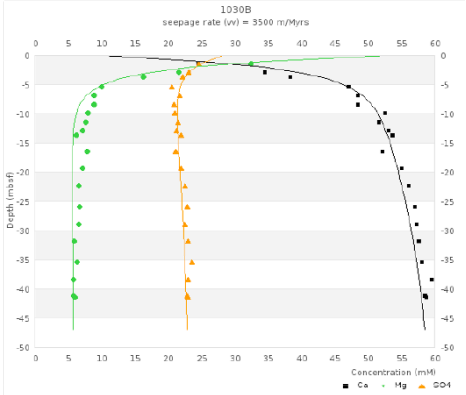
1030B
seepage rate (vv) = 3500 m/Myrs
Depth (mbsf)
Concentration (mM)
Ca
Mg
SO4

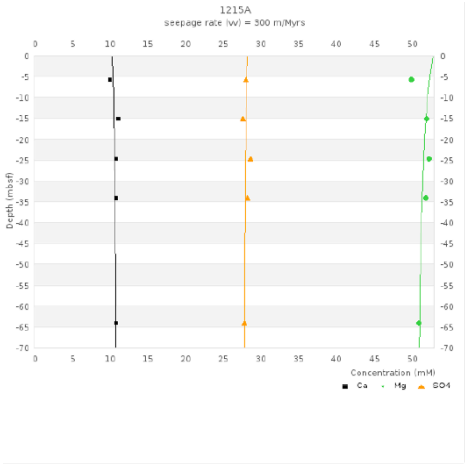
1215A
seepage rate (w) = 300 m/Myrs
Depth (mbsf)
Concentration (mM)
Ca
Mg
SO4

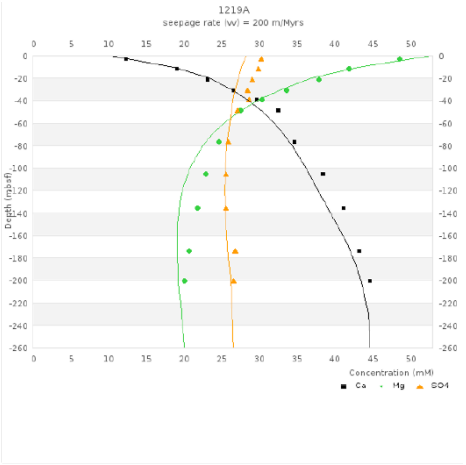
1219A
seepage rate (w) = 200 m/Myrs
Depth (mbsf)
Concentration (mM)
Ca
Mg
SO4

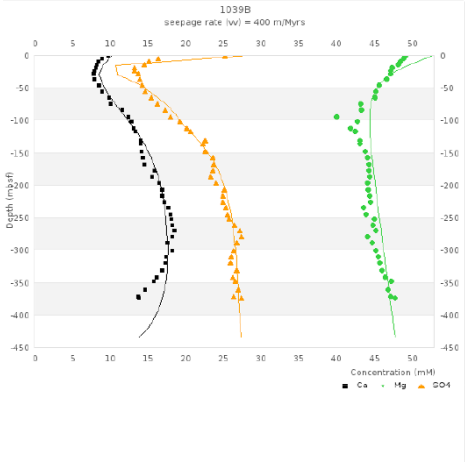
1039B
seepage rate (w) = 400 m/Myrs
Depth (mbsf)
Concentration (mM)
Ca
Mg
SO4

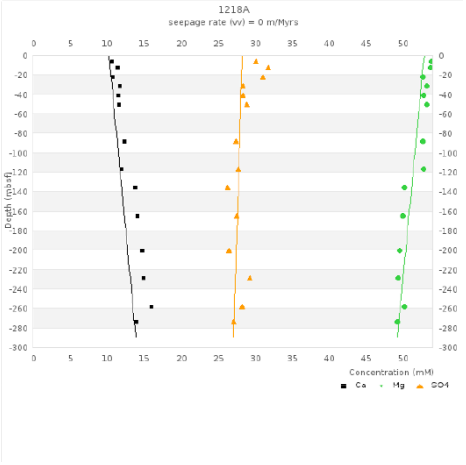
1218A
seepage rate (w) = 0 m/Myrs
Depth (mbsf)
Concentration (mM)
Ca
Mg
SO4

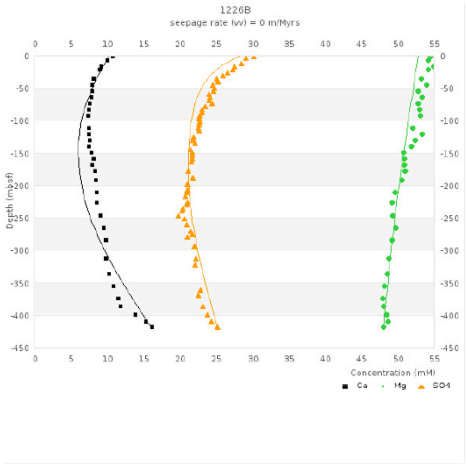
1226B
seepage rate (w) = 0 m/Myrs
Depth (mbsf)
Concentration (mM)
Ca
Mg
SO4

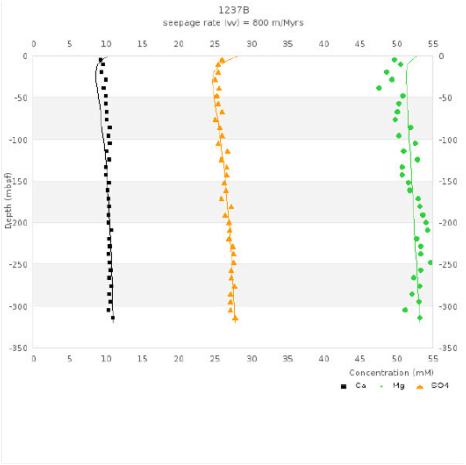
1237B
seepage rate (w) = 800 m/Myrs
Depth (mbsf)
Concentration (mM)
Ca
Mg
SO4

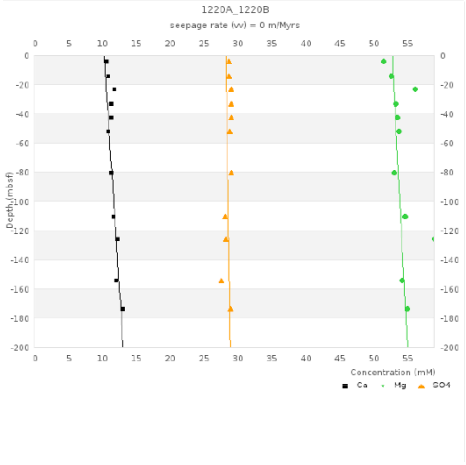
1220A_1220B
seepage rate (w) = 0 m/Myrs
Depth (mbsf)
Concentration (mM)
Ca
Mg
SO4

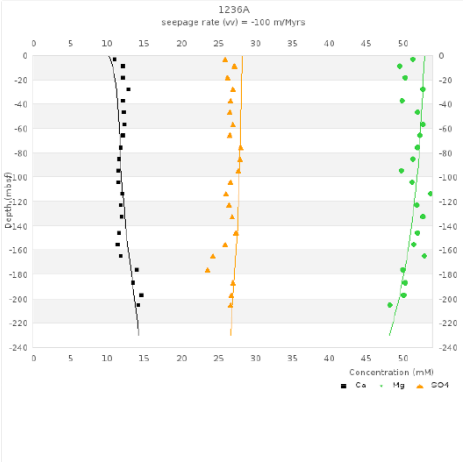
1236A
seepage rate (w) = -100 m/Myrs
Depth (mbsf)
Concentration (mM)
Ca
Mg
SO4

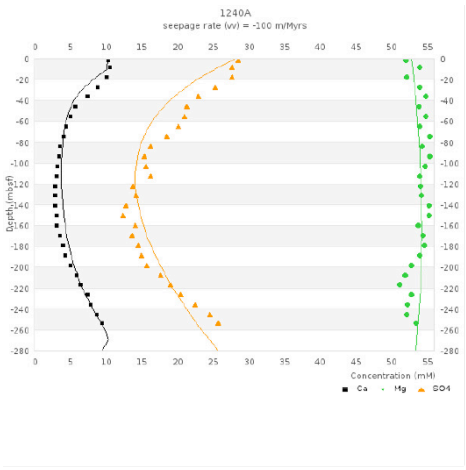
1240A
seepage rate (vv) = -100 m/Myrs
Depth (mbsf)
Concentration (mM)
Ca
Mg
SO4

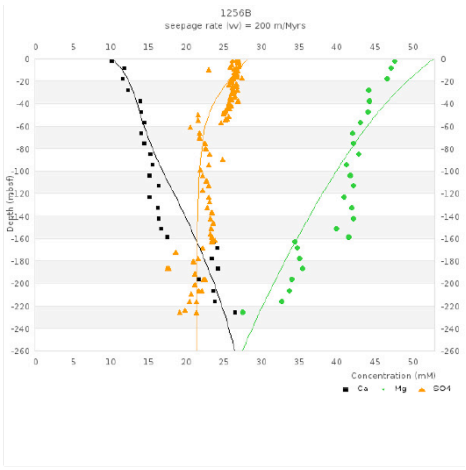
1256B
seepage rate (vv) = 200 m/Myrs
Depth (mbsf)
Concentration (mM)
Ca
Mg
SO4

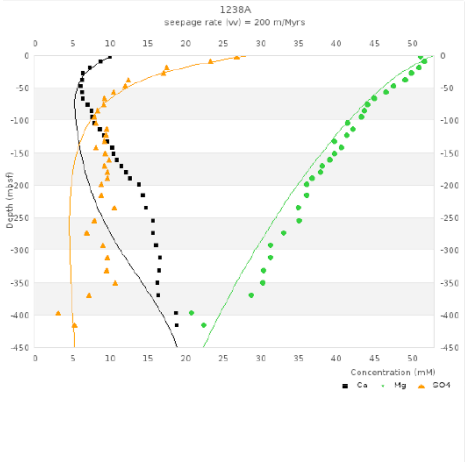
1238A
seepage rate (vv) = 200 m/Myrs
Depth (mbsf)
Concentration (mM)
Ca
Mg
SO4

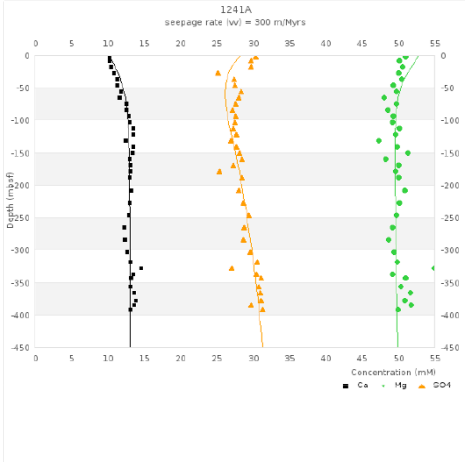
1241A
seepage rate (vv) = 300 m/Myrs
Depth (mbsf)
Concentration (mM)
Ca
Mg
SO4

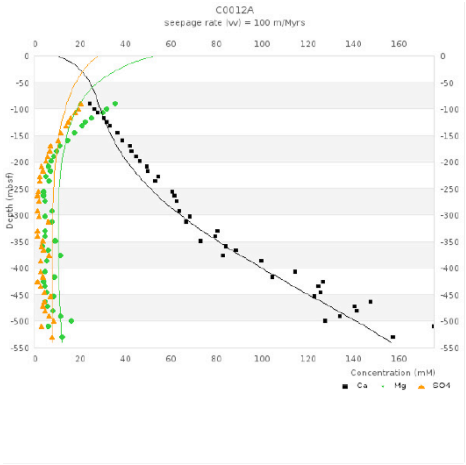
C0012A
seepage rate (vv) = 100 m/Myrs
Depth (mbsf)
Concentration (mM)
Ca
Mg
SO4

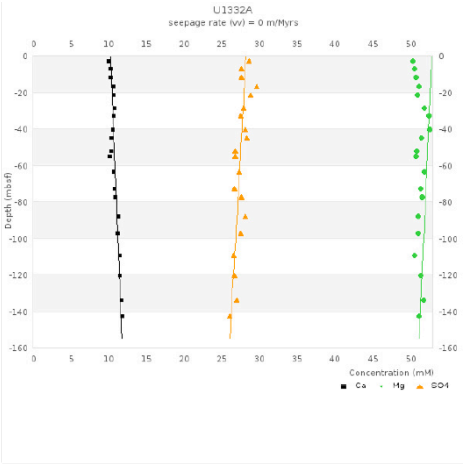
U1332A
seepage rate (vv) = 0 m/Myrs
Depth (mbsf)
Concentration (mM)
Ca
Mg
SO4


1301C_1301D
seepage rate (vv) = 200 m/Myrs
Depth (mbsf)
Concentration (mM)
Ca
Mg
SO4

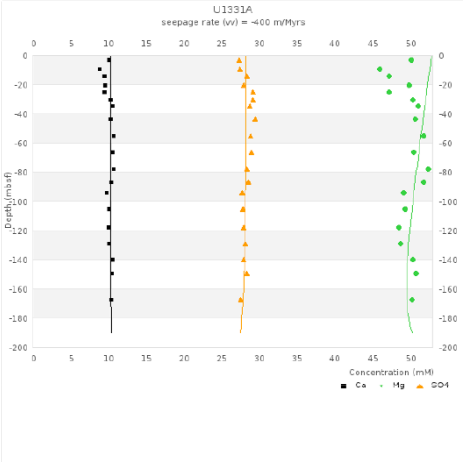
U1331A
seepage rate (vv) = -400 m/Myrs
Depth (mbsf)
Concentration (mM)
Ca
Mg
SO4

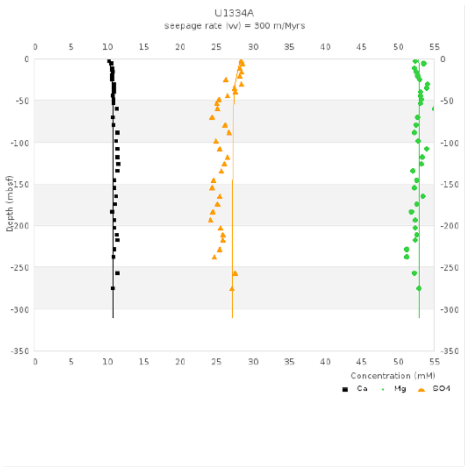
U1334A
seepage rate (w) = 300 m/Myrs
Depth (mbsf)
Concentration (mM)
Ca
Mg
SO4

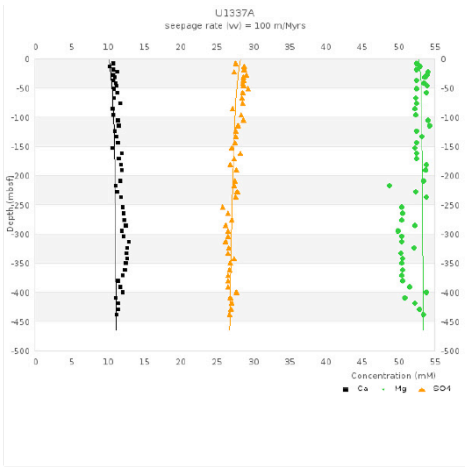
U1337A
seepage rate (w) = 100 m/Myrs
Depth (mbsf)
Concentration (mM)
Ca
Mg
SO4

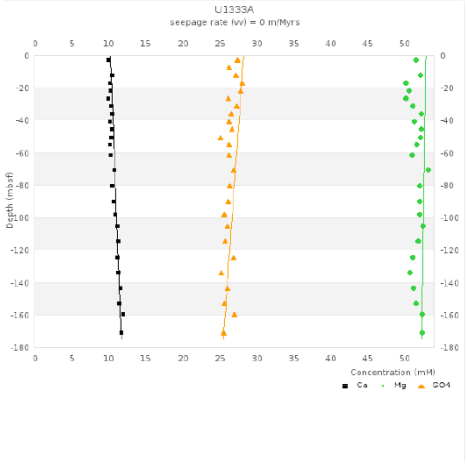
U1333A
seepage rate (w) = 0 m/Myrs
Depth (mbsf)
Concentration (mM)
Ca
Mg
SO4

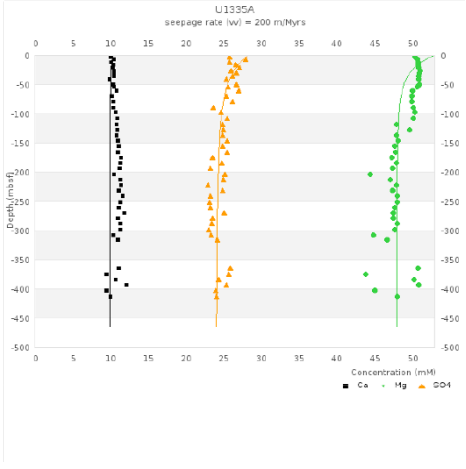
U1335A
seepage rate (w) = 200 m/Myrs
Depth (mbsf)
Concentration (mM)
Ca
Mg
SO4

Appendix F – Comparison of seepage rates estimated in Chapter 4 to rates estimated in other studies

Hole	Crustal Age (Myrs)	Sediment Thickness (m)	Specific Discharge (V_v, m Myrs^{-1}) This Study *	Specific Discharge (V_v, m Myrs^{-1}) Other Study	Reference
598	18	55	220 (70 to 430)	300 to 1200	[*Gieskes*, 1986]
599	9	41	> 280	300 to 1200	[*Gieskes*, 1986]
677A	6	309	-1100 (-650 to -1200)	-1000 to -2000	[*Mottl*, 1989]
678B	6	178	1600 (1100 to 3300)	1000 to 2000	[*Mottl*, 1989]
1023A	0.8	192	-230 (-290 to -170)	-910	Rudnicki et al. [2001]
1024B	1.0	168	0 (-120 to 180)	-300	Rudnicki et al. [2001]
1025B	0.9	98	190 (0 to 250)	95	Rudnicki et al. [2001]
1026C	3.3	229	180 (-60 to 240)	130	Rudnicki et al. [2001]
1028A	1.6	131	120 (60 to 250)	300	Rudnicki et al. [2001]
1029A	1.6	120	120 (-170 to 170)	0	Rudnicki et al. [2001]
1030B	1.3	47	2400	2000	Rudnicki et al. [2001]
				1700 to 2000	[*Giambalvo et al.*, 2002]
1031A	1.2	41	3800 (3600 to 4500)	>4000	Rudnicki et al. [2001]
				3600 to 4500	[*Giambalvo et al.*, 2002]

***** The specific discharge that best fits SO_4^{2-}, Mg^{2+} and Ca^{2+} simultaneously. The range of specific discharge rates in which the calculated misfit is within 15% of the best fit is in parentheses.

Appendix G – Comparison of heat flow between nearby measurement locations

The figure below shows differences in heat flow fraction (the ratio of measured conductive heat flow to predicted total lithospheric heat flow) between pairs of heat flow measurements within 500 m of one another from the global marine heat flow compilation [*Hasterok et al.*, 2011]. Heat flow measurements from continental margins are excluded. Heat flow fraction differences between measurements separated by tens of metres are generally no smaller than differences between measurements that are farther apart. This suggests heat flow measured *near* to oceanic drill holes cannot reliably predict heat flow at the drill holes themselves.

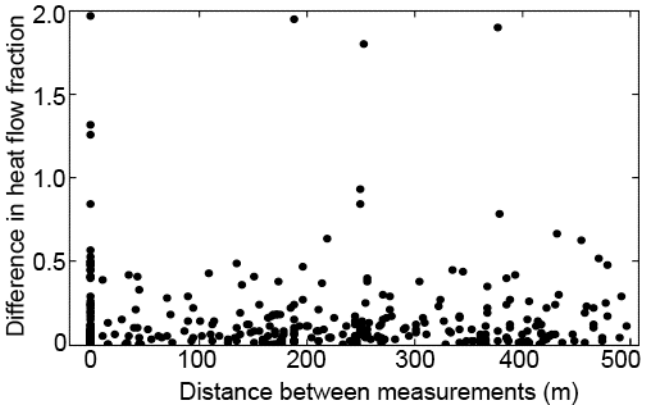

Appendix H – Uncertainty in chemical reaction parameters

The graphs below compare the best fitting reaction parameter values to uncertainty in related reaction parameters. The apparent calcium carbonate solubility product ($k`_{sp}$) and the first order reaction parameter k_{CaCO3} both affect Ca^{2+} reactivity. The initial metabolizable organic carbon (G_0) and the constant A both affect SO_4^{2-} reactivity.

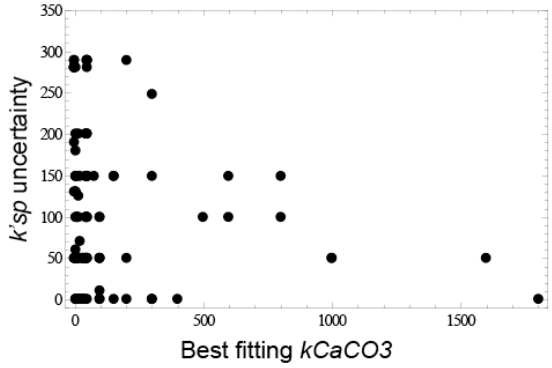

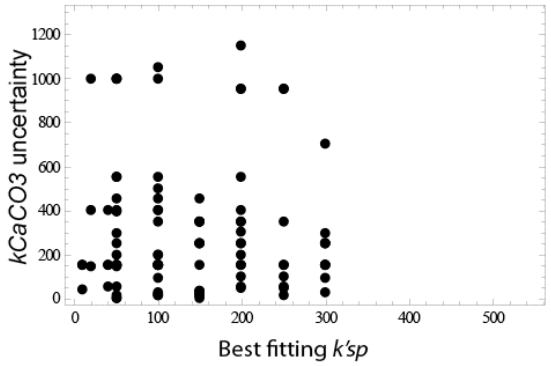

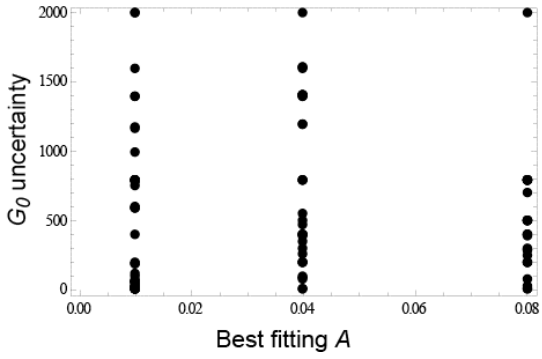

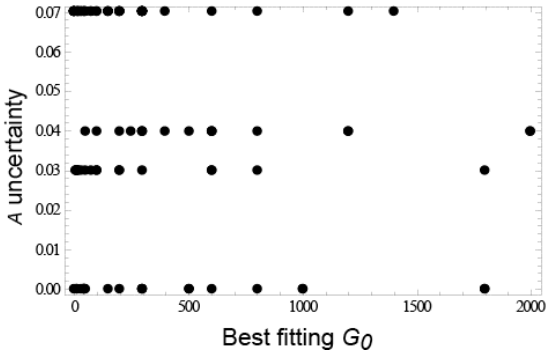

Appendix I – Comparison of chemical reaction parameters to sediment type

The graphs below compare the best fitting reaction parameters values to sediment type. Holes in which the reaction parameter values are not well constrained (where the uncertainty is >20% of the total range of values tested in the modelling) are excluded.

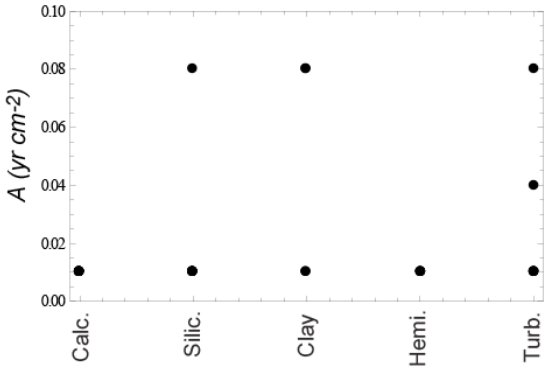

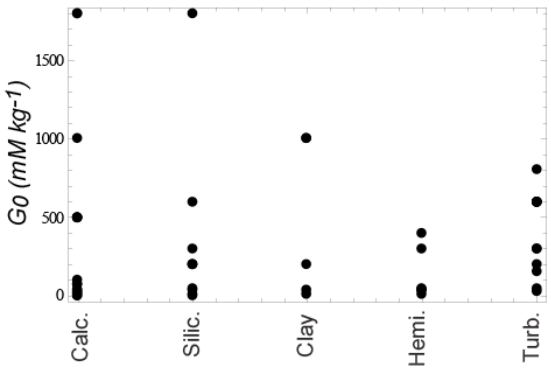

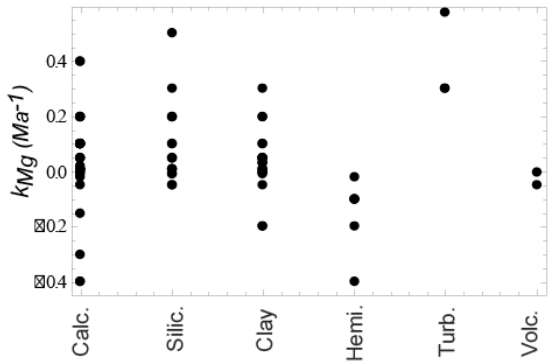

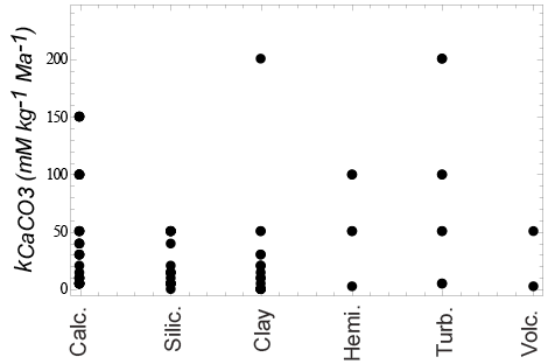

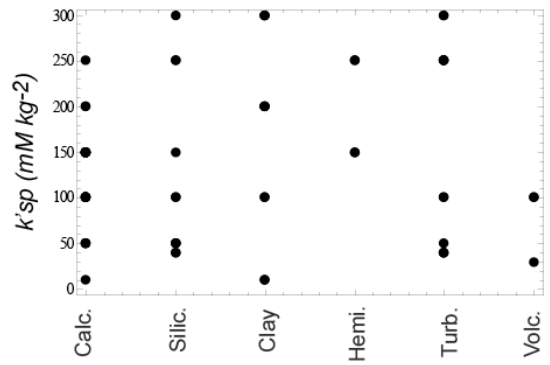

Appendix J - DVD

This appendix refers to the companion DVD containing the following digital materials:

- model computer codes
- data compilations
- supplementary tables